# A TPC (Time Projection Chamber) for axion searches in the CAST experiment at CERN

Memoria presentada por
**Berta Beltrán Lizarraga**
para optar al grado de Doctor
en Ciencias Físicas

**Laboratorio de Física Nuclear y Altas Energías**
Departamento de Física Teórica
Área de Física Atómica, Molecular y Nuclear
UNIVERSIDAD DE ZARAGOZA

Mayo 2006

# Acknowledgements

In first place I would like to thank professor Julio Morales, who offered me the possibility of joining and profiting from the knowledge and experience from the Particle Physics group in Zaragoza, together with the unique experience of being an active part of an international collaboration running a leading experiment placed at CERN. His full support and availability to attend any of my worries or ideas have been always remarkable.

From Igor G. Irastorza I must thank the trust he has shown in my person, always tutoring and guiding me in the work that I have developed within the CAST collaboration. Working with him always has meant to learn leading statistical and data analysis techniques, as he has opened to me a door to the most beautiful and intriguing scientific knowledge and methodology.

The enriching experience of working and living at CERN is one of the things that I will gratefully remember from this period of my life. For this I must thank the whole CAST group for the nice discussions and the always friendly enviroment where we all have developed our work. Prof. Konstantin Zioutas and Martyn Davenport are the motor of the CAST experiment, and the collaboration is the moving machinery that makes CAST a real thing. I would like to thank specially all the people (even the CAST outsiders) with whom I have shared most of my time at CERN: Theopisti, Biljana, Marie, Donghwa, Georgos, Thomas, Jaime, Daniel, Rob, Julia, David... and the large queue that I am missing for not filling a page just with names.

The thesis presented here aims to introduce the work that I have developed within the CAST experiment, analysing the data gathered with the TPC. None of this could have even happened without all the work from the people that contributed setting up the detector: from L. Di Lella who designed it, passing through D. Autiero, M. Hasinoff and B. Lakic, who collaborated building and characterising it, and finally I. Irastorza who designed and wrote the acquisition and analysis software that I have extensively used in the ongoing on my job.

Finally I would to thank also the Zaragoza group for hosting and coaching me, and also for the nice coffee and dinner moments that I have shared within all of them.

This work has been supported by the *Diputación General de Aragón* (D.G.A.) and the MEC (former CICyT) under the projects FPA2001-1767

and FPA2004-00973.

Por supuesto no puedo acabar este apartado sin mencionar a mis padres y hermanos, ya que en ellos radica todo lo que soy. Su incondicional apoyo y compañía me han arropado siempre, mientras que su eterna paciencia y comprensión me han ayudado en los momentos en que más lo he necesitado.

# Una TPC para búsqueda de axiones en el experimento CAST del CERN

El objetivo de esta memoria es el análisis de los datos tomados con uno de los detectores del experimento CAST, la cámara de proyección temporal (TPC en sus siglas en inglés), durante los años 2003 y 2004. El experimento CAST (CERN Axion Solar Telescope), situado en el CERN, reutiliza un imán de pruebas del LHC como un helioscopio de axiones. Estas hipotéticas partículas fueron inicialmente postuladas por R. Peccei y H. Quinn para resolver un problema que aparece en QCD, y podrían ser uno de los candidatos a la materia oscura fría del Universo. Es por esto que la búsqueda de axiones es un campo muy activo de la Física de Astropartículas, en el cual CAST y sus resultados juegan un papel primordial, ya que estos han permitido disminuir la cota superior a la constante de acoplo axión-fotón, proporcionado el valor más restrictivo obtenido hasta la fecha en el rango de masas de hasta 0.02 eV.

## Introducción

Para entender qué son los axiones, uno debe remontarse al llamado *strong CP problem* del modelo estándar de las partículas elementales, el cual predice que la fuerza fuerte debería violar una de la simetría fundamentales de la naturaleza, la llamada CP, al igual que lo hace la fuerza débil. Pero hasta la fecha ningún experimento ha detectado dicha violación, hecho que empezó a intrigar a los físicos de partículas a comienzos de los años 70.

En 1977 R. Peccei y H. Quinn introdujeron en el modelo estándar de las partículas elementales un nuevo mecanismo teórico para preservar dicha simetría en la fuerza fuerte, el cual hasta la fecha es la solución más elegante a este problema. Posteriormente, en 1978, F. Wilczeck y S. Weimberg se dieron cuenta independientemente de que una nueva partícula aparecía de forma natural en el marco de esta nueva teoría, y la bautizaron con el nombre de *axión*. Así, un nuevo bosón pseudoescalar entraba a formar parte del ya

de por si extenso zoo de las partículas elementales, y es su observación lo que permitirá confirmar el mecanismo Peccei-Quinn.

Los axiones podrían formar parte de la materia no-bariónica del Universo, tanto como componentes fósiles provenientes de los primeros momentos del Universo, o como partículas recién creadas en el centro de una estrella. De hecho, en el primer caso, la densidad de axiones en el Universo podría ser suficiente como para que los axiones compusiesen la omnipresente Materia Oscura.

Este bosón interacciona de una forma muy débil con la materia, convirtiéndose así en una partícula muy esquiva, imposible de detectar de forma directa. Su observación supone, por tanto, un reto para los físicos, ya que se debe recurrir a métodos sofisticados e inteligentes para su búsqueda. Desde que los axiones fueron propuestos, diferentes técnicas para su búsqueda han sido propuestas, a cada cual más ingeniosa y pintoresca, aunque todas ellas tienen el común denominador de estar basadas en el efecto Primakoff, el cual postula que los axiones podrían convertirse en fotones y viceversa en presencia de campos eléctricos o magnéticos. Por ejemplo, cavidades de microondas resonantes ajustables, embebidas en un campo magnético, esperan detectar los axiones fósiles que se encontrarían en el halo de nuestra galaxia, mientras que helioscopios son apuntados al Sol esperando así poder detectar los axiones que escaparían de su centro. También en un laboratorio estos elusivos bosones podrían ser creados y por tanto detectados usando un haz láser que atraviesa el seno de un campo magnético.

## El experimento CAST

El experimento CAST es un helioscopio de axiones de los mencionados en la sección anterior. El principio básico de funcionamiento de este tipo de experimentos aparece esquematizado en la figura 1.

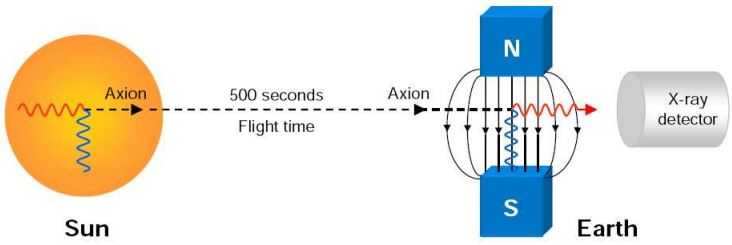


Figura 1: *Principio esquemático de funcionamiento de un telescopio solar de axiones. Un axion viajando hacia la tierra desde el centro del Sol se transformaría en un fotón en el campo magnético transversal del imán, incidiendo este posteriormente en un detector de rayos X.*

El principal componente de CAST es un imán de 10 m de largo capaz de

generar un campo magnético transversal de hasta 10 Teslas en su interior, que inicialmente fue diseñado y construido para probar la viabilidad de la tecnología necesaria para los imanes del LHC. Este imán está colocado sobre un plataforma con capacidad de movimiento, de forma que todo el conjunto puede seguir al Sol durante aproximadamente una hora y media al amanecer y otro tanto al anochecer. La figura 2 muestra un esquema de dicho experimento.

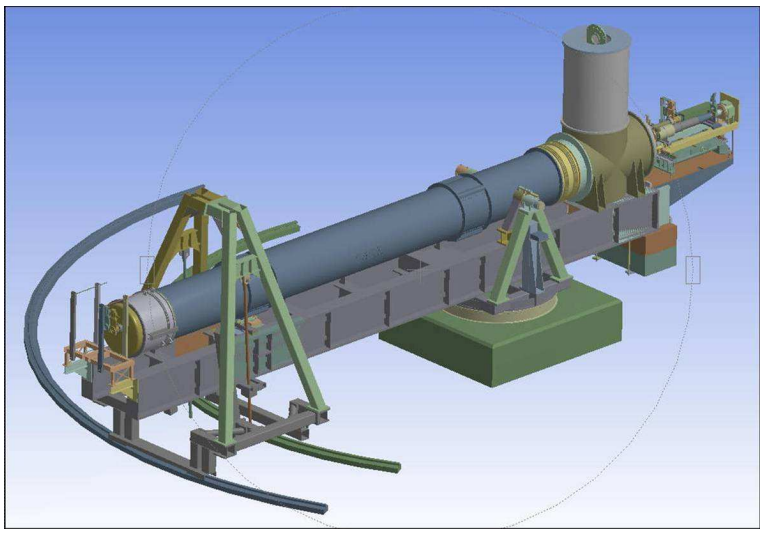

Figura 2: *El experimento CAST en el CERN.*

En CAST tres detectores distintos buscan este exceso de rayos X. Para detectar los fotones producidos cuando se apunta al Sol durante hora y media al amanecer hay una CCD (*Charge Coupled Device*), acoplada a un telescopio que focaliza la señal proveniente del imán en un punto de 3 mm de diámetro, incrementando así de una forma considerable el cociente señal/fondo. Junto al mismo se encuentra una cámara proporcional que usa una tecnología muy novedosa para recoger la señal llamada Micromegas. Una cámara de proyección temporal, (*TPC, Time Proyection Chamber*) situada en el extremo opuesto del imán recoge los fotones que vendrían cuando se sigue al Sol durante la otra hora y media al anochecer.

En la figura 3 se muestra un dibujo esquematizado de la cámara junto con sus dimensiones.

## Resultados

### Datos tomados durante el año 2003

Durante el año 2003 la TPC tomó $\sim$ 783 horas de datos siendo aproximadamente un 9 % de ellas tomadas con el imán apuntando al Sol. Los datos

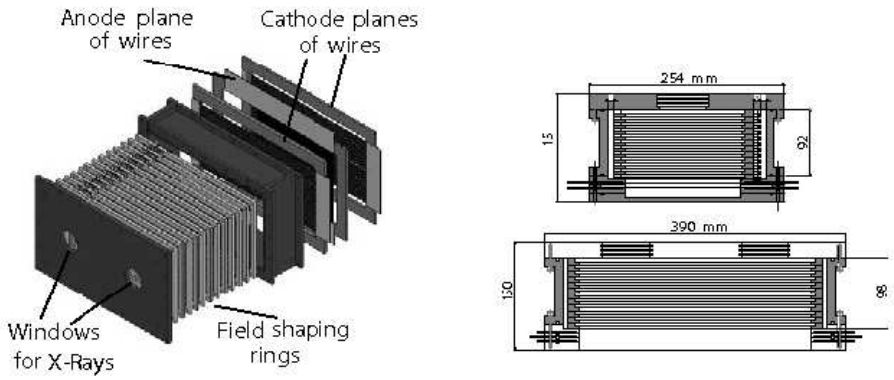


Figura 3: *Diseño esquemático de la TPC de CAST.*

recogidos durante los periodos de tiempo en que el imán no sigue al Sol son posteriormente utilizados para estimar qué proporción del espectro de energías construido con los datos tomados durante el tiempo de alineamiento son debidos al fondo ambiental. En este año inicialmente ambos espectros, el de alineamiento con el Sol y el de fondo, eran incompatibles y por tanto se llevaron a cabo varias chequeos para comprender el origen de dicha discrepancia. Finalmente se pudo probar que una fuerte dependencia de los datos con respecto a la posición de la TPC dentro del área experimental fue la causa de dicha discrepancia.

Un *fondo efectivo* fue construido usando solo aquellos datos que habían sido tomados en la mismas posiciones que los de alineamiento, siendo además pesados de manera adecuada con la exposición relativa de cada una de estas posiciones.

Comparando el espectro de alineamiento con el de fondo para los datos tomados en la zona de la TPC expuesta a los rayos X provenientes de las apertura el imán, se vio que eran compatibles y por tanto no apareció señal de axiones alguna por encima del fondo. Esto hecho quedó confirmado de manera cuantitativa con el resultado del test de hipótesis nula,

$$\chi^2_{nula}/d.o.f = 18{,}2/18. \tag{1}$$

Esta ausencia de señal permite la obtención de un límite superior para la constante de acoplo axión-fotón, que fue calculada de una forma conservadora tomando el limite que abarca el 95 % de la distribución de probabilidad Bayesiana, con una función previa para $g^4_{a\gamma}$ constante y positiva. El límite así obtenido con los datos tomados por la TPC durante el 2003 es,

$$g_{a\gamma}(95\,\%\text{C.L}) < 1{,}55 \times 10^{-10}\,\text{GeV}^{-1} \;\text{ para }\; m_a \lesssim 0{,}028\,\text{eV}, \tag{2}$$

que aparece dibujado con la línea azul en la figura 5.

Como este resultado ha sido calculado usando un fondo efectivo, es de esperar que esté influenciado por un cierto error sistemático. Existe una zona de la TPC en la que no se espera señal alguna ya que no está directamente expuesta a los eventos provenientes de las dos aperturas del imán. Es obvio que en este caso los espectros de alineamiento y de fondo deberían ser compatibles, ya que en ambos casos solo están compuestos por radiación ambiental. Para estimar un límite superior a este error podemos recurrir a los datos tomados en esta zona. Variando artificialmente el espectro de fondo hasta que el test de hipótesis nula, $\chi^2_{nula}$, dé un resultado cuya probabilidad según la distribución $\chi^2$ sea menor de un 5 %, se puede calcular el correspondiente intervalo permitido de variación de esta cota superior de $g_{a\gamma}$ dada en 2, obteniendo en el caso de los datos del 2003 que dicho intervalo es de un 15 %.

Combinado el resultado de la TPC con el obtenido con los otros dos detectores de CAST se llegó finalmente la siguiente cota superior para la constante de acoplo axión-fotón,

$$g_{a\gamma}(95\,\%\text{C.L}) < 1{,}16 \times 10^{-10}\,\text{GeV}^{-1} \;\text{ para }\; m_a \lesssim 0{,}028\,\text{eV}. \qquad (3)$$

## Datos tomados durante el año 2004

Durante el año 2004 la TPC pasó alineada con el Sol $\sim$ 203 horas, mientras que aproximadamente 142 días estuvo tomando datos de fondo. Esto significa que los datos de alineamiento tomados en este año fueron un factor $\sim$ 3 mas abundantes que en el 2003, y en el caso de los de fondo el factor sube hasta $\sim$ 5. Estos datos fueron tomados de una forma homogénea en el tiempo.

Como en el año 2003 los datos de la TPC estaban influenciados por una dependencia con su posición dentro del área experimental, en el 2004 se siguió un estricto procedimiento de toma de fondo, de forma que todas las posiciones de la TPC en el experimento contribuyesen de la misma manera al fondo total.

Por otro lado un blindaje pasivo diseñado y construido por el grupo de astropartículas de Zaragoza fue instalado este año alrededor de la TPC (ver figura 4).

Dicho blindaje está compuesto, desde fuera hacia dentro, por un capa de 22 cm de polietileno que termaliza los neutrones de altas energías, seguida de una lámina de 1 mm de espesor de cadmio que absorbe la mayor parte de estos neutrones termalizados. Una pared de 2.5 cm de espesor de plomo actúa como moderadora del flujo de rayos gamma de alta y media energía que alcanza el detector, seguida finalmente por una caja de cobre de 5 mm de espesor, que actúa como una caja de Faraday ofreciendo además soporte mecánico a toda la estructura. Todo el blindaje está herméticamente cerrado

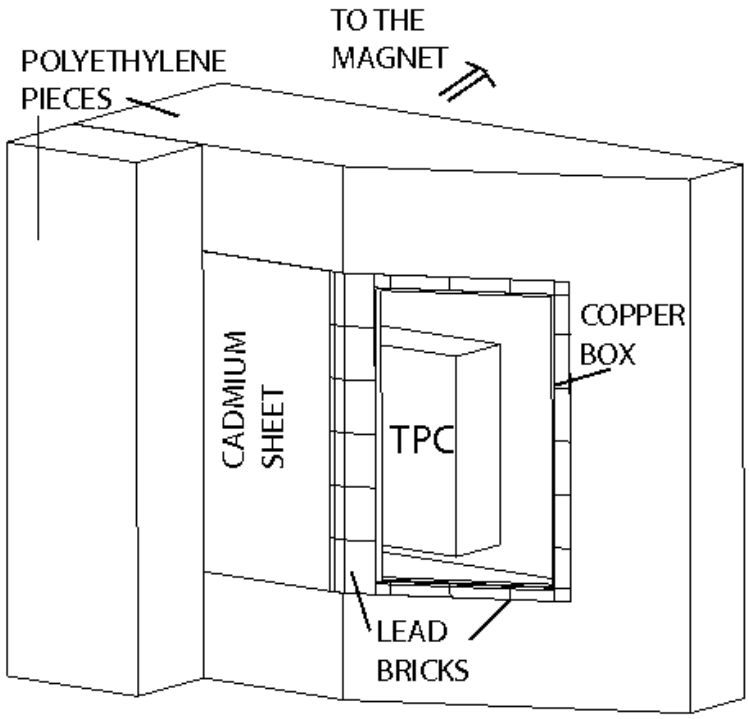


Figura 4: *Dibujo mostrando las distintas capas que componen el blindaje instalado alrededor de la TPC durante el 2004.*

por una bolsa de PVC que nos permite insuflar la parte interna con gas nitrógeno para limpiar este espacio de radón.

Gracias al blindaje el nivel de fondo alcanzado en el 2004 se redujo en un factor $\sim 4{,}3$ con respecto al caso de la TPC completamente descubierta, siendo en promedio de $(4{,}15 \pm 0{,}01) \times 10^{-5}$ cuentas/keV/s/cm$^2$. También en este año los datos tomados por al TPC en distintas zonas del experimento presentaron un nivel de homogeneidad muy alto, demostrando así que el blindaje es capaz de reducir en gran manera las preocupantes variaciones que afectaron a los datos tomados en el 2003.

Tal y como se hizo en el año 2003, antes de proceder al análisis de los datos tomados en el 2004 es preciso estudiarlos por si hubiese algún otro efecto sistemático que diferenciase el espectro de alineamiento del de fondo y por tanto no podamos extraer el fondo durante los periodos de alineamiento de este últimos. Para esto nuevamente se recurrió a los datos de la zona de la TPC sin señal, y esta vez, tal y como se esperaba, el espectro de alineamiento era compatible con el total de fondo dentro del error. Esto fue

así mismo confirmado matemáticamente mediante el test de hipótesis nula al obtener:

$$\chi^2_{nula}/d.o.f = 28{,}69/29. \tag{4}$$

A la vista de este resultado vemos que para los datos tomados durante el 2004 no hubo necesidad de construir un fondo efectivo ya que el blindaje logró reducir las variaciones del fondo con respecto a la posición.

Restando a los datos de alineamiento los de fondo, se ve que también este año lo obtenido es compatible con la hipótesis de ausencia de señal,

$$\chi^2_{nula}/d.o.f = 18{,}67/18, \tag{5}$$

de forma que nuevamente podemos dar una cota superior a la constante de acoplo axión-fotón de,

$$g_{a\gamma}(95\,\%\text{C.L}) < 1{,}29 \times 10^{-10}\,\text{GeV}^{-1} \;\text{ para }\; m_a \lesssim 0{,}028\,\text{eV}. \tag{6}$$

Dicho valor aparece representado por la línea roja en la figura 5.

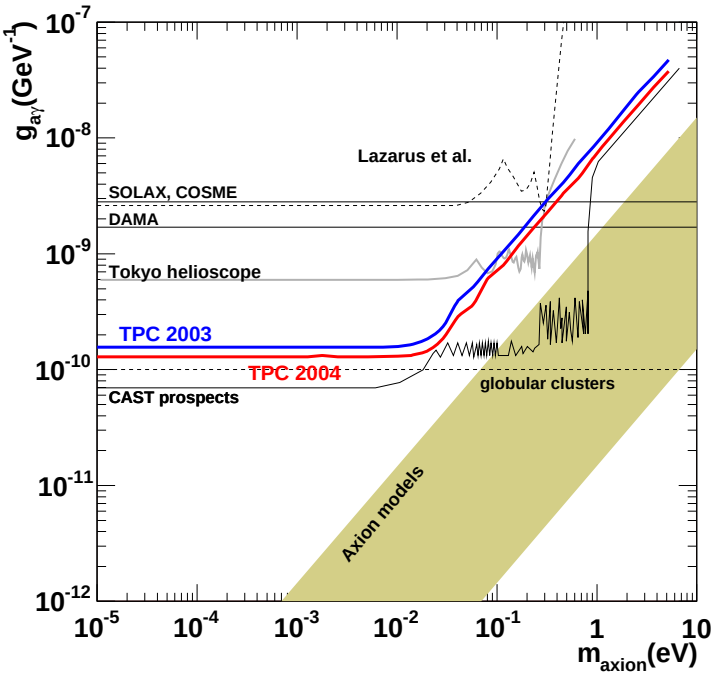


Figura 5: *Gráfica de exclusión (95 % C.L) para los datos del año 2003 (línea azul) y los del 2004 (línea roja) tomados por la TPC. También se muestran los resultados de experimentos previos para demostrar la mejora alcanzada con estos datos.*

# Introduction

The QCD theory, which describes the strong interactions, suffers from the so-called *strong CP problem*: the CP symmetry could be violated by the interactions described by it, yet Nature has never exhibited this behaviour in any experiment. The most elegant solution to this problem was proposed in 1977 by R. Peccei and H. Quinn by introducing a new symmetry in the theory. Immediately and independently S. Weinberg and F. Wilczek realized that, since this new symmetry should be spontaneously broken, its appearance on the theory should be accompanied by a new massless boson, the axion.

Axions could be a component of the non-baryonic matter of our Universe, both as an aged relic coming from the early times of the Universe, or as a new born particle in the core of a star. Furthermore, in the former case, the density of axions in the Universe could be enough for them to account for the ubiquitous cold Dark Matter.

Since axions were proposed, several ingenious and colourful techniques have come out to join the race on being the first one on detecting these intriguing particles, being most of them based on the Primakoff effect, which states that axions can turn into photons, and vice versa, in the presence of electric or magnetic fields. As an example, tunable microwave cavities permeated with a magnetic field are waiting for the relic axions which could fill our galactic halo, while *helioscopes* track our Sun expecting to detect the axions that would have escaped from its core. In a laboratory, these elusive bosons could be generated by means of a laser beam travelling along a strong magnetic field.

The CAST (CERN Axion Solar Telescope) experiment belongs to the axion helioscopes category. This experiment is built upon a refurbished 10 m long twin aperture magnet, initially designed as a test of the technology used for the LHC magnets, which can reach a nominal magnetic field of 9 T. A moving platform holds the magnet, allowing it to track the Sun for $\sim$1.5 h during the sunset, and just as much during the sunrise. The working principle of an axion helioscope is illustrated in figure 6.

At both ends of the magnet, three different detectors are placed to look for any X-ray excess when the magnet is pointing to the Sun. Facing sunrise axions a small gaseous detector with novel MICROMEGAS (micromesh

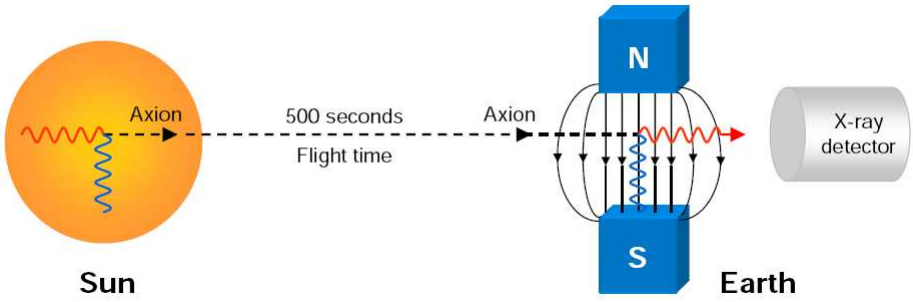


Figure 6: *Schematic representation of the axion helioscope working principle: an axion coming from the Sun core would be transformed under the effect of a trasverse magnetic field into a photon which will be further recorded by an X-ray detector.*

gaseous structure) readout is placed behind one of the magnet bores, while in the other one a X-ray mirror telescope would focus the axion-converted-photons to a $\sim 6$ mm$^2$ spot on a pn-CCD detector. The enhanced signal-to-background ratio achieved thanks to the use of this focusing device substantially improves the sensitivity of the experiment. On the other magnet's end, covering both bores, a conventional TPC (Time Projection Chamber) is looking for the X-rays from the sunset axions. The operation of the CAST experiment is forseen in two different phases:

- Phase I (completed): During the years 2003 and 2004 the magnet operated with vacuum inside the magnet bores, being sensitive to axions with mass up to $\lesssim 0.02$ eV since the coherence between the axion and the photon fields inside the magnet for higher axion masses is lost.
- Phase II: In order to restore the lost coherence the magnet bores are filled with a buffer gas, thus extending the sensitivity of the experiment up to masses of $\sim 0.8$ eV.

The aim of the present book is to summarise the work that has been developed in the last four years to look for solar axions using the TPC X-ray detector of the CAST experiment. During this time the detector has gone under the commissioning and fully operation stages, having provided already results for both the 2003 and 2004 data taking periods.

In the first part of this work the theoretical motivation for the axion, together with its properties and its production mechanisms will be reviewed. The second part is devoted to the description of both the CAST experiment and the TPC detector, in order to set the proper framework for the introduction of the last part of the work where the analysis of the collected data will be explained, also quoting the results obtained.


Figure 7: *CAST logo.*

# Contents

# Part I

# Axions

# Chapter 1

# The axion field

In this chapter the origin of the Strong CP problem and the most attractive solution to it pointed out by R. Peccei and H. Quinn in 1977 -from which the axion appears as a first consequence- will be studied. The different axion models and properties are going to be mentioned, followed by all the cosmological and astrophysical mechanisms involucrated in the production of this neutral boson. Since the presence axions in the Universe nowadays would have detectable consequences, the bound on its mass coming form the lack of any positive cosmological or astrophysical observation of it will be quoted. Finally, the wide range of original techniques that have been developed along the years to detect axions will be explained.

Very nice reviews on the matter exists already, (see for example [1, 2, 3]) and therefore here only a brief review on the matter will be given.

## 1.1. The Strong CP problem and its solutions

### 1.1.1. The Strong CP problem

QCD is the universally accepted theory for describing the strong interactions, but it has one serious blemish: the so-called "Strong CP Problem", which will be described in what follows.

Before 1975, QCD was described by the Lagrangian:

$$\mathcal{L} = -\frac{1}{4g^2} Tr F_{\mu\nu} F^{\mu\nu} + \bar{q}(i\gamma^\mu D_\mu - M_q)q, \tag{1.1}$$

where $q$ and $M_q$ are the quark field and quark mass matrices, and:

$$\begin{aligned} &F_{\mu\nu} = \partial_\mu A_\nu - \partial_\nu A_\mu - i[A_\mu, A_\nu], \\ &A_\mu = \sum_a A_\mu^a (\lambda^a/2), \\ &\lambda^a = \text{Gell} - \text{Mann matrices.} \end{aligned} \tag{1.2}$$

In the 1970s, solutions to the classical field equations in the 4 dimensional Euclidean space (instantons [4]) were extensively studied, being found that QCD has a very rich vacuum structure because of the existence of non-trivial vacuum gauge configurations. The topological number $n$, known as Pontryagin index:

$$n = \frac{1}{32\pi^2} \int \mathrm{d}^4 x F_{\mu\nu}^a \widetilde{F}_{\mu\nu}^a, \tag{1.3}$$

being $\widetilde{F}_{\mu\nu} = 1/2\epsilon_{\mu\nu\rho\sigma} F_{\rho\sigma}$ the dual of the field strength, classifies all these degenerate vacuum configurations of the theory, which thus are denoted by:

$$\ldots|-1\rangle, |0\rangle, |1\rangle, |2\rangle, \ldots |n\rangle \ldots \tag{1.4}$$

Figure 1.1 shows a scheme of the degenerated vacuum structure of the theory, where every state is labelled by its Pontryagin index n. Since a well-defined gauge transformation G exists, which shifts the configuration $|n\rangle$ into $|n+1\rangle$ for any $n$, the $|n\rangle$ can not be the properly defined vacuum state of the theory. Instead, the true vacuum is a superposition of all these degenerate states $|n\rangle$:

$$|\Theta\rangle = \sum_n e^{(-in\Theta)} |n\rangle, \tag{1.5}$$

which maps into itself under G. In the literature, this state is quoted as the $\Theta$-vacuum. A priori, the angle $\Theta$ is an arbitrary parameter of the theory, which can run from 0 to $2\pi$. States of different $\Theta$ are the physically distinct vacua for the theory, each with a distinct world of physics built upon it.

By appropriate means the effects of this $\Theta$-vacuum can be recast into a single, additional non-perturbative term in the QCD Lagrangian:

$$\mathcal{L}_{QCD} = \mathcal{L}_{pert} + \bar{\Theta} \frac{g^2}{32\pi^2} \mathrm{Tr} F_{\mu\nu} \widetilde{F}^{\mu\nu}, \quad \bar{\Theta} = \Theta + \mathrm{Arg}\,\mathrm{det}\mathcal{M} \tag{1.6}$$

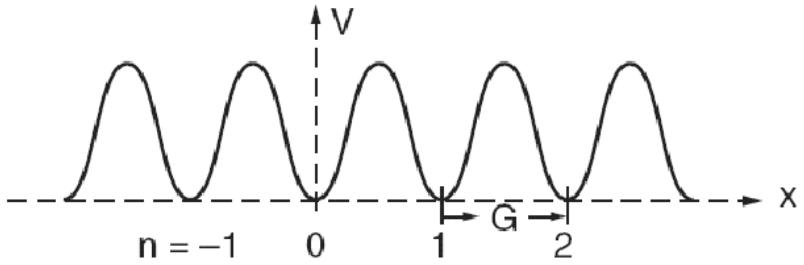


Figure 1.1: *Cartoon of the potential for the QCD theory [5].*

where $\mathcal{M}$ is the quark mass matrix. This extra term arises due to two separate and independent effects: the $\Theta$ structure of the pure QCD vacuum, and electroweak effects involving the quark masses, being both unrelated contributions, which a priori have no reason to cancel.

Such a term in the QCD Lagrangian clearly violates CP, T and P in the case of $\bar{\Theta} \neq 0$, yet Nature has never exhibited this in any experiment. Moreover, the value of the neutron electric dipole moment depends on $\bar{\Theta}$, and the present experimental bound [6] $d_N < 6.3 \times 10^{-26}$ e.cm constrains $\bar{\Theta}$ to be less than (or of the order of) $10^{-10}$. The mystery of why the *arbitrary* parameter $\bar{\Theta}$ must be so small is the strong CP problem.

### 1.1.2. Peccei and Quinn solution

Various theoretical attempts to solve this problem have been postulated [1, 7], being the most elegant solution the one proposed by R. Peccei and H. Quinn in 1977 [8]. Their idea was to make $\bar{\Theta}$ a dynamical variable with a classical potential that is minimised by $\bar{\Theta} = 0$. This is accomplished by introducing an additional global, chiral symmetry, known as PQ (Peccei-Quinn) symmetry $U(1)_{PQ}$, which is spontaneously broken at a scale $f_{PQ}$. Technically, this new symmetry is not quite an exact one, but it is a pseudo-symmetry, broken only by non-perturbative or instanton effects, and this is why it works as desired. Immediately and independently, S. Weinberg [9] and F. Wilczek [10] realized that, because $U(1)_{PQ}$ is spontaneously broken, there should be a pseudo-Goldstone boson, "the axion" (or as Weinberg originally referred to it, "the higglet").

Taking this new symmetry into account, the QCD effective Lagrangian will be:

$$\begin{aligned}\mathcal{L}_{QCD} =& \mathcal{L}_{pert} + \bar{\Theta}\frac{g^2}{32\pi^2}\mathrm{Tr}F_{\mu\nu}\widetilde{F}^{\mu\nu} + \\ &+ C_a\frac{a}{f_{pq}}\frac{g^2}{32\pi^2}\mathrm{Tr}F_{\mu\nu}\widetilde{F}^{\mu\nu} - \frac{1}{2}\partial_\mu a\partial^\mu a + k,\end{aligned} \tag{1.7}$$

where $C_a$ and $k$ are model dependent quantities and a is the axion field. The second and third terms on the r.h.s of this Lagrangian amount to an effective potential for the axion field, which is then minimised by:

$$\langle a \rangle = -\frac{\bar{\Theta} f_{pq}}{C_a}. \tag{1.8}$$

The physical axion, of course, is defined as the excitation with its vacuum expectation removed:

$$a_{phys} = a - \langle a \rangle. \tag{1.9}$$

Then, in terms of this field on has:

$$\mathcal{L}_{QCD} = \mathcal{L}_{pert} - \frac{1}{2}\partial_\mu a_{phys}\partial^\mu a_{phys} + k + C_a \frac{a_{phys}}{f_{pq}} \frac{g^2}{32\pi^2} \mathrm{Tr} F_{\mu\nu}\widetilde{F}^{\mu\nu}. \tag{1.10}$$

We see here thus how the presence of the extra $U(1)_{PQ}$ symmetry[1] has eliminated the offending P, T, and CP violating $\bar{\Theta}$ parameter from the QCD Lagrangian, replacing it by a dynamical field: the axion.

### 1.1.3. Axions models

#### Visible axion models

In the original Peccei-Quinn model, which is a little bit different from what it has been presented here, the scale of the $U(1)_{PQ}$ breaking, $f_{PQ}$ was of the order of the electroweak symmetry breaking scale. As it will shown in the next section, the coupling of axions to ordinary matter are proportional to $(f_{PQ})^{-1}$, and hence with their assumption of the value of $f_{PQ}$, they would be of the order of the typical weak-interaction strength. This implies that the axion should roughly be as visible as a neutrino.

Accelerator data soon ruled out this *visible axion* model (see [1] for some examples). As there is no phenomenological reason why the Peccei-Quinn scale $f_{PQ}$ could not be much higher, a new model was born, the *invisible axion*, an extremely light particle with almost undetectable weak couplings.

#### Invisible axion models

If the Peccei-Quinn scale $f_{PQ}$ is to be split from the electroweak breaking one, some complex scalar SU(2)×U(1) singlet field $\sigma$ which carries PQ charge and possesses a vacuum expectation value $f_{PQ}/\sqrt{2}$ should be introduced, being the axion field contained on its phase. Two different models have been postulated regarding the invisible axions between 1979 and 1981 (see [11] for a nice historical review on their birth), mainly differing in the transformation properties of ordinary quarks and leptons under the extra chiral

[1] Such a global symmetry often arises in supersymmetric and superstring-inspired models in any case.

symmetry. The resulting axions from these models have different couplings to the ordinary fermions and photons.

- **The KSVZ axion:** This model was first presented by Kim [12] and by Shifman, Vainshtein and Zakharov [13]. Here the already known quarks and leptons do not feel the PQ symmetry, but $n$ new exotic heavy quarks carrying PQ charge $X_j$, $(j = 1...n)$, may be introduced (in the very original model $n$=1). The only free parameter of the model will be then $f_a = f_{PQ}/N$ with $N = \sum_j X_j$ ($f_a = f_{PQ}$ in the simple case of having only an extra heavy quark). Thus, in this model axions are entirely decoupled from the ordinary particles and, at low energies, they interact with matter and radiation only by virtue of their two-gluon coupling, which is generic for the PQ scheme. This model belongs to the *hadronic axions models* category, because the axion has not tree level coupling with leptons.

- **The DFSZ axion:** Invisible axions of this kind were first suggested by Zhitnitskiĭ [14] in a not very diffused paper written in Russian. Later, Dine, Fischler and Srednicki [15], whom did not know about this former paper, also presented this model. Here ordinary quarks and leptons do carry PQ charge, so one necessitates on the theory two Higgs doublets fields, $\Phi_1$ and $\Phi_2$, which also contains small components of the axion field. Since the fermions in the theory do not couple directly to $\sigma$, they feel the PQ breaking only trough these Higgs potentials. In this model $N$ is the number of standard families (presumably 3) and the remaining free parameters are again the $f_a = f_{PQ}/N$ and the new one $x = f_1/f_2$.

## 1.2. Axion properties

If axions are found experimentally, the Peccei-Quinn mechanism will be proven. In order to search for them, one must know how they couple to ordinary matter, their properties, and their production mechanisms. In what follows their main properties will be reviewed.

### 1.2.1. Axion mass

Because $U(1)_{PQ}$ suffers from a chiral anomaly, the axion acquires a small mass which is proportional to the curvature of the effective potential.

$$m_a^2 = \left\langle \frac{\partial^2 V_{eff}}{\partial a^2} \right\rangle = -\frac{C_a}{f_{PQ}} \frac{g^2}{32\pi^2} \frac{\partial}{\partial a} \langle F\widetilde{F} \rangle \Big|_{\langle a \rangle = -\frac{\bar{\Theta}}{C_a} f_{PQ}} . \tag{1.11}$$

By means of current algebra methods [16] this mass can be found to be[2]:

$$m_a = \frac{f_\pi m_\pi}{f_{PQ}/N}\left(\frac{z}{(1+z+w)(1+z)}\right)^{1/2} \simeq 0.6\,\mathrm{eV}\,\frac{10^7\mathrm{GeV}}{f_{PQ}/N}, \tag{1.12}$$

where $f_\pi \sim 93$ MeV and $m_\pi = 135$ MeV are the decay constant and mass of the pion respectively, and

$$\begin{aligned} z &= m_u/m_d = 0.553 \pm 0.043, \\ w &= m_u/m_s = 0.029 \pm 0.0043 \end{aligned} \tag{1.13}$$

the quark mass ratios [18].

It is noticeable that $m_a \propto (f_{PQ})^{-1}$, so the larger the constant $f_{PQ}$, the smaller the axion mass.

### 1.2.2. Axions couplings to matter

The strength of the axion's coupling to normal matter and radiation are given by the effective coupling constants $g_{a\gamma}$, $g_{ae}$, $g_{an}$,... for the coupling of axions to photons, electrons and nucleons. Expressions for such couplings can be found in references [16, 19, 17]. The triangle diagram coupling of axions to gluons (figure 1.2), is the most generic property of axions, and because of this, axions necessarily mix also with pions.

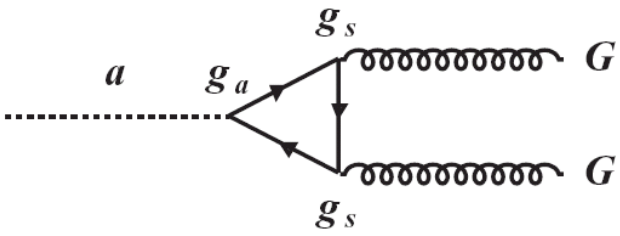


Figure 1.2: *The triangle loop of the interactions of axions to gluons, where $g_s$ is the strong coupling constant, and $g_a$ the axion fermion Yukawa coupling.*

The tree level coupling of axions to charged leptons is, however, optional. In the hadronic models (KSVZ) there are no axion coupling to electrons, while in the DFSZ they do exist, and are of the same strength as the tree level coupling to quarks.

As in the KSVZ model the hadronic axions do not couple to the light quarks at tree level, naively it should be expected that the axion-nucleon

[2]Following the notation in [17].

coupling is suppressed. But this is not the case, due to axion-pion mixing mentioned before. Because of this, the axion coupling to nucleons is comparable for both models.

Much of the same can be said for the axion coupling to photons, the one used in CAST to search for axions. Again two different effects contribute to it:

- By the generic coupling to gluons, axions couple to photons according to[3]:

$$\mathcal{L}_{QCD} = -\frac{1}{4} g_{a\gamma}\, F^{em}_{\mu\nu} \widetilde{F}^{\mu\nu}_{em}\, a = g_{a\gamma}\, \mathbf{E} \cdot \mathbf{B}\, a, \tag{1.14}$$

  where here $F^{em}$ is the electromagnetic field strength tensor. This intercation is shown in the diagram refereed as ii in the lower part of figure 1.3.

- In DFSZ models, as the quarks and leptons which carry PQ charges also carry electric charges, there is an extra contribution from a triangle loop (upper part of figure 1.3).

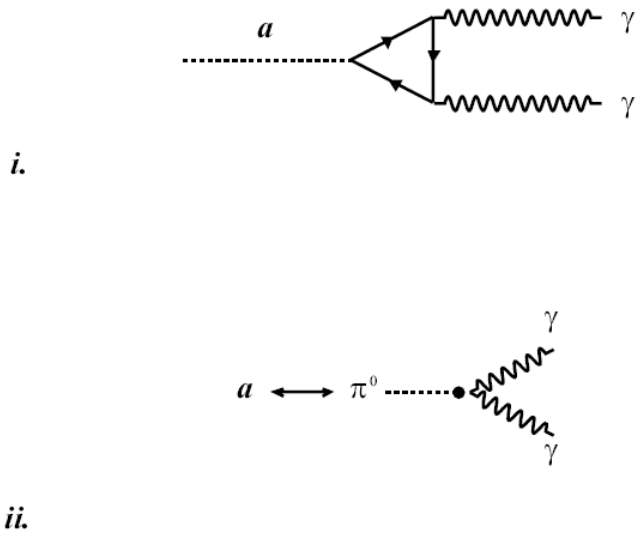


Figure 1.3: *The two contributions to the axion-photon coupling: the upper one arrives from the coupling to fermions that carry PQ charge (DFSZ) and the lower from the generic axion-pion mixing.*

[3]Again the notation in [17] is followed.

The total axion-photon coupling is then [16, 19]:

$$\begin{aligned} g_{a\gamma} =& \frac{\alpha}{2\pi(f_{PQ}/N)}\left(\frac{E}{N} - \frac{2(4+z+w)}{3(1+z+w)}\right) = \\ & \frac{\alpha}{2\pi(f_{PQ}/N)}\left(\frac{E}{N} - 1.93 \pm 0.08\right), \end{aligned} \tag{1.15}$$

where $\alpha$ is the fine structure constant and $z$ and $w$ have been defined in equation 1.13. Here $E$ and $N$ are the electromagnetic and colour anomalies respectively, such that in the DFSZ models their quotient is fixed to $E/N = 8/3$. For the hadronic axions models, however, this quotient could take different values, according to the fine tuning of each model. Simple hadronic axions models can yield $E/N = 2$ [19], in which case the axion to photon coupling is strongly suppressed and may actually vanish. Quoting Kaplan in [19]: "*Such a cancellation is immoral, but not unnatural.*"

The coupling of axions to photons allows for the decay $a \to 2\gamma$ as well as for the Primakoff conversion [4] $a \leftrightarrow \gamma$ in the presence of external electric or magnetic fields.

The most important feature of all the axion couplings ($g_{aii}$) is that they are proportional to $(f_{PQ})^{-1}$ or, equivalently, to $m_a$: the smaller the axion mass, or the larger the scale $f_{PQ}$, the more weakly the axion couples.

## 1.3. Axion sources in the Universe

### 1.3.1. Cosmological axions

In this section the axion production by cosmological mechanisms [2, 21] is reviewed.

**Axion strings decay.** In most axion models PQ symmetry breaking occurs when the complex scalar field $\sigma$ develops the vacuum expectation value $f_{PQ}/\sqrt{2}$ (first transition in figure 1.4). For this to happen, the Universe temperature $T$ has to cool down to the Peccei-Quinn scale $f_{PQ}$. In this stage the effective potential develops its expectation vacuum value, but still has rotational symmetry and thus the value of $\bar{\Theta}$ is not fixed yet. Here the axion appears as this massless degree of freedom $\bar{\Theta}$.

One intriguing consequence of the $U(1)_{PQ}$ symmetry breaking is the appearance of axion strings as topological defects [2]. The contribution to the density of axions today $\Omega_a$ coming from the string decay, depends crucially on when inflation took place. If the reheating temperature is less than $f_{PQ}$, the axion field gets homogenised during the process, and these axion strings

[4] Named after the analogous reaction involving neutral pions which was originally used to measure the pion-photon interaction strength [20].

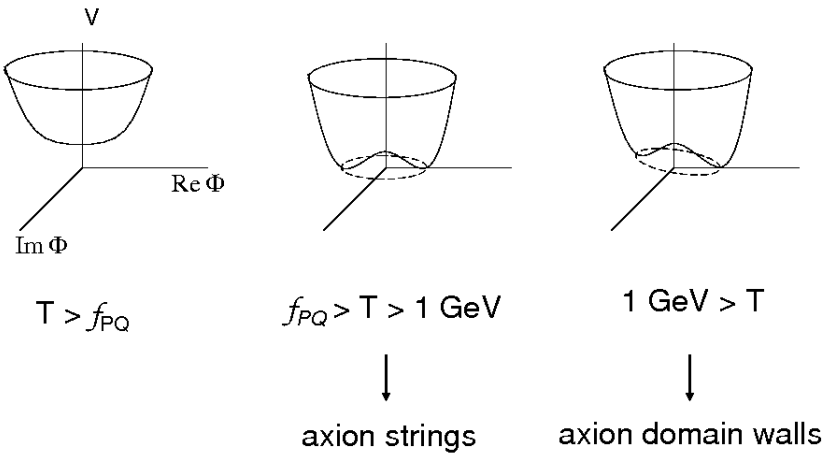


Figure 1.4: *Evolution of the effective axion potential as a function of the temperature T of the Universe.*

are blown away. If, on the other hand, inflation occurs with reheating temperature higher than $f_{PQ}$, it has no influence on the axion production and history and, therefore, for our purposes it is like inflation does not occur at all.

In this case the axion strings will radiate axions until T approaches the QCD scale $\Lambda_{QCD}$, when instanton effects start to play a role turning on the axion effective potential, and the axion adquires its mass (which at T>> it is very temperature dependent [2]). This new transition is represented in the last transition of figure 1.4. At this point each string will become the boundary of a domain wall[5], which eventually will decay away as it is unstable, contributing this way also to the axion density.

In order to calculate the number density of axion production via axion strings emission, the axion spectrum radiated by an axion string must be estimated, and here is where the debate heats up. Battye and Shellard [22] found using computer simulations that the dominant source of axion radiation are strings loops rather than the long strings, and that the axion radiation is strongly peaked at wavelengths of the order of the loop size. In their model the loop contribution to the cosmic axion density is [23]:

$$\Omega_{strings}h^2 \approx 88 \times 3^{\pm 1}[(1+\alpha/\kappa)^{3/2} - 1]\left(\frac{1\mu\text{eV}}{m_a}\right)^{1.175}. \qquad (1.16)$$

[5]Properly speaking each axion string can become the boundary of N domain walls, but if N>1 there is a domain wall problem because axion domain walls end up dominating the energy density, resulting in a Universe very different from the one observed today[21]. Hence here it is assumed that N=1.

Here $\Omega_{strings}$ is the ratio of the axion density $\rho_a$ to the critical density for closing the universe $\rho_{crit}$, $h$ is the Hubble constant in units of 100 km s$^{-1}$ Mpc$^{-1}$, and the stated range reflects the recognised uncertainties of the cosmic conditions at the QCD phase transition and of the temperature-dependent axion mass. The values of $\alpha$ and $\kappa$ are not known, but probably $0.1 < \alpha/\kappa < 1.0$, taking the expression in squared brackets to 0.15-1.83. On the other hand, Sikivie *et al.* [24] found, using independent computer simulations, that the motion of global strings is strongly damped, leading to a flat axion spectrum. In this picture more of the string radiation energy goes into axion kinetic energy than in the previous one, so that ultimately there are fewer axions. In their case the axion density is [23]:

$$\Omega_{strings}h^2 \approx 1.9 \times 3^{\pm 1} \left(\frac{1\mu\text{eV}}{m_a}\right)^{1.175} . \tag{1.17}$$

Yamaguchi, Kawasaki and Yokoyama [25] had done computer simulations of a network of strings in an expanding universe, obtaining a result which lies between the former two. The contribution from wall decays is probably subdominant compared to the string one [26].

**Vacuum misalignment.** As mentioned in the previous paragraph, when the temperature of the Universe approaches the QCD scale $\Lambda_{QCD}$, the axion field acquires a mass. At time $t_1$ so that $m_a(t_1)t_1 = 1$, (whose corresponding temperature is T $\simeq$ 1 GeV [27]), the axion field starts to oscillate in response to the turn on of its mass (figure 1.5). While for T$>$ $\Lambda_{QCD}$ all the values

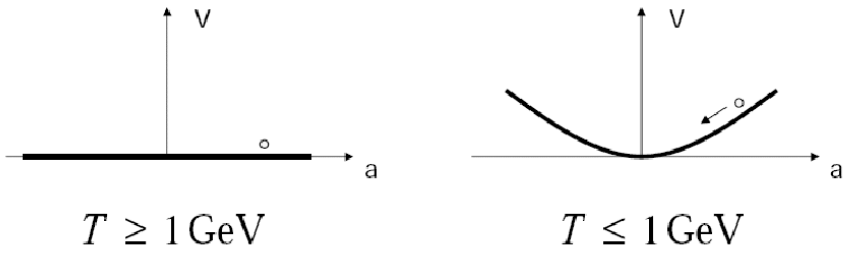


Figure 1.5: *Turn on of the axion effective potential at $T \simeq$ 1 GeV and the initial value of $\bar{\Theta}$ at this moment.*

of $\bar{\Theta}$ were equally probable, once the axion mass turns on the axion field beings to roll towards its nowadays value $\bar{\Theta} = 0$ and, of course, overshoots it. The axion field oscillations do not dissipate in other forms of energy and hence contribute also to the cosmological energy density today. The density of axions produced by this *vacuum realignment* mechanism is proportional to the initial realignment angle, i.e., the angle $\bar{\Theta}_1$ where the axion field was sitting for T$>$ $\Lambda_{QCD}$.

Again the contribution to the total axion density today in the universe through this mechanism depends on inflation occurring before or after the PQ symmetry breaking. In the first case, the value of $\bar{\Theta}_1$ is uniformly distributed in the non causally connected volumes of the Universe, while inflation has the power to uniformise its value to the entire Universe, which could then happen to lie close to cero (see [2] for a long discussion on this). Therefore inflation could have also suppressed this axion production mechanism.

The contribution to the cosmic critical density by this mechanism is given by [23]:

$$\Omega_{mis}h^2 \approx 1.9 \times 3^{\pm 1} \left(\frac{1\mu\text{eV}}{m_a}\right)^{1.175} \bar{\Theta}_1^2 F(\bar{\Theta}_1). \tag{1.18}$$

Here the function $F(\bar{\Theta})$ accounts for anharmonic corrections to the axion potential. In order to avoid fine-tuning of the initial misalignment conditions it should be expected that $\bar{\Theta}_1^2 F(\bar{\Theta}_1) \sim 1$, in which case we have that this axion density contribution would be of the same order as the one given by the axion strings decay as calculated by Sikivie *et al.* in equation 1.17. Battye and Shellard calculation, on the other hand, yields a contribution approximately ten times larger than the vacuum realignment, while Yamaguchi, Kawasaki and Yokoyama's estimation over passes this one by a factor of $\sim$3.

**Thermal production** Since the axion coupling to matter happen to be proportional to $(f_{PQ})^{-1}$, if $f_{PQ}$ is sufficiently small so that axion can interact sufficiently strongly, they will thermalize in the early universe. Roughly speaking, it can be said that when the reaction rate $\Gamma$ for a given process that creates and destroy a particle specie occurs rapidly compared to the expansion rate of the Universe $H$, this particle specie will be in thermal equilibrium. There is a time interval in the early universe, which depends on the main axion processes considered for the calculation of $\Gamma$, where these condition in fulfilled and axions are in good thermal contact with the universal plasma. Then, when the condition $\Gamma \gtrsim H$ is not satisfied anymore ($\Gamma$ is strongly temperature dependent), thermal axion decouple while they are still very relativistic, and survive until today as thermal relics, much on the way as light neutrinos do.

Thermal production of axions was first studied by Turner [28], whose main concern was to study the possibility that a thermal axion density greater than the one produced by the processes mentioned before could exist. Eventually he found this to happen for axions with $f_{PQ} \lesssim 10^8$ GeV. In his first paper Turned considered the main axion creation and destruction reactions to be the Primakoff process $\gamma + q \leftrightarrows a + q$, where $q$ is a light quark, and photoproduction $\gamma + Q \leftrightarrows a + Q$ where now $Q$ is a heavy quark. Later on he also included an axion-pion conversion $N + \pi \leftrightarrows N + a$, where $N$ is a nucleon.

More recent reviews on the matter, considering different thermalizing

processes, have appeared. Massó, Rota and Zsembinszki [29] study processes coming from the coupling of axion to gluons, which are model independent, and find that the condition to have thermalized axions in the early Universe is less restrictive than Turner's one: $f_{PQ} \lesssim 10^{12}$ GeV. Hannestad, Mirizzi and Raffelt [30], focus themselves in hadronic models and study the process $\pi + \pi \leftrightarrows \pi + a$.

All models anyhow find a present day axion density of thermal axions of the order of 1 to 100 cm$^{-3}$, with the characteristic that:

$$\Omega_{the} h^2 \propto m_a \tag{1.19}$$

contrary to the other two production mechanisms, where we were having:

$$\Omega_{string,\,mis} h^2 \propto (m_a)^{-1} \tag{1.20}$$

If there are non-thermal axions in the thermalizing epoch produced by the former mechanisms, they will end up thermalized as they will also interact with the QCD plasma, and we will end up then with a single thermal population of axions in the present epoch.

### 1.3.2. Axions as a Dark Matter candidate

Several facts, such as galactic rotational curves or the cosmic microwave background anisotropies, hint the fact that most of the matter density of the Universe today is composed of a non-luminous and non-absorbing component, called Dark Matter (DM) [31]. Its determining property is that it does not emit any electromagnetic radiation, and therefore can be only inferred by its gravitational effects. Two possibilities exist for the nature of the DM: either it is like the conventional matter, i.e., made of atoms (baryonic dark matter) but it has not yet been heat up enough to emit light, or it is not-baryonic. As axions are bosons, we will only worry about this last component.

The non-baryonic dark matter is usually divided in two groups: hot (relativistic on the onset of galaxy formation) dark matter (HDM), and cold (non-relativistic) dark matter (CDM). Axions could account for the two depending on their mass, as it is shown in figure 1.6. If $f_{PQ}$ is so large ($\sim$ small mass) that they never reached the thermal equilibrium, the thermal production is suppressed and then the misalignment mechanism will take over. As axions are not relativistic from the moment of their first appearance at 1 GeV temperature, they may be an important component of the CDM (depending on the axion mass they may even be the main component). In this case, as it has been pointed out in the previous section, the axion density is inversely proportional to its mass, and this explains the behaviour of the left part of the plot in figure 1.6.

If, on the other hand, the Peccei-Quinn scale is small enough for the axion to thermalize in the early Universe, a relativistic axion density would

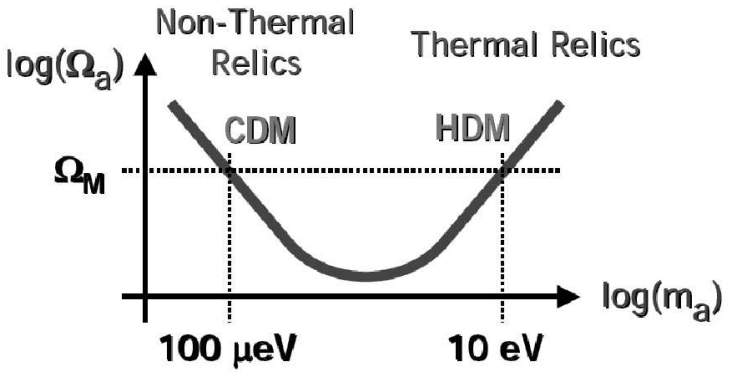


Figure 1.6: *Lee-Weinberg curve for axions, where their density contribution to the DM is shown as a function of the axion mass.*

exist today, which could contribute to the HDM component. In this case the density of axions is proportional to the axion mass, which will be of the order of eV since we are dealing with thermic axions. As CAST is sensitive to axion masses of this order, it is also sensitive to hot dark matter axions.

### 1.3.3. Astrophysical axions

Axions can be also produced in the stelar plasma, although their production rates and mechanisms are, again, very model dependent [32]. In the DFSZ model, where we have seen that axions can interact with charged leptons, the dominant creation process in low mass stars (main-sequence stars, red giants, horizontal brach stars and white dwarfs) is the Compton and bremsstrahlung processes (see figure 1.7). The Primakoff effect, in which a photon transforms into an axion in presence of the fluctuating electric field from the charged particles of the hot stelar plasma, is common for both models and the only relevant process for hadronic axions. In neutron star matter, the most important emission process is nucleon bremsstrahlung, NN $\rightarrow$ NNa again for both types of axions.

#### Primakoff process

As CAST looks for axions produced in the core of the Sun by this nearly-model-independent Primakoff process $\gamma + Ze, e^- \rightarrow Ze, e^- + a$, lets have a detailed look at it.

The Primakoff process cross section on a particle with charge $Ze$ and *infinite* mass is given by [32]:

$$\frac{d\sigma_{\gamma\rightarrow a}}{d\Omega} = \frac{g_{a\gamma}^2 Z^2 \alpha}{8\pi} \frac{|\mathbf{K_a} \times \mathbf{K}_\gamma|^2}{|\mathbf{K_a} - \mathbf{K}_\gamma|^4}, \tag{1.21}$$

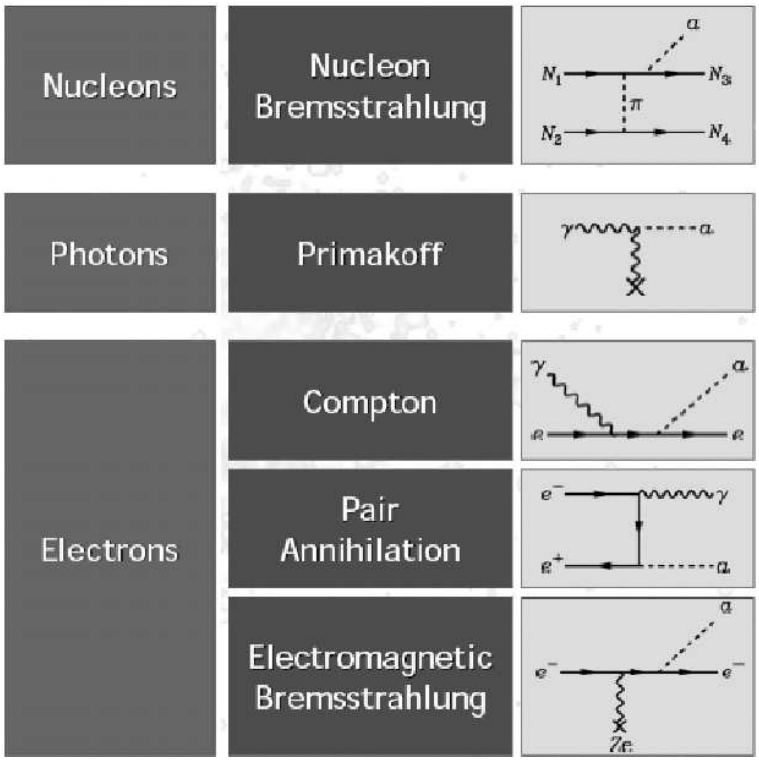


Figure 1.7: *Axion emission processes in stars. The couplings to nucleons and photons are allowed in the two axion models: DFSZ and KSVZ, while only the former one allows the coupling to electrons.*

where $\mathbf{K}_\gamma, \mathbf{K_a}$ are the initial-state photon and final-state axion momentums respectively, and $\alpha$ is the fine structure constant. It must be pointed out that the vacuum Primakoff cross-section diverges logarithmically due to the Coulomb logarithm. For massive axions, the particle mass provides a cutoff for this divergence, but for the invisible axions model, with masses much smaller than the temperatures in a typical stelar plasma, the screening or correlation effects (which take into account the charged media where the interaction takes place) are the dominant ones to moderate this Coulomb divergence. Thus, the Primakoff cross section on a target *Ze in a plasma* $(d\sigma_{\gamma\to a}/d\Omega)_{plasma}$ is given by the one in vacuum $(d\sigma_{\gamma\to a}/d\Omega)_{vacuum}$, (equation 1.21), corrected by a structure factor:

$$(d\sigma_{\gamma\to a}/d\Omega)_{plasma} = (d\sigma_{\gamma\to a}/d\Omega)_{vacuum}(\mathbf{K_a} - \mathbf{K}_\gamma + \kappa^2). \tag{1.22}$$

Here $\kappa^2$ is the screening scale for a non relativistic and non degenerate plasma:

$$\kappa^2 = \frac{4\pi\alpha}{T_\odot}\sum_j Z_j^2 n_j, \qquad ((\kappa^2)_{sun} \sim 12) \tag{1.23}$$

where $T_\odot$ is the temperature of the Sun ($\sim$1.3 keV in the solar centre) and j runs over the ions and electrons of the media, being $n_j$ their number density and $Z_j$ their charge.

The conversion rate can be found by summing the cross section over all the targets (averaging over all photon polarisations) and integrating over all the solid angles:

$$\begin{aligned}\Gamma_{\gamma\to a} &= \frac{g_{a\gamma}^2 T_\odot \kappa^2}{32\pi}\left[\left(1+\frac{\kappa^2}{4E^2}\right)\ln\left(1+\frac{4E^2}{\kappa^2}\right)-1\right] \\ &\approx \left(\frac{g_{a\gamma}}{10^{-10}\mathrm{GeV}^{-1}}\right)^2 10^{-15}\ \mathrm{s}^{-1}\ \text{for few keV energy photons (Sun).}\end{aligned} \tag{1.24}$$

The Solar axion luminosity can be calculated folding equation 1.24 with the black-body photon distribution on the Sun $f_B = (e^{E/T}-1)^{-1}$:

$$L_a = \frac{4R_\odot^3}{\pi}\int_0^1 dr r^2 \int_{\omega_p}^\infty dE E^2 \kappa_\gamma f_B \Gamma_{\gamma\to a}. \tag{1.25}$$

Here $R_\odot$ represents the radius of the Sun ($R_\odot = 6.9598\times10^{10}$ cm [33]), and $\omega_p$ the plasma frequency of the photons in the system:

$$\omega_p^2 = \frac{4\pi\alpha_e}{m_e}, \tag{1.26}$$

whose value depends on the radial position within the Sun. $\kappa_\gamma$ is the photon wave number, which is related to the plasma frequency by the dispersion relation:

$$E^2 = \kappa_\gamma^2 + \omega_p^2, \tag{1.27}$$

and $L_\odot$ is the solar photon luminosity ($L_\odot = 3.8418\times10^{33}$ erg s$^{-1}$ [33]).

Given this luminosity, the total axion number at the Earth, whose average distance from the Sun is $D_\odot$ ($D_\odot = 1.50\times10^{13}$ cm) is given by:

$$\Phi_a = \frac{R_\odot^3}{\pi^2 D_\odot^2}\int_0^1 dr r^2 \int_{\omega_p}^\infty dE E \kappa_\gamma f_B \Gamma_{\gamma\to a}, \tag{1.28}$$

and the differential number flux is therefore given by:

$$\frac{d\Phi_a}{dE_a} = \frac{R_\odot^3}{\pi^2 D_\odot^2}\int_0^1 dr r^2 E \kappa_\gamma f_B \Gamma_{\gamma\to a}. \tag{1.29}$$

**Old solar model** Based on Bahcall *et. al.* old standard solar model from 1982 [34], van Bibber *et. al.* [35] found a numerical result for the solar axion flux from which they gave an analytic approximation:

$$\frac{d\Phi_a}{dE_a} = \left(\frac{g_{a\gamma}}{10^{-10}\mathrm{GeV}^{-1}}\right)^2 4.02\times10^{10}\mathrm{cm}^{-2}\mathrm{s}^{-1}\mathrm{keV}^{-1}\frac{E_{keV}^3}{e^{E_{keV}/1.08}-1}, \tag{1.30}$$

where $E_{keV} = E/keV$ is the axion energy. This flux is represented with red crosses in figure 1.8, being its average axion energy $\langle E_a \rangle = 4.2$ keV.

In order to analyse the data collected with CAST in 2003 the expected axion flux at the Earth considered was slightly different from 1.30, as it was the one proposed in [36], however with a modified normalisation constant to match the total axion flux predicted by a more recent solar model [37]:

$$\frac{d\Phi_a}{dE_a} = \left(\frac{g_{a\gamma}}{10^{-10}\mathrm{GeV}^{-1}}\right)^2 3.821{\times}10^{10}\mathrm{cm}^{-2}\mathrm{s}^{-1}\mathrm{keV}^{-1}\,\frac{E_{keV}^3}{e^{E_{keV}/1.103}-1}. \quad (1.31)$$

Also here the average energy is $\langle E_a \rangle = 4.2$ keV.

**New solar model** Based on the new 2004 solar model given by Bahcall and Pinsonneault [33] G. Raffelt and P. Serpico [38] have calculated numerically again the axion flux as represented by the blue triangles in figure 1.8. They find that the function which best fits the data is given by:

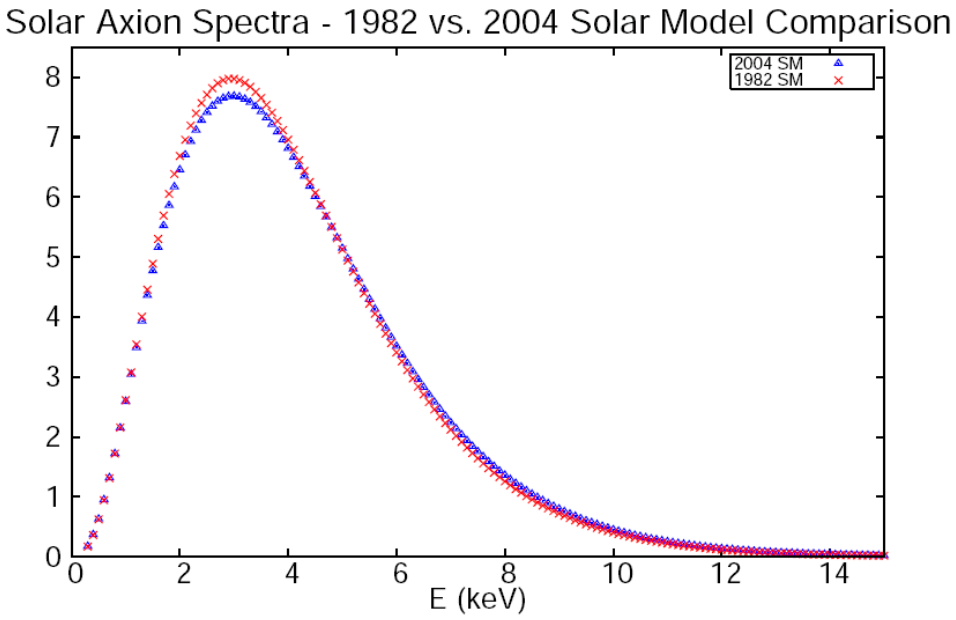


Figure 1.8: *Numerical axion flux from the 2004 solar model [33] (blue triangles) compared with the one from calculated by van Bibbler et. al., [35] (red crosses).*

$$\frac{d\Phi_a}{dE_a} = \left(\frac{g_{a\gamma}}{10^{-10}\mathrm{GeV}^{-1}}\right)^2 6.020\times10^{10}\mathrm{cm}^{-2}\mathrm{s}^{-1}\mathrm{keV}^{-1}E_{keV}^{2.481}e^{-E_{keV}/1.205}. \quad (1.32)$$

They also have calculated the axion "surface luminosity" on the solar disk $\varphi_a(E,r)$ (with $r = R/R_\odot$ the dimensionless radial coordinate), which is the

axion luminosity per unit square on solar disk, which is shown in figure 1.9. From here we see that indeed most of the axions are produced in the very core of the Sun.

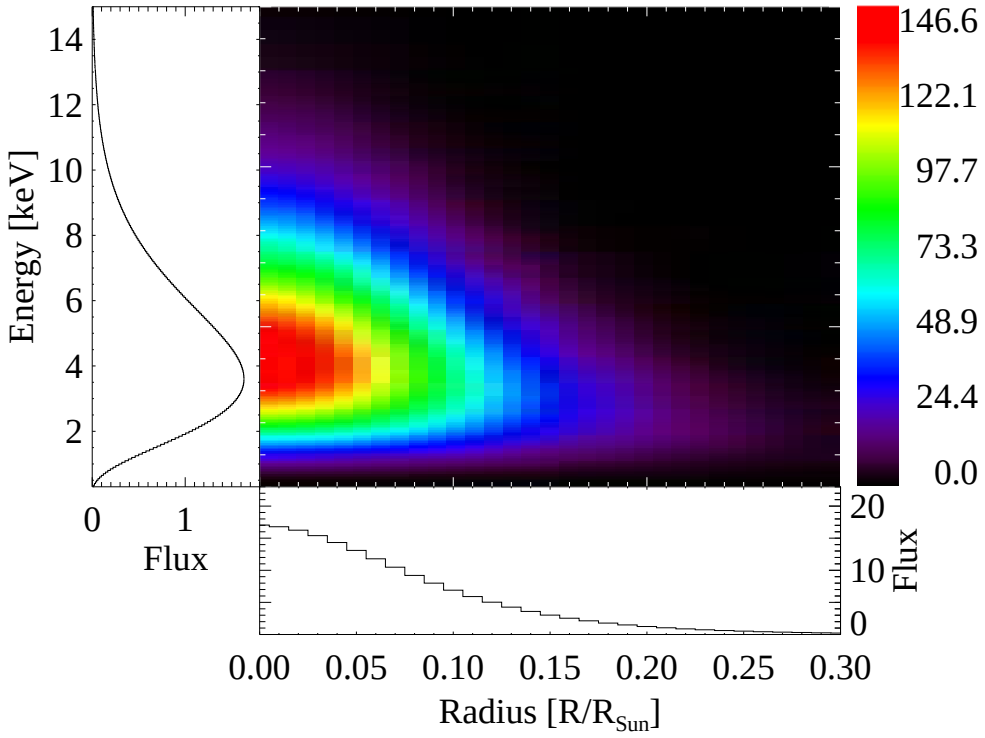


Figure 1.9: *Axion surface luminosity of the solar disk, $\varphi_a$, as seem from the Earth as a function of the axion Energy E and the dimensionless radial coordinate r on the solar disk. The units are $cm^{-2}s^{-1}keV^{-1}$ per unit surface on the solar disk (plot done by M. Kuster).*

### Other processes

The Primakoff process is not the only way through axion can be produced in the Sun. It has been pointed out in [39] that this light particle could be produced by nuclear M1 reactions by means of the favourable reaction:

$$p + d \longrightarrow^{3} He + \gamma \; (5.5\,\mathrm{MeV}) \tag{1.33}$$

occurring frequently in the main solar reaction chain, where the axion could substitute the photon.

Almost monochromatic hadronic axions can be also produced in the solar interior during M1 nuclear transitions between the first, thermically excited state of 14.4 keV and the ground state of $^{57}$Fe, as pointed out in [40]. In [41]

also the production of 478 keV monochromatic hadronic axions is extended to the de-excitation of $^7$Li, also present in the solar core.

Hadronic axion could also be produced in the Sun by the electron-positron annihilation process:

$$e^+ + e^- \longrightarrow \gamma + a\,(511\,\mathrm{keV}). \tag{1.34}$$

### 1.3.4. Cosmological and astrophysical axions bounds

Once the production mechanisms has been reviewed we know that if axions exist, their presence in the Universe will be very copious. Because of this its allowed parametric space for the constant $f_{PQ}$ can be strongly constrained, since their presence could be detectable by several different phenomena. In figure 1.10 the different constraint mechanisms are shown, together with the exclusion range for $f_{PQ}$ given by each of them.

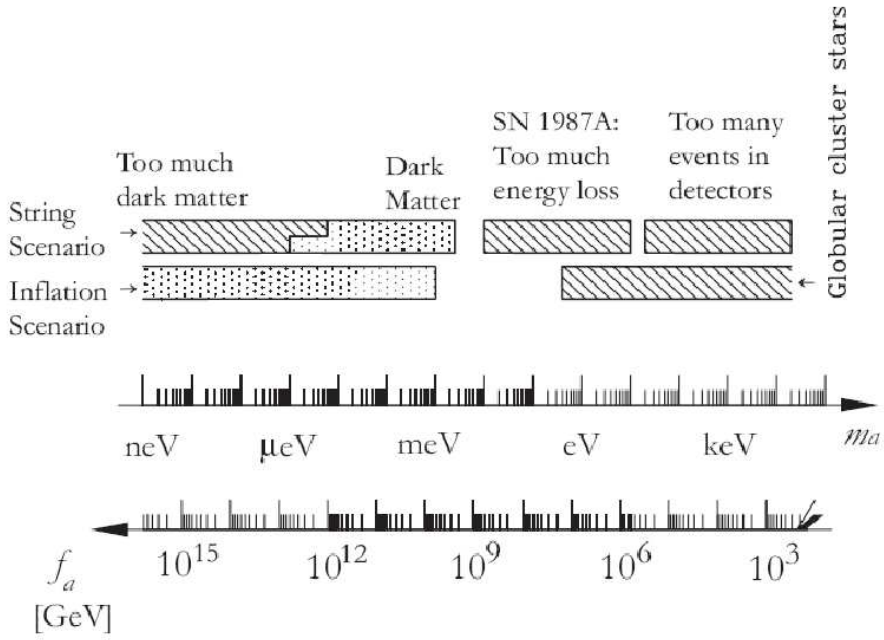


Figure 1.10: *Astrophysical and cosmological exclusion regions (hatched) for the axion mass $m_a$ or equivalently the Peccei-Quinn scale $f_{PQ}$. The dotted "inclusion" regions indicate the regions where axions could plausibly be the cold dark matter of the Universe (from [23]).*

Lets start talking about the cosmological constraints. In the situation where inflation takes place after the PQ phase transition (considered the "inflation scenario" in figure 1.10) the axion strings are blown away and therefore will no contribute to the axion density. In this case only the axions

created by the vacuum realignment mechanism are present today, being an excellent candidate for the cold dark matter of the universe. The condition of the axion density being the appropriate to account for the cold dark matter of the Universe, is the one that sets an upper limit of $m_a < 10^{-3}$ eV. This inclusion area appears as the dotted band on figure 1.10.

If, on the other hand, inflation took place before the PQ phase transition, to this initial misalignment population the axions from strings decay have to be added ("string scenario" on figure 1.10). In this case anyhow it has been mentioned that their contribution for the total density has been debated over the years being either equal to the misalignment one or up to ten times larger. Now the condition of these axions to be the dark matter of the universe sets an upper limit on their mass $m_a < 2.5 \times 10^{-3}$ eV and the requirement that they do not over-close the Universe ("too much dark matter" condition in figure 1.10) implies the constraint $m_a < 6 \times 10^{-6}$ eV in the former model or $m_a < 6 \times 10^{-5}$ eV in the later one [23, 21]. It is because of this that the transition from hatched to dotted in the band is not fixed.

Turning into astrophysical constraints, we have that the strength of axion interaction with photons, electrons and nucleons (or equivalently its mass in each case) can be constrained from the requirement that stellar evolution time scales are not modified beyond the observational limits. The existence of an axion would mean a novel energy-loss mechanism for stars. A possible axion emission would carry energy away from them, producing an increase in the fuel which the stars burn to compensate the energy loss, thus speeding up their evolution and therefore shortening their live time.

Both the Red giants and Horizontal branch stars from globular clusters provide restrictive bounds to the couplings of axions to electrons when they are allowed (DFSZ models) and photons. In the former case, a bremsstrahlung process like the one shown in figure 1.7 would delay the helium flash in the Red giants' core producing a increase in its mass. Observations restrict therefore the axion coupling to electrons:

$$g_{ae}^{DFSZ} \leq 2.5 \times 10^{-13} \text{ GeV}^{-1}. \tag{1.35}$$

Concerning the axion to photon coupling, globular clusters stars provide its most restrictive bound shown in figure 1.10:

$$g_{a\gamma} \leq 0.6 \times 10{-}10 \text{ GeV}^{-1} \tag{1.36}$$

which for the mass of the axion this constraint is translated into $m_a \leq 0.4$ eV for $E/N = 8/3$ as in the DFSZ model [23].

The axions produced by nucleon-nucleon-axion bremsstrahlung are bounded by the SN 1987A signal seen by Kamiokande II and Irvine-Michigan-Brookhaven (IBM) water Cherenkof detectors. Axions would have carried away energy from the core and therefore accelerate its cooling down being the observable

effect of this to shorten the neutrino burst. This sets a limit on the axion pseudoscalar Yukawa coupling to nucleons:

$$3 \times 10^{-10} \leq g_{aNu} \leq 3 \times 10^{-7}. \tag{1.37}$$

The strong coupling side is allowed because in this case axions escape only by diffusion, quenching thus their efficiency as an energy-loss channel.

In order to avoid excess of counts in the water Cherenkov detectors also the range

$$10^{-6} \leq g_{aNu} \leq 10^{-3} \tag{1.38}$$

is forbidden.

In terms of the Peccei-Quinn scale $f_{PQ}/N$ the axion couplings to nucleons are $g_{aNu} = C_{Nu} m_{Nu}/(f_{PQ}/N)$ $(Nu = n \; or \; p)$. Taking this into account the SN 1987A limit for the axion mass turns out to be:

$$\begin{aligned} m_a &\leq 0.0008 \text{ eV for KSVZ axions} \\ m_a &\leq 0.01 \text{ eV for DFSZ axions.} \end{aligned} \tag{1.39}$$

It must be pointed out that for the DFSZ axions the value quoted is just an approximation, as the limit can vary between 0.004 and 0.012 depending on the angle that measures the ratio of the two Higgs vacuum expectation values [23].

The weak points of the supernova argument lie on the uncertainties in the calculations of the nucleon-nucleon bremsstrahlung in a hot and dense medium, where many-body effects are important, and also in the uncertainties in modeling of supernovae.

All these observations and calculations leave only a small window from $\mu$eV to decades of meV in the mass range for axions to exist, although it must be stressed that both the astrophysical and cosmological bounds are rather uncertain, and have not stopped experiments to look for axions in the excluded regions.

## 1.4. Axion searches

Axions can be searched for through different experiments, based mostly on the axion-to-photon conversion. In what follows the different techniques will be reviewed, and the results attained from them will be quoted.

### 1.4.1. Searches for cosmological axions

In order to detect cosmological axions two main techniques have been used: optical and radio telescope searches, and the microwave cavity experiments.

### Optical and radio telescope searches

Thermally produced axions with mass in the so-called "multi-eV" range (2-30 eV) accumulated in galaxies and cluster of galaxies halos could spontaneously decay into two photons: $a \rightarrow 2\gamma$. These ones would be monoenergetic, with a wavelength $\lambda$ given by the ultimate mass of the axion. Observations of three well studied clusters (Abell 1413, 2218, and 2256) at Kitt Peak National Observatory [42, 43] in the range of 3,100-8,300 Å (which corresponds to axions masses from 3 to 8 eV) have not found such a line, excluding an axion-to-photon coupling constant smaller than:

$$g_{a\gamma} < 10^{-10}\,\mathrm{GeV}^{-1}. \tag{1.40}$$

This limit is represented in the axion-to-photon coupling constant versus axion mass exclusion plot shown in figure 1.11.

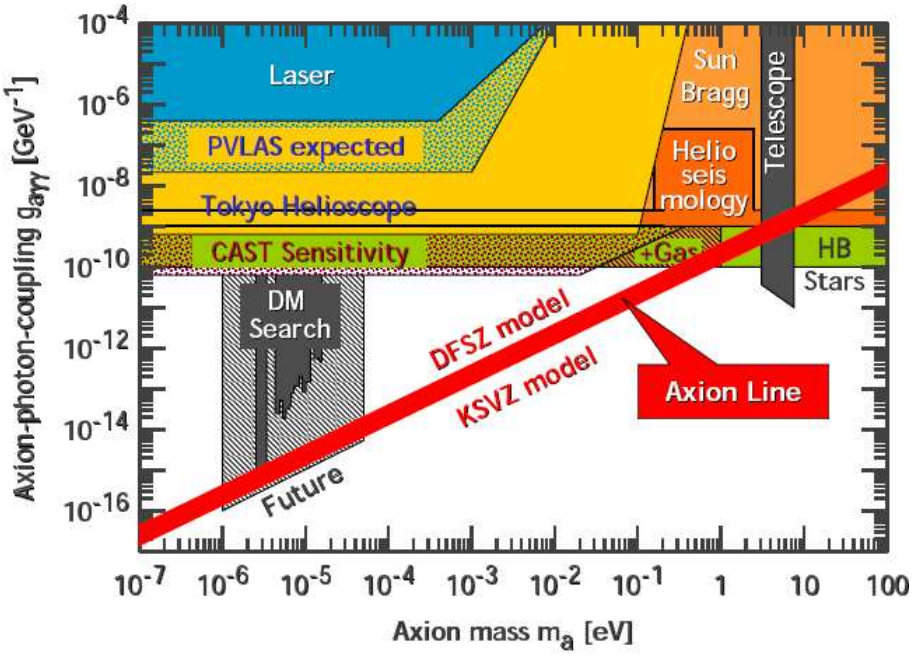


Figure 1.11: *Axion-to-photon coupling constant versus axion mass exclusion plot, where the excluded areas from the different experiments results are shown.*

### Microwave cavity experiments

In order to search for cosmological axions which are candidates for the cold dark matter of the Universe, Sikivie [44] proposed a very interesting mechanism using resonant cavities. In figure 1.12 the schematic working principle of such kind of detectors is shown. The basic idea underneath is

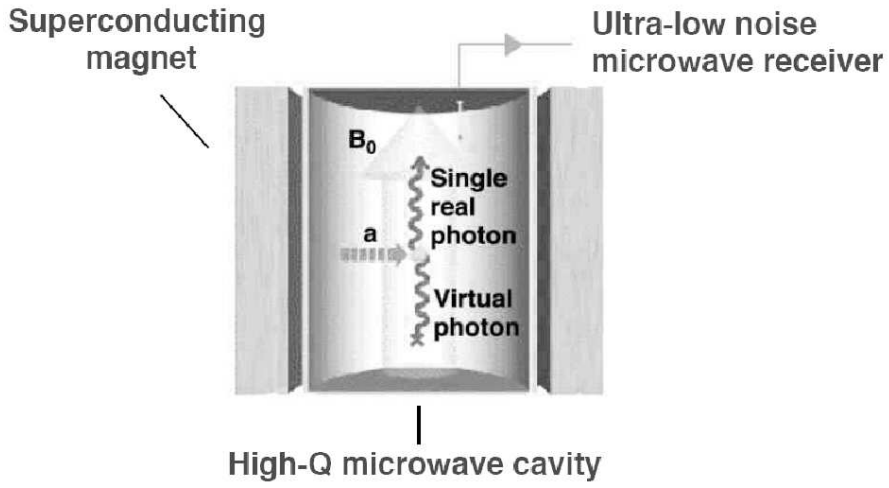


Figure 1.12: *Schematic principle of the microwave cavity experiment to look for cold dark matter axions [44].*

that fine-tuning the frequency of the cavity so that it matches the one of the axion field (related to its mass $m_a$), axions will convert resonantly into quasi-monochromatic photons (see [45] for more details). The width of the peak would represent the virial distribution of thermalized axions is the galactic gravitational potential, and also the signal may posses finer structure due to axions recently fallen into the galaxy and not yet thermalized [46], as shown in figure 1.13.

In the 80s the Rochester-Brookhaven-Fermilab (RBF) [47] and the University of Florida (UF) [48] experiments established the feasibility of the technique using small volumes ($\sim$1 l) for the cavity and HFET amplifiers. Their results were able to preclude, in the axion mass range of 4.5 to 16.3 $\mu$eV, an axion to photon coupling constant bigger than:

$$g_{a\gamma} < 10^{-12}\,\mathrm{GeV}^{-1}, \tag{1.41}$$

but still they were lacking by 2 or 3 orders of magnitude the sensitivity to search into the theoretically motivated region in the axion parametric space.

Second generation experiments, where the sensitivity will be enhanced thanks to the use of a novel technology for the amplifiers, are already taking data or being built. The AMDX experiment [49] is currently taking data with a similar improved technology as the precedent experiments, being sensitive to an axion mass range of 1.9 to 3.3 $\mu$eV and having already excluded an axion to photon coupling constant bigger than:

$$g_{a\gamma} < 10^{-15}\,\mathrm{GeV}^{-1}, \tag{1.42}$$

.

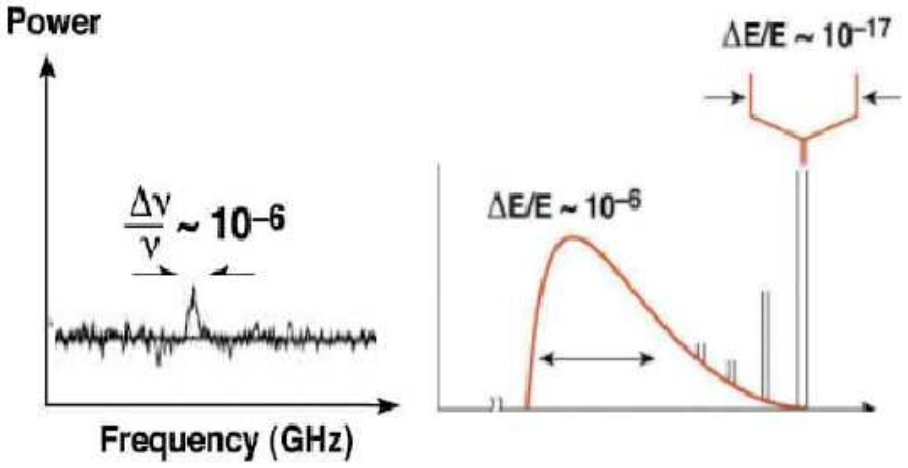


Figure 1.13: *Left: Representation of the signal expected in a microcavity experiment. Right: Zoom showing the shape of the expected peak showing the fine structure details.*

In order to further improve the sensitivity of these experiment so that they will be able to search into the theoretical motivated region, a new technology to produce improved amplifiers, based on the Superconducting Quantum Interference Devices (SQUID) is under R&D now.

Also a similar device has been constructed in Japan by the CARRACK2 collaboration [50]. They use a Rydberg atom single-quantum detector that has been already working for their prototype CARRACK1, being the data still under analysis.

### 1.4.2. Searches for Solar axions

As it has been mentioned in section 1.3.3 axion could be produced in the core of the Sun by the Primakoff process, being the expected spectrum due to these axions on the Earth shown in figure 1.8. Two different types of "helioscopes" have been built:

- As it was pointed out by E. A. Paschos and K. Zioutas [51], solar axions could convert into photons in the electric field created by the atomic nuclei in well defined crystals. Due to the Bragg diffraction of the axions in crystal layers, the expected signal would have a well defined temporal structure that would make it clearly distinguishable. Two different collaborations, COSME [52] and SOLAX [53], which were using Germanium detectors with the main purpose of searching for Dark Matter WIMPs, analysed also their data searching for the expected axion signal. Both of them were able to yield very similar mass-independent bounds to the axion to photon coupling constant in the absence of any

signal:

$$\begin{aligned} g_{a\gamma} &< 2.7 \times 10^{-9}\ \text{GeV}^{-1} \quad \text{[SOLAX]} \\ g_{a\gamma} &< 2.8 \times 10^{-9}\ \text{GeV}^{-1} \quad \text{[COSME]}. \end{aligned} \tag{1.43}$$

The DAMA collaboration [54] also achieved the limit:

$$g_{a\gamma} < 1.7 \times 10^{-9}\ \text{GeV}^{-1} \quad \text{[DAMA]}, \tag{1.44}$$

using NaI(Tl) crystals.

- The second type of helioscopes, to which CAST is included, provides the axions coming from the Sun with a magnetic field, transverse to their course, so that they are converted in "to-be-detected" photons. The first implementation of such device was done by D. M. Lazarus *et. al.,* [55] and was able to explore two regions of the axion mass range, setting the following limits:

$$\begin{aligned} g_{a\gamma} &< 3.6 \times 10^{-9}\ \text{GeV}^{-1} \quad \text{for } m_a < 0.03\ \text{eV} \\ g_{a\gamma} &< 7.7 \times 10^{-9}\ \text{GeV}^{-1} \quad \text{for } 0.03\ \text{eV} < m_a < 0.11\ \text{eV}. \end{aligned} \tag{1.45}$$

  A more recent experiment with improved sensitivity was performed in Tokyo [56], being able to set the following limits:

$$\begin{aligned} g_{a\gamma} &< 6 \times 10^{-10}\ \text{GeV}^{-1} \quad \text{for } m_a < 0.03\ \text{eV} \\ g_{a\gamma} &< 6.8 - 10.9 \times 10^{-10}\ \text{GeV}^{-1} \quad \text{for } m_a < 0.3\ \text{eV} \end{aligned} \tag{1.46}$$

### 1.4.3. Searches for laser induced axions

Given the coupling of axions to photons, it is expected that axions could be created when a light beam (usually a laser) travels in a transverse magnetic field. Two different kind of experiments profit from this feature.

#### "Shining through the walls" experiments

This experiment was first proposed by van Bibber *et. al.,* [57] in 1987. The basic idea is that a laser beam propagates inside a transverse magnetic field (with $\mathbf{E} \parallel \mathbf{B}$), being blocked at some point of its path so that only the axions created before will be able to pass through this "wall". For light axions with $m_a^2 l/2\omega << 2\pi$, where l is the length of the magnetic field, the axion beam produced is colinear and coherent with the photon beam, being the conversion probability given by $P(a \to \gamma) \approx (1/4)(g_{a\gamma} B l)^2$. After, a fraction of these axions will turn back into detectable photons, as they are further propagated in the magnetic field, being the overall probability given by $P(a \to \gamma \to a) = P^2(a \to \gamma)$.

An experiment using this technique was performed using two magnets of length $l = 4.4$ m and $B = 3.7$ T, excluding couplings of [58]

$$g_{a\gamma} < 6.7 \times 10^{-7}\,\mathrm{GeV} \tag{1.47}$$

for masses

$$m_a < 10^{-3}\,\mathrm{eV} \tag{1.48}$$

at 95% C.L.

### Polarisation experiments

If axions are produced when a laser is propagated in a transversal magnetic field, this could affect the polarisation of the laser in two different and observable ways, as it can be seen in figure 1.14.

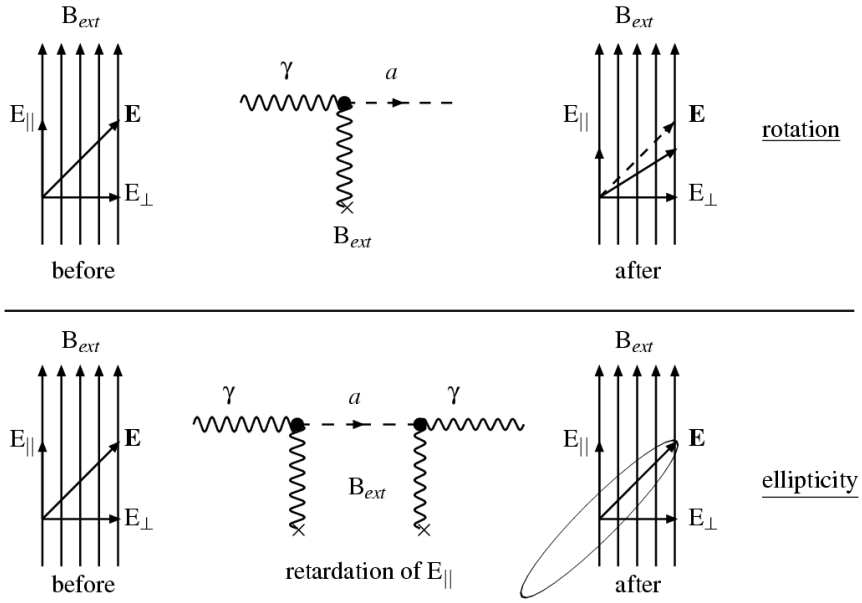


Figure 1.14: *Up: Linear Dichroism or rotation of the polarisation vector by and angle $\epsilon$. Down: Linear Birefringence or induction of an ellipticity $\Psi$ in an initially linear polarised beam.*

**Dichroism** If a linearly polarised laser beam propagates in the magnetic field, the component of the electric field ($\mathbf{E}_{||}$) parallel to the magnetic field (and only this component) will be depleted by the appearance of real axions, resulting in a measurable rotation of the polarisation vector by and angle $\epsilon$.

**Vacuum Birefringence** In this case, if some of the axions created in the previous step are converted back into photons, a delay will appear in the parallel component of the laser beam to the magnetic field, being this reflected in an induced ellipticity $\Psi$ on the original linearly polarised beam. Higher-order QED effects can also induce vacuum birefringence in a laser beam, having anyhow negligible effects on the dichroism.

A search for both effects was carried out with the same magnets used in the *shining through the walls* experiment quoted before [58], setting a bound on the axion to photon coupling constant of

$$g_{a\gamma} < 3.6 \times 10^{-7}\,\mathrm{GeV} \tag{1.49}$$

for masses

$$m_a < 5 \times 10^{-4}\,\mathrm{eV} \tag{1.50}$$

at 95% C.L.

Very recently the Italian PVLAS experiment (see [59] and references therein) has been taking data to test the vacuum birefringence in the presence of a magnetic field with a 1 m long dipole magnet operated at a maximum field of 5.5 T, therefore improving the sensitivity of the previous experimental setups. For the first time they have measured a positive value for the amplitude of the rotation $\epsilon$ of the polarisation plane in vacuum with $B \approx 5$ T (quoted with a $3\sigma$ uncertainty interval) [59]:

$$\epsilon = (3.9 \pm 0.5) \times 10^{-12} rad/pass. \tag{1.51}$$

This signal would be translated on an allowed region for the mass $m_b$ and the inverse of the coupling constant to two photons $M_b$ of a neutral light pseudoscalar boson:

$$\begin{aligned} &2 \times 10^5\ \mathrm{GeV} \lesssim M_b \lesssim 6 \times 10^5\ \mathrm{GeV} \\ &1\ \mathrm{meV} \lesssim m_b \lesssim 1.5\ 1.5\mathrm{meV} \end{aligned} \tag{1.52}$$

As it has been seen, both astrophysical and experimental bounds on the axion-to-photon coupling go far from this estimate. Anyhow, a recent paper by E. Massó and J. Redondo [60] suggests that both results could be accommodated in models were axion-like particles suffer a strong interaction that traps them in the stellar plasma, or models where the axion-photon vertex could be suppressed in the solar core.

Several experiments are already under construction in order to crosscheck their result like the one proposed by P. Pugnat *el.al.,* [61] using a long LHC 15 m and $B \approx 9$ T dipole, or the one proposed by A. Ringwald *el.al.,* [62].

# Part II

# The CAST experiment at CERN

# Chapter 2

# CAST, The CERN Axion Solar Telescope experiment

The CAST experiment uses a 10 m long twin aperture magnet as an axion to photon conversor to detect the axions that could come from the Sun core. For this, the magnetic field should be aligned with its centre as much time as possible, thus requiring the whole experiment to be a moving structure. The international CAST collaboration is composed by ∼70 scientist from 11 different countries all around the world.

In this chapter first the principle of detection will be point out. Then, the CAST experiment together with its X-ray detectors will be reviewed. Finally the experimental site and radioactive background will be described. An overall description of the experiment can be found in [63] while companion papers are devoted to each of the detectors.

## 2.1. Principle of detection

As it has been mentioned in chapter 1, the Sun would be a strong axion source, and a strong laboratory magnetic field could be used to convert the axions back into X-rays. The expected number of these photons that reach the X-ray detector is:

$$N_\gamma = \int \frac{d\Phi_a}{dE_a} P_{a\to\gamma}\, S\, t\, dE_a, \tag{2.1}$$

where $d\Phi_a/dE_a$ is the axion flux at the Earth quoted in section 1.3.3, $S$ is the magnet bore area, $t$ is the measurement time and $P_{a\to\gamma}$ is the conversion probability of an axion into a photon. If we take some realistic numbers for one year of data taking in CAST ($g_{a\gamma} = 10^{-10}$ GeV$^{-1}$, $t = 100$ h and $S = 15$ cm$^2$) this number of photons would be nearly 30 events.

The conversion probability in vacuum is given by:

$$P_{a\to\gamma} = \left(\frac{Bg_{a\gamma}}{2}\right)^2 2L^2\, \frac{1-\cos(qL)}{(qL)^2}, \tag{2.2}$$

where $B$ and $L$ are the magnetic field and its length (both given in natural units), and

$$q = m_a^2/2E \tag{2.3}$$

is the longitudinal momentum difference (or momentum transfer) between the axion and an X-ray of energy $E$. The conversion process is coherent when the axion and the photon fields remain in phase over the length of the magnetic field region. The coherence condition states that [55, 65]

$$qL \leq \pi \tag{2.4}$$

so that a coherence length of 10 m in vacuum requires $m_a \leq 0.02\,\text{eV}$ for a photon energy 4.2 keV. The condition given in equation 2.4 can be obtained having a look at equation 2.2, where $qL$ is the product of terms appearing in the fraction of the r.h.s, and involves both magnet characteristic in $L$ and properties of the axion flux expected through $q$:

$$\frac{1-\cos(qL)}{(qL)^2}. \tag{2.5}$$

When $qL > \pi$ this fraction tends to zero, thus turning the conversion probability inside the magnet negligible. In figure 2.1 we can see the number of photons expected in the detector versus the mass of the axion. When there is vacuum inside the magnet we see that indeed for masses higher that $\sim 0.01$eV this number drops down rapidly.

Coherence can be restored by filling the magnetic conversion region with a buffer gas [35] so that the photons inside the magnet pipe acquire an

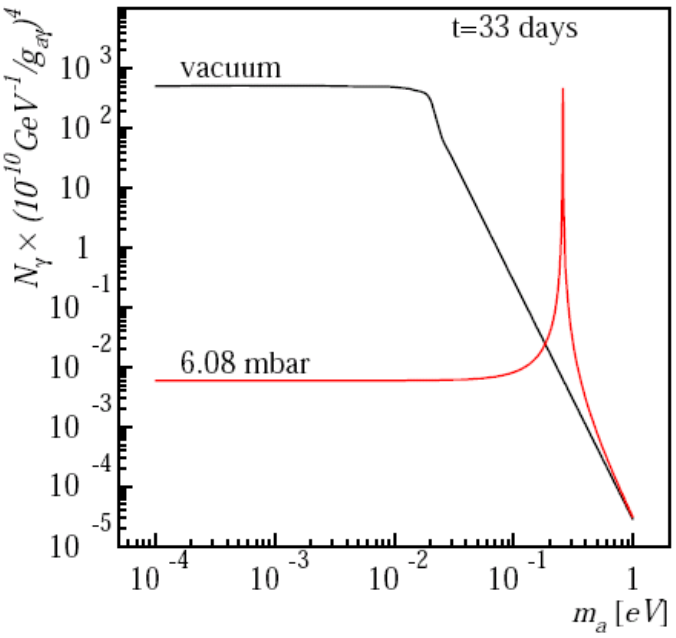


Figure 2.1: *Number of photons that would reach a X-ray detector placed at the end of the magnet vs the mass of the incoming axion. The upper line stands for the case where there is vacuum inside the magnet, while for the lower one there would be helium at 6.08 mbar.*

effective mass $m_\gamma$ whose wavelength can match that of the axion. For an appropriate gas pressure, coherence will be preserved for a narrow axion mass window. as we can see in the lower line in figure 2.1. Thus, with the proper pressure settings it is possible to scan for higher axion masses. When the magnet pipes are filled up with a buffer gas, the transition rate $P_{a\to\gamma}$ has to be recast into the more general equation:

$$P_{a\to\gamma} = \left(\frac{Bg_{a\gamma}}{2}\right)^2 \frac{1}{q^2+\Gamma^2/4}[1+e^{-\Gamma L}-2e^{-\Gamma L/2}cos(ql)]. \tag{2.6}$$

Here $\Gamma$ is the inverse photo absorption length for the X-rays in the medium. In this case the momentum transfer becomes:

$$q = \left|\frac{m_\gamma^2 - m_a^2}{2E_a}\right| \tag{2.7}$$

for $m_\gamma$ the photon effective mass (given the plasma frequency) in the buffer gas

$$m_\gamma \simeq \sqrt{\frac{4\pi\alpha n_e}{m_e}} = 28.9\sqrt{\frac{Z}{A}\rho} \tag{2.8}$$

where $n_e$ is the number density of electrons in the medium, $m_e$ the mass of this electrons. The second expression in 2.8 accounts for the dependence of $m_\gamma$ on characteristics of different mediums: $Z$ is the atomic number of the buffer gas, $A$ its mass and $\rho$ its density in g cm$^{-3}$. Since the gas which will used is helium the ideal-gas equation can be used to obtain the more convenient expression:

$$m_\gamma(eV) \simeq \sqrt{0.02\frac{P(mbar)}{T(k)}} \tag{2.9}$$

as the experimental measured parameters will be the pressure $P$ and temperature $T$ of the helium inside the pipes.

Now the coherence is restored for a narrow axion mass window, for which the effective mass of the photon matches that of the axion such that

$$qL < \pi \implies \sqrt{m_\gamma^2 - \frac{2\pi E_a}{L}} < m_a < \sqrt{m_\gamma^2 + \frac{2\pi E_a}{L}} \tag{2.10}$$

which brings the sensitivity of CAST with a helium buffer gas up to an axion mass of 0.82 eV for $T = 1.8$K and $P = 60$mbar.

The agenda of the CAST experiment foresees two phases in order to cover the wider range of potential axion masses:

- **First phase of CAST** During the years 2003 and 2004 the CAST experiment has gone through the so-called first phase, where the data has been taken with vacuum inside the magnetic field area, so that we were sensitive to axion masses up to $m_a \leq 0.02\,\mathrm{eV}$.

- **Second phase of CAST** In order to extend the range of axion masses to which we are sensitive, the magnet pipes are filled with Helium gas in phase II. This gas at a given pressure provides a refractive photon mass so that the coherence of the photon and axion fields is restored for a certain range of axion masses. The second phase of the experiment is very challenging because, for the first time, a laboratory experiment will search for axions in the theoretically motivated range of axion parameters, as shown in figure 2.2, where the CAST prospects are shown.

  Data taking for this second phase started at the end of 2005, with low pressure $^4$He gas inside the pipes at 1.8 K, the magnet's operating temperature. There is a limit in the pressure that we can reach with $^4$He before it liquefies, so in order to be able to extend the mass axion searches up to $\sim 0.82\,\mathrm{eV}$ we will have to switch to $^3$He, which has a higher vapour pressure. These steps are scheduled to occur during 2006 and 2007.

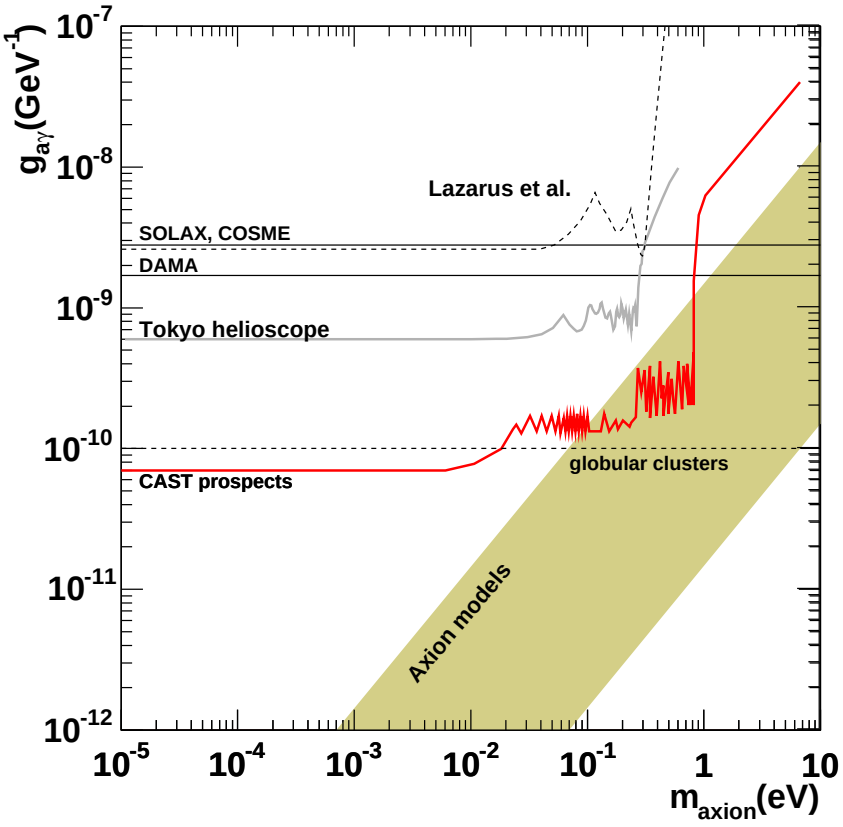


Figure 2.2: *Exclusion plot in the axion parametric space, where the CAST prospects are shown in red. For the second phase, the search of axions with $m_a$ between 0.02 eV and 0.8 eV will go in the theoretically motivated band. For comparison other experiments previous results are shown.*

## 2.2. Technical description

### 2.2.1. The experiment

Figure 2.3 shows a schematic drawing of the CAST setup. The main components are the LHC magnet, the cryogenics station and the platform which holds the magnet and guides its movement tracking the Sun using two motors for the horizontal and vertical movements respectively. A complex software calculates the position of the Sun in galactic coordinates and guides the magnet structure to follow it. The environmental parameters of the experimental area and the magnet status are recorded every minute with the help of a software program named Slow Control. In what follows all these components are reviewed with some detail.

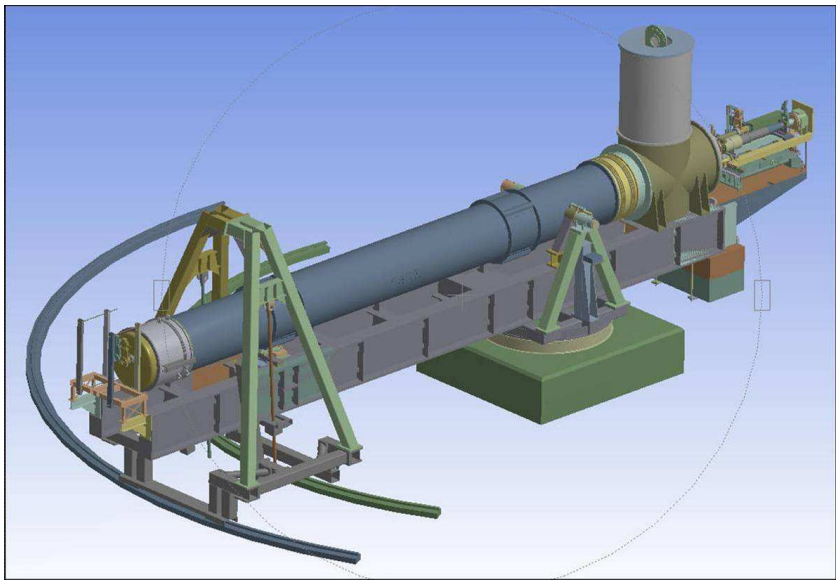

Figure 2.3: *Schematic representation of the CAST experiment.*

**A little bit of history...**

In order to check whether the high magnetic fields needed for the Large Hadron Collider (LHC) would be able to be reached with reliable technology, a set of test magnets were designed and built as a collaboration between CERN and the INFN (Italian institute for Nuclear Physics). Two 10 m long twin aperture dipoles including NbTi superconducting cables and 1.8 K cryostats were order to an Italian industry. The first of them, called A1 was delivered to CERN in January 1994 and the second one A2 in May of the same year. These two prototypes succeeded all the stability tests, and their characteristic parameters were within the accuracy required for an LHC magnet [64]. Once the technology in these magnets was tested, they were not needed anymore and thus they were decommissioned.

The possibility of using one of them as a host for the axion to photon conversion was pointed out in [65]. Eventually in April 2000 the CAST experiment to look for solar axions using one of these LHC magnets (A2) was approved by CERN and by November 2002 it was advanced enough in its construction to be able to track the Sun for the fist time. In figure 2.4 we see a picture of the final setup.

**The magnet**

The magnet is a straight twin aperture 10 m long dipole. It uses NbTi superconducting cables to create the magnetic field, which have to the cooled down to 1.8 K in order to reach the superconducting state. Figure 2.5 shows a

Figure 2.4: *Picture of the final setup.*

calculation of the magnetic field lines created by such assembly. Two parallel

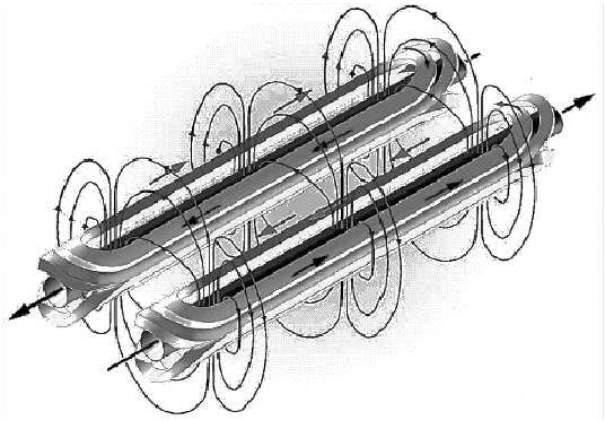

Figure 2.5: *Drawing showing how the superconducting cables loop around the beampipes and the direction of the field lines.*

9.26 m long pipes sustain the magnetic field inside. Together they present a cross-sectional area of A = 2×14.5 $cm^2$, being the aperture of each of them wide enough to cover the potentially axion-emitting solar core ($\sim 1/10^{\text{th}}$ of the solar radius). A cross-sectional view of one LHC magnet is shown in figure 2.6. The maximum field value safely reached is 9 T, corresponding to a current flow of 13,330 A through the superconducting cables. A whole cryogenic plant [66] needed to support and maintain the operation of the magnet was set up by recovering and adapting parts from the dismounted

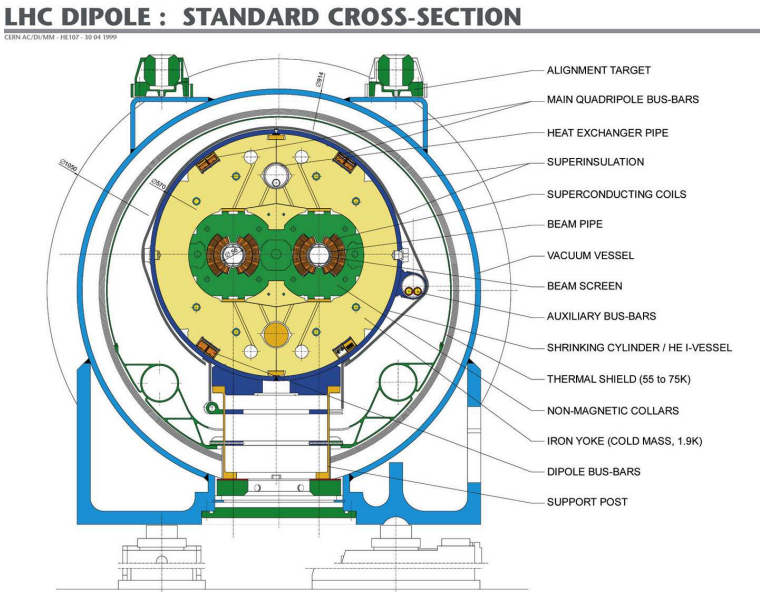


Figure 2.6: *Cross sectional view of an LHC dipole.*

LEP collider and the DELPHI experiment. Connected to the right end of the magnet in figure 2.4 the Magnet Feed Box (MFB) is placed, through which all the cryogenic and electrical feed is done to the magnet via 7 flexible transfer lines that connect to the liquid helium supply, gaseous helium pumping group and the quench recovery system.

The wire that makes up the magnet can be subject to some influences, say for example magnetic or mechanical, which can cause local differences in its electrical conductivity. This will be translated into a change in the voltage of the magnet further detected by its power system. This one will trigger the discharge of large capacitors into the magnet, designed to raise its temperature evenly in order to avoid local hot spots which could burn out the magnet. This overall heating then causes the helium to rise above 2.17 K where is not superfluid anymore, causing all the cable to be normal-conducting and unable to support the large amount of current for very long. A *quench* of the magnet refers to this process of the cables becoming normal-conducting. A quench signal is triggered when the resistive transition of the magnet is detected, and produces the immediate ramp down of the current. A big amount of heat is released on the process, which warms up the cold mass up to temperatures $\sim$40 K, making some part of the helium inside the vessel to turn into gas. The gas pressure increases and some part of it has to be released to the atmosphere when it overpasses the secure limits. Once the equilibrium is recovered, the helium is again cooled down to its nominal values of 1.8 K in a process that can take from 6 to 8 hours.

A system of gate valves protect and are able to isolate the magnet bores

from the detectors. In normal data taking they are open so that the hypothetic photon coming from the axion conversion inside the pipe can reach eventually the X-ray detectors. But in the case of a quench or a detector malfunction for example, this valves immediately close, isolating the magnet bores from the detectors and therefore protecting both of them.

### Platform and motors

The magnet is implemented on a moving platform (figure 2.3) which allows us to align it with the Sun. The horizontal movement is carried over the two rails shown in figure 2.3, with a covering range of 80°, which encompasses nearly the full azimuthal movement of the Sun throughout the year. The allowed vertical range of movement is only ±8° from the horizontal due to mechanical constraints in the magnet. Because of this the maximum time of alignment is approximately 3 hours per day (∼1.5 during sunrise, and the same time during sunset).

Two motors, each of them dedicated to one direction, move the platform holding the magnet. An encoder system keeps track of the position of the platform in each moment. Independently a system of angle encoders are installed on the horizontal and vertical pivots of the magnet, giving also an alternative measurement of its position.

This magnet moving system receives instructions from a software program named *tracking software*, responsible for directing the magnet to the Sun or for any other movement in general.

### The tracking software

This program, written in LabVIEW programming language, performs the following tasks:

- Guiding the magnet when it is in the Sun tracking mode.
- Providing to the user an interface to move the magnet to some input position, which can be both in encoder or galactic coordinates.
- Recording of some parameters of the experimental area, such as the temperature in the experimental hall or the value of magnetic field on the magnet.
- Producing daily files where all the information concerning the position and movement of the magnet, together with the status of the parameters recorded, are written with one minute frequency.

When it is in the Sun tracking mode, every minute it calls to an executable file based on NOVAS (Naval Observatory Vector Astrometry Sub-

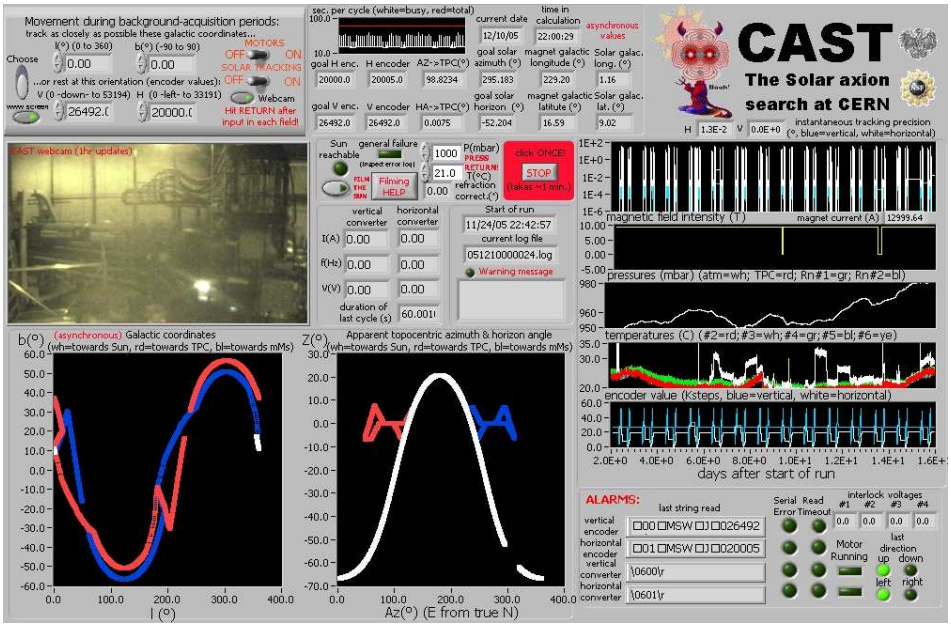


Figure 2.7: *Screen shot showing the user interface of the Tracking program.*

routines) [67] which, taking as an input the local time and date from the PC [1], together with the CERN coordinates (46°15'N, 6°5'E, 330 m above the sea level) calculates the solar azimuthal angle and zenith distances (AZ,ZD) for the incoming minute. Then it performs a change of coordinates to translate these values into the local encoder grid ($V_x$, $V_y$), which are the ones the motors understand, by looking up on an already pre-recorded table $V_x$(AZ,ZD),$V_y$(AZ,ZD). Reading the actual values of the encoders it calculates the speed that the motors have to take in order to arrive to the position required in the following minute.

Given its importance, the table $V_x$(AZ,ZD),$V_y$(AZ,ZD) was constructed with the help of the surveyors from the EST division at CERN, who measured the (AZ, ZD) coordinates for every point of a precise grid of magnet encoder positions (90) with an accuracy of 0.001°.

The overall CAST pointing accuracy is better than 0.01°, as it can be inferred from the study of the different possible error sources listed in table 2.1.

Twice a year, in mid-March and mid-September, the opportunity to verify the pointing accuracy of the tracking system comes out by direct optical observation of the Sun, as it passes by a window in the experimental hall. If the weather permits it, a special software developed for the purpose, which

[1] The inaccuracy due to the clock of the PC is negligible, as the system is checking the time with two CERN servers, and a NTP daemon which produces a continuous time synchronisation to the order of 1 ns is always running.

| Error source | Typical value | Maximum value |
|---|---|---|
| Astronomical calculations | 0.002° | 0.006° |
| Grid measurements | 0.001° | |
| Uncertainty of CERN coordinates | ∼0.001° | |
| Interpolation of the grid measurements | 0.002° | <0.01° |
| Horizontal encoder precision | ∼0.0014° | |
| Vertical encoder position | ∼0.0003° | |
| Perfect linearity of motor speeds | <0.002° | |
| TOTAL | <0.01° | |

Table 2.1: *Possible error sources of inaccuracy when pointing to the Sun.*

takes into account that the Sun is seen in an apparent position different than the real one due to the refraction of light in the atmosphere, points the magnet to it. A webcam equipped with cross-wires in combination with an optical telescope which is aligned with the optical axis of the magnet, films during the movement allowing us to check the precision of the tracking by having a close examination of the images recorded. In figure 2.8 examples of some pictures taken are shown[2].

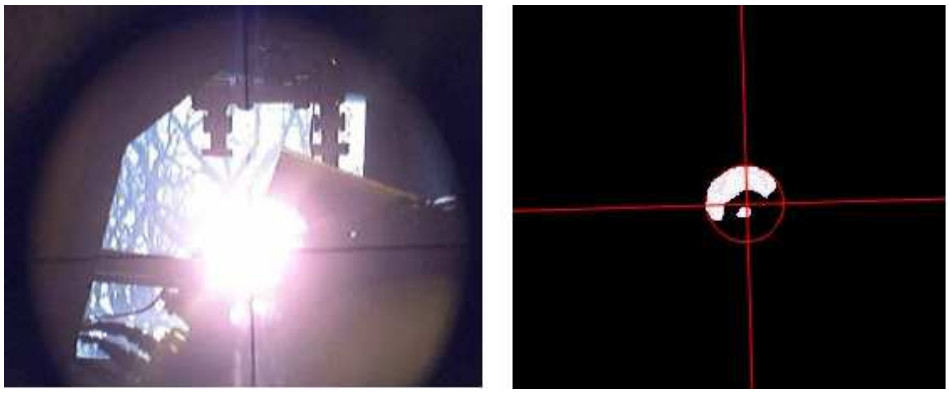

Figure 2.8: *Left: One frame taken while tracking the Sun. Right: Superposition of many frames (taken with filters). The cross indicates the centre of the Sun as it is followed, which is in good agreement with the image.*

### Slow Control program

The parameters being recorded by the tracking software proved to be insufficient to have a control over all the effects which could influence the data collected, and therefore the need of an extended recording became apparent.

[2] A movie of one filming session is shown in the following URL: http://cast.web.cern.ch/CAST/edited_tracking.mov

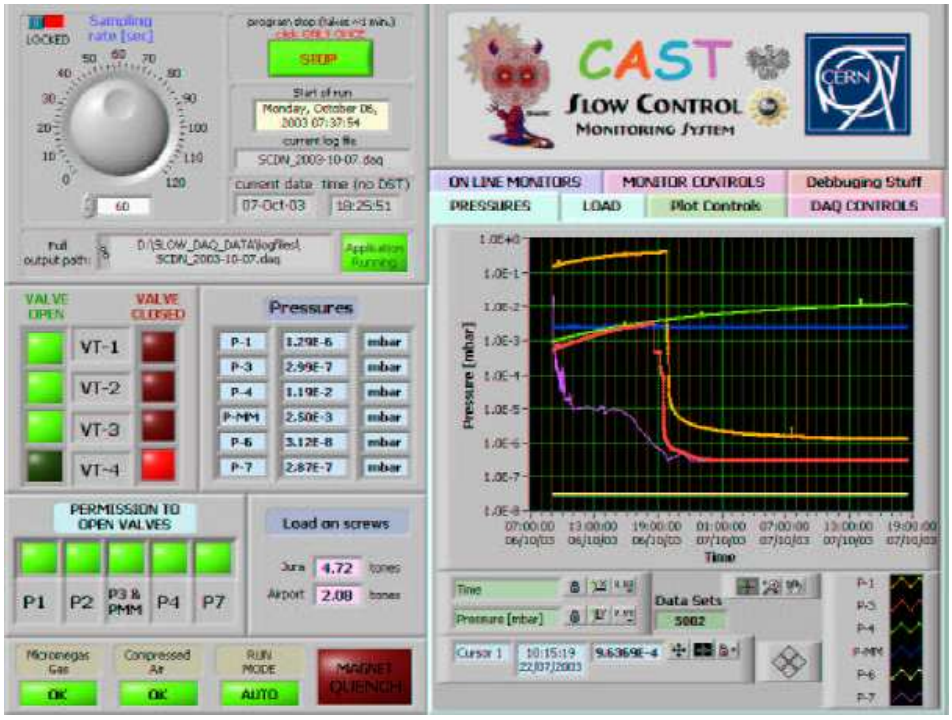


Figure 2.9: *Screen shot showing the user interface of the Slow Control program.*

In late July 2003 a new program, written also in LabVIEW language, started to run in a different PC from the tracking one, with the only aim of controlling these extra parameters. In the same way as the tracking program, it creates daily files where all the information recorded every minute is written. The experimental parameters controlled are:

- The temperature and pressure inside the cryostat and in front of each detector.
- The total load carried by each of the two lifting screens which allow the magnet to move vertically.
- The position of the magnet in motor encoders and in the independent angle encoders positioning system.
- The condition of the magnet valves (open or not), together with the permission (or lack of it) to open then.
- Indication of different alarms, such as the quench one, regarding the system.

This program has the capability of sending warnings and alarms to a defined set of phone numbers as SMS messages when one or several of these parameters drifts out of they nominal value range.

### 2.2.2. The detectors

At both ends of the magnet four different detectors are placed to search for the excess of X-rays from axion conversion in the magnet when it is pointing to the Sun. Facing "sunrise" axions, a gaseous chamber with novel MICROMEGAS readout is placed behind one of the magnet bores, while in the other one a focusing X-ray mirror telescope is working with a Charge Coupled Device (CCD) as the focal plane detector. Covering both bores of the other magnet end, a conventional Time Projection Chamber (TPC) is looking for "sunset" axions. A fourth crystal scintillator detector was installed during 2004 behind the MICROMEGAS to search for high-energy axions. In what follows these devices will be reviewed.

#### MICROMEGAS

The MICROMEGAS [68] (for MICRO MEsh GAseous Structure) gaseous detector is sitting on the west side of the magnet (see figure 2.17), looking for "sunrise" axions as shown in the right picture of figure 2.10. The detector is

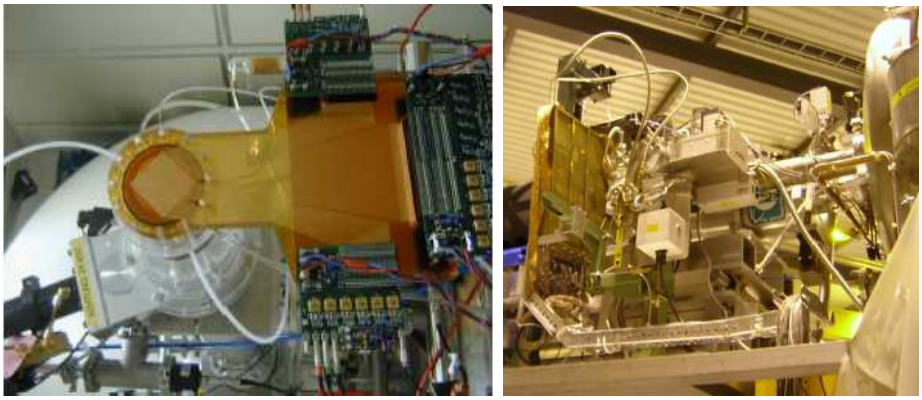

Figure 2.10: *Left: The MICROMEGAS detector sitting in the laboratory bench, equipped with four electronic cards and the gas pipes. Right: The CAST magnet with the MICROMEGAS attached to it.*

fastened to one of the magnet bores in this end with the help of an aluminium tube of ∼1m long and a flange. In order to couple the detector to the magnet bore with a maximum transparency to X-rays with the minimum argon-isobutane (95:5) gas leak towards the magnet bore the solution of two windows with a differential pumping system between them was adopted. Both windows are made of a 4 $\mu$m aluminised polypropylene foil, holding

the one closer to the detector a higher pressure difference that makes it to be glued to a stainless steel strongback in order to make the system stronger. The gas of the chamber leaks to the space between the two windows, where a clean pump removes it, being therefore the effective leak to the magnet really low ($\sim 10^{-9}$ mbar l $s^{-1}$). The detector is enclosed in a copper Faraday cage to help eliminating any induced charges into the conductive elements of the detector.

A ~25 mm thick conversion gap (figure 2.11) lays between the window described before (biased to -1200 V) and a metallic grid with acts as the cathode, named *micromesh*, and biased to -390 V. This micromesh is the very

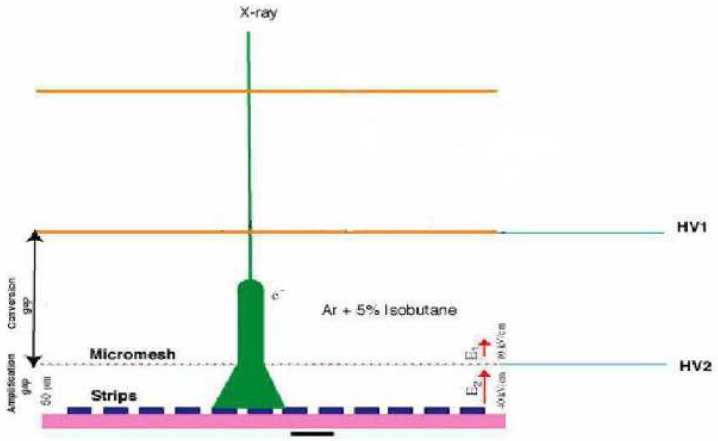


Figure 2.11: *Schematic view of the MICROMEGAS structure, where the conversion and amplification gaps are shown.*

characteristic element of a MICROMEGAS detector and plays an essential role more than just being the boundary between the conversion and the amplification regions (see [69] for further details on this).

The amplification region is only 50 $\mu$m thick from this micromesh to the read out structure. The innovation of the CAST prototype is the introduction of a x-y structure in this read out pad: the charge is collected on 192 X and Y strips of ~350 $\mu$m pitch, placed all of them in the same plane. A kapton substrate is doubly clad so the connections for the X and Y strips are in different sides, passing through vias on the Y pads as figure 2.12 shows. As a result of this the space resolution of the detector is very good, ~100 $\mu$m. With the given number and width of the strips, the active area is ~45 $cm^2$.

The detector threshold have been proven to be below 0.6 keV by experimental calibration in the Panter X-ray facility in Munich.

A Doctoral thesis [70] have been written about the MICROMEGAS detector installed on CAST and the results obtained with it from analysing the

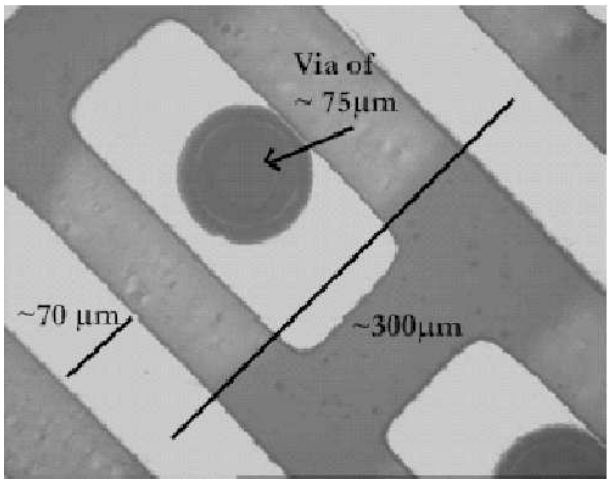


Figure 2.12: *The two dimensional reading of the strips.*

data collected during 2003 and 2004.

### The X-ray focusing system

On the same end as the MICROMEGAS, but on the east side of the magnet, the system of the focusing X-rays mirror telescope coupled with a CCD is placed. This X-ray mirror telescope would produce an "axion image" of the Sun by focusing the photons from axion conversion onto the X-ray CCD (figure 2.13). The photons coming from an area of $\sim$15 cm$^2$ are focused on a spot of 7 mm$^2$, being therefore compressed a factor $\sim$200. Because of this the signal to noise ratio is increased by two orders of magnitude. Also the data collected on the rest of the CCD during the Sun alignment periods can be used a background, reducing the systematic effects. The focusing telescope efficiency is $\sim$35%.

The Wolter I type X-ray mirror telescope of CAST is a prototype of the German X-ray satellite mission ABRIXAS [71]. It consists of a combination of 27 nested, gold coated parabolic and hyperbolic mirror shells with a focal length of 160 cm. The maximum diameter of the outer mirror shell is 163 mm while the smallest one is 73 mm. A spider like structure supports the individual mirror shells on the front side, and divides the aperture of the telescope in six sectors. Given that the diameter of the CAST magnet bore is 43 mm, only a fraction of the full aperture of the telescope is used and therefore only one of the six mirror sectors is illuminated by the nearly parallel X-ray beam coming from the magnet, as the telescope is mounted non-centrally. As any contamination and absorption on the mirror reflective surface would result in a degradation of the efficiency, the whole system has to be operated under vacuum conditions ($< 10^5$ mbar).

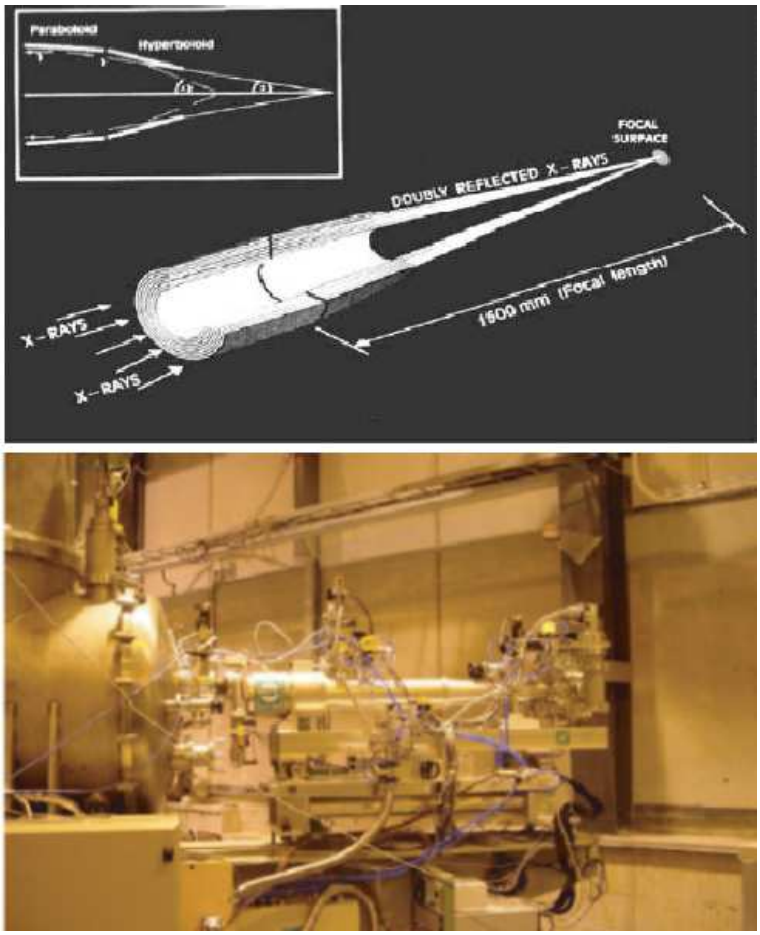


Figure 2.13: *Left: The principle of the Wolter I type telescopes. Right: The X-ray telescope of CAST (X-ray focusing device-pnCCD) as installed in the CAST experiment.*

The pnCCD detector, on which the X-rays are focused, is a prototype developed for the European XMM-Newton X-ray observatory, and its operation principle, along with its performance are described in detail in [72] and the references therein. A thin (20 nm) uniform radiation entrance window enables the detector to reach an efficiency of almost 100% over the range of interest, since it can work in vacuum directly connected to the magnet vessel, without the need of any additional window. The chip has a set of $200\times64$ pixels, each of a size of $150\times150$ $\mu$m$^2$, being its sensitive area $1\times3$ cm$^2$.

To reduce the background level a shielding was installed both inside and outside the detector's vessel (figure 2.14). The shield consists of a 2 cm thick layer of low activity copper and a 2.2 cm thick layer of low activity, ancient lead encapsulated in copper. An additional 2.5 cm lead shield is installed

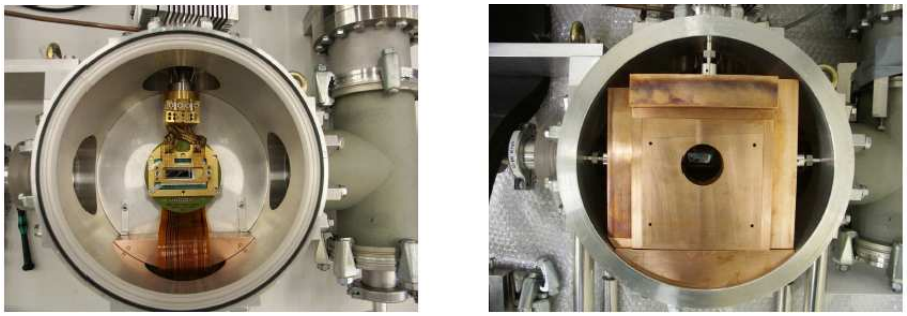

Figure 2.14: *Left: Front view of the pn-CCD detector vessel, showing the chip (centre) and vacuum components (right side of the image) Right: the detector with the inner shielding components.*

outside the detector's vacuum housing.

### The Time projection chamber

The subject of this work is the analysis of the data collected with the TPC detector in 2003 and 2004, and this requires a comprehensive description of the detector, a whole chapter (chapter 4) is devoted to it.

### The Calorimeter

As it has been mentioned in section 1.3.3 the Sun could be also a source of axions with energies higher than the 1-10 keV standard range. In order to search for these high-energy axions or axion-like particles a calorimeter was installed in 2004, sensitive to axion-induced gammas in the range of $\sim$100 keV to $\sim$150 MeV. It should be pointed out that for axions of these energies the coherence condition given in equation 2.3 is preserved for higher values of the axion mass $m_a$ as $E_a$ takes bigger values.

The detector (figure 2.15) is a large cylinder (45×50 cm$^2$, 0.64 g) of inorganic scintillator crystal ($CdWO_4$). It implements low background techniques in its design (ancient lead for the shielding, photomultiplier with low $^{40}$K content in the glass, radon displacement by flushing $N_2$) and uses a powerful pulse shape discrimination technique for the data treatment, being able to distinguish internal $\alpha$ decays, spurious PMT pulses and cosmic neutrons events from $\gamma$-induced events.

The detector was installed on February 2004 behind the MICROMEGAS one (figure 2.16) as the later is transparent to photons with energies higher than a few tens of keV. It has been taking data till November, when it was definitively dismounted. It should be mentioned here that it has been the first time that such a high energy sensitive device was placed behind an axion helioscope.

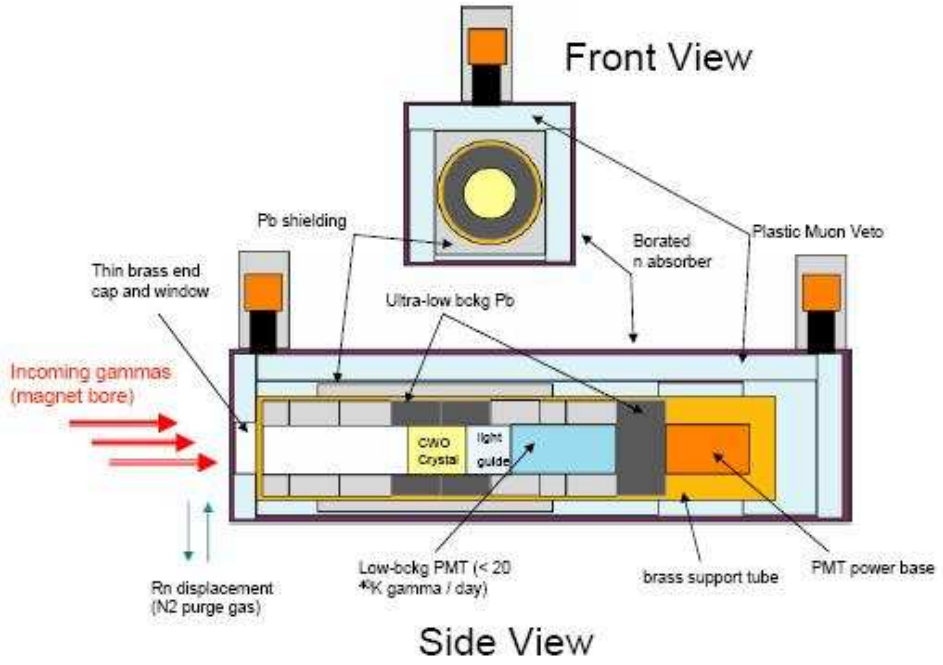


Figure 2.15: *A scheme of the design of the CAST high energy calorimeter.*

### 2.2.3. Experimental site and radioactive background

The CAST experiment is located at one of the buildings in the SR8 experimental area at CERN, placed at ground level. The lower part of the walls around is made of concrete, while the materials for the upper part are, however, very different: plastic in the north one, and concrete for the east and south walls (figure 2.4). The inhomogeneity of the building materials is evident, and it affects the data, as we will see later on the TPC data analysis chapters. Since this is an experiment at sea level, the environmental background is abundant and very rich due to the cosmic rays and the site radiation. Simple requirements in the data collected allow to eliminate via offline cuts the background contribution due to charged particles from the cosmic rays, $\alpha$ and $\beta$ radiation. Therefore the main source of background for the detectors of the CAST experiment are the $\gamma$ rays, to which the X-ray detectors would be in principle blind, but that can generate X-rays via the Compton effect with the materials surrounding the detector, and neutrons, whose signal in the detectors can mimic those from the X-rays.

By far, the most important contribution to the background is the gamma radiation coming from the radioactive chains (uranium and thorium series) and potassium-40 decay in laboratory soil, building and experimental materials. In 2004, a set of measurements to quantify the level of radiation

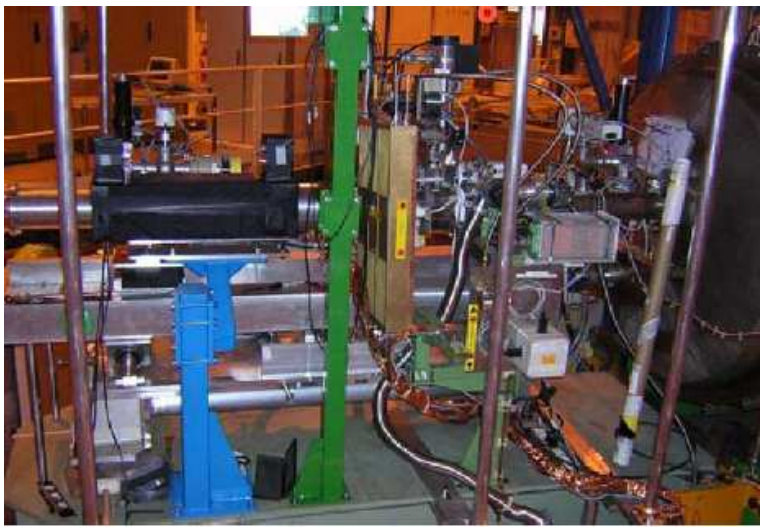

Figure 2.16: *The calorimeter installed behind the MICROMEGAS detector.*

(from 50 keV till 3 MeV) in the different zones were taken with a high purity germanium (HPGe) gamma spectrometer system [73]. In figure 2.17 the different positions in the experimental hall where these measurements were taken are shown.

These measurements confirmed the three main components mentioned before as the sources of the $\gamma$ background, and also showed that the different materials on the walls were making very different contributions to the overall level, as it can be seen in figure 2.18.

Radon is also present anywhere due to its gaseous nature, and its concentration can vary widely depending on causes such as walls or soil proximity, ventilation, and atmospheric temperature, pressure and humidity [74]. Radon isotopes have a rather sort decay time ($\sim$3 days the longer one), and they have their origin on the radioactive chains. The disintegration chain of this material involves $\alpha$ and $\beta$ emission and $\gamma$ particles due to the deexcitation of its daughter nucleus. During 2005 the radon concentration in the CAST experimental site was continuously measured in a point close to the south wall, first along an eight weeks period in summer (from July 28$^{\text{th}}$ till September 26$^{\text{th}}$) and later during four weeks more in winter (November 16$^{\text{th}}$ till December 11$^{\text{th}}$). Examples of the result from these measurements are shown in figure 2.19. From these plots it can be seen that in summer the average radon concentration was around 15 $\mathrm{Bq\,m^{-3}}$, although a clear daily variation patten of even up to a 100% is observed. This behaviour may be due to a poor air recycling during the night, together with the increase of humidity and decrease of temperature during the sunrise, which can make the radon concentration to increase. On the other hand, the winter measurements yield an similar average concentration with nearly no daily

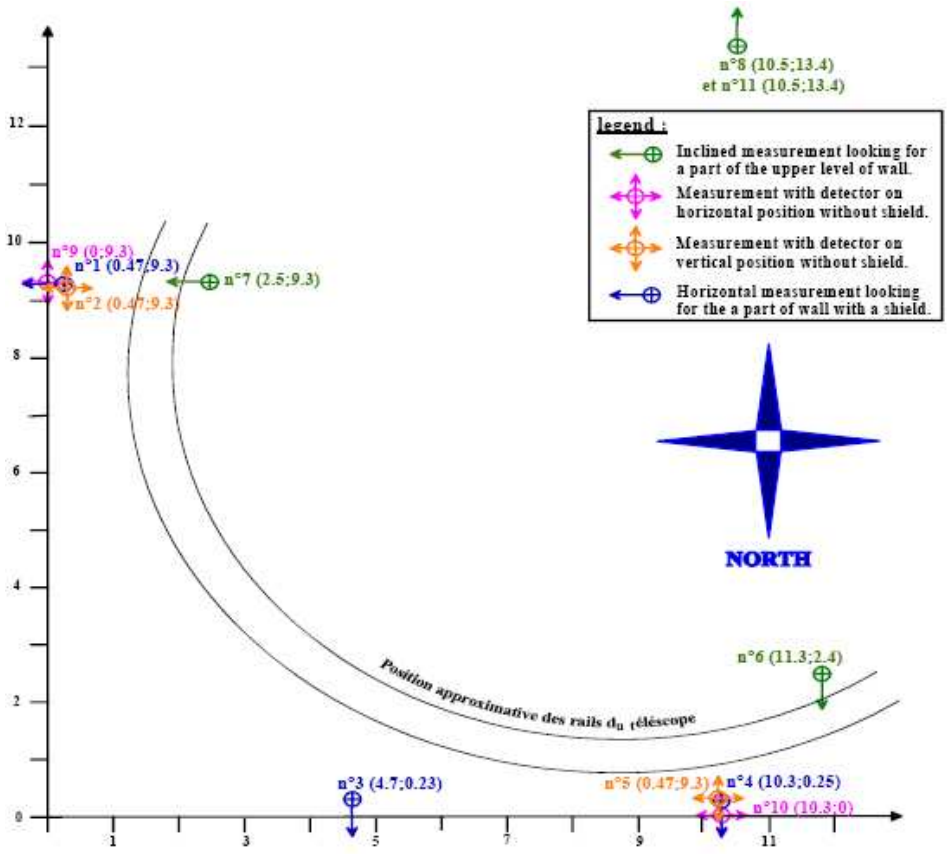


Figure 2.17: *Positions in the experimental hall where the different $\gamma$ rays measurements were taken [73].*

variations.

The neutron component of the background is below the level of the typical gamma background. Quantitative measurements of the neutron background were performed also in the experimental site with a $BF_3$ detector, showing a nearly homogeneous flux of $3 \times 10^{-2}\text{cm}^{-2}\text{s}^{-1}$. This value, and its homogeneity, points out to a cosmic source.

A more detailed explanation on the background seen by the TPC can be found in [75].

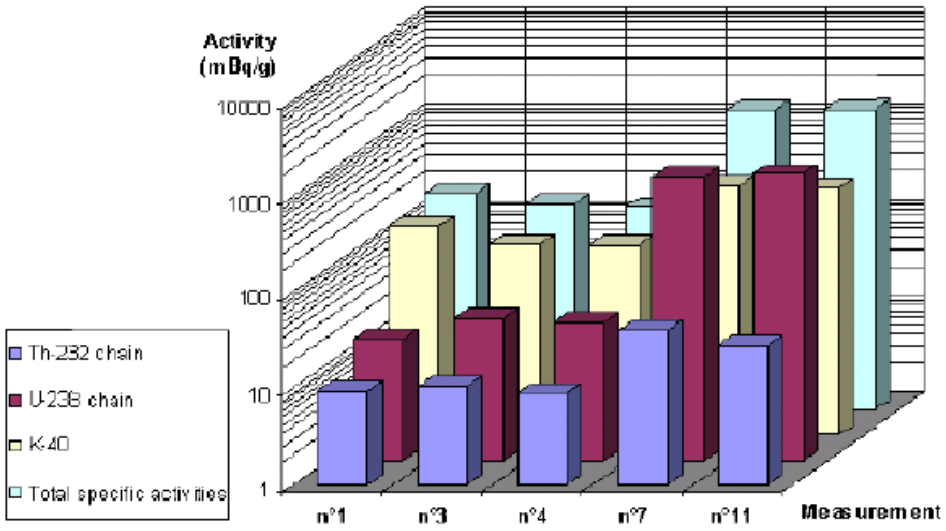


Figure 2.18: *Radioactive level in different areas of the experimental hall [73].*

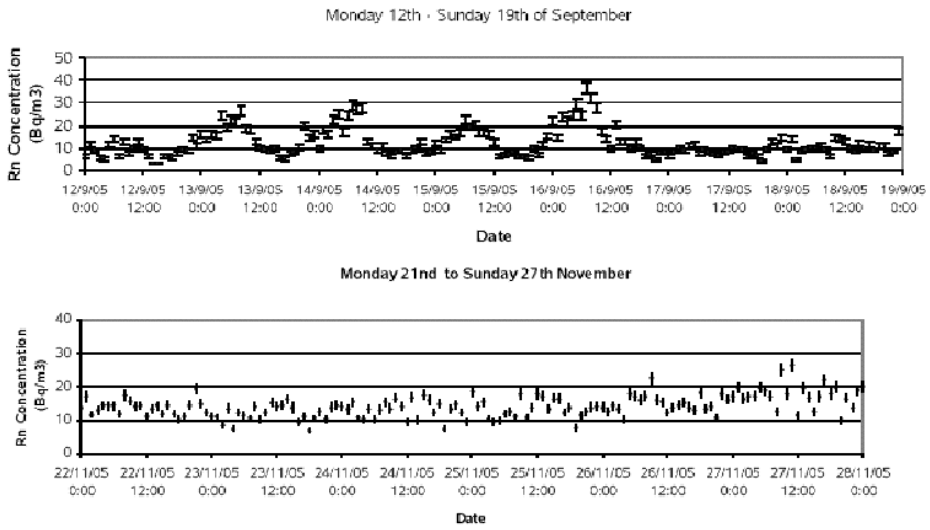


Figure 2.19: *Radon concentration variation during two different weeks, the first is summer (up) and the second in winter (down) in the CAST experimental area (plots done by E. Ferrer).*

# Chapter 3

# The Time Projection Chamber working principle

A review on the basic processes that take place in this kind of gaseous detectors will be helpful to understand the basic CAST Time Projection Chamber (TPC) features and design, and therefore will be described with some detail in what follows.

In short, a charged particle or a photon in a TPC will ionise the gas liberating electrons (usually called $\delta$-electrons in the literature), which will produce more electrons with lower energy while drifting towards the amplification area. Here, the avalanche process will take place, due to the high electric field gradient in the area close to the anode wires. Electric signals, that contain information about the original location and charge deposit of the initial interaction, will be generated in the wires due to the proximity of these charges and processed and recorded by the acquisition electronics. A good text on gas-filled detectors is the one given by G. Rolandi and W. Blum [76]

In what follows these processes will be reviewed with some detail, focusing in the detection of photons.

## 3.1. Ionisation processes

In general, it is the electromagnetic interaction of the photons with the media in their flight path the main process that allows for these particles to be detected [77, 78]. The interaction, unlike what generally happens with an charged particle, will be usually a single localised event. The total cross-section $\sigma$ may be broken down into partial components as follows (neglecting Rayleigh processes):

$$\sigma = \sigma_{PE} + \sigma_C + \sigma_{PP}. \tag{3.1}$$

The individual cross-sections are related to the *Photoelectric effect*, the *Compton effect* and *pair production* respectively. The factor Z embodies the assumption that all the atomic electrons contribute individually (and incoherently) to Compton scattering. This will be true only when the photon energy is much greater than the K-shell ionisation energy of the atom. Here elastic (Rayleigh) scattering has been neglected, since it does not remove photons from a beam unless collimation is very fine. In figure 3.1 we have the total cross section for photons in argon as a function of the photon energy, together with the individual contributions of the different processes described. As can be seen, at low energies, up to several keV, the dominant process is photoelectric conversion; them Compton scattering takes over, up to energies of a few hundreds keV, and at even higher energies electron-positron pair production is the most probable process. As in CAST we are interested in the detection of photons with energies varying from 1 to 10 keV, the photoelectric effect is the one that concerns us, and therefore the one that we will review in detail.

### Photoelectric effect

Photoelectric absorption is a quantum process involving one or more transitions in the electron shells of a molecule. If we denote by $\mathrm{E}_j$ the energy of a given shell $j$, photoelectric absorption in the shell can take only place for photons at energies $\mathrm{E}_\gamma \geq \mathrm{E}_j$, being the inner most shells the ones to be more likely involved in the process. The absorption is maximum at the edge, and then very rapidly decreases with energy. The absorption of a photon of energy $\mathrm{E}_\gamma$ in a shell of energy $\mathrm{E}_j$ results in the emission of a photoelectron of energy $\mathrm{E_e} = \mathrm{E}_\gamma - \mathrm{E}_j$; the excited atom returns to its ground state mainly through two mechanisms:

- **Fluorescence**: the transition of an electron from an energy shell $\mathrm{E}_i < \mathrm{E}_j$ into the $j$-shell, with the emission of a photon of energy $\mathrm{E}_j - \mathrm{E}_i$.
- **Auger effect**: internal rearrangement involving several electrons from the lower energy shells, with the emission of an electron of energy very close to $\mathrm{E}_j$.

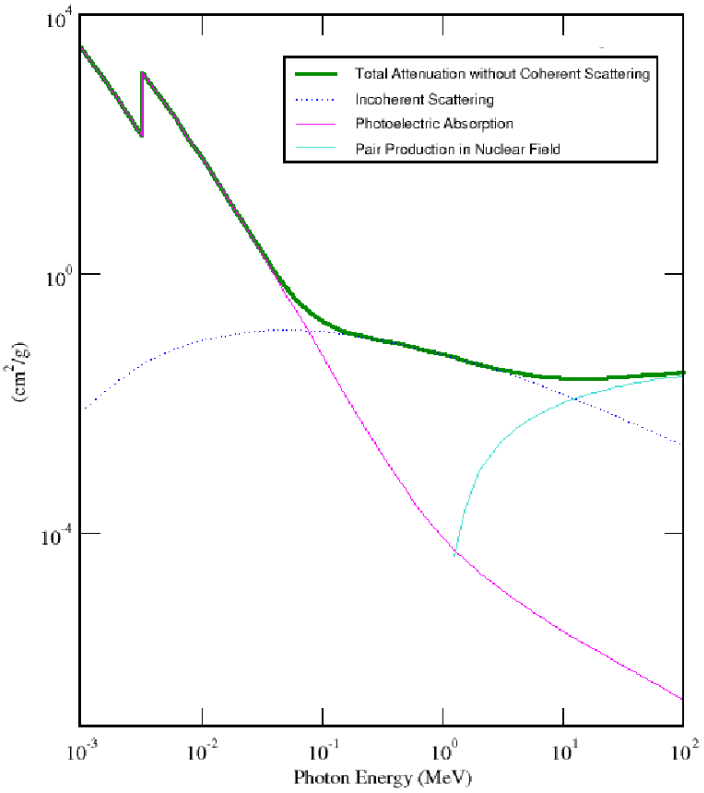


Figure 3.1: *Total photon cross-section in argon versus its energy, and the different contributions*

The fraction of de-excitations producing the emission of a photon is called *fluorescence yield*. For the K-shell, the fluorescence yield increases with the atomic number. In argon, about **15%** of the photoelectric absorptions are followed by the emission of a photon [77]. The secondary photon, emitted at an energy just below the K-edge, has a very long mean free path for absorption and can, therefore, escape from the volume of detection. This produces the characteristic escape peak of argon, at energy $E_\gamma - E_K$.

### $\delta$-electrons ionisation

Once the photoelectric process has taken place, and the primary photoelectron and, if so, Auger electron have been emitted, they both will start to ionise themselves the gas in their encounters with the atoms in the media as long as they have enough energy to do so.

These charged particle can interact in many ways in a gaseous or condensed medium, but from all the possible interactions (strong, weak, etc...) only the electromagnetic one (Coulomb interactions, bremsstrahlung, tran-

sition radiation, Čerenkov) is the relevant one, as it is many orders of magnitude more probable than the others.

As these electrons propagate, their electromagnetic field will interact with the one in the atoms (A) in the medium, resulting in either ionisation:
$e^- A \rightarrow e^- A^+ e^-$
or excited states A*, being this the metastable state of a noble gas in most common drift chambers. It is a common procedure to have a mix of a noble gas with a molecular additive called "quencher" (see section 3.3) and, providing the excitation energy of A* is above the potential ionisation of the quencher (B) we can have the following process (*Penning effect*):

$A^* \rightarrow AB^+ e^-$

The relative individual contribution from all these cases to the final amount of charge is still in most cases unknown.

**Statistics of ionisation**

The average number of final electron-ion pairs that can be produced per single photon of energy $E$ interaction can be conveniently expressed by:

$$n_T = \frac{E}{W} \tag{3.2}$$

where $W$ is the average energy to produce one single pair, which depends on the energy and nature of the incident particle as well as on the gas composition and density. As mentioned before, the energy $W$ depends on the ionisation and excitation mechanics, and it has to be determined by experiment. For pure noble gases, $W$ varies between 46 eV for He and 22 eV for Xe; for pure organic vapours the range between 23 and 30 eV is typical. Ionisation potentials of the atoms are smaller than $W$ by factors that are typically between 1.5 and 3, which give us a hint of the energy that goes to excitation.

There is a fluctuation associated with the number of electron-ion pairs created in every interaction of a single photon. A priori, such parameter would be expected to be Poisson distributed, as it is the common assumption to do for any variable that can only have discrete values. But experimentally this was discovered not to be the case. To quantify how far the variance of the final distribution is from the naive Poissonian one, the Fano factor F was introduced. In a Poissonian distribution we know that the variance is equal to the mean, which in our case would be $n_T$. Then the real variance of the distribution will be given by

$$\sigma = \mathbf{F} n_T. \tag{3.3}$$

In figure 3.2 we can see two examples of the number of electrons distribution obtained for 3 and 8 keV photon interaction on argon respectively, simulated with Garfield program [79], which uses Heed routines to calculate the interaction of the particles with the gas [80]. We see that indeed these

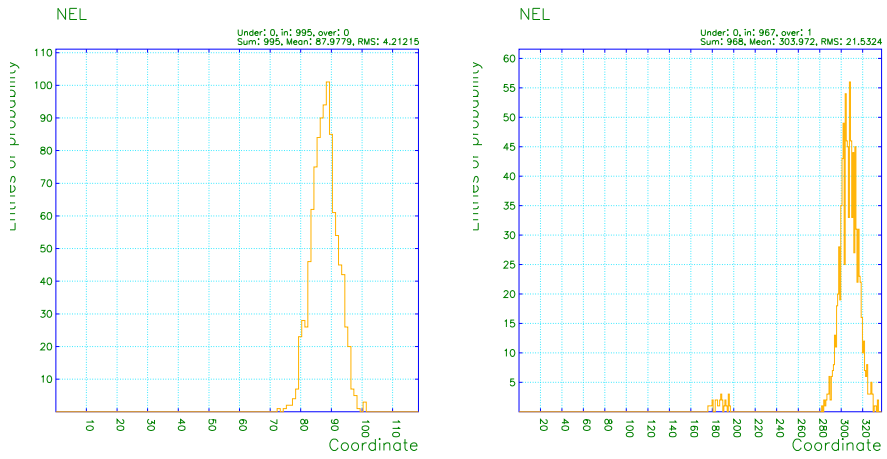


Figure 3.2: *Spread in the number of electrons produced by the interaction of 3 keV (left) and 8 keV (right) photons in argon simulated with Garfield [79] program. On the right plot we see also the contribution from the escape peak.*

distributions look like narrow large mean Poissonians.

In drift chambers the energy deposition will be related to the amount of charge which is recorded in the sense wires. Then, as it can be guess, the energy resolution of a drift chamber is ultimately determined by this factor F, as for the same deposited energy not always the amount of charge gathered will be the same. F tells about the magnitude of this spread. It has been seen that it can depend on the nature and energy of the incident particle, as well as on the gas mixture and conditions [81].

## 3.2. Drift of electrons and ions in gases

Once the photon interaction has taken place and the secondary charges have been created, we must now study their drift due to the electric field E applied. The behaviour of a drift chamber will depend on this process, and therefore we will study it with some detail.

The phenomenon that we want to describe is the motion of electron and ion swarms through neutral gases when an electric field is applied. To address this problem the kinetic classical theory based on the linear Boltzmann transport equation is used. This can be done when the de Broglie wavelength of the swarming electrons is much smaller that the spacing between atoms, which will be the case until the gas reaches pressures of $\sim$ 100 atm. A nice introductory review on the matter is given by Kumar [82].

As in the CAST TPC there is not magnetic field applied, only the case B=0 will be developed, for further information the reader is again directed to the reference quoted before.

### Drift and diffusion of electrons

If there were no electric field in the gas chamber, the charges produced in the interaction of the photon would quickly lose their energy in multiple collisions with the gas molecules and assume the average thermal energy distribution of the gas. Simple kinetic theory of gases provides the average value of the thermal energy, $\epsilon_T = (3/2)kT \approx 0.04$ eV at normal conditions, being the Maxwellian distribution of the energies given by:

$$f(\epsilon) = C\sqrt{\epsilon}\, e^{-(\epsilon/kT)}. \tag{3.4}$$

If a electric field is applied, the free electrons will continue to have a nondirectional velocity $v$ (and a different energy $\epsilon$) but they will also exhibit a drift along the field direction, with a much lower mean drift velocity $w$. As the electrons are scattered on the gas molecules, this drift velocity will derivate from the average, owing to the random nature of the collisions, and the swarm will show as a net diffusion that increases with time. Wagner *et al.*[83] discovered that the value of electron diffusion along the electric field can be quite different from that in the perpendicular direction. The determination of these parameters, drift velocity $w$ and transversal and longitudinal diffusion coefficients $\mathrm{D}_T, \mathrm{D}_L$, together with their relation with the microscopic parameters of the swarm, is of crucial interest on gas chamber design and development. In this way, the spatial resolution of a chamber will depend directly on the value of $\mathrm{D}_T$, and its temporal resolution on $\mathrm{D}_L$. In what follows how these swarm theories cope with the determination of these parameters will be briefly explained.

The probability of finding any electron at location $\mathbf{r}$ with a velocity $\mathbf{v}$ is the quantity of interest as a starting point. As this quantity may well change over time, we must also consider its dependence upon time t, $f(\mathbf{r}, \mathbf{v}, t)$. The Boltzmann transport equation states that:

$$\left(\frac{\partial}{\partial t} + \mathbf{v}\nabla_r + \frac{e}{m}(\mathbf{E} + \mathbf{v} \times \mathbf{B})\nabla_v + \mathbf{J}f(\mathbf{r}, \mathbf{v}, t)\right) = 0, \tag{3.5}$$

where $\mathbf{J}$ denotes the collision operator. In swarms the phenomena are controlled by collisions between the charged particles and the background gas. Therefore interactions between the particles themselves play no role, as it has been proven experimentally varying the charged particle densities by several orders of magnitude and showing that the transport characteristics are not affected by this. Because of this, the Boltzmann collision operator can be taken to be linear.

We can define the density $n(\mathbf{r}, t)$ of charged particles in the gas, and it is straightforward to see that this parameter can be calculated from the distribution function $f$ by:

$$n(\mathbf{r}, t) = \int f(\mathbf{r}, \mathbf{v}, t) d\mathbf{v}. \tag{3.6}$$

The equation of continuity for $n(\mathbf{r},t)$ provides the link between theory and experiment. In its usual notation it is given by (providing that the electric field is in the z direction):

$$\partial_t n = -\alpha n - w\partial_z n + D_T(\partial_x^2 + \partial_y^2)n + D_L\partial_z^2 n. \tag{3.7}$$

Here $\alpha$ is the attachment coefficient and represents, as it will explained later with more detail, the rate of electrons being lost because of recombination. This equation is just a representation of the evolution in space and time of the swarm of electrons as it drifts towards the electrodes.

Solving this set of differential equations (3.5, 3.6, 3.7) would give us the relation of the transport coefficients with the microscopic picture of the system.

But this is not an easy task to do, and some approximations are required. First of all it is of extended use to develop the distribution function $f$ in spherical harmonics:

$$f(\mathbf{r},\mathbf{v},t) = \sum_{l=0}^{\infty}\sum_{m=-l}^{l} f_m^l(\mathbf{r},\mathbf{v},t)Y_m^l(\widehat{v}). \tag{3.8}$$

The *classical* theory of electron transport properties, that was widely accepted until the late 1970s, was assuming that the electrons were undergoing only elastic collisions with the neutral molecules. In this case, when an electron of mass m and a neutral molecule of mass M exchange a fraction ($\sim 2\mathrm{m}/\mathrm{M} \ll 1$) of their energy, even if the swarm is driven though the gas by a strong electric field, energy and momentum gained from the field would be distributed in all directions, which has the effect of randomising directions of electron velocity vectors $\mathbf{v}$ without significantly altering their magnitude. When the distribution function is isotropic in phase space this series of spherical harmonics should be rapidly convergent and the "two-term" approximation ($l_{max} = 1$) can be taken. Palladino and Saudolet [84] were the first ones to apply this formalisms to drift chambers. Just for illustration purposes, the two-term derivation will be quoted here, giving the results that can be attained.

Based on the conditions of the typical experiment setup, these two-term theories are usually developed in the *hydrodynamic* regime, where swarm evolution is unaffected by boundary conditions and has no memory of its initial configuration. This allows us to neglect the spatial and temporal dependencies of $f$, regarding it as a function of velocity alone $f = f(\mathbf{v})$. The regime of elastic scattering, as well as good part of the regime inelastic scattering can be described by two functions: an effective cross section [1] $\sigma(v)$ and the fractional electron energy loss per collision $\lambda(v)$. In the normal working conditions of a drift chamber the energy of the electrons due to the

[1] This parameter is often called the momentum transfer cross-section

field is much more higher than the thermic one and, as an approximation also here we neglect their thermal motion. With all these assumptions the distribution of the random velocities can be given by:

$$f(v) \propto \exp\left(-\frac{3}{e^2}\left(\frac{N}{E}\right)^2 \int_0^{\epsilon} \lambda\sigma^2\epsilon d\epsilon\right), \tag{3.9}$$

where the total energy of the electron is related to its instantaneous velocity by $\epsilon = 1/2mv^2$. Figure 3.3 shows the energy distribution of these electrons $f(\epsilon)$ for different electric field values.

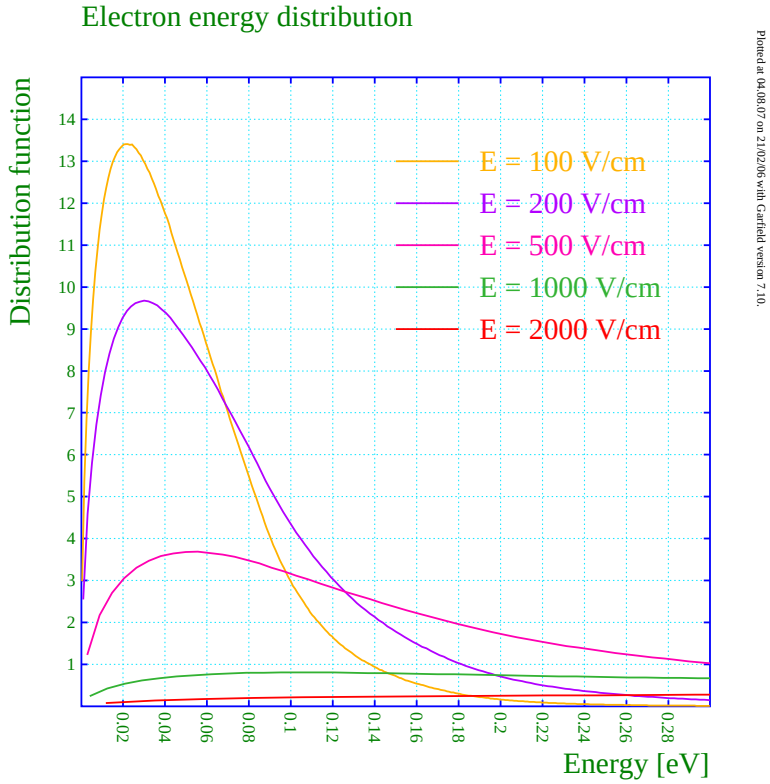


Figure 3.3: *Energy distribution of electrons moving in a gas where a electric field E is applied (Calculated with Garfield).*

With such distribution the drift velocity is given by:

$$w = -\frac{4\pi}{3}\frac{e}{m}\frac{E}{N}\int_0^{\infty}\frac{v^2}{\sigma}\frac{df(v)}{dv}dv, \tag{3.10}$$

where N is the number of atoms of the gas per unit volume.

As we have assumed an isotropic approximation the diffusion coefficient is going to be also isotropic:

$$D = \frac{4\pi}{3N}\int_0^{\infty}\frac{v^3}{\sigma}f(v)dv. \tag{3.11}$$

If we were calculating the electric anisotropy of diffusion we should retain in the distribution $f(v)$ its dependence on position.

As it has been said before, we must notice that this expressions depend on the momentum transfer cross-section $\sigma(v)$ and on the fractional energy transfer $\lambda(v)$, and therefore we should expect to determine then experimentally. But indeed it is simpler to determine from experiments the drift velocity and the diffusion coefficients of a given gas, than to measure its cross-section. It is using the equations 3.10 and 3.11 that the cross section for given gases can be deduced. It has been found that this parameter varies for some gases very strongly with the electric field, going through maxima and minima (Ramsauer effect). This is a consequence of the fact that the electron wavelength approaches those of the electron shells of the molecule, and complex quantum-mechanical processes take place there. In figure 3.4 we can see the argon cross-section as a function of the energy for the different processes that can take place.

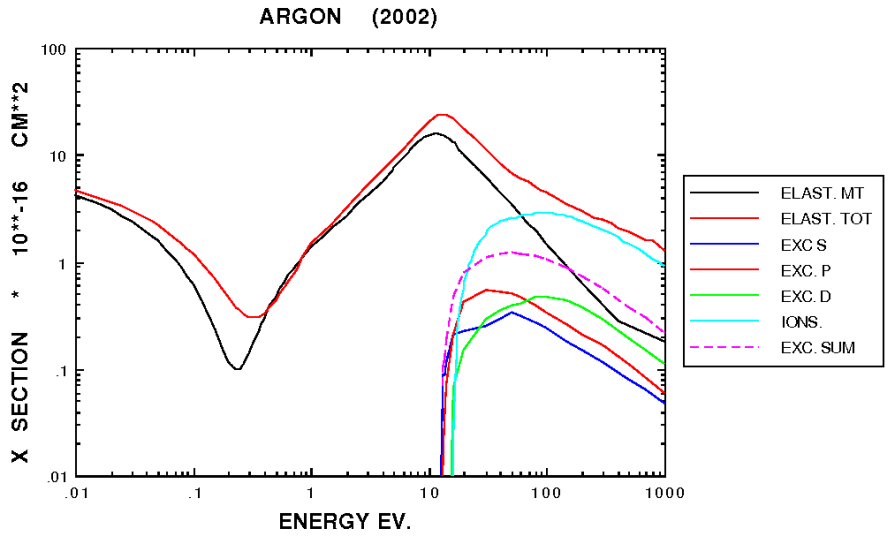


Figure 3.4: *Argon cross section as a function of the energy for the different processes that can take place, as used by the Magboltz simulation toolkit*

Soon it was realized that these approximations made this expression often hopelessly inadequate for many typical situations encountered in gas detectors. Indeed, when two or more gases are mixed together, it has been observed that the calculated electron drift and diffusion properties differ from the measured ones although the gases separately can be accurately described by a Boltzmann transport equation. Therefore nowadays it is widely stabilised, that if high accurate (around 0.1%) theoretical values of

electron transport coefficients are required, "multiterm" solutions of Boltzmann's equation are needed [85].

Also now a computer toolkit called Malgbotz [86] for simulation of particles swarms is gases is available. The Monte Carlo technique that this software uses allows the solution of the transport equations to be independent of the series expansions in Legendre Polynomials or Spherical Harmonics required by analytic solutions of the Boltzmann equations. All electron scattering, excitation, ionisation and attachment are treated, and the accuracy that can be attained is better than 1 % for the drift velocity and 2 % on the diffusion coefficients, depending on how well the cross section are known. For example, the cross section of argon used by this software is shown in figure 3.4.

In figure 3.5 we can see the simulated (Garfield [79]) interaction of X-rays in argon (Heed [80]) and the consequent drift of the electron swarm (Malgbotz [86])

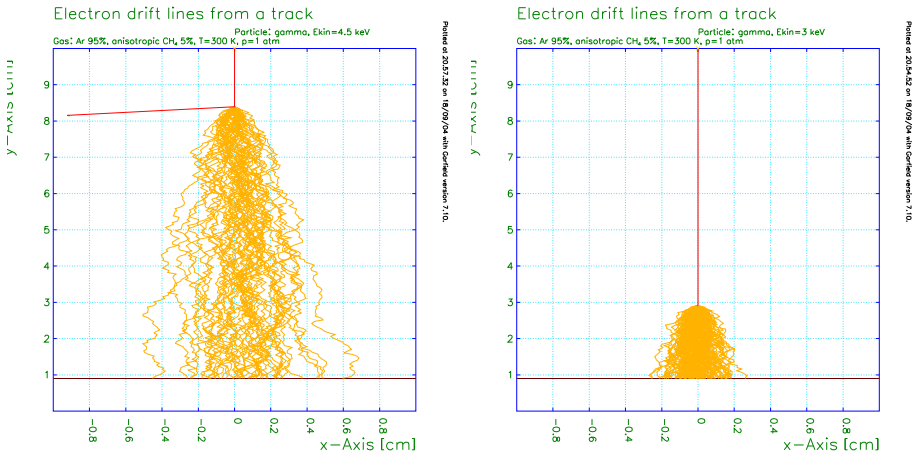


Figure 3.5: *Left: Interaction and drift of a 4.5* keV *photon in argon:*$CH_4$ *(95:5) simulated with Garfield in interaction with Heed (ionisation) and Malgbotz (drift). Right: the same for a 3* keV *photon.*

### Drift of ions

The drift of ions can also be described within the framework of the Boltzmann equation explained in the previous section. But there is a crucial difference now, given by the fact that the mass of the ions this time is of the same order as the mass of the surrounding atoms. Also the chemical reactions involved in their interaction with such atoms are different.

Ions in similar field acquire, on one mean-free path, an amount of energy that is similar to that acquired by electrons. But a good fraction of this

energy is lost in the next collision, and the ion moment is not randomised as much. Therefore far less energy is stored in the motion, and the energy of ion will be mostly thermal. Also the diffusion will be several orders of magnitude smaller than that of the electrons in similar fields.

The drift velocity is found experimentally to be proportional to the reduced field E/p (electric field/pressure of the gas) up to high fields. It is therefore convenient to define a quantity called *mobility* $\mu$ as:

$$\mu = \frac{w_i}{E}, \tag{3.12}$$

where $w_i$ is the average drift velocity of the ions. A constant mobility is the consequence of the fact that, up to very high fields, the average energy of ions is almost unmodified, which of course is not the case for electrons, as it has been explained.

In order to find a expression that would relate the mobility $\mu$ with the microscopic parameters of the chamber a very simple model of collision of rigid spheres can be used. Applying the most basic kinematics to it [76] the following expressions can be deduced:

- **Low field:** When the field applied to the chamber is lower than the one in which the ion, over a mean free path, would pick up an amount of energy equal to the thermal one, the following expression is obtained:

$$\mu = \left(\frac{1}{m} + \frac{1}{M}\right)^{1/2} \left(\frac{1}{3kT}\right)^{1/2} \frac{e}{N\sigma}, \tag{3.13}$$

  where m and M are the masses of the ion and the gas molecule respectively. We see that for low fields it is characteristic of the mobility to be independent of the field strength E.

- **Large field:** In this case this expression turns out to be:

$$\mu = \left(\frac{e}{m^* N\sigma E}\right)^{1/2} \left(\frac{\lambda m}{2m^*}\right)^{1/4}, \tag{3.14}$$

  where the reduced mass $m^*$ is given by $1/m^* = 1/m + 1/M$. In this case we see that mobility does depend on E as $1/\sqrt{E}$.

Also this classical argument leads to the following relation between the diffusion coefficient of the ions $D$ and their mobility $\mu$:

$$\frac{D}{\mu} = \frac{kT}{e} \tag{3.15}$$

known as the *Nernst-Townsend* or the *Einstein* formula.

In figure 3.6 we can see the mobility of several species of ions in argon for E/N 10 Td (low field). The solid line represents the expected value assuming the model where both the ions and the gas atoms are rigid spheres.

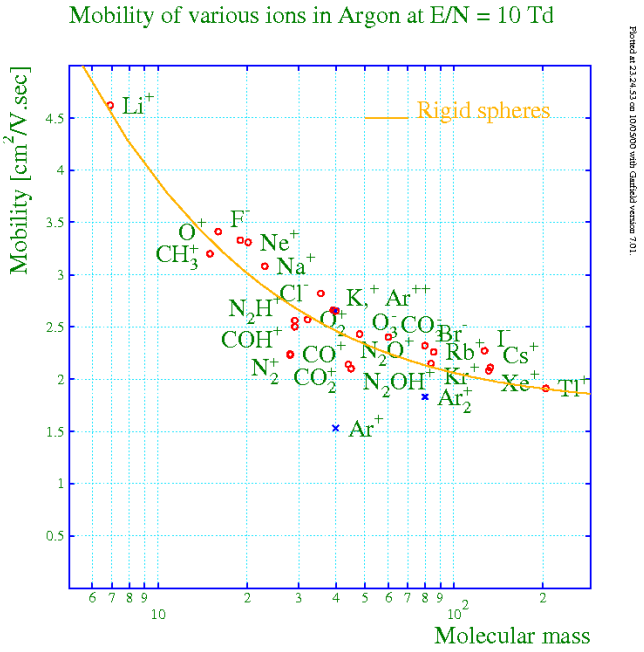


Figure 3.6: *Mobility of ions in argon at E/N 10 Td* [87]

### Electron attachment

During their drift, electrons may be absorbed in the gas by the formation of negative ions. Whereas for noble gases collisions energies of several electronvolts (which are bigger than the energies reached during the drift is gas chambers) are required to form stable negative ions, there are some molecules, often present in the gas as impurities, that are capable of attaching electrons at much lower collision energies. Among all the elements, the largest electron affinities are found with the halogenides (3.1-3.7 eV) and with oxygen ($\sim$ 0.5 eV). Therefore we have in mind contaminations due to air, water, and halogen-containing chemicals.

The rate of attachment is a very complex quantity that will depend on the mean energy of the electrons ($\bar{\epsilon}$) and on the nature and concentration of the molecular components of the gas. For example, the three-body $O_2$ attachment coefficient involving the methane molecule is large enough to cause electron losses in chambers where methane is a quenching gas. With 20% $CH_4$ at 8.5 bar, an oxygen contamination of 1 ppm will cause an absorption of a 3%/m of drift at a velocity of 6 cm/$\mu$s.

In general, for the operation of drift chambers the absorption of electrons is a nuisance because the signal is being attenuated. Therefore this effect is always avoided as much as possible using clean gases.

## 3.3. Amplification of ionisation

### Phenomenology

Up to now we have a cloud of electrons drifting due to the constant electric field in the chamber. But to really "detect" the incident photon we need to convert them into an electric signal, which is not an easy task to do, given the feeble nature of the electron swarm. Because of this an amplification stage is required where the number of electrons is multiplied by a factor that can oscillate from $10^3$ till $10^8$ depending on the detector. To archive this, these drifting electrons are driven through an increasing electric field where they will acquire enough energy to start ionisation avalanches. The simplest and most used example of "amplifier" is the proportional wire, which I will explain here in detail, as it is the one used in the CAST TPC. It owns its name to the fact that the signal is proportional to the number of electrons collected.

As an electron drifts towards the wire it travels in an electric field which is not constant anymore, but has a radial dependence given by:

$$E(r) = \frac{\lambda}{2\pi\epsilon_0}\frac{1}{r}, \tag{3.16}$$

being $\lambda$ the linear charge density and $r$ the radial distance from the wire. It is very close to the wire when the field starts to be radial and therefore the avalanche develops in the very near vicinity of the anode, being its longitudinal extent typically of the order of 50 to 100 $\mu$m.

When the electric field that the electrons feel is higher than a few kV/cm the energy that these ones can pick up between collisions is enough to produce inelastic phenomena, excitation of various kinds and ionisation, much the same as discussed in section 3.1. In general the physical process inside the avalanche are quite complicated and not well known yet.

A very interesting role is played by the photons from de-excitations, which are as abundant as electrons because the relevant cross-sections are of the same order of magnitude. Some of these photons will be energetic enough to ionise the gas and that involves a very dangerous phenomena for the proportionality of the avalanche. If it happens that these ionising photons travel further, on the average, than the original size of the avalanche, then the electrons that they produce will each give rise to another full avalanche and the counter may break down. To absorb these far-travelling photons an organic quench gas is mixed with the noble gas. The molecules of this gas, can be exited in rotational and vibrational modes, which are radiationless, opposite to what happens to a noble gas, where the only excitation modes go through radiation absorption and emission. Therefore most of this energy will be dissipated thanks to the addition of this organic vapour to the noble gas, and therefore the proportionality of the avalanche will be ensured.

### Amplification factor

Now we are interested in quantifying the magnitude of the multiplication. As described in the previous section, the physics processes involved in the avalanche are not well known yet and therefore there is not a microscopic expression that could give us the number of electrons that we will have at the end per initial one. To calculate this a pure experimental parameter was introduced called the first Townsend coefficient ($\alpha$). This coefficient represents the number of ion pairs that are being produced per electron and per unit of length. This being known, the increase of the number of electrons $dN$ per path $ds$ will be given by:

$$dN = N\alpha ds. \tag{3.17}$$

The amplification factor on a wire will be given by integrating this expression between the point $s_{min}$ where the field is just sufficient to start the avalanche and the wire radius $a$:

$$\frac{N}{N_0} = exp \int_{s_{min}}^{a} \alpha(s) ds, \tag{3.18}$$

where $N$ and $N_0$ are the final and initial number of electrons, and the ratio $N/N_0$ is called *gain* (G). Expression 3.18 can be recast in a more convenient way if the dependence on the electron path s is tranformed on a dependence on the electric field E. In this case $s_{min}$ will correspond with $E_{min}$, which is the minimal field to start multiplication, and corresponds with the energy required to ionise the molecules divided by the mean free path between collisions. Therefore $E_{min}$ will be proportional to the gas density. In this way we will have:

$$G = exp \int_{E_{min}}^{E(a)} \frac{\alpha(E)}{dE/ds} dE. \tag{3.19}$$

In the case of the proportional wire we know that the electric field is given by equation 3.16, and substituting this in equation 3.19 we have:

$$G = exp \int_{E_{min}}^{E(a)} \frac{\lambda\alpha(E)}{2\pi\epsilon_0 E^2} dE. \tag{3.20}$$

Therefore, if the dependence of the first Townsend coefficient with the electric field were known for a certain detector configuration and gas mixture, it would be possible to get an analytic expression for the gain. But in general, as it has been explained before, no fundamental expression exists for $\alpha$ and it must be measured for every gas mixture. In figure 3.7 we can see the measured dependence of this coefficient on the electric field divided by the pressure of the gas. As it can be seen they are proportional, as the ionisation cross section goes up when the energy $\epsilon$ of the electrons increases.

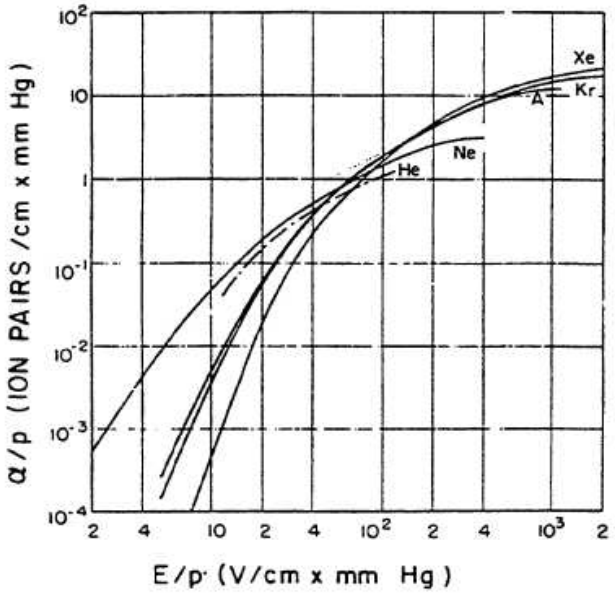


Figure 3.7: *First Townsend coefficient as a function of the reduced electric field for different noble gases [77]*

The Magboltz simulation toolkit mentioned in section 3.2 can also calculate the first Townsend coefficient given the gas configuration and the electric field, although still the results obtained are not very accurate due to the lack of understanding of the different avalanche effects, mainly photo- and Penning ionisation [88].

### Statistical Fluctuation of the gain

Once the amplification of the charge has been studied introducing the "gain" of a gaseous detector, some little attention will have to be paid to the statistical fluctuation of this parameter, as this also will limit the ultimate energy resolution capability of the detector. If the approximation of every electron generating its own avalanche independently of the presence of the others near by is taken, then the distribution of the total number of electrons at the end of the avalanche can be given by adding up the probability distributions P(n) of having n electrons at the end of the individual little avalanches. There are several different models to determine P(n), and here the most common ones will be quoted.

**Yule-Furry Process** In this model we will assume that an electron at every moment can split in two, being the probability for the birth of another electron in any interval $\Delta t$ proportional to the number of electrons $n$ and a

constant parameter $\lambda$:

$$n\lambda\Delta t. \tag{3.21}$$

In this case the probability distribution for the number of electrons is given by:

$$P(n) = \frac{1}{\bar{n}}\left(1 - \frac{1}{\bar{n}}\right)^{n-1}, \tag{3.22}$$

where $\bar{n}$ is its mean. The limit of $\bar{n} \to \infty$, which is quite appropriate for avalanches, yields the following distribution:

$$\mathrm{P(n)} = \frac{1}{\bar{\mathrm{n}}}\mathrm{e}^{-\mathrm{n}/\bar{\mathrm{n}}} \tag{3.23}$$

with variance $\sigma^2 = \bar{n}^2$. So we see that the Yule-Furry process has an exponential distribution, being the small signals the most probable ones and the r.m.s width is equal to the mean.

This exponential distribution is observed in small electric fields (see Rolandi and Blum book for an example of experimental measurements) but, for high values of E, the main assumption of this theory is not fulfilled because in this case the instantaneous probability of ionisation does depend on the previous history of the electron, in particular, on the distance r which the electron has covered towards the anode after the last ionisation. To explain the experimental results a new model was introduced by Byrne in 1962 [89]

**Byrne Process** To cope with the dependence on the distance to the wire Byrne introduces a function $\theta$(r) in the expression 3.21 of the probability for the birth of a new electron which now will be given by:

$$n\lambda\theta(r)\left(b + \frac{1-b}{n}\right)\Delta r. \tag{3.24}$$

The dependence on n in this ansatz represents the idea that a fluctuation to large n in the first part of the avalanche reduces the rate of development in the second part. Also a undefined parameter b is introduced because we will be lead to a class of distributions that include the Yule-Furry distribution for b=1, and the strongly peaked around the media Poisson distribution for b close to 0.

If a reasonable assumption for the function $\theta$(r) in given, the expression of P(n) derived from 3.24 is:

$$P(n) = \frac{1}{b\bar{n}}\frac{1}{k!}\left(\frac{n}{b\bar{n}}\right)^k e^{-n/b\bar{n}}, \tag{3.25}$$

where $\bar{\mathrm{n}}$ is the media, $\sigma^2 = \mathrm{b}\bar{\mathrm{n}}^2$ the variance, and k=1/b-1. Different expressions for $\theta$(r) will be reflected in a different value for the media of the distribution. Here the asymptotic assumption $\bar{\mathrm{n}} \to \infty$ have been used also.

This distribution is called *Polya* or *negative binomial*, and as it has been mentioned before, when b=1 it yields the expression 3.23, shifting to the Poissonian distribution when b moves to zero.

The ratio that decides the distribution function of the final number of electrons produced in the avalanche is:

$$\chi = \frac{\mathrm{E}}{\alpha(\mathrm{E})\mathrm{U_{ion}}}, \tag{3.26}$$

where E is the electric field, $\alpha$ the first Townsend coefficient and $\mathrm{U}_{ion}$ the ionisation potential of the gas. The average distance that electrons can travel between two successive ionising collisions is equal to $1/\alpha$ by definition of the first Townsend coefficient. Then $E/\alpha$ is the energy that these electrons can pick up in this distance. When this quantity is much bigger than the ionisation energy $\mathrm{U}_{ion}$ of the gas we can say that the probability for the creation of a new electron does not depend on the previous history of the electrons which are already in the media, which is the ansatz for the Yule-Furry process. Due to the dependence of $\alpha$ with E (see figure 3.7) the ratio $\chi$ usually decreases with increasing E, and knowing this it can be understood why the probability distribution corresponding to the Yule-Furry process is valid only for low fields strengths.

When the geometry of the avalanche is driven by a wire we have a full range of field strengths. In this case it can be expected that the shape of the distribution is determined mainly by the weaker fields at the beginning of the avalanche because it is more influenced by the statistics of the small numbers than by the intensity variations in the fully developed avalanche.

Up to now we have been talking about single electron distributions, but in general we have N electrons generated in the primary radiation interaction. The probability distribution of these N ions, F(N) is usually given by the central-limit theorem of statistics, provided this number N is large enough. N will be given by the sum:

$$\mathrm{N} = \mathrm{n_1} + \mathrm{n_2} + \mathrm{n_3} + ... + \mathrm{n_k} \tag{3.27}$$

where each of the independent variables $n_i$ has the distribution function P(n) calculated before with mean $\bar{\mathrm{n}}$ and variance $\sigma^2$. Then the theorem states that the distribution F(N) will be given by:

$$\mathrm{F(N)} = \frac{1}{\mathrm{S}\sqrt{2\pi}}\exp\left[\frac{(\mathrm{N}-\bar{\mathrm{N}})^2}{2\mathrm{S}^2}\right] \tag{3.28}$$

with mean $\bar{\mathrm{N}} = \mathrm{k}\bar{\mathrm{n}}$ and variance $\mathrm{S}^2 = \mathrm{k}\sigma^2$.

If the energy resolution were a crucial point on the design of a gaseous detector, variable electric field in the amplification zone should be avoided and the electric field should be big enough to ensure the Poisson-like Polya

distribution regime (b close to zero), where the smallest variances in relation with the mean can be achieved. Indeed proportional counters energy resolution depends upon may factors including anode wire non-uniformity (deposits on old wires), electron attachment to gaseous impurities, amplifier noise and others. Of all these factors only statistical fluctuations occurring in the number of primary ion pairs produced by the ionisation radiation (driven by the Fano factor, see section 3.1)and the number of secondary electrons produced in the avalanche initiated by each primary electron fundamentally limits the resolution, and can not be eliminated in principle.

## 3.4. Creation of the signal

The moving charges between electrodes of a chamber are the source of the electric signal picked up by amplifiers connected to these electrodes. Therefore, the pulse signal is formed by induction, rather than the actual collection of the charges itself. Before the avalanche, the total amount of charge is negligible, and therefore is only when the avalanche starts taking place that the signal induced in the electrodes is above the electric noise.

In general the read out area of a gaseous detector is formed by several electrodes which may be wires -as it is the case of the traditional MWPC (Multy Wire Proportional Chamber)- or, as it is the usual tendency now, stripes or pixels. Determining the signal that one moving charge induces in this read out is a complicated electrostatic problem which is commonly addressed by means of the *Ramo's theorem* [90]. It describes the situation where a charge $Q$ is moving in the space between several electrodes, causing charges to flow into and out of the electrodes, each of which is connected at some potential to an infinite reservoir of charge. This theorem states that the current $i(t)$ induced by this moving charge $Q$ in the particular electrode i can be calculated by:

$$I(t)_i = Q \cdot \mathbf{E_{W_i}} \cdot \mathbf{v}(t), \tag{3.29}$$

where $\mathbf{E_{W_i}}$ is the "weighted field" defined as the electric field calculated with the electrode i biased to 1 Volt and having the rest of the electrodes grounded. Its unity is $[E_W]$= 1/m. Here $\mathbf{v}(t)$ is the drift velocity of the charge moving in this electric configuration. The prof of this theorem is quite simple, and can be found for example in reference [76]. It makes sense that this expression is proportional to the charge as we know that in the proportional mode the intensity(voltage) must be proportional to it. We see also that the drift velocity of the charge plays a role in this expression, as the faster the charge moves, the more pronounced the change in the intensity will be.

If now we take the situation where a pair electron-ion is created during the avalanche in the vicinity on an electrode, we see that the contribution

from the electron to the intensity in this wire will be a very fast pulse as it drifts very fast compared to the one the ion. As the charge is the same in the two cases, the area covered by each contribution to the pulse must be also the same, but the ion one will be a very slow replica of the electron signal. Hence, as a general characteristic of gas chambers, the signal current has a fast and large in V component due to the electrons, superimposed to the ion current with is much smaller in V but orders of magnitude longer in time. Since the electron component may be less than 1ns in duration, very fast electronics is needed to see it.

In the general case we have a lot of ion pairs created during the evolution of an avalanche generated by one single primary electron, and depending on the geometry of the drift situation, these ionisation electrons may arrive to the wire staggered in time. The resulting pulse will be a superposition of many pulses displaced in time.

The calculation of the current Intensity evolution in a wire due to a moving charge by means of the Ramo's theorem is implemented in Garfield [79] toolkit, and therefore it can be used for electric simulations.

# Chapter 4

# The CAST Time Projection Chamber

The signal expected in any of the CAST detectors is a low intensity photon flux at the keV level coming from the magnet bores. The TPC was designed to have its maximum detection efficency for these kind of events, making necessary some original approaches in its construction. In this chapter first both the hardware (detector and electronics setup) and the software (data acquisition and analysis) of the chamber will be described in detail. Then, the characterisation of the chamber will be presented, determined from a set of extensive X-ray calibrations that cover most of the CAST signal energy range. Finally a shielding built to reduce and homogenise the background level recorded by the TPC will be described.

## 4.1. TPC hardware

### 4.1.1. Description of the chamber

As it has been said, the properties of the signal expected in the CAST experiment are very specific and well defined. This led to a very characteristic properties of the detector, which will be reviewed in what follows.

Due to the very low intensity of the hypothetic axion signal (a few tens of events per year) it is mandatory in CAST to accumulate statistics for the longest possible period of time. Therefore the CAST detectors are required to have a robust and stable operation in time, together with good background discrimination capabilities. As the energy spectrum of the signal goes from 1 to 10 keV, peaking at $\sim$ 4 keV, the detectors must also have a good detection efficiency in this range, which involves a low detection threshold at around 0.5-0.7 keV. Last but not least, the axion signal would be traduced in a photon flux coming parallel to the magnet bore, and therefore a CAST detector must have enough position resolution to reject the events coming from other directions different than this one.

In figure 4.1 we have a drawing of the TPC where its main components can be seen. The material chosen to build the detector was plexiglass due to

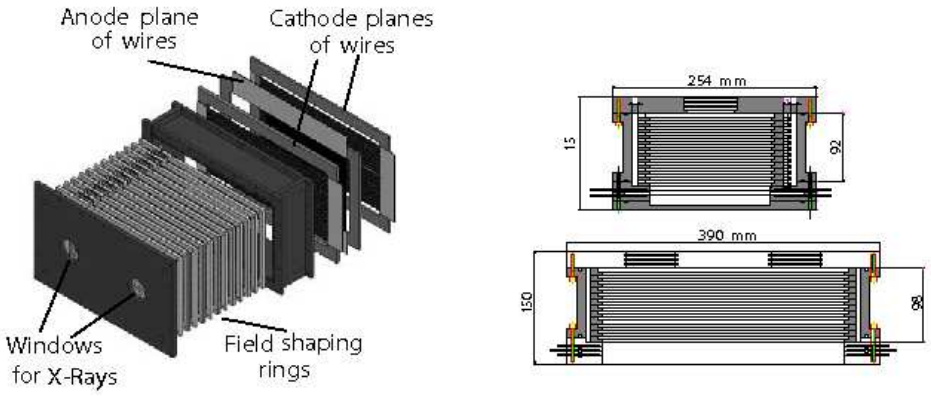


Figure 4.1: *Left: General view of the different components of the TPC. Right: Both side views of the TPC to illustrate the different dimensions.*

its low level of radioactivity. This material was previously measured at the Canfranc Underground Laboratory facility [91], finding it to have an activity level of <100 mBq/kg of $^{238}$U, <10 mBq/Kg of $^{235}$U, <5 mBq/kg of $^{232}$Th and <30 mBq/kg of $^{40}$K. With the exception of the electrodes themselves, plus the screws and the Printed Circuit Board (PCB), all the chamber is made from this material. The thickness of the plexiglass wall delimiting the gas region is 17 mm. As the low energy X-ray photons would be stopped by this material, the TPC side facing the magnet has two 6 cm diameter holes to allow the hypothetic signal to go into the chamber, covered with two thin

aluminised mylar windows isolating the detector from the magnet bores. The material was chosen because of its strength and high transparency to X-rays. Anyhow, to hold the $\sim$ 1 atm pressure difference between the chamber gas and the magnet bore vacuum, the foil is stretched on a metallic strongback making the system more robust (figure 4.5). For calibration purposes three round holes exists on the plexiglass wall, two of them facing these windows on the back of the chamber, while the third one is on a lateral side, being all of them also protected with thin mylar foils.

The gas inside the TPC has a conversion volume of $10\times15\times30$ cm$^3$, being the 10 cm drift direction parallel to the magnet beam axis, and therefore the section of $15 \times 30$ cm$^2$ perpendicular to it. These dimensions are by far enough to cover the two magnet bores, which have a diameter of 42 mm each and their centres are separated 18 mm. This way a big amount of the background radiation is detected on the edges of the chamber and easily rejected offline by a fiducial cut.

The gas chosen to fill the conversion volume in the TPC is argon mixed with methane as a quencher in a 95:5 proportion. A continuous flow of new gas to the chamber with a 2 l/h rate ensures the gas purity, important for the proper working conditions of the chamber, as explained in the previous chapter. This mixture was chosen by its good detection efficiency for photons in our range of interest. In figure 4.2 the mean free path of photons in several gases at normal conditions, argon being among them, is represented as a function of the energy of the incident photon. As it can be seen, there is a maximum in this parameter when this energy is around 3 keV, which is the binding energy of the K-shell of the argon atom, and then decreases very rapidly as the incident energy increases. The chamber was designed with such a long drift longitude to have distance enough for most of these $\sim$3 keV photons to interact and therefore not lose efficiency in this energy range, which is close to the peak of the axion signal spectrum.

The electrostatics is driven by a drift electrode located on the inner side of the chamber wall closest to the magnet, and by two cathode and one anode planes of wires placed on the other end of the chamber, as it can be seen in figure 4.1. The drift electrode is an aluminium layer covering the plexiglass and the mylar windows, biased at -7 kV. On the back side of the TPC the anode plane is also biased at +1.8 kV and placed between the two grounded cathode planes. The first cathode plane is located at 9 cm from the drift electrode and at 3 mm from the anode plane, which itself is 6 mm far from the last cathode plane. This asymmetry in the distance between the anode and cathode planes was designed on purpose to enhance the induced signal from the movement of the ions produced in the avalanche in the first cathode plane, which is the one being read out by the electronics, together with the anode wires plane.

Each cathode plane contains 96 wires of 100 $\mu$m diameter each (gold plated tungsten) that run parallel to the narrower side of the chamber. On

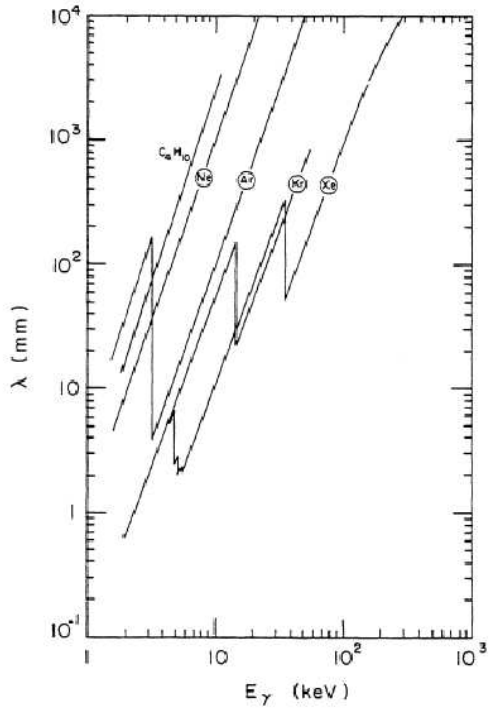


Figure 4.2: *Photon mean free path in several gases at normal conditions versus the photon energy $E_\gamma$.*

the other hand the anode plane has 48 wires of 20 $\mu$m each running perpendicular to the cathode wires, and thus providing two dimensional information for each event. The distance between wires is in all cases 3 mm. Since an X-ray deposit in a gaseous detector is a very localised event, it will fire only up to $\sim$3 wires in the anode plane, contrary to what happens in general with a charged particle background. Figures 4.3, 4.4 show examples of such depositions for a background event (left) and for an X-ray (right). The plots on figure 4.3 display the time evolution of the charge pulse generated in each wire for the row of anodes, while in figure 4.4 the same is shown for the row of cathode wires. The very characteristic profile of an X-ray event provides the framework for a selective analysis.

The linear electric field from the drift electrode to the first cathode plane is close to 800 V/cm and, in order to keep its linear shape even close to the edges of the chamber, several rectangular (15 cm $\times$ 30 cm) rings at intermediate voltages stepping from 0 to -7 kV are used, as it can be seen in figure 4.5. From the first cathode plane to the anode one the electric field is much higher and starts having a radial profile at a few radius distance from the anode wires, where the avalanche starts taking place.

Figure 4.6 shows, on the left, a view of the complementary piece of the

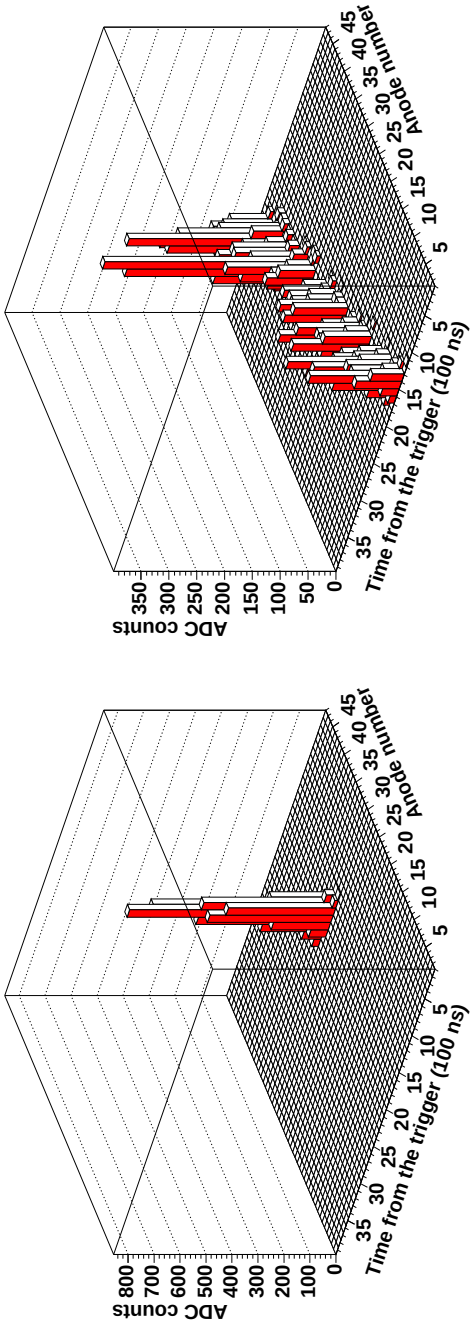


Figure 4.3: *Time evolution of the charge pulse generated in each wire of the anodes plane as recorded by the flash-ADCs. On the left a background event is plotted, while on the right a X-ray like deposition is shown.*

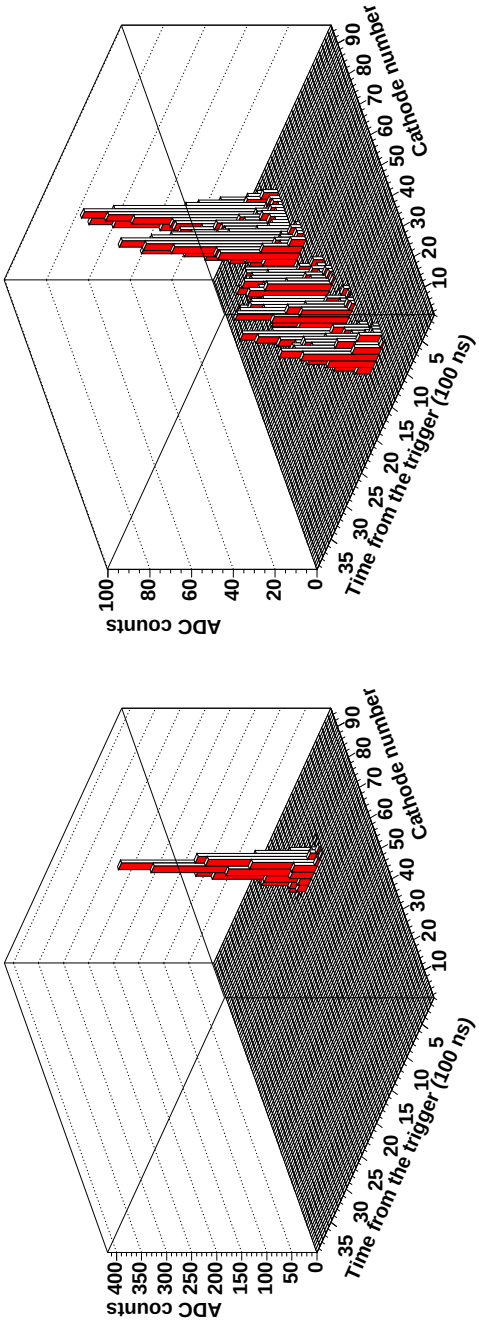


Figure 4.4: *Time evolution of the charge pulse generated in each wire of the cathodes plane as recorded by the flash-ADCs. On the left a background event is plotted, while on the right a X-ray like deposition is shown.*

chamber to the one on the right in figure 4.5, where also the plexiglass walls, together with the Printed Circuit Board can be seen. On the right, a closer detail of the inner part of this cage is shown, where the crossed wires planes and the calibration holes can be observed.

The TPC is attached to the magnet by means of two *chimneys* that couple it to the magnet bores. They are painted with black paint so that there is no external light going into the TPC. On the left figure of 4.7 we can see an upper-view of the chamber coupled to these two chimneys, and on the right there is a view of the chamber attached to the CAST magnet.

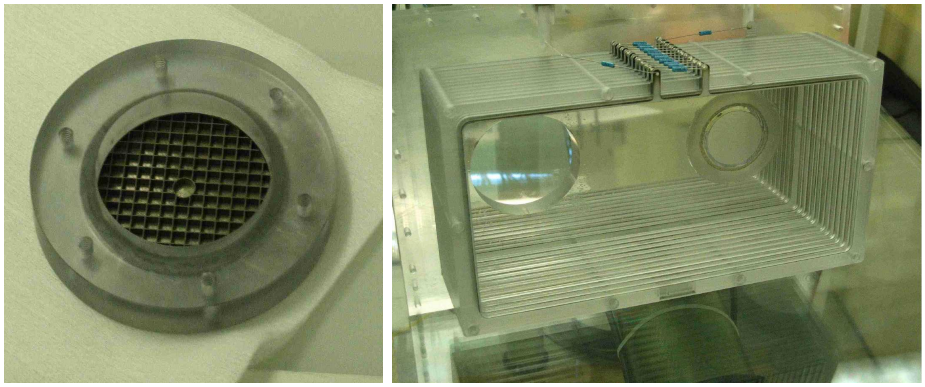

Figure 4.5: *Left: picture of one of the windows that isolates the chamber for the magnet bore. Here the metallic strongback can be appreciated. Right: detail of the plexiglass chamber cage. In the front the field-shaping rings can be seen, together with the holes that face the magnet bore and where the mylar windows are placed.*

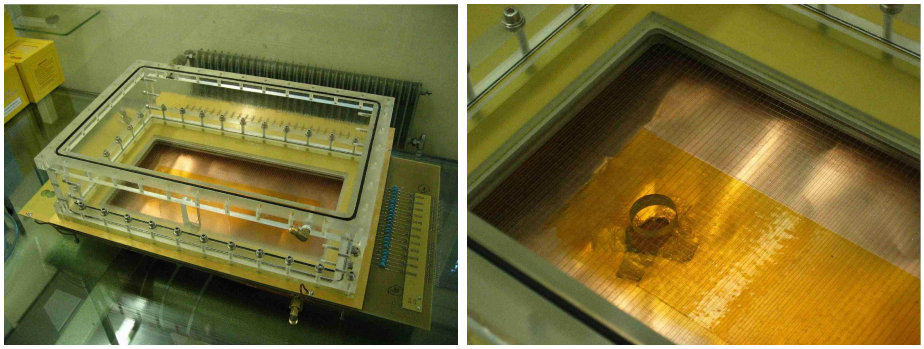

Figure 4.6: *Left: TPC complementary piece to the one shown on the left in the previous figure. Right: detail of the wires and the calibration hole.*

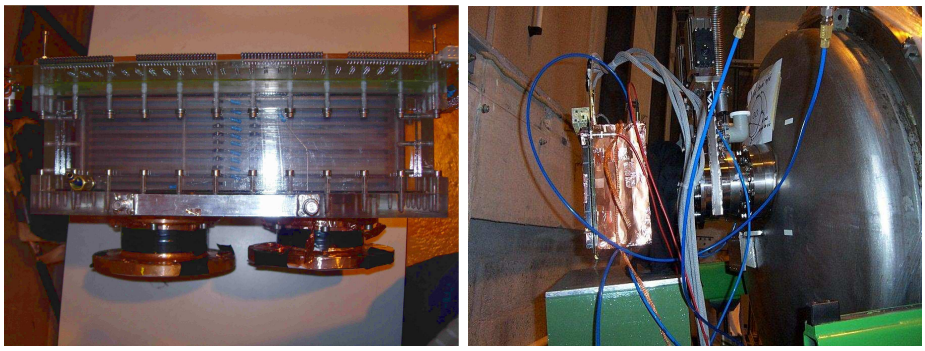

Figure 4.7: *Left: Upper view of the chamber where the two chimneys that connect it with the magnet can be appreciated. Right: TPC attached to the magnet.*

### 4.1.2. Front-end electronics

The front end electronics for the CAST TPC consists on 144 independent channels. Each of them takes the data through three basic units, as shown in figure 4.8: a charge sensitive amplifier/shaper, an FlashADC (Analog to

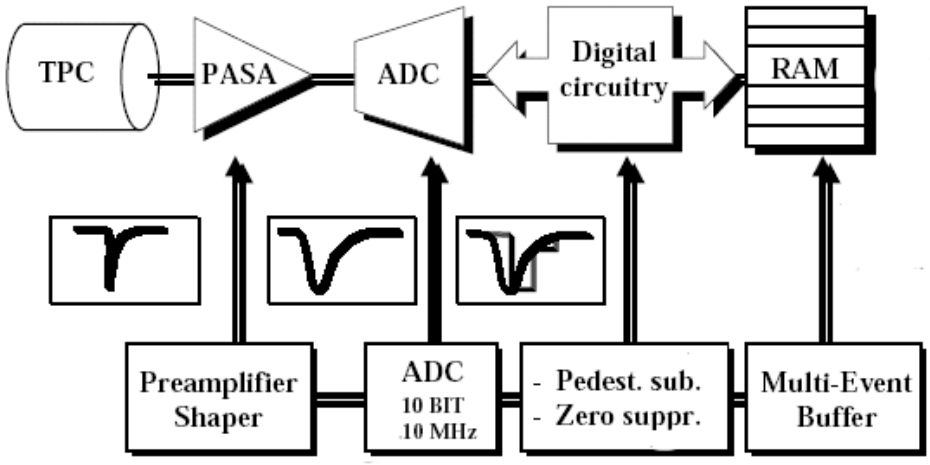


Figure 4.8: *Schematic diagram of TPC signal processing [92].*

Digital converter) chip, and a digital circuit which can perform the pedestal subtraction and zero suppression on the digitalised data. These two last features are arranged in the same chip, called ALTRO (ALICE TPC Read-Out) and developed at CERN for the ALICE experiment [92]. The same modules have been used in the HARP and CERES (NA45) experiments at CERN. A card called FEC (Front End CARD) controls 48 ALTRO chips and therefore the CAST TPC makes use of three of them in order to process

the 144 different channels.

#### Preamplifiers

The processing of the raw signal induced on the wires starts in a set of 4-channel ALCATEL SMB302 preamplifiers/shapers ( PASA, Pre-Amplifier Shaping Amplifier) positioned on the same printed circuit board that supports the wires. They are based on a Charge-Sensitive Amplifier (CSA) which integrates the pulse coming from the wire, being the voltage output proportional to the charge with a conversion gain of 6 mV/fC. This output goes then through a semi-Gaussian pulse shaper. This model was specially designed for the analog read out of a TPC and for this it can provide fast preamplification, shaping for tail cancellation (to remove the long contribution of the ions drift to the signal that can introduce dead time in the detector), excellent base line restoration and of course stability under repetitive conditions.

A coaxial cable using kapton as a insulator to shield the signal from external interferences drives the preamplifiers output signal to the next step on the signal process.

### 4.1.3. Electronics general scheme

Figure 4.9 shows a logic scheme of the TPC acquisition system, which uses standard NIM and VME electronics. The signal cables coming from the cathode plane are directly fastened to the FEC, while the ones carrying the anodes signal stop before doing so in the trigger card. Here these signals are compared with a given threshold value set by software. The total trigger is built for the OR of all these signals and therefore always that the analogic voltage pulse coming from an anode is bigger than this value, this card will send a trigger signal. The threshold during normal CAST data-taking operation is safely set to a value that would correspond to energy depositions of about 800 eV in the gas conversion region. By doing this the electronic noise coming from the experiment can be prevented.

This *raw* trigger signal goes first through a module which acts as a discriminator and converts it to NIM standard. To build the effective trigger this signal is driven to a coincidence module, shown in the centre of the scheme, where it can be vetoed by two different one-valued flags.

- One of them comes from the VME *busy card* (red signal in the scheme) which holds the flag to one when the system is busy processing an event.

- The other one comes from the VME Input/Output register (blue line), which communicates with the daq acquisition, allowing thus the user to veto the trigger signal when necessary.

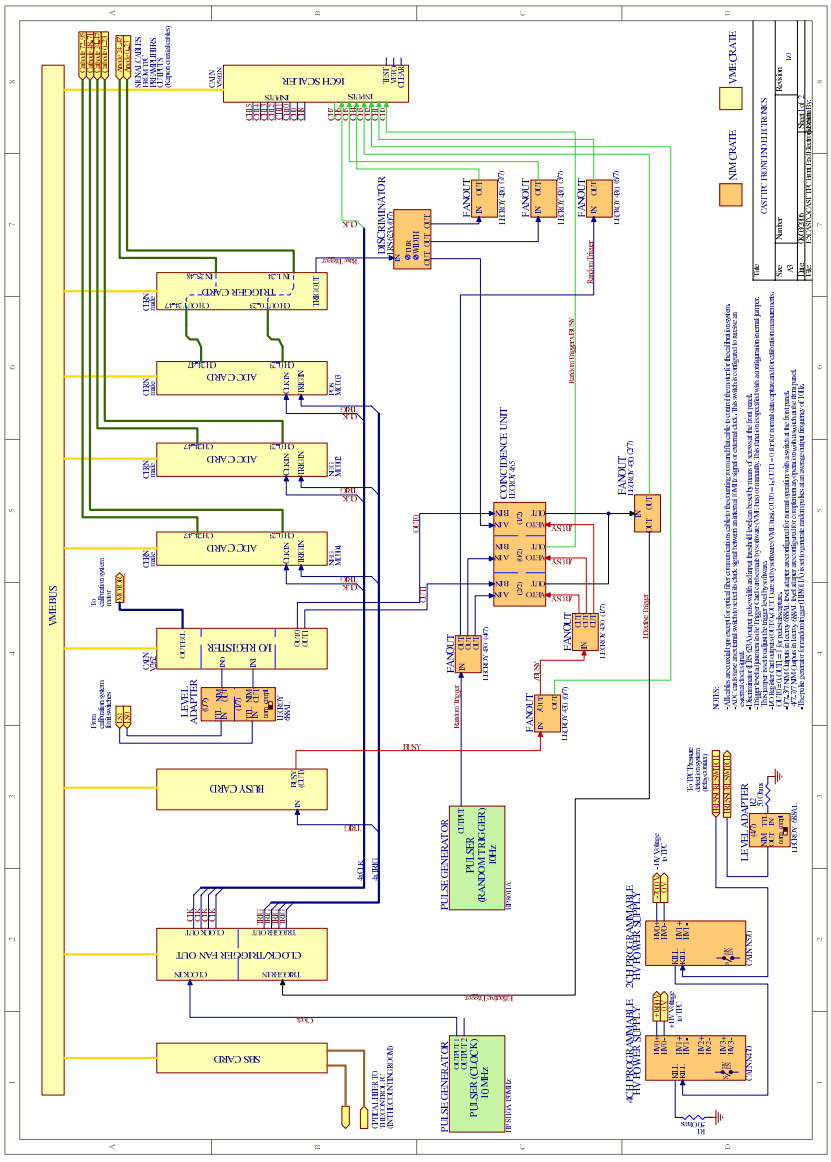


Figure 4.9: *Data acquisition electronics for the CAST TPC.*

If the signal is not stooped in this coincidence module, it is directed to the VME Clock/Trigger module, as it can been in the scheme (black line). As soon as it gets this flag, it sends a signal to the busy card so that it starts vetoing the new triggers while the event is being processed by the DAQ, and another one to the FEC for them to start processing the data. It is the DAQ computer the one that, once the event is processed and saved, will send a signal to the busy card to stop it from vetoing the new incoming trigger signals. As it can be seen also on the picture, all there signals (raw trigger, busy or effective trigger) are being *counted* in a VME scaler so that the effective trigger rate or the dead time (given by the length of the busy flag) can be known.

**Data processing with the FECs cards**

Once the FECs receive the trigger signal from the Clock/trigger module, they start processing the pulse coming from the preamplifiers. As it has been mentioned before, every single pulse goes through two chips, being the first one used to digitalise this analogic signal. The sampling frequency is 10 MHz, and the available range for the output in ADC units is a 10 bit-word, which corresponds to values from 0 to 1023. The time window for the sampling is about 7 $\mu$s, which is long enough to encompass the maximum drift time of the chamber. The posterior digital treatment of these samples is done by the ALTRO chip. The version of this chip used in the CAST TPC contains 4 processing channels, each of them performing pedestal subtraction, zero-suppression, formating, and data storage on a multi-event memory. Figure 4.10 represents a block diagram scheme where this processes are shown.

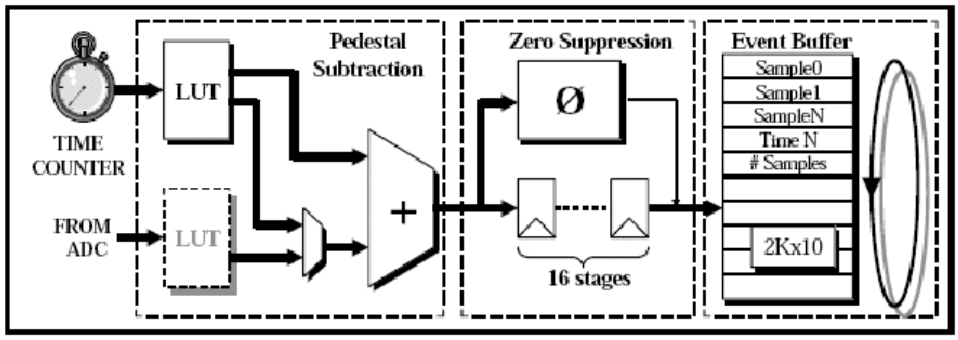


Figure 4.10: *ALTRO block diagram.*

**Pedestal subtraction** In the Pedestal Subtraction Unit (PSU) any possible systematic instability on the baseline of the pulse is corrected by subtracting to the input data some values, called pedestals, which are stored

on a look-up table (LUT). The chip allows this subtracted values to the either fixed or time dependent. In the CAST TPC, these values are constant and are stored in a register. In normal data-taking periods every six hours a pedestal run is taken, where these fixed values are recalculated and overwritten. In these pedestal runs the trigger signal is generated by a random pulse generator with a mean frequency of 10 Hz. Meanwhile the I/O register sends a veto signal to the coincidence module where the *real* trigger is stopped. Because of this the samples taken by the ADC will not, in most of the cases, contain any event information but just the noise level line. The pedestal value of every channel is defined then as these collected samples mean, being its $1\sigma$ error also stored. A pedestal run lasts around $\sim$ 20 sec, which is the time needed to process 1000 random trigger signals, so that their mean is properly calculated.

**Zero suppression** In the zero-suppression unit (ZSU) the samples whose value is close to a fixed threshold are considered as noise and therefore discarded, mainly for storage reasons. Moreover, a glitch filter checks for a consecutive number of samples above this threshold to further prevent the noise. In normal CAST data taking this threshold value is safely set to the pedestal plus $10\times\sigma$, being $\sigma$ the pedestal error as defined in the paragraph above. In order to keep enough information for further feature extraction, the complete pulse shape must be recorded and a sequence of pre-samples (samples before the signal overcomes the threshold) and post-samples (samples when the signal returns below the threshold) are also recorded, as shown in figure 4.11. The ALTRO chip allows the storage of a number of samples collected previous to the trigger signal.

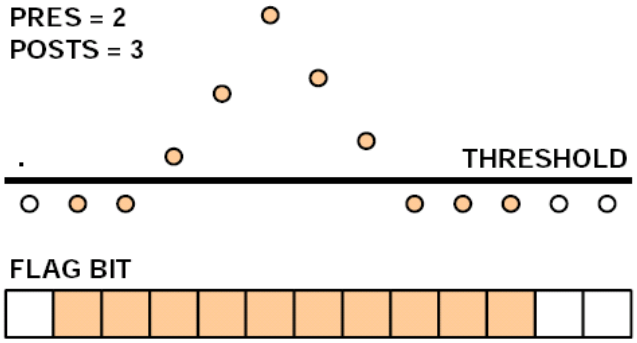


Figure 4.11: *Scheme showing the samples being recorded.*

**Event buffer** The data format unit (DFU) is illustrated in figure 4.12. Due

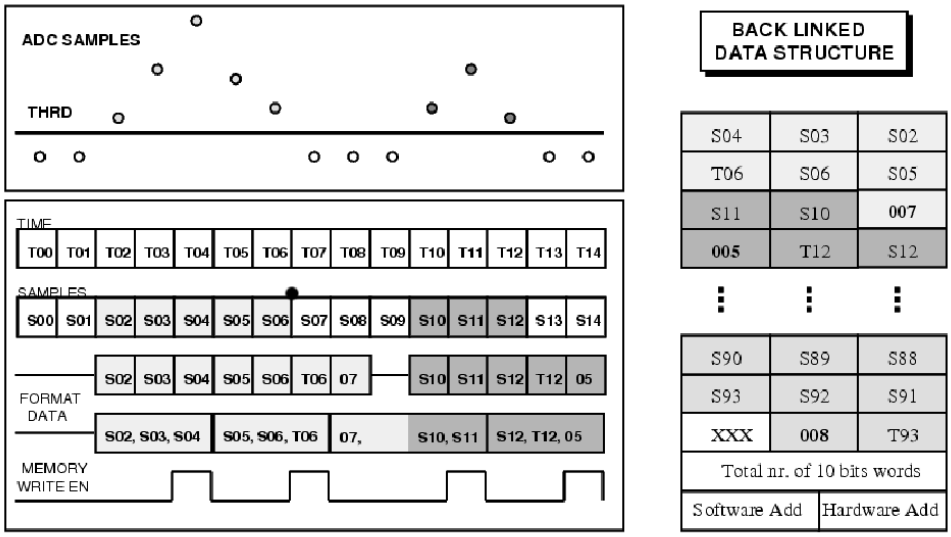


Figure 4.12: *Data formating by the ALTRO chip used in the CAST TPC.*

to the removal of a variable number of samples between accepted clusters of samples, the timing information can be lost during the zero-suppression process thus making mandatory to include time information to each accepted set of samples. This is accomplished by adding to the data string a 10-bits word time stamp which defines the time distance of the last sample from the trigger signal (e.g. "T06" in figure 4.12). Since both the samples and the time stamp are encoded in a 10-bit word and therefore are indistinguishable, an extra 10-bits word is added at the end of the cluster, containing the information of the number of words in the cluster including itself and the time stamp (e.g. "07" in figure 4.12). If these data are later on read backwards it will be straight forward to identify and separate every single cluster.

Once the total number of samples for the event has been processed, the 10 bit-words are encoded into 30 bits-word, and two extra 32-bit words are added at the end of the package, as it can be seen on the right part of figure 4.12. The fist one is fundamental to decode the data packet, as it provides the position of the last 10-bit word in the data packet. The second trailer word contains in the first 16 bits a software identifier, while a hardware one containing the information of the channel and chip addresses fills the other 16 bits. Finally these data are stored in a multiple-event buffer, a 512 words 32 bits wide RAM that can hold up to eight events.

## 4.2. TPC software

### 4.2.1. Data acquisition

The acquisition software is *TPCDAQ*, a C-coded software running in a dual processor PC, which uses a SBS BIt-3 1003 adapter on a fiber-optic link to the electronic modules described before. Through it, TPCDAQ communicates with the VME to configure, initialise and control these electronic modules. Once a trigger is detected, its task is basically to dump the contents of the FECs onto disk, without further data treatment, so as not to add any dead time. This way, per single run of the TPC, it produces two files:

- One of them, called runxxxx (being xxxx the number defining the run), which contains the raw data read from the FECs.
- The other, named runxxxx.out, contains the data read by the VME scaler.

*TPCDAQ_auto*, a script written in Bash Shell language (for Linux operative systems), allows for a fully automatic data taking protocol, as the data taking procedure can be completely defined there. As a rule, the acquisition runs continuously without distinguishing data belonging to Sun-tracking or background measurements in order to avoid possible systematic errors. During 2003 and 2004 data taking, the acquisition runs were being stopped every six hours to take a pedestal run in the case of 2003, or a pedestal plus a two calibration runs (one per calibration hole in the TPC) in 2004, and then being resumed immediately after.

This program, TPCDAQ, maintains also a log file called "tpcdaq.log" with information of every run, such as the number of counts taken, the time of start and stop, or a user defined comment about the run. Figure 4.13 shows an extract of it. Also this file will be used later on as a starting point

```
run3752    [  229571] 08/05/2004 18:21:10 -- 09/05/2004 00:21:10 | Background/Tracking
run3753    [    1000] 09/05/2004 00:21:21 -- 09/05/2004 00:21:23 | pedestals
run3754    [   50000] 09/05/2004 00:22:47 -- 09/05/2004 00:26:03 | calibration_mMside
run3755    [   50000] 09/05/2004 00:28:45 -- 09/05/2004 00:32:07 | calibration_CCDside
run3756    [  236497] 09/05/2004 00:33:39 -- 09/05/2004 06:33:39 | Background/Tracking
run3757    [    1000] 09/05/2004 06:33:50 -- 09/05/2004 06:33:52 | pedestals
run3758    [   50000] 09/05/2004 06:35:16 -- 09/05/2004 06:38:33 | calibration_mMside
run3759    [   50000] 09/05/2004 06:41:15 -- 09/05/2004 06:44:38 | calibration_CCDside
run3760    [  219614] 09/05/2004 06:46:10 -- 09/05/2004 12:46:10 | Background/Tracking
run3761    [    1000] 09/05/2004 12:46:21 -- 09/05/2004 12:46:23 | pedestals
run3762    [   50000] 09/05/2004 12:47:47 -- 09/05/2004 12:50:58 | calibration_mMside
run3763    [   50000] 09/05/2004 12:53:40 -- 09/05/2004 12:57:04 | calibration_CCDside
```

Figure 4.13: *Extract of the file tpcdaq.log maintained by TPCDAQ in order to keep information of every run taken by the TPC.*

for the analysis program, as it provides information about the new runs being recorded since the last time the analysis was run.

### 4.2.2. Monitoring

As it has been mentioned before, the DAQ computer has two processors, TPCDAQ using one of them, while in the other a monitoring C-code software named TPCQOD (TPC Quality Of Data) is running continously without interfering with the acquisition (and therefore without adding dead time). This program was developed with two main goals:

- To perform on-line monitoring of the incoming data parameters to check its quality and detect possible problems in the acquisition.
- To keep a history recording of some important DAQ parameters, such as TPC trigger rate or dead time percentage, so their evolution with time can be followed.

For the first task a set of histograms appearing in the computer screen is continuously being updated with the incoming data from the detector. Figure 4.14 shows a screen-shot picture as an example of this program output. Features such as the trigger rate, event distribution on the chamber, hits

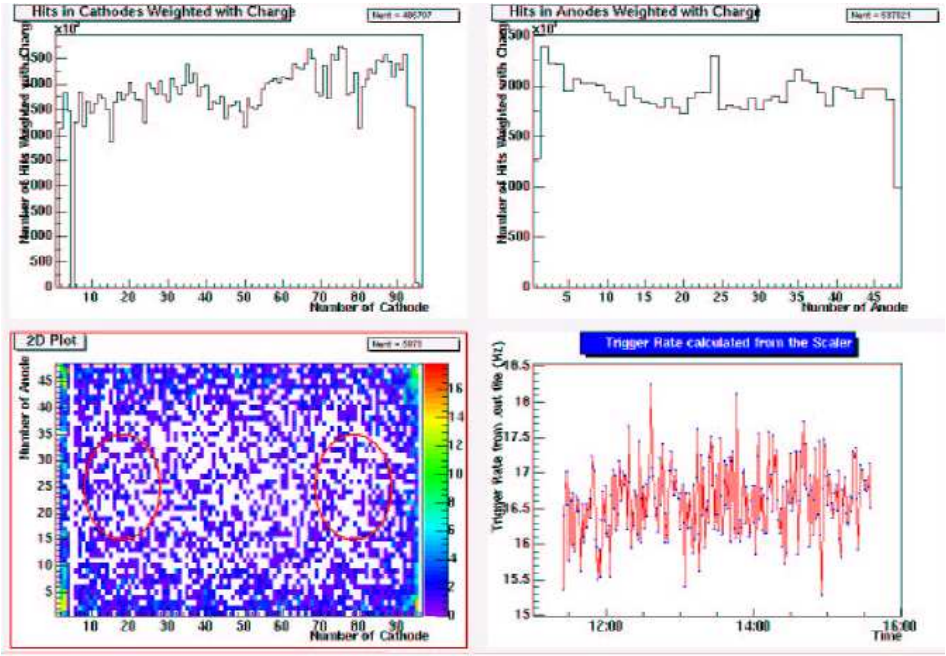


Figure 4.14: *Screen shot showing the appearance of TPCQOD.*

distribution on the anodes and cathodes wires, energy distribution of the incoming data, etc... can help to control the proper working of the chamber. At the end of every TPC run a file is created where all these plots are keep so they can be cross-checked later on if necessary.

### 4.2.3. Data analysis

In this section the different steps that the basic data analysis software, TPCANA, takes in order to extract the significant information from the very raw data collected in the detector will be explained. This is a code written in C language, which uses the libraries developed at CERN within the Root toolkit framework. Root [93] is an object-oriented data analysis framework developed by René Brun and Fons Rademakers. Its aim is to provide the scientific community with a large scale data analysis and simulation toolkit that would profit from the progress made in computer science over the past 15 to 20 years, especially in the area of Object-Oriented design and development. TPCANA uses Root features in order to store the TPC processed data since they are designed to optimise the space used, and to plot the variables that can be of interest in the final analysis. A schematic overview of the steps this software goes through is shown in figure 4.15.

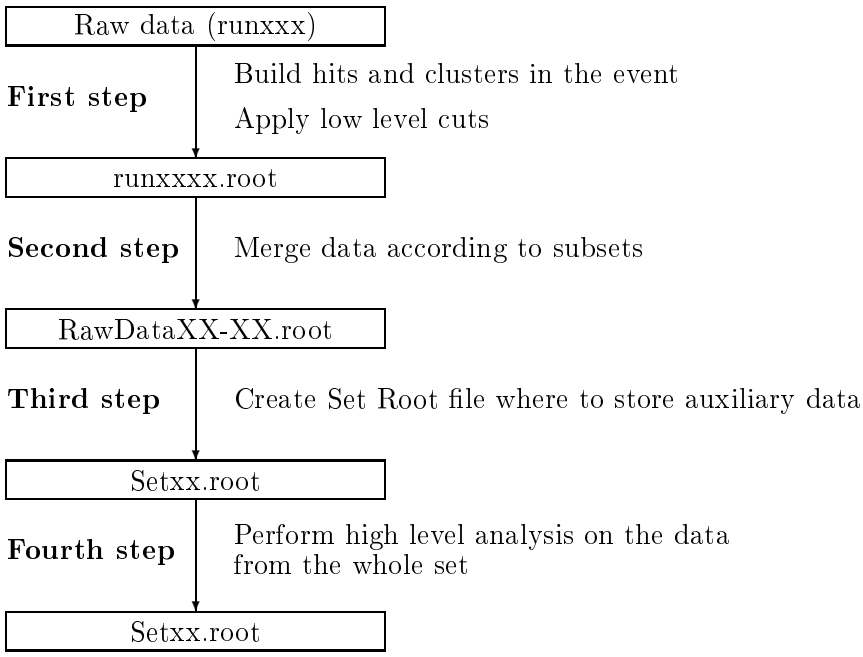


Figure 4.15: *Schematic view of the TPCANA data analysis software*

#### First step

In the first step TPCANA searches for the new data that has been collected since the last time it was executed. All these new runs, except the pedestals and calibration ones, go then through the very first stage of the analysis. Here, for every event, some entities named *hits* that will help in

extracting the meaningful information from the deposit left in each wire are built. As it has been explained in the previous section, these charge pulses are shaped by a preamplifier and sampled by the FlashADCs. To assign a unique charge and time to these deposits a parabola that fits the three highest points of those samples is calculated, as shown in figure 4.16. The

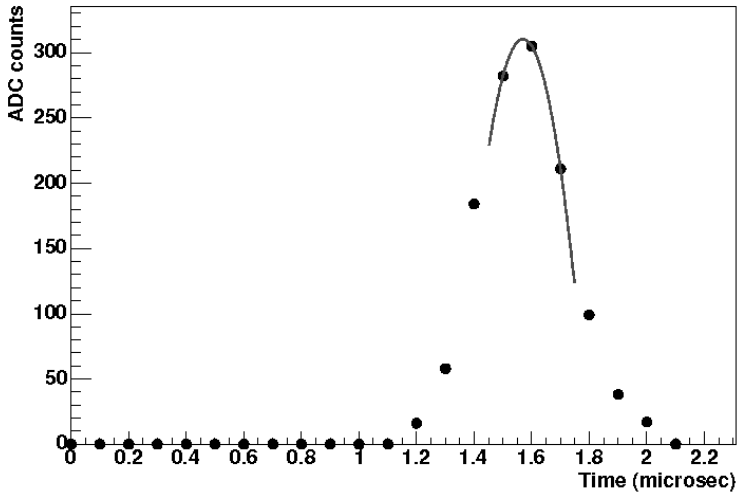


Figure 4.16: *ADC samples from an anode pulse (dots), and the parabola calculated from the three highest points (line).*

values (Time, ADC counts) from the vertex of the parabola will correspond respectively to the time and charge of the hit. Furthermore, to calculate its position a grid is constructed using the fact that the distance between anodes and cathodes is the same. Thanks to this a coordinate system can be build being this distance its length unit, and each wire a basic integer position. In figure 4.25 an example of this grid can be seen. Therefore the position of the hit in this grid will be given by the number of the wire that has been fired.

Once the charge, time and position of all the hits in one event are known, we proceed to build a more sophisticated entity called *cluster*. Since the signal expected in the CAST experiment is X-ray like, most of the analysis is focused on the recognition of this kind of events over the rest, which we will call generically background in what follows. These clusters will help in the discrimination of these kind of events over the background. A cluster is a group of hits with the following characteristics:

- It will be formed gathering all the contiguous hits whose time difference is less than 0.05 $\mu$s.
- Its charge (in ADC counts) is then defined as the sum of the charges

(also in ADC units) from all these hits.

- Its position is given by the charge-weighted mean of the hits position, and therefore it can be a decimal number.
- Its time, related to the trigger one, is calculated from the charge-weighted mean of the times of every hit.

Of course the construction of this entities is performed independently on the signal coming from the anodes and the cathodes.

One important factor on the construction of the clusters is the assumption of having a similar gain in every wire, which most of the times is not the case for a TPC, mainly due to small geometrical and mechanical imperfections in the construction of the chamber. This is traduced in a different ACD counts to energy corresponding factor for different wires or, even, in different positions of the same one. This effect can affect the energy resolution of the chamber, making it worse by a $\sim$ 2-3%.

To correct it, the gain of every wire is measured independently by means of a special set of $^{55}$Fe calibrations, long enough to obtain a energy spectrum per wire as seen in figure 4.17. This is done usually once per data taking period, as the condition of the chamber can change when it is dismounted from the magnet, which is the case during the shutdown periods. The peak

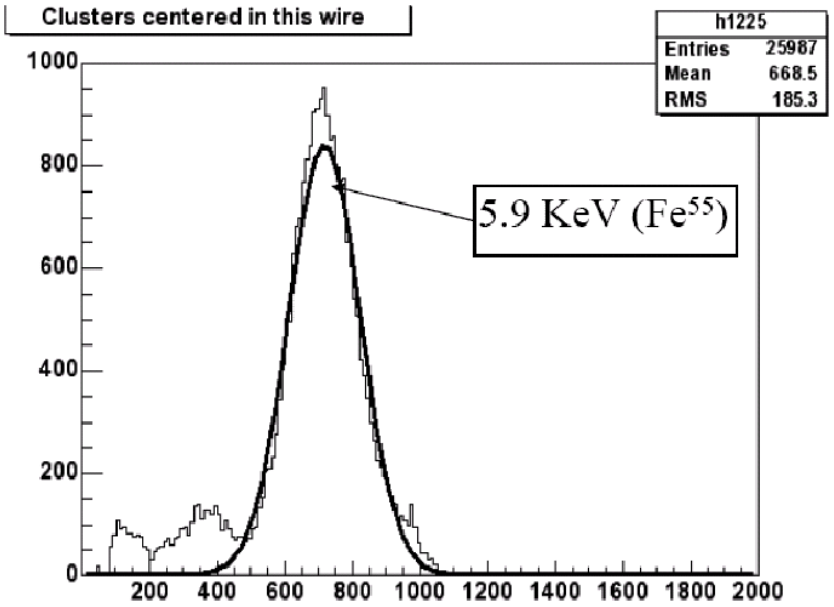


Figure 4.17: $^{55}$Fe *calibration spectrum in one of the wires of the TPC.*

corresponding to the 5.9 keV depositions of this radiation source is fitted with a Gaussian function, being its mean $\mu$ in ACD channel units the coefficient assigned to this energy.

As mentioned in section 4.1.1 there are two calibration windows in the back of the chamber, each of them facing the windows on the other side of the TPC to the magnet bores. This configuration allows us only to characterise the wires that goes through this windows as are the only ones being fired by the calibration photons. For each one of these wires the coefficient $\mu_i$ is determined, going the differences observed in this values up to a $\sim 15\%$ of this value. If we bear in mind the TPC chamber design, we know that every window is facing just a group of cathodes and the mean $\mu_{mean}$ of the $\mu$s measured from each of these two groups of wires is calculated. These parameters $\mu_i$ and $\mu_{mean}$ are stored in a file called "channel_calibration". Then, during normal data taking, the charge of every hit in a wire $i$ is scaled by the factor $\mu_i/\mu_{mean}$. For the ones outside the windows, this factor is just reduced to the unity. For the anodes, as one same wire pass trough the two different windows, the effect of the variation of the gain ($\sim 3\%$ ) with the positions in a wire can be clearly observed. Therefore, first the mean of the two coefficients obtained for the same wire is calculated $(\mu_i)_{mean}$, and then the mean $\mu_{mean}$ from all these independent wire values. Once this is done, to apply this factor to the measured data we proceed in a similar way as done with the cathodes: the charge recorded in every hit is multiplied by the factor $\mu_i/\mu_{mean}$.

Since already some processed information per event exist, as a first discrimination process, a set of low level cuts is applied to the events. These cuts are:

- Only the events that have a solely cluster in the anodes and in the cathodes are kept.

- The multiplicity (number of wires fired by the event) has to be in between one and three wires in the anodes.

- In the cathodes, on the other hand, the multiplicity will have to lie in between two and eight wires.

The parameters of these cuts have been determined experimentally from the calibrations taken in the Panter facility (see section 4.3). They are very conservative in the sense that the efficiency loss in signal detection is very small.

For the events that have passed the cuts, the crucial information about the cluster (position, charge and time in both anodes and cathodes), together with some extra data, is stored in a Root structure called *tree* whose basic components are *leaves*. The purpose of this structure is to save data in a very efficient way, so that it does not use a lot of space. Once this first stage of the analysis is performed a Root file per every single run (see figure 4.18) will have been created.

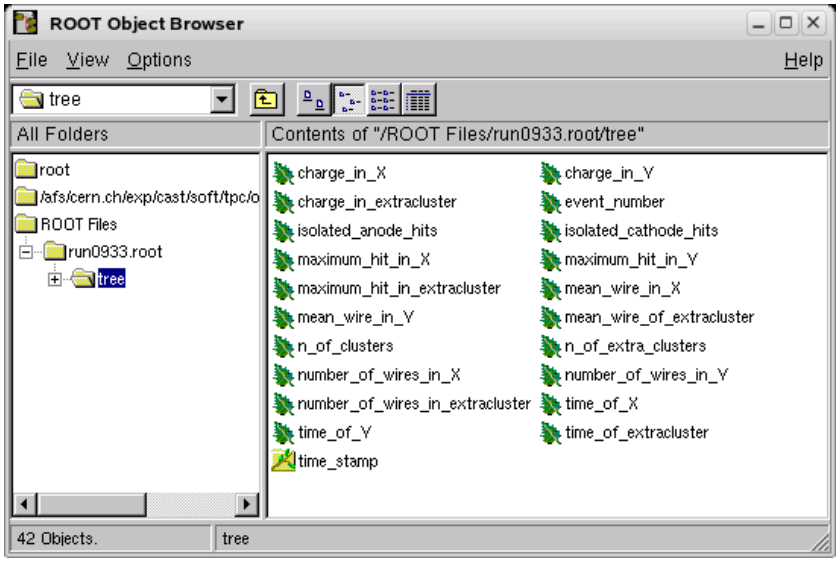


Figure 4.18: *Basic Root file containing the information of a single run.*

### Second step

For the TPC of CAST sets are created to put together data taken under the same experimental conditions, while these sets are later split in subsets just for practical reasons. In order to have the data from all the runs stored together, the next step of TPCANA simply merges all this files runxxx.root in a single one corresponding to every subset, called RawDataXX-SS.root, where XX defines the set number, and SS the subset one. Apart from the fact that the number of events stored in this file is bigger that the one in the files runxxxx.root, there is no further difference between these files.

### Third step

To analyse the data, apart from the raw runs collected in the chamber, some extra information in needed. For example, we must know when the magnet is tracking the Sun in order to distinguish the axion sensitive data from the background or, in order to control possible systematics, some variables related to the experimental hall must be carefully cross checked with the data. Therefore the third step in the analysis is to read this extra information recorded in the experimental site, plotting the temporal evolution of the relevant variables for the TPC. All these graphs are stored in a folder called Slow-Control-Data, which will be kept in a file created also in this step called SetXX.root. Later in the analysis, this file will be filled also with the output folders from the high level analysis. In figure 4.19 we can see an example of several of the graphs produced by TPCANA with the data from the Slow Control of the experiment, while in figure 4.20 we have a screen-shot

from the Slow-Control folder, where it can be seem all the graphs created.

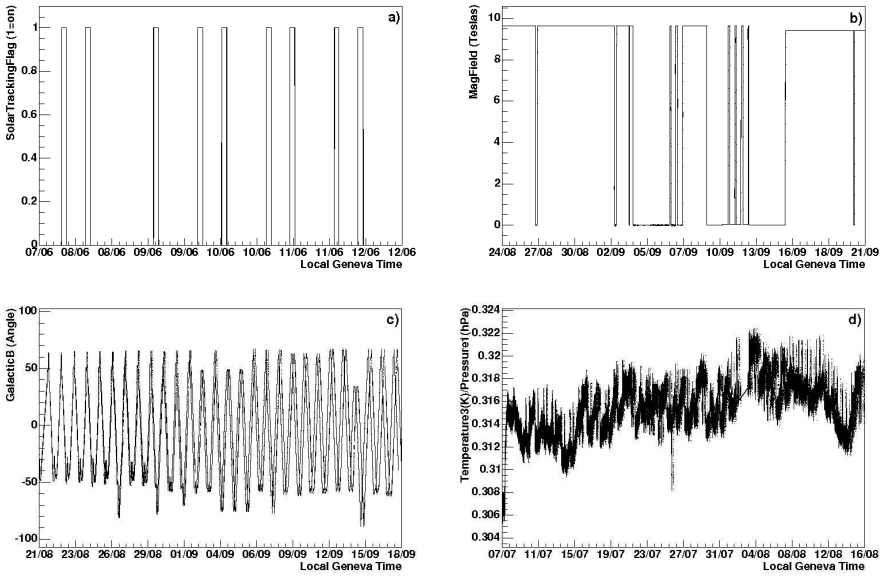


Figure 4.19: *Several examples of the extra information taken from the Slow Control program: a) Solar flag, that tells us when we are tracking the Sun (SF=1), b) Value of the magnetic field inside the magnet, c) Position of the TPC in Galactic Coordinates, d) Temperature/pressure of the gas inside the TPC.*

### Fourth step

Once the raw data taken with the TPC have been preprocessed, and the extra information from the experiment site needed for the analysis has been read, we are ready to go for the last step of TPCANA, where the high level analysis is performed. Here the events from the RawDataSS-XX.root file will be read and processed one by one.

**High level cuts** First of all these events pass a new set of high level cuts in a sequential order. An index called *icut* is assigned to each event according to which of these cuts it has gone through; that is, icut will equal 0 if the event can not pass the first cut, icut=1 if it is stopped by the second one, etc... These cuts, given in the order to which they are applied, are:

- **Cathode-anode clusters time difference:** The time difference between the cathode and anode clusters must be in the range -0.15 to 0.02 $\mu$s.

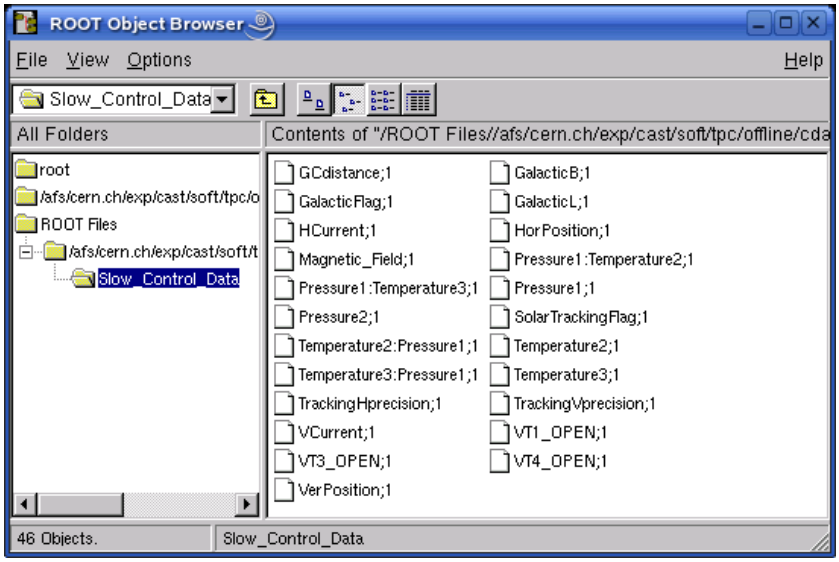


Figure 4.20: *Screen-shot of the Slow-Control folder where all the experimental parameters plotted by TPCANA are shown.*

- **No saturation:** We do not allow for a single hit in the cathodes to reach the upper part of the flash-ADCs dynamical range. If this were happening we could not then ensure that the energy assigned to the event is the real one, because the charge deposit on the wire has been higher than the one the FlashADC can handle. The cut is applied only to the hits in the cathodes because the gain for these ones is lower than the anodes one so, even if the signal of the anodes is saturated, still the one in the cathodes can be used to calculate the energy of the event. It is only when the cathodes are saturated that the energy information of the event fully loosed.

- **Anode-cathode clusters charge ratio:** The ratio of charge deposited in the anode cluster to the cathode one must be less than 1.6.

The number in these cuts have been settled by studying the energy dependent calibrations taken in the Panter facility described in the next section. The upper plot of figure 4.21 shows, for example, the result of plotting the cathode-anode time difference versus the energy for every event.

As expected, this number does not depend on the energy of the incident particle, since it is related to the drift time of the electrons and ions, after the avalanche has taken place, towards the anode and cathode wires respectively. This plot presents a double horizontal line pattern, although only the zero-centred is the physical one. The fact that the line below is centred in 0.1 $\mu$sec, which is the sampling time of the flash-ADCs, tells us about its artificial origin. This one is due to a small mismatch in the origin of the sampling

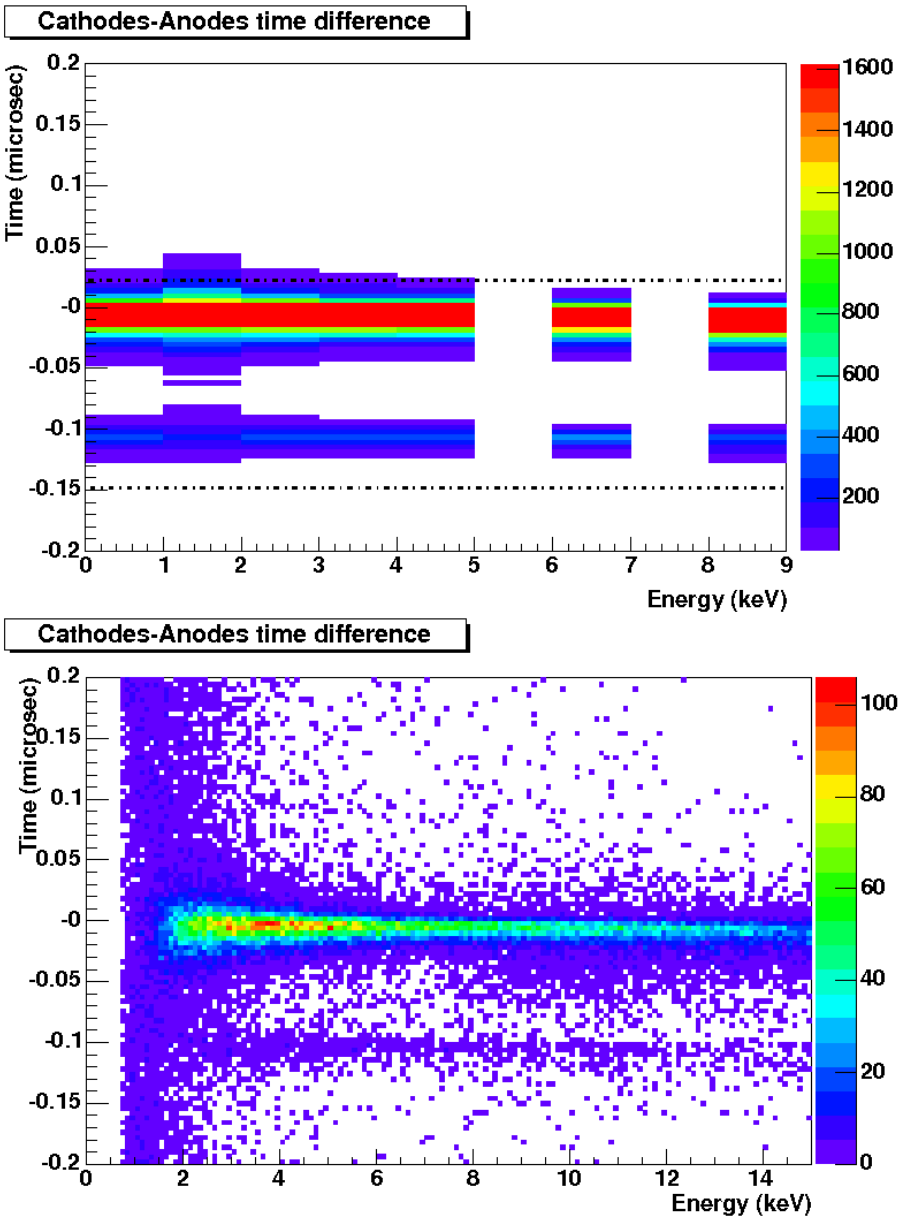


Figure 4.21: *Cathode-anode cluster time difference for the calibrations taken in Panter, where the dashed lines represent the cuts lines (up), and for 2004 background data (down).*

time for some of the events, given by the fact that the signal in the anodes starts being recorded one FlashADC-step before the cathodes one. But still these events are signal for us, and this is why the gap for allowed time difference is asymmetric and does not cover only the values around zero, as we would have naively imagined attending only physical reasons. At low energies (below 3 keV) the physical band is wider because of the efficiency of the TPC being lower at these energies and, therefore, the bremsstrahlung contamination of the Panter beam, together with the background of the chamber appears more evident.

In the lower plot of figure 4.21 we can see the same variable, now plotted for the background data. For energies above 4 keV the data follows the same pattern as the calibration one (we should not forget that these data has gone through the cluster cut already, being left only the X-ray like events) and it is only below these energies where this cut plays an important role. The origin of most of those low energy rejected events lies clearly in the electronic noise, which produces random time differences and is more likely to occur at lower energies.

The cut to prevent the saturated events is not very strong because the gain in the cathodes is very low, and therefore only a very small fraction of the events will reach this saturation level in the cathodes.

The anode-cathode charge ratio requires also a little bit more detailed study. In figure 4.22 we have this parameter plotted for the Panter calibrations (up) and for background data (down). As it can be seen, for the calibration data this rate is always higher than 1.6, being thus this value the lower bound established to reject non X-ray-like events. But, having a look at this parameter for the background data, again for low energies a band of events for which this quantity can have arbitrary values is seen, being this once more the effect of the electronic noise.

Indeed, if as a cross check, the two variables (time difference and charge ratio) are plotted, each of them after the other one cut (figure 4.23), we see that mostly both variables are rejecting the same events, which do not follow any physical pattern. A real event[1] in the TPC would have to keep this time and charge proportions, which are determined solely by geometry of the chamber.

Coming back to figure 4.22, we should also observe that in the background data, as the energy increases, this ratio trends to decrease. This is telling us that the proportion anode ADC counts to cathode ADC counts is being loosed due to the saturation effect of the FlashADCs for the anode data, which are the one with higher gain.

Similar to what happened with the low level cuts, these ones are very conservative because the efficiency has clear preference over the background

[1]We must bear in mind that most of the background events in the TPC are environmental X-rays and neutrons, whose signal mimic the former ones.

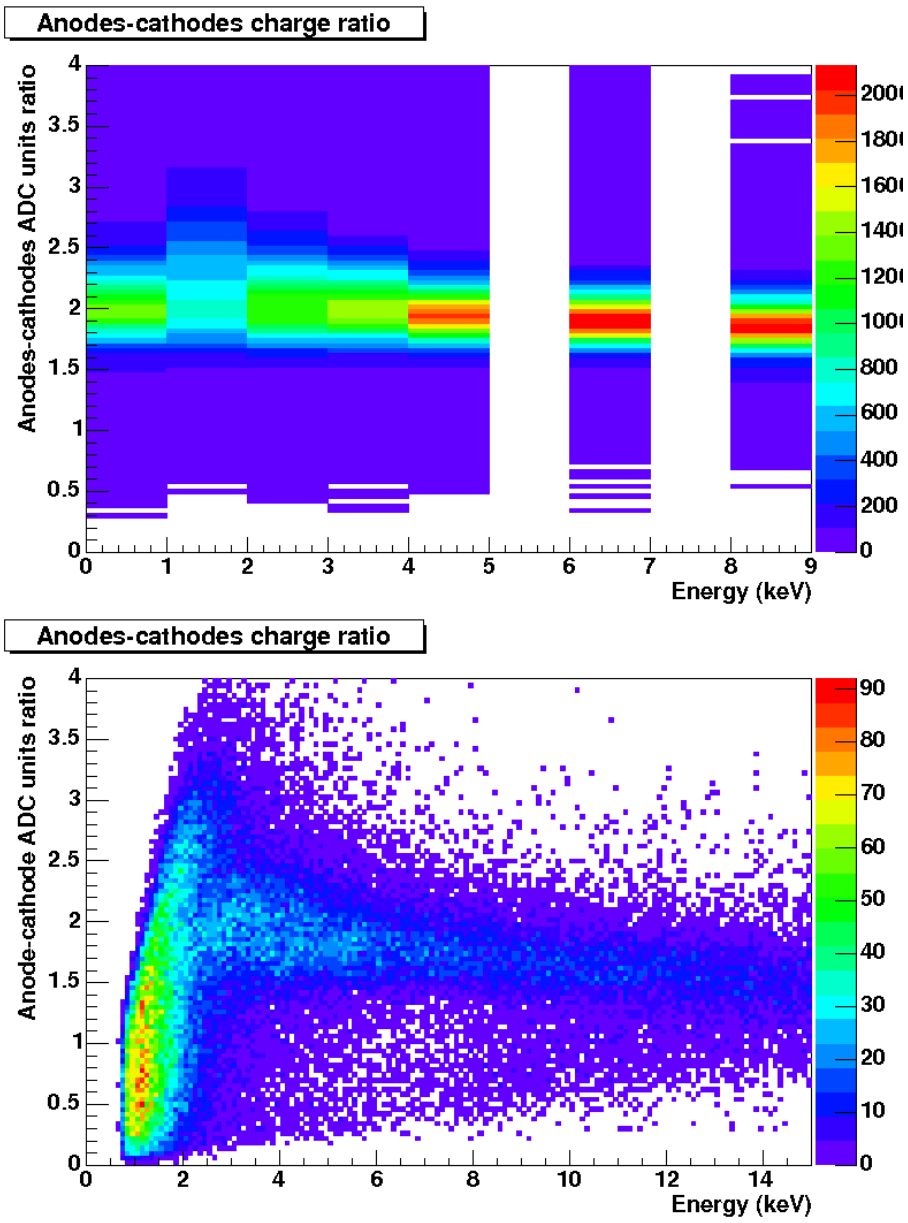


Figure 4.22: *Anode-cathode cluster ADC counts rate for the calibrations taken in Panter (up) and for 2004 background data (down).*

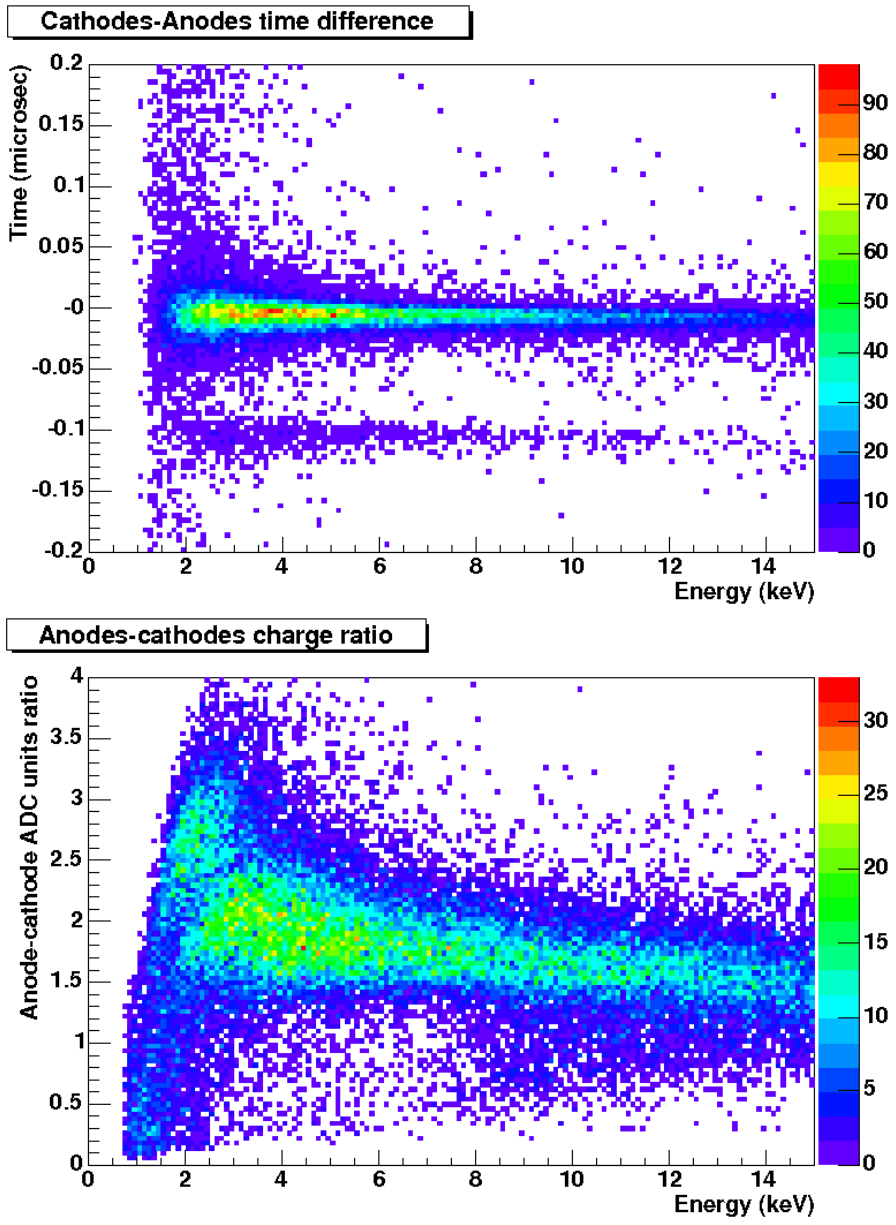


Figure 4.23: *Cathode-anode clusters time difference, after the charge ration cut (up) and anode-cathode clusters ADC counts rate after the time difference cut (down).*

level reduction. In this sense CAST is a special experiment due to the fact that the signal is obtained subtracting the background energy spectrum from the Sun tracking one. Because of this, the level of the background itself is not really significant as it disappears, and therefore we only have to care about its statistic fluctuation. Since this fluctuation scales with the square root of the number of counts, indeed the quantity that should be maximised in deciding how restrictive the cuts should be is:

$$\frac{efficiency}{\sqrt{background}} \tag{4.1}$$

In figure 4.24 we can see the efficiency in detecting X-rays of these high level cuts versus the energy of the X-rays calculated upon the Panter calibrations.

**Background and tracking data selection** The distinction between what is Sun tracking or background data was being done offline. A new flag called *itype* is assigned to every event, according to whether it has been taken during Sun tracking (itype=1) or not (itype=0). The logic condition for the former case is:

- The "Solar tracking" flag given by the magnet-control software must be one valued, which means that the Sun is in a position on the sky where can be reached by the CAST magnet, say $\pm 8^\circ$ around the horizon.
- But we must also ensure that the magnet is indeed tracking the Sun by asking two parameters, the horizontal and vertical precision, to be $< 0.1^\circ$.
- Of course, since the TPC tracks the Sun during the sunset, while the Micromegas and CCD do it during the sunrise, we must make sure that for us the tracking data are only the one collected in the evening.

**Chamber regions** To make the data analysis simpler, the 2-dimensional anodes-cathodes plane in the chamber is logically divided into several regions, and a new index named *ireg* is assigned to each event, according to the zone it has hit. In figure 4.25 we can see a view of the anode-cathode plane of the TPC where these regions are drawn. The data corresponds to the background events taken during 2003 after the cuts.

The two circles cover the area where the axion signal would be expected, because it is the region facing the two magnet bores. This area is called *two-windows* zone. Surrounding it, there is a square-shaped region called *out* zone, where the events distribution is quite homogeneous. Finally, we have the region that covers the edges of the chamber, where the rate of events is much higher than in the other two.

This last zone acts as a natural shielding, for a big part of the environmental background will not travel to the two-windows area, but will interact

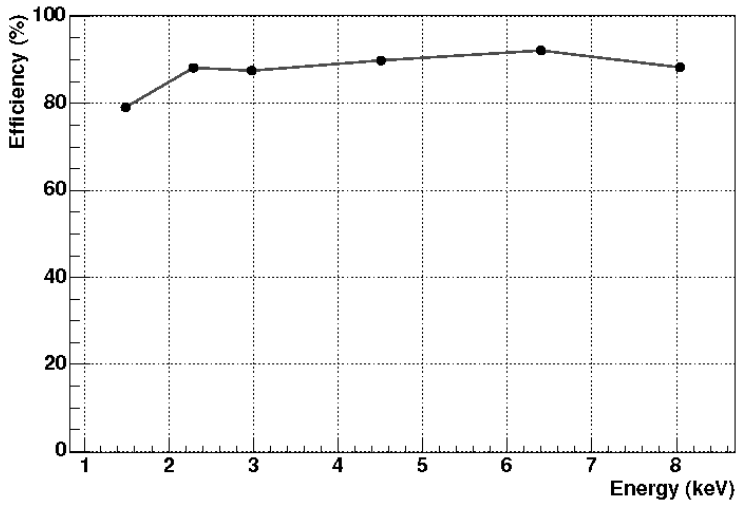


Figure 4.24: *Efficiency of the high level cuts of TPCANA*

already there. For example, the mean free path in argon of low energy (less than 3 keV) X-rays is less than one centimetre, and therefore all of them will just interact as soon as they reach the active region of the chamber.

**Energy calibration** The way of determining the energy of an event from the ADC counts was different in 2003 and 2004, and therefore both methods will be explained in more detail in their respective chapters. In short, in 2003 continuous measurements of the pressure and the temperature of the gas inside the chamber were used to calculate its gain, while in 2004 experimental calibrations were being taken every six hours.

**Final output of the high level analysis** Now that all the information needed to classify the events which are left after all the cuts is already stored, different dependences can be studied:

- **Rate evolution:** To visualise the rate of events in the chamber versus time can provide very useful information related to the proper function of the chamber. In this sense this rate is represented for several time bins, energy ranges, different level of cuts, or different regions of the chamber.

- **TPC two dimensional plots:** This type of representation, of which figure 4.25 is an example, shows the event distribution on the chamber, which is also a different crosscheck of the proper function of the chamber together with a interesting source of information for the final

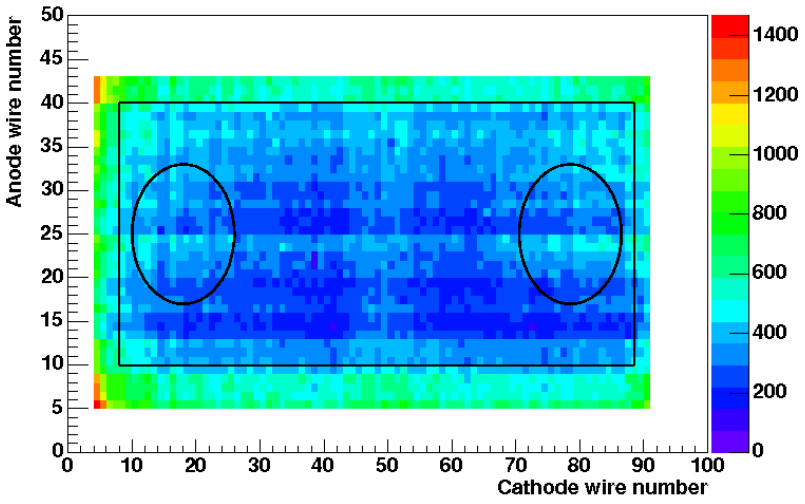


Figure 4.25: *Different chamber regions*

axion analysis, since in the case of a positive signal, it should be clearly seen only in the two windows region.

- **Energy spectrum distribution plots:** For the final axion analysis this representation is the most important one, as it is the one used to look for a solar axion signal. Again this is represented for a wide range of different circumstances, as it can be solar tracking or background data, different cuts or energy bins... etc. As a subrange of these spectral distribution the solar tracking minus the background data spectrum is calculated as a function of the energy. In the case of a positive signal, the solar axion energy spectrum should be left here.

What has been explained here is the basic core of the analysis TPC data software, TPCANA, which was mostly developed for the time the first data started to arrive in 2003. As time was passing by, several features were added to its basic output, although this will be explained in the following chapters, where it corresponds.

## 4.3. Chamber characterisation

In summer 2002 the TPC was transported and mounted at the PANTER facility of the Max Planck Institute for Extraterrestrial Physics (MPE) in Munich [94]. This facility, designed for the calibration and characterisation of X-ray telescopes, provides a parallel X-ray beam with a very accurately calibrated energy and intensity. Since the signal expected in CAST would come as a X-ray flux, a set of calibrations of the TPC with this beam can yield

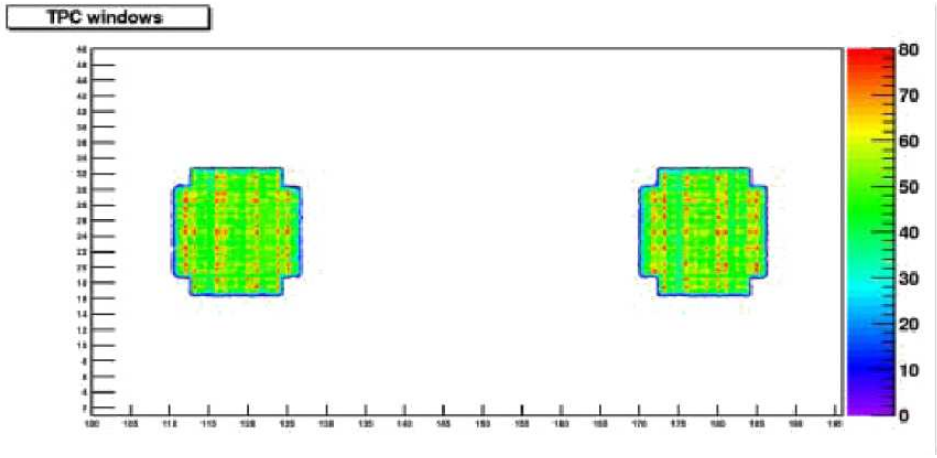


Figure 4.26: *X-Ray beam of Panter, as seen by the TPC.*

a very important information about the characteristics of such a signal in the TPC. Also some important features of the chamber, such as the efficiency in X-ray detection, the energy resolution and the linearity of the detector response in the whole range of energies of interest were investigated. As mentioned in the previous section, with the help of this data also the efficency loss in the off-line analysis of the data was calculated (figure 4.24). As a parallel issue, the transparency to X-rays of the mylar windows was tested to crosscheck the curve provided by the fabricant. In figure 4.26 we can see a "picture" of the X-ray beam in the TPC chamber. The x and y axis correspond to the grid conformed by the cathodes and anodes wires, while the colours just represent the number of photons detected. The shape of the TPC windows and their strongback are clearly seen in the distribution of detected events.

The efficiency curve of the detector has been determined by comparing the counts detected in each corresponding run with the expected rate deduced from the calibrated PANTER detector. The energies provided by PANTER were: 0.3, 0.9, 1.5, 2.3, 3.0, 4.5, 6.4 and 8.0 keV. Due to the fact that the beam comes contaminated with a bremsstrahlung continuum for the low energy cases (from 0.3 up to 3 keV), and the fact that the chamber spectra shows the presence of a small amount of background and, in the case of high energies (from 4.5 up to 8 keV), a second peak due to escape in the argon, the precise counts corresponding to the main peak have been extracted by means of full fittings of the spectra. Examples of such fits are given in figure 4.27.

The result of this analysis is given in figure 4.28. Here the dots represent the experimental values and the lines are theoretical computations. The thick grey line is a naive calculation of the efficiency of the chamber where

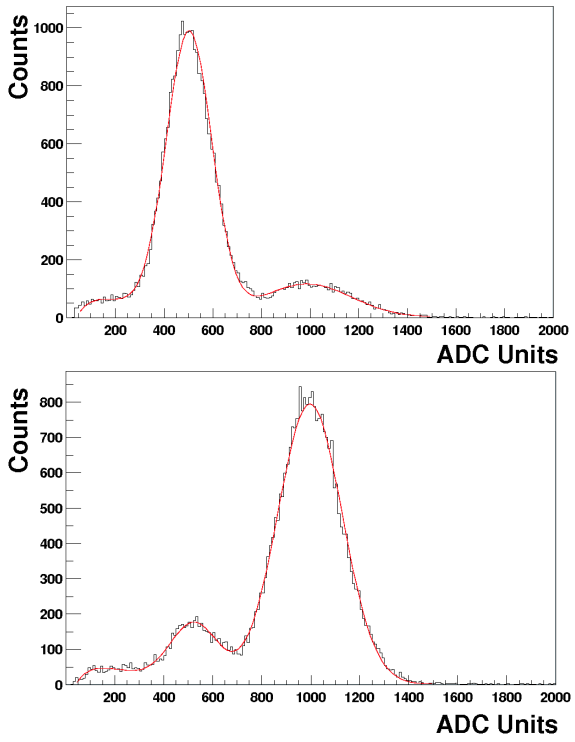


Figure 4.27: *TPC spectrum for the 3 keV (left) and 8 keV (right) X-ray energy of the PANTER tests. In both figures the line shows the combined fit of the peaks plus background.*

only the two main physical effects, i. e., the gas opacity to the incident X-rays (remember figure 4.2) and the window transmission are taken into account. As mentioned in section 4.1.1 the windows that isolate the TPC from the magnet have a metallic strongback to make them stronger. The geometrical opacity of this strongback is about 8% while the mylar foil is practically transparent for X-rays down to the keV energies ($\sim$ 30% transparency for 1 keV, $\sim$ 85% for 2keV and $\sim$ 95% for 3keV). The window transmission contribution is singled out by the thin black line [95], so one can easily see the contribution of both effects separately. Also this transmission factor was measured in Panter as it can be seen in figure 4.29, agreeing very well with this theoretical calculation.

The measurements (black dots) for each tested PANTER energy closely follow the values expected by the window transmission computation for energies below 3 keV, lying below the grey line for energies above 3 keV due in part to the increasing probability of emission of a fluorescence photon with energy, that would produce partial or split energy depositions in the chamber, which are rejected in our off-line analysis. This loss of efficiency is acceptable because of the high background reduction obtained by this

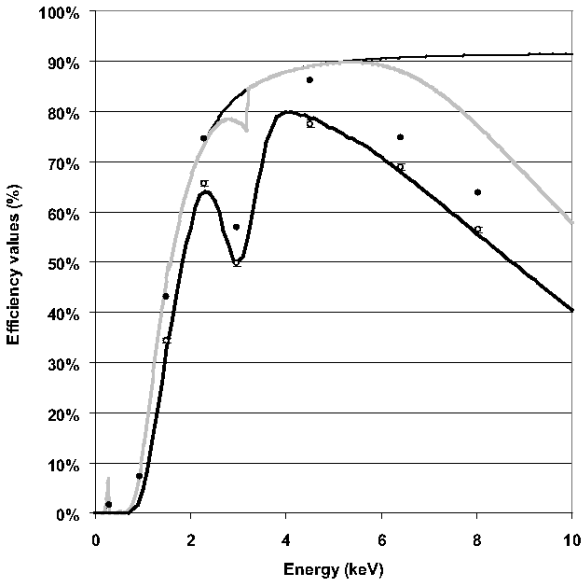


Figure 4.28: *The dots represent experimental measurements of the efficiency of the TPC, before (black) and after (white) the off-line analysis cuts are applied to the data. The upper thin black line represents the theoretical computation of the window transmission, while the grey line includes also the opacity of the gas in the chamber. The thick black line is an analytical function used to interpolate the experimental points in the final analysis.*

approach.

The final off-line analysis (white dots) implies an additional loss of efficiency of about 5–10% depending on the energy (figure 4.24). The thick black line is an analytical function used to interpolate the definite measured efficiency points. By convoluting this function with the expected solar axion spectrum, we obtain an overall efficiency for solar axions of 62%.

The PANTER data show also the linearity of the TPC response. The position of the main peak versus energy for each measured PANTER energy point is plotted in the right plot of figure 4.30, and this verifies the linearity of the detector gain. The points of each set (two different days and therefore different gas P and T conditions) closely follow a straight line, so the linearity of the chamber response has been demonstrated down to the lowest tested x-ray energies.

The run with the lowest available PANTER energy, 0.3 keV, proved that the TPC was sensitive to these energies, although with a very low efficiency (for this run a special lower trigger threshold was set in the acquisition electronics). The linearity of the detector response is also preserved down to these low energies. Although the sensitivity threshold of the TPC itself is

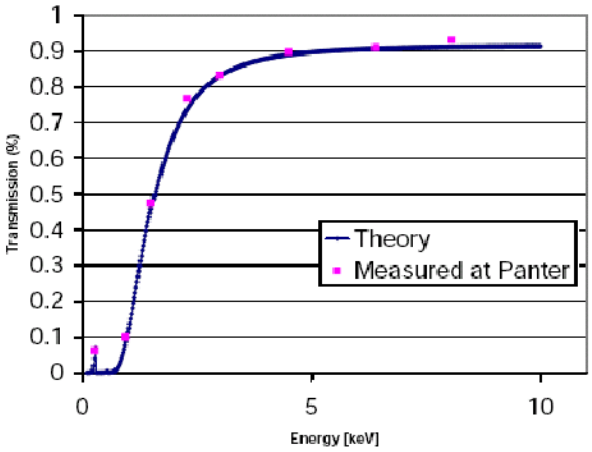


Figure 4.29: *Theoretical curve of the transparency of the windows to X-rays, confronted with the experimental measurements.*

about 0.3 keV, the effective threshold during CAST data taking is somewhat higher due to the presence of electronic noise in the experimental area.

Finally, the energy resolution of the detector can be extracted from this body of data. The left plot of figure 4.30 shows the resolution in terms of Full Width at Half Maximum (FWHM) versus energy.

## 4.4. Shielding

As described in chapter 2, the site background is mainly composed of Compton X-rays and neutrons. To reduce the amount of detected particles by the TPC from these two components, a shielding was designed by the Particle Physics group of the Zaragoza University at the beginning of 2002. Its design is the result of some simulations carried out to study the response of the TPC embedded in the CAST hall to different shielding configurations. From inside to outside the shielding (see figure 4.31) was decided to be composed of:

- **Copper box, 5 mm thick:** it reduces the electronic noise, as a Faraday cage, and stops low energy X-rays produced in the outer part of the shielding by environmental gamma radiation. It is also used for mechanical support purposes.
- **Lead wall, 5 cm thick:** To reduce the low and medium energy environmental gamma radiation. Later, in the data taking time, the width of the lead wall was reduced to 2.5 cm due to mechanical constraints.
- **Cadmium layer, 1 mm thick:** to absorb the thermal neutrons slowed down by the outer polyethylene wall.

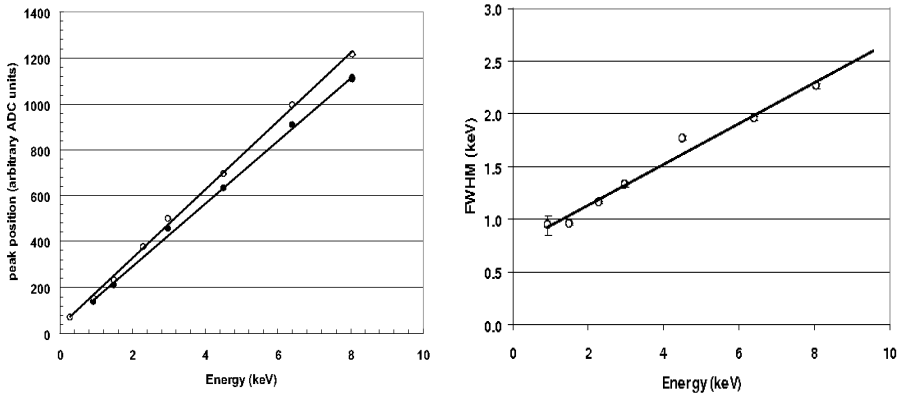


Figure 4.30: *Left: Peak position in arbitrary ADC units versus energy. The black points and the white points were taken on two different days, showing a different gain due to different atmospheric conditions. Right: Measurements of the energy resolution of the TPC detector in terms of the FWHM of the peak for the energies of interest.*

- **Polyethylene wall, 22.5 cm thick:** to slow the medium energy neutrons down to thermal energies.
- **PVC bag:** to cover the whole shielding assembly. This tightly closes the entire set-up allowing us to flush the inner part with pure $N_2$ gas coming from liquid nitrogen evaporation in order to purge this space of radon.

The mixed composition, using both lead and polyethylene, was the best option since only one layer of lead would reduce properly the gamma flux, but would produce an increase in the number of interacting neutrons. This effect can be seen in figure 4.32, where the number of detected neutrons in the region from 0.2 to 10 keV per simulated neutron[2] is represented versus their initial energy. When there is no shielding surrounding the chamber only the neutrons up to 6 MeV contribute to the detected rate form 0.2 to 10 keV, while for faster ones the chamber is transparent. A 5 cm layer of lead alone has the effect of increasing the number of detected neutrons for all the energies since it slowns down the higer energy ones, proving therefore that a shielding should be designed carefully, as certain configurations can worsen the background detected in the chamber. On the other hand, a compound shield made of polyethylene and lead allows to reduce the fraction of neutron

[2]During all the simulations an energy-averaged argon quenching factor of 0.28 was used for nuclear recoils, which was calculated using the Lindhard theory.

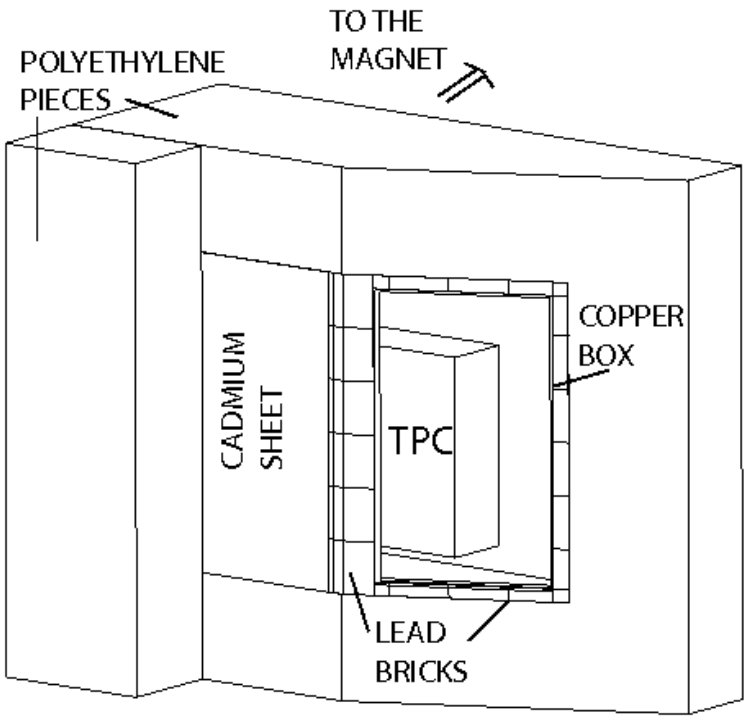


Figure 4.31: *TPC chamber inside the open shielding showing all the layers: copper box, lead, cadmium and polyethylene.*

events detected in the region of interest for almost all the neutron energies, as the polyethylene slows down the neutrons to thermic energies. In the final setup built surrounding the TPC a 1 mm thick cadmium layer, which presents a high absorption cross section to thermal neutrons, was placed between the polyethylene and the lead to absorb these thermalized particles.

Regarding the effect of the shielding for a simulated gamma background, figure 4.33 shows a comparison between the photons detected in the region of interest for the naked chamber and the ones collected using the shielding. Below 1 MeV the contribution of the gamma background in the shield chamber virtually disappears, while for higher energies it is $\sim$ 2 orders of magnitude smaller. It should be pointed out that in the case of the naked chamber, the fact that a fraction of photons with energies $>$ 50-100 keV do interact is due to the thickness of the plexiglass box. The gas by itself should be transparent for this energy range particles, but the plexiglass slows them down to the energy range where still there is some probability for them to

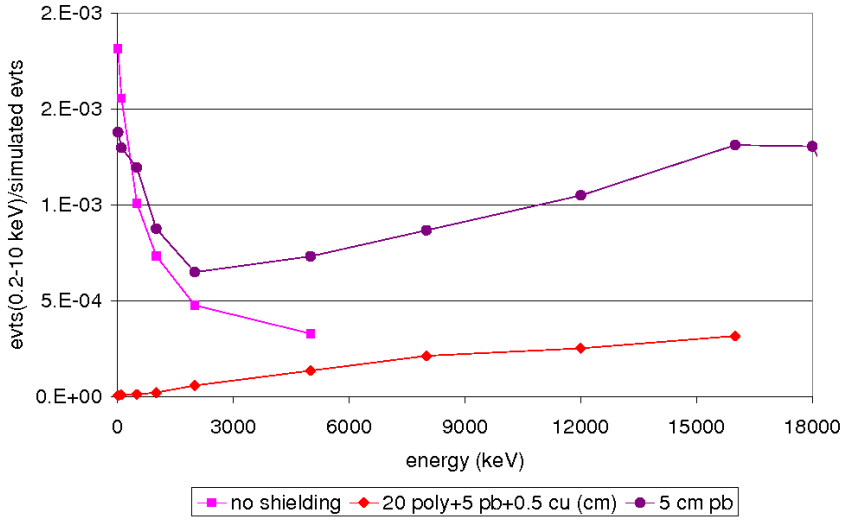


Figure 4.32: *Simulation of the number of neutrons that interact in the chamber between 0.2 and 10 keV per neutron versus their initial energy. The different curves correspond to different shielding conditions.*

give a signal.

Once the final configuration was decided, the shielding was built and tested mounted around the TPC in summer 2002. At this time the TPC was not yet in the magnet but being tested in one laboratory at CERN. The integrated background level from 1 to 10 keV was measured to be of $2.00 \times 10^{-4}$ counts/keV/s /cm$^2$ with the naked chamber, being the effect of the shielding to lower this value down to $2.37 \times 10^{-5}$ counts/keV/s/cm$^2$, which leads to a reduction factor of $\sim 8$. Therefore this test proved the capacity of the designed shielding to reduce the background level.

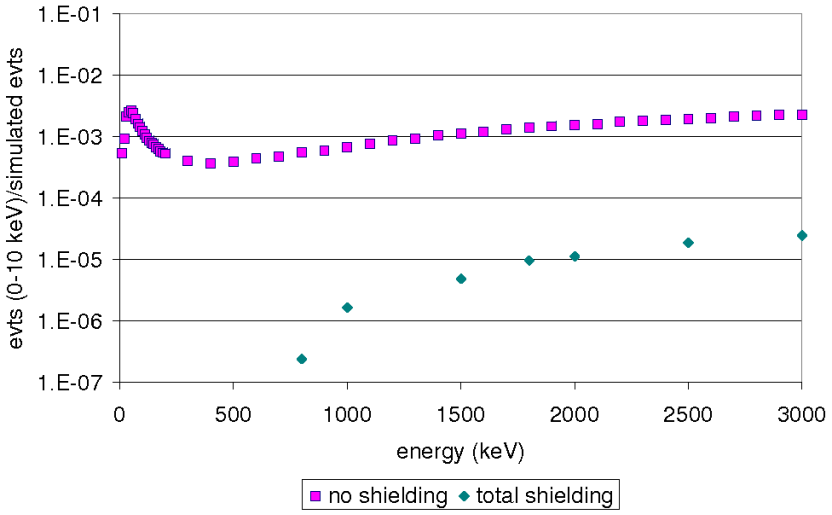


Figure 4.33: *Simulated gammas detected with energies up to 10 keV per event versus the energy of the incident gammas. The upper curve correspond to the naked chamber, while for the lower one a shielding made of 0.5 cm Cu+ 5 cm Pb+ 20 cm Polyethylene has been implemented in the code.*

# Part III

# TPC results

# Chapter 5

# First TPC results: 2002 and 2003 data taking

After a commissioning data taking period in 2002, the CAST experiment started operating in May 2003, and kept doing so for nearly six months along the year. During most of this time the TPC detector was also operative, attached to the magnet bores. In this chapter, firstly, the different sets of data gathered will be described, paying special attention to any systematic effects which could affect the data behaviour. After, the result on the axion to photon coupling constant derived from data identified as of good quality will be presented [96].

## 5.1. 2002 data: commissioning period

In table 5.1 a summary of the first two sets of data collected mostly at the end of 2002 is given.

| Set number | Date | Comments |
|---|---|---|
| #1 | 08/10/02-27/11/02 | Inhomogeneities in the data counting rate. $^{55}$Fe calibrations taken regularly. |
| #2 | 28/11/02-14/01/03 | Detector standing in a table. Homogeneous counting rate. Gas pressure and temperature recorded. |

Table 5.1: *Summary of the sets accumulated during the 2003 TPC data taking*

During the time the set #1 was collected, the TPC was attached to its position in the magnet bores, moving solidly with it. The exposure time was $\sim 30$ effective days, being a total of $\sim 25$ hours of them taken with the magnet aligned with the Sun. As the axion signal would be contained only in the data collected in this condition, in what follows the energy spectrum composed with these data will be called "*Sun tracking spectrum*". The rest of the data will be represented in an independent spectrum called just "*background*". The temporal evolution of the counting rate can be seen in the upper plot of figure 5.1, for those events belonging to a fixed ADC range which corresponds roughly to the 3-7 keV energy interval. The rate of counts accumulated in this set exhibits big variations of up to 100 % in its level and, therefore, all the possible dependencies with parameters related with the detector and the experimental area were studied to find which ones could have influenced this data behavior. It has been learnt in chapter 3 that changes in the pressure and temperature of the gas induce variations in the gas gain and, therefore, in its efficiency. In order to take this effect into account, $^{55}$Fe calibrations were taken every two or three days, being the data gain corrected accordingly. However the variation remained, and thus it was thought that maybe a more systematic gain characterisation be needed for future incoming data. For this, a thermocouple and a pressure gauge were installed on the chamber at the end of this set, in order to have a continuous monitoring of the gas pressure and temperature and deduce the gain value from them.

On the lower plot of figure 5.1 again, the counting rate evolution is shown, this time for the data collected during set #2. During this second part the TPC was not attached to the magnet anymore, but just standing in a table under it. It was expected that this data would shed some light

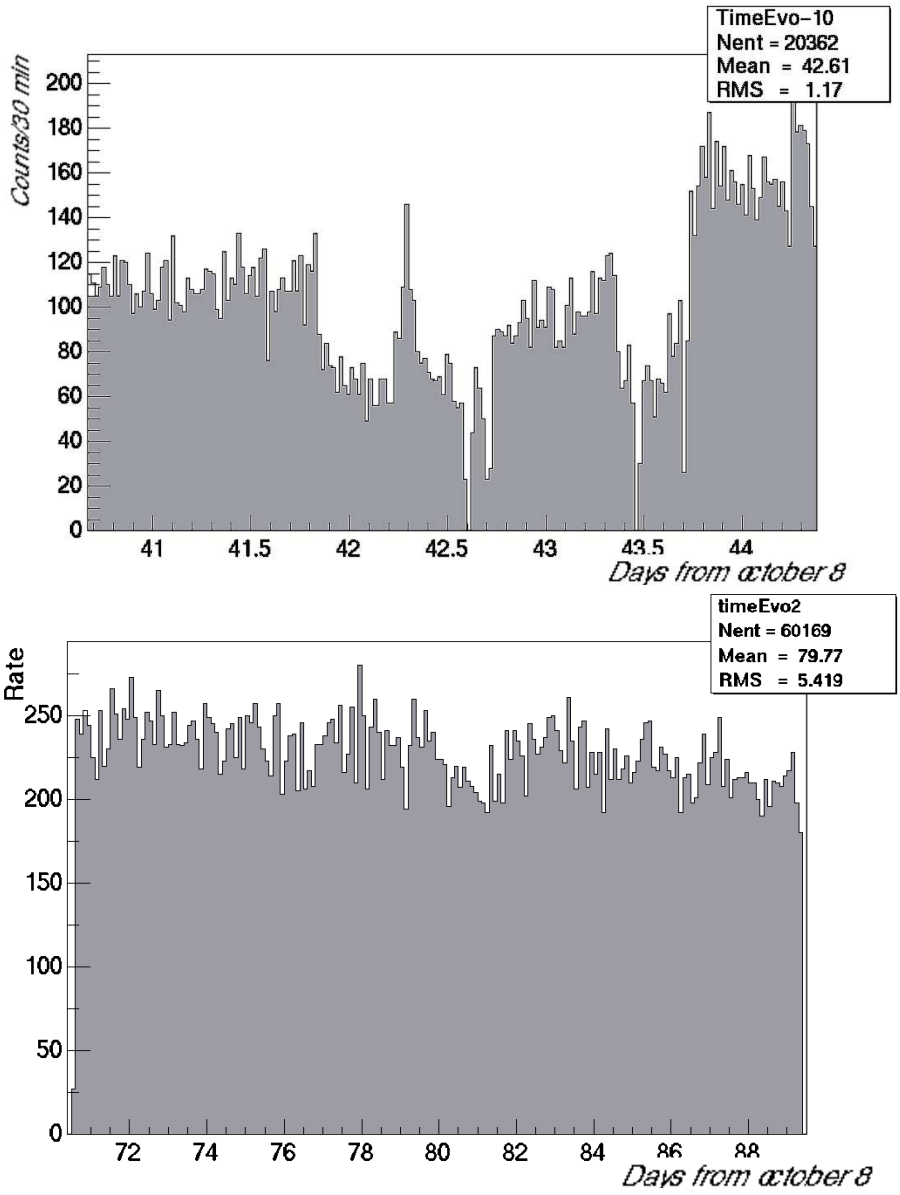


Figure 5.1: *Counting rate evolution for 5 days in set #1 and for the whole period of set #2. Giving the different width of the two periods, the binning in the plots does not match.*

on the problem of the instabilities of the counting rate since this time the temperature and pressure of gas were carefully recorded. But in this set, in spite of the fact that these parameters presented a similar behaviour than to the previous one, the background showed this time a great stability in rate. This effect hinted the possibility of the dependence being caused by intrinsic inhomogeneities in the background of the experiment site, instead of being due to gain changes. Since CAST is a moving experiment while it tracks the Sun, the TPC covers along this movement a very wide area of the experimental site, being susceptible to the inhomogeneous background level. But at that time it was impossible to prove none of this two options due to the lack of external parameters recording.

## 5.2. Set of hourly calibrations

In order to characterise the gain of the TPC versus the pressure and temperature of the gas inside the chamber, a set of hourly calibrations where taken during 5 days in January 2003, together with a systematic recording of these two parameters of the gas. In figure 5.2 we can see the evolution of the $^{55}$Fe peak in ADC channel units (up) together with the variation of the T/P parameter (given in Kelvin/hPascals units) during these five days (down).

From these plots it is clear that there is a very strong correlation between these two variables, as it is widely known to happen in drift chambers. Indeed, this dependence should be proportional to [76]:

$$\text{Gain} \propto \exp\left(k\mathbf{T}/\mathbf{P}\right). \tag{5.1}$$

To extract the value of the proportionality constants in equation 5.1 for the particular case of the CAST TPC, the $^{55}$Fe peak evolution in ADC channel units was represented versus the variation of the T/P parameter, being the result fitted with the function 5.1. The best fit values obtained were:

$$5.9 \text{ KeV channel} = \exp(1.12 + 18(\frac{\mathbf{T}}{\mathbf{P}})). \tag{5.2}$$

For the 2003 data analysis this dependence was used to determine the gain of the chamber, and for every event, the energy was being obtained from the value of its charge in ADC units, correlated with the value of P and T of the gas in the moment when the event was taken by equation 5.2.

On January 14$^{\text{th}}$ 2003, the TPC was completely disconnected from he magnet and taken to the workshop in order to be checked and kept in a clean environment till the data taking would be resumed.

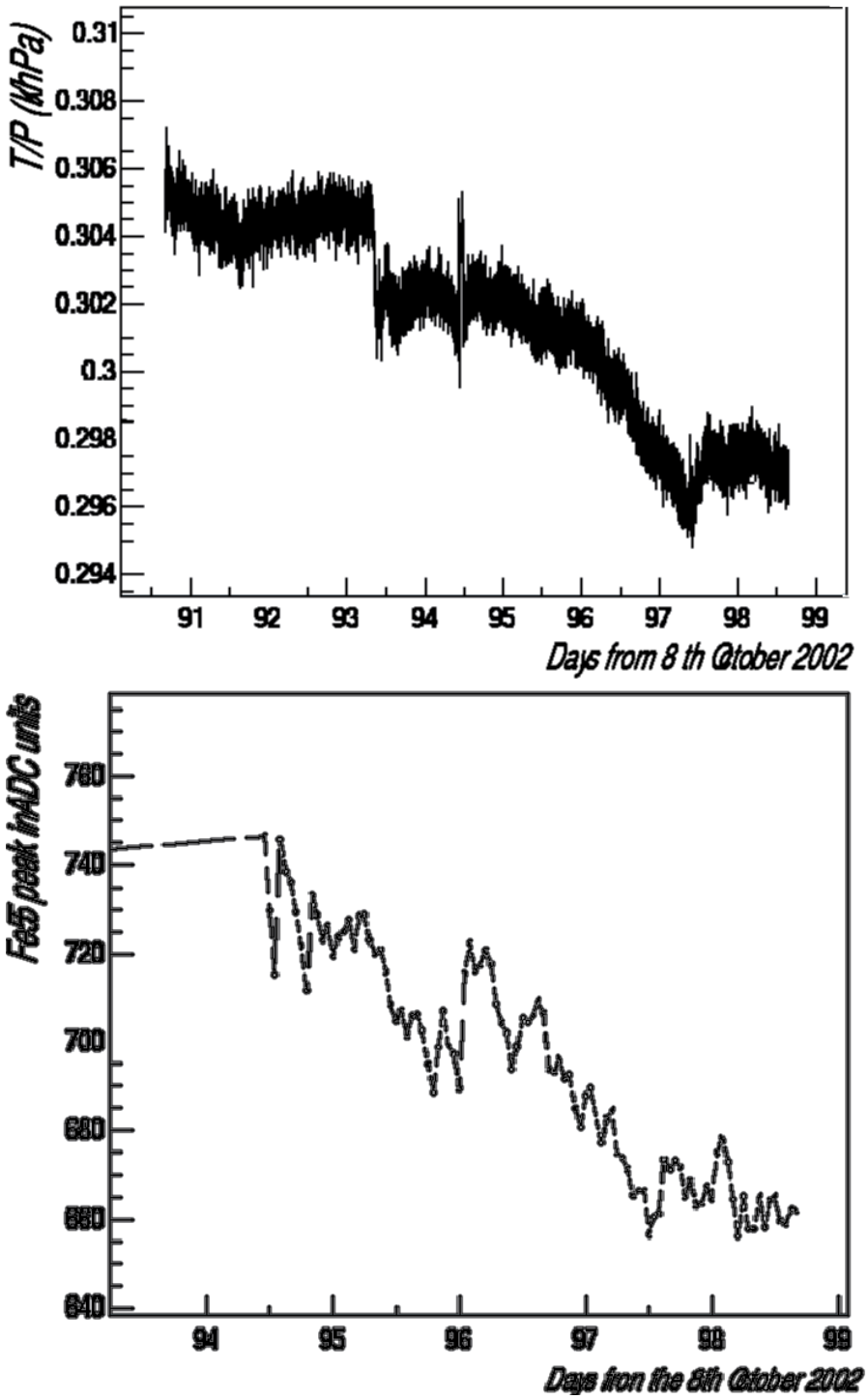


Figure 5.2: *Up: T/P quotient evolution. Down: Evolution of the $^{55}Fe$ main peak in ADC units during the same period*

## 5.3. TPC 2003: Continuous data taking

### 5.3.1. 2003 data taking

#### Experiment performance

In mid-April 2003 the whole CAST set up was finally ready to begin a systematic data taking. The TPC was fully operational again on the magnet since the last week of April, and its first solar tracking run of the year was taken on May 1$^{\text{st}}$. Having learnt from the experience in 2002, a continuous recording of several parameters related to the experiment and the detectors were performed, since the Slow Control software (see section 2.2.1) started running in the experiment.

During May all three detectors were taking data, but at the end of the month a problem of gripping in the magnet lift mechanism became apparent and magnet movement was finally stopped on May 31$^{st}$. Engineers at CERN were consulted about the problem because unfortunately the personnel responsible for the design and assembly of this mechanism had left CERN in 2002. The expert advice received was that the mechanical movement system of the magnet was over-constrained, being these constraints translated into lateral forces on the lifting mechanism. In order to resume data taking in a short time, the engineers proposed to add some mechanical play into the lifting system mechanism, to make a factory inspection of the lifting jacks and to improve the lubrication system. Because of all these modifications on the magnet system, some precision was lost in the pointing accuracy of the magnet system, being nevertheless still within the limits required by the X-ray telescope, which is the most sensitive device in the experiment to this parameter. Eventually data taking restarted after a stoppage of 6 weeks. Sun tracking runs then continued without incident related to the magnet until data taking ended in mid-November.

#### TPC performance

In 2003 a systematic data taking started to take place. The automatic procedure during this year consisted on 6 hours of data taking, stopped just to take a run of pedestals. Due to the long working period, some problems in the TPC started to become apparent. The two main ones were the electronic noise, whose origin was not completely understood and forced us to reject some data; and the gas leak rate from the thin windows facing the magnet bores. In table 5.2 a summary of the different sets that were collected during the 2003 data taking period is shown.

As it can be seen, some data were taken before the magnet movement was stopped because of the failure in the lifting system. In section 4.4 it has been mentioned that a shielding was designed and built to work together with the TPC during the data taking periods. But the complete structure of

| Set number | Date | Comments |
|---|---|---|
| #3 | 01/05-18/06 | First 2003 data without shielding.<br>Problem with the lifting system of the magnet. |
| #4 | 18/06-23/06 | Test with all the shielding installed on the TPC.<br>No magnet movement. |
| #5 | 23/06-15/07 | Intermittent electric noise.<br>Different shielding conditions. |
| #6 | 15/07-23/08 | High quality data.<br>Problem with the leak rate of the windows. |
| #7 | 20/09-17/11 | Bad quality data. |

Table 5.2: *Summary of the sets accumulated during the 2003 TPC data taking.*

the shielding is 1.2-ton heavy, and therefore its permanent installation in the magnet moving structure was commissioned by an engineers group at CERN to precisely determine its impact from the safety point of view. While this study was going on, the TPC was first naked during the set #3.

Due to the fact that during the short stop the magnet was safely and still standing over some concrete blocks, it was possible to install the whole shielding in order to test its result in-situ for $\sim$ one week. Figure 5.3 shows a comparison between the energy spectra collected with different shielding conditions.

The average normalised counts between 1 and 10 keV is $1.85 \times 10^{-4}$ counts/keV/cm$^2$/s for the case of the TPC completely exposed as gathered in the previous set # 3, while the effect of the shielding by itself lowers this number down to $6.83 \times 10^{-5}$ counts/keV/cm$^2$/s. If the $N_2$ flux is also connected, and therefore the radon purged from the detector closer environment, the total average downs to $4.38 \times 10^{-5}$ counts/keV/cm$^2$/s, a factor $\sim$ 4 less from the completely exposed case.

The reduction factor achieved in this case is only half of the one obtained when the shielding was tested in the laboratory, as mentioned in section 4.4. One of the reasons of this discrepancy lies on the fact that the lead layer thickness on the CAST experimental site is half of the one used in the laboratory due to mechanical constraints. Also in this case the TPC is directly attached to the magnet pipes, and thus partially not shielded from it being therefore still sensitive to a gamma background contribution from the experimental materials.

Once the problem in the lifting system of the magnet was solved, the data taking was resumed. The shielding was dismounted, leaving in site only the

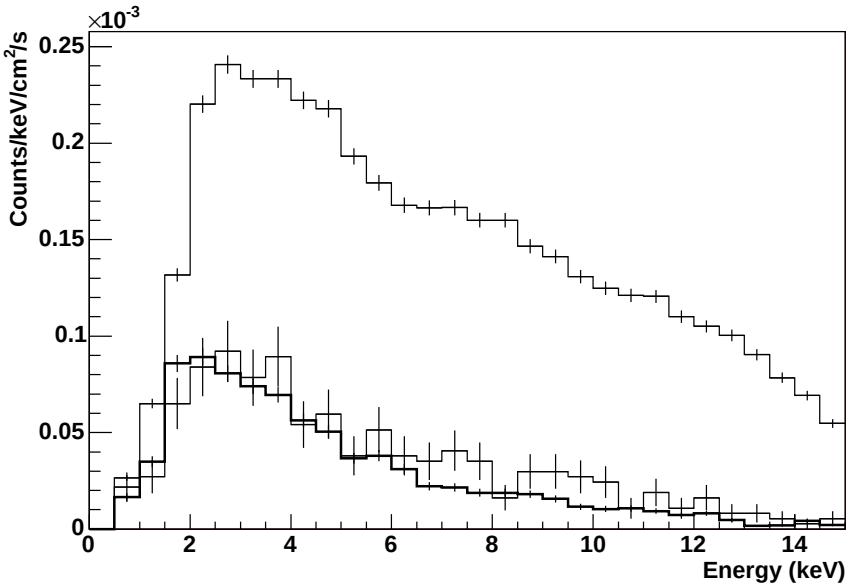


Figure 5.3: *Energy spectra of the TPC for different shielding conditions. The upper line represent the no-shielding one, while the lower ones represent the whole shielding (thin line) and the shielding + $N_2$ flux.*

copper box around the TPC and the $N_2$ flux connected in order to purge it. In the first days the intermittent appearance of electric noise made the data taken not valuable, but after a while the problem was solved by improving the electronic shielding and grounding. From July $15^{\text{th}}$ till August $23^{\text{rd}}$ the TPC performance was good, as it was very stable, and finally this data set # 6 was the one used to perform the *axion parameters analysis*.

Unfortunately, once the electric noise problem was solved, the deterioration of the thin windows started to become a serious nuisance. In the upper plot of figure 5.4 we can observe the evolution of the leak of chamber gas towards the magnet during this period. By the end of August this rate became dangerous for the stability of the magnet and the TPC was finally removed the $25^{\text{th}}$ in order to substitute the windows. The removed ones showed under the microscope holes in regions where the aluminium layer had came off, as it can be seen in the lower plot of figure 5.4.

Therefore it was obvious that the 38 nm thick aluminium coating used in these windows was not enough to provide the required leak thickness and strength to the system. New widows were developed with an extra 50 nm thick Al coating over the original.

The chamber was reinstalled back on the magnet on September $13^{\text{th}}$ and took data again until the middle of November, when the general shutdown stopped the whole CAST experiment. With the extra Al coating the windows

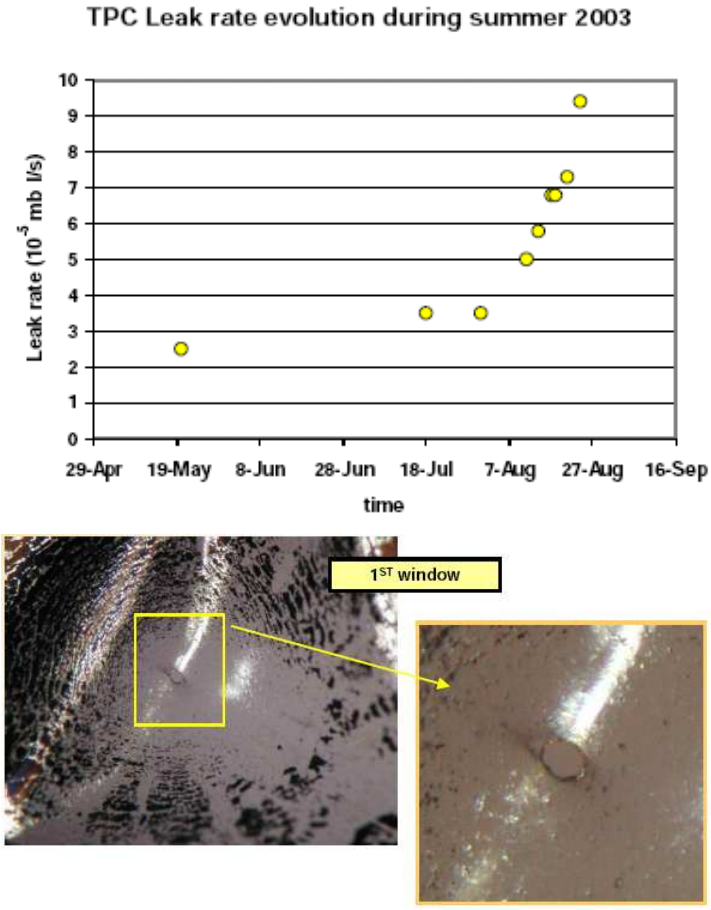


Figure 5.4: *Up: TPC gas leak rate to the magnet evolution during summer 2003. Down: A hole in one of the thin windows used in the TPC. The order of magnitude is of some $\mu$m.*

worked properly during this period, keeping a stable safe leak rate towards the magnet bores of 2-3 $\times 10^{-5}$ mb l/s.

### 5.3.2. 2003 data behaviour

As a summary, although the data taking period of 2003 lasted for about 6 months, much of this time corresponds to commissioning operation, periods when data taking was temporarily stopped due to specific technical interventions in the experiment or in the TPC itself (replacement of leaky windows, for example) or periods when data were taken but they did not pass the quality requirements regarding homogeneity of operation, due to the relatively frequent interruptions in the experiment, mainly due to magnet quenches, and to a lesser extent to episodes of electronic noise pick-up

in the detector (set #7).

As a result, the effective amount of data qualified for analysis obtained by the TPC in 2003 was ∼783 hours, all of them concentrated in the months of July and August (set# 6). Out of these data, ∼63 hours (9%) were taken when the magnet was tracking the Sun. The stability and continuity of operation of the detector during this time can be appreciated in figure 5.5, where the exposure in days for the background data and in hours for the tracking ones are shown.

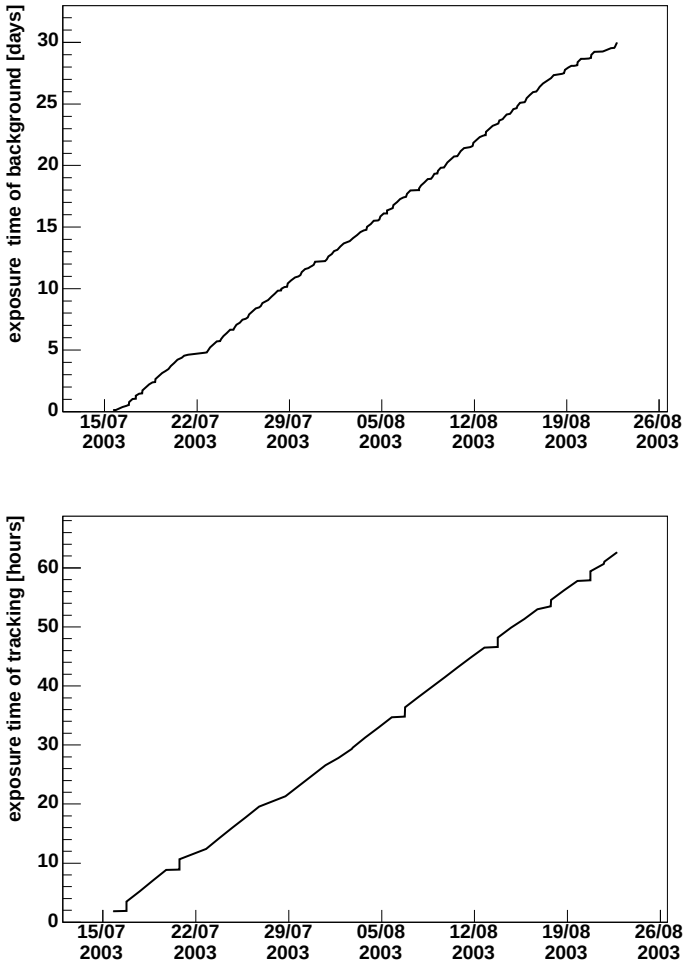


Figure 5.5: *Up: Exposure in days for the background data. Down: Exposure in hours for the Sun tracking data.*

### Position dependence

All the systematics effects hinted in section 5.1 concerning the inhomogeneity of the background became apparent in the new data. In figure 5.6 we can see the total Sun traking spectrum (thick line) superimposed with the background data (thin line). Obviously they are completely incompat-

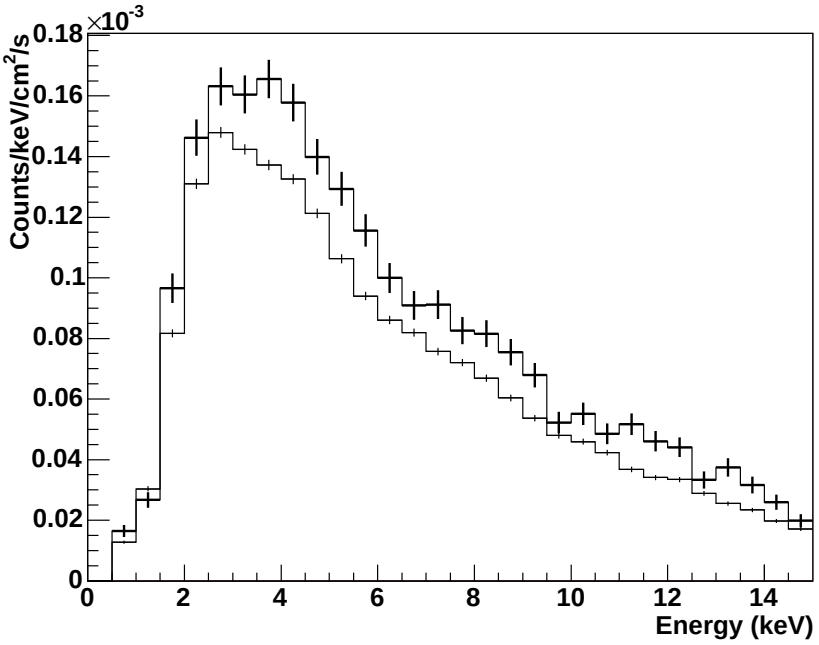


Figure 5.6: *Sun tracking spectrum (thick line) superimposed to the background one (thin line) for the data taken in the 2W area of the TPC during the set # 6.*

ible, and thus the main task at that time was to study the origin of this discrepancy and solve it as far as it can be done.

Given the measured inhomogeneity in the gamma ray background at the experimental site (see chapter 2), and the fact that most of the Sun tracking data were taken in a certain area different from the one where the background was being collected, soon a position dependence was thought to be the reason.

In order to prove and quantify this dependence, as well as to have a tool to correct it, new features were introduced in the analysis program, TPCANA. Given that the position of the TPC within the experimental hall is recorded every minute, it is possible to see the rate of counts and the energy spectrum of the data accumulated in different areas of the experimental site. For this two 2D grids -named coarse with 3×3 cells, and fine with 7×7- were defined to distribute the space in the experiment. A new extra index, called *imag*,

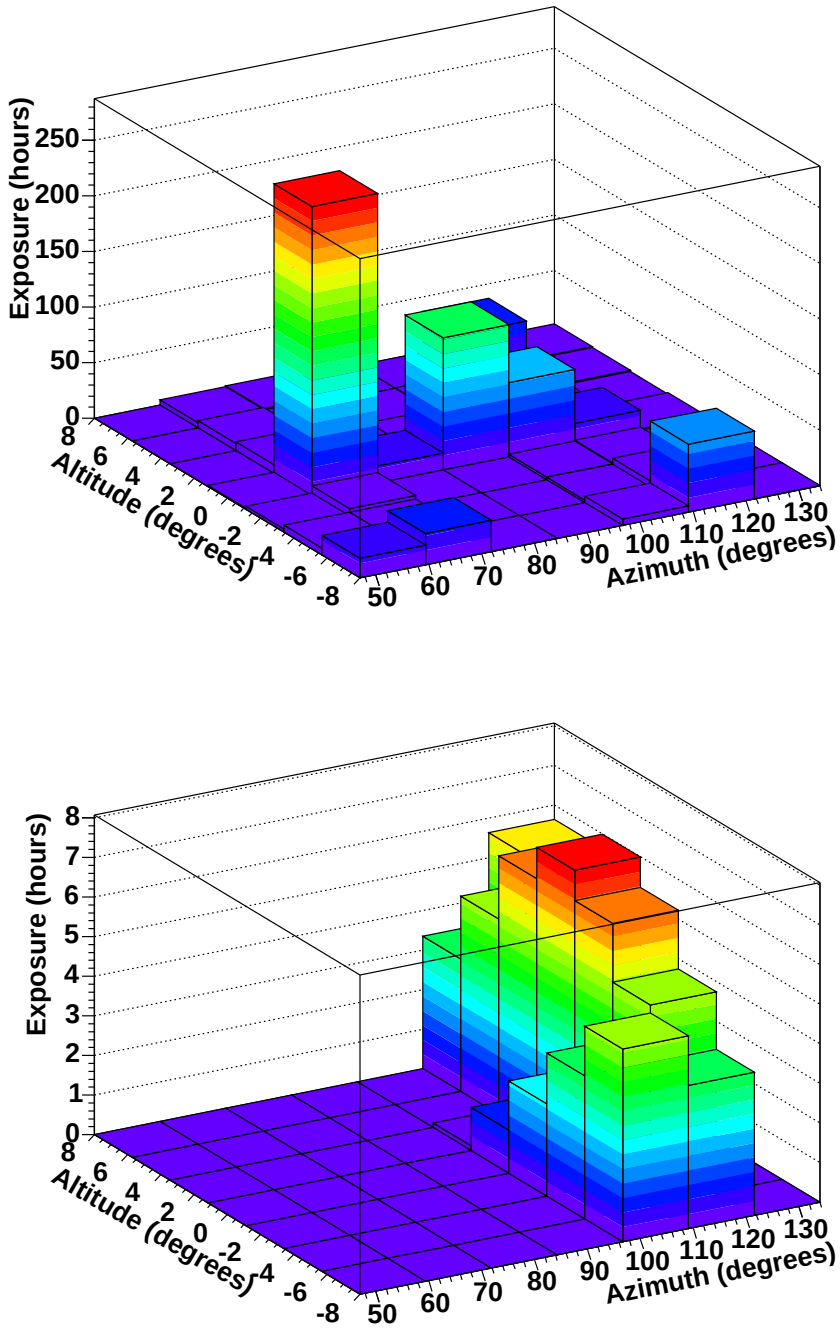


Figure 5.7: *Exposure hours of background (up) and Sun tracking (down) data for the different cells in the fine grid.*

was added to the set of the previously described ones (see section 4.2.3) to every event recorded in the chamber. In this index the information about the cell where the TPC was positioned when the event was collected is stored. With this information it was easy to introduce a new set of 3D histograms representing the rate of counts in every cell, and a new set of plots $S_i$ with the energy spectrum in each one of these cells (labelled by the index $i$). In order to normalise this histograms properly, a routine to calculate the exposure reached in every cell of the grid was also developed. In figure 5.7 we can see the exposure in hours for every cell both for the background and Sun tracking data in the fine grid. The coordinates used here to determine the position are the *local* system used in the CAST area, where the azimuth angle specifies the position of the magnet on the rail, and can vary from 40° (in the very north-west position) 140° (south-east), while the angle tell us about the vertical position, which goes from -8°, where the TPC is very near to the soil, to +8°, where the TPC is in its highest position. It can be seen in the upper plot that, during 2003, the positions to take background were not uniformly distributed, since most of the times after tracking the Sun the magnet used to be "parked" in a centric position. Therefore in this figure the obvious difference in the position of the TPC where the Sun tracking data were collected (high azimuth values) to the usual background data collection position (medium-low azimuth values) can be appreciated.

The rate (counts/hour) of events collected with energy between 3 and 7 keV in the 2W area of the TPC is shown in figure 5.8. Before pointing up any conclusion we must be aware of the fact that not all the cells have gathered data for the same amount of time, and therefore this plot must be studied in conjunction with the lower plot in figure 5.7. Both the cells with the higher number of counts (and marked in red) corresponding to vertical positions of +8° are statistics artefacts due to the very sort time that the TPC collected data in these cells, and should not be taken into account. Apart from them, what we can see from here is a tendency of having higher number of counts when the magnet is pointing to the upper part of the south-east wall, where the concrete experimental wall is thicker.

In figure 5.9 the three most position-different spectra are shown, the big difference between them being obvious.

### Introduction of the *weighted background*

It is clear that this position dependence is strong enough to be the main reason for the discrepancy between the Sun tracking and the background spectra in figure 5.6. In order to be able to do any axion analysis the way to compensate this position dependence should be found. What is obvious is that only the background taken in the same cells as the Sun tracking data should be used if we are to reproduce its spectrum. Moreover, this selected background should be weighted according to the fraction of the time the TPC

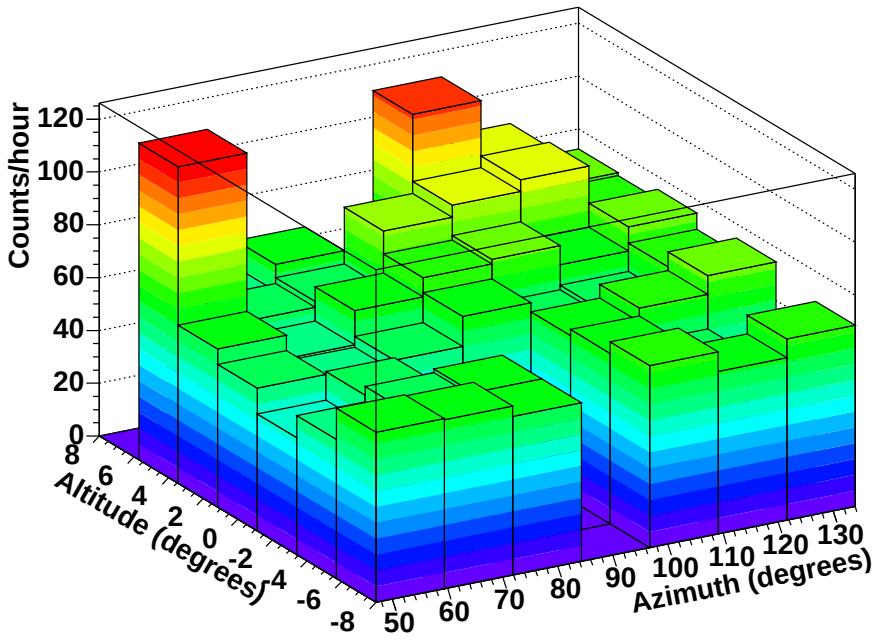


Figure 5.8: *Counts/hour rate taken in the different cells of the experiment. Here only the data from 3 to 7 keV taken in the 2W area of the TPC are shown.*

has spent in each one of these cells during the signal taking runs. Only in this way we will ensure that they will contribute the same for the background spectrum as they did for the Sun tracking one.

Taking this into account, a *weighted background* spectrum $S_w$ was built according to:

$$S_w = \sum_i^{N_t} S_i \left( \frac{t_i}{\sum_i^{N_t} t_i} \right) = \frac{\sum_i^{N_t} S_i t_i}{\sum_i^{N_t} t_i}, \tag{5.3}$$

being $N_t$ the total number of cells where the Sun tracking spectrum have been collected, $S_i$ the background spectrum gathered in these cells and $t_i$ the total time that the TPC has spent in the cell $i$ collecting Sun tracking data. In figure 5.10 we can see the comparison between the Sun tracking (thick line) and the weighted background spectra. In the upper one the weighted background has been built with the spectra from the cells of the coarse grid, and therefore the error bars are smaller. The lower one shows the background spectrum composed by adding the ones of the fine grid. It is clear that both Sun tracking and background spectra agree now much more that what was shown in figure 5.6. Anyhow, this should be considered just

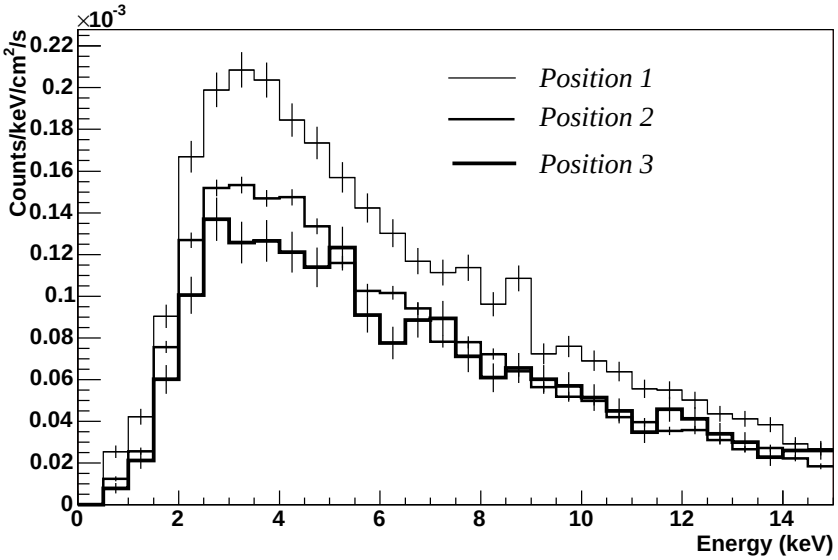


Figure 5.9: *Background spectra for different cell positions in the coarse grid.*

an indicative sign of the fact that the position dependence is indeed the main reason of the previous disagreement. Still the Sun tracking spectrum could contain a signal over the background contribution, so it could happen that they do not agree for this reason.

To really crosscheck how good this weighting method is, the data taken in the out area of the TPC can be used, as the Sun tracking spectrum collected there does not contain any signal, and therefore should be similar to the background one. In figure 5.11 this comparison is shown, proving that the degree of agreement is as good as in figure 5.10. The $\chi^2_{null}$ test performed over the spectrum obtained by subtracting them yields a value of $\chi^2_{null}/d.o.f = 26.68/18$. It is known that for a given variable distributed according to a $\chi^2$ p.d.f., the probability of obtaining a value S such that $S/d.o.f > 1.44$, which is our case, is of a 10%. This value tells us that it must not be forgotten we are handling an artificially manipulated background which allows us to extract from the data the axion parameters that we are looking for, solving to some extent the position dependence problem. In what follows we will focus on the axion parameters extraction from these data, and in a later section (5.3.3) the accuracy of the weighting method will be reviewed.

As both the coarse and fine bin weighted background spectra seems to suffer only slightly from the position dependence, in what follows the coarse bin weighted background will be used to perform the axion analysis, since the smaller the error bar, the better the result.

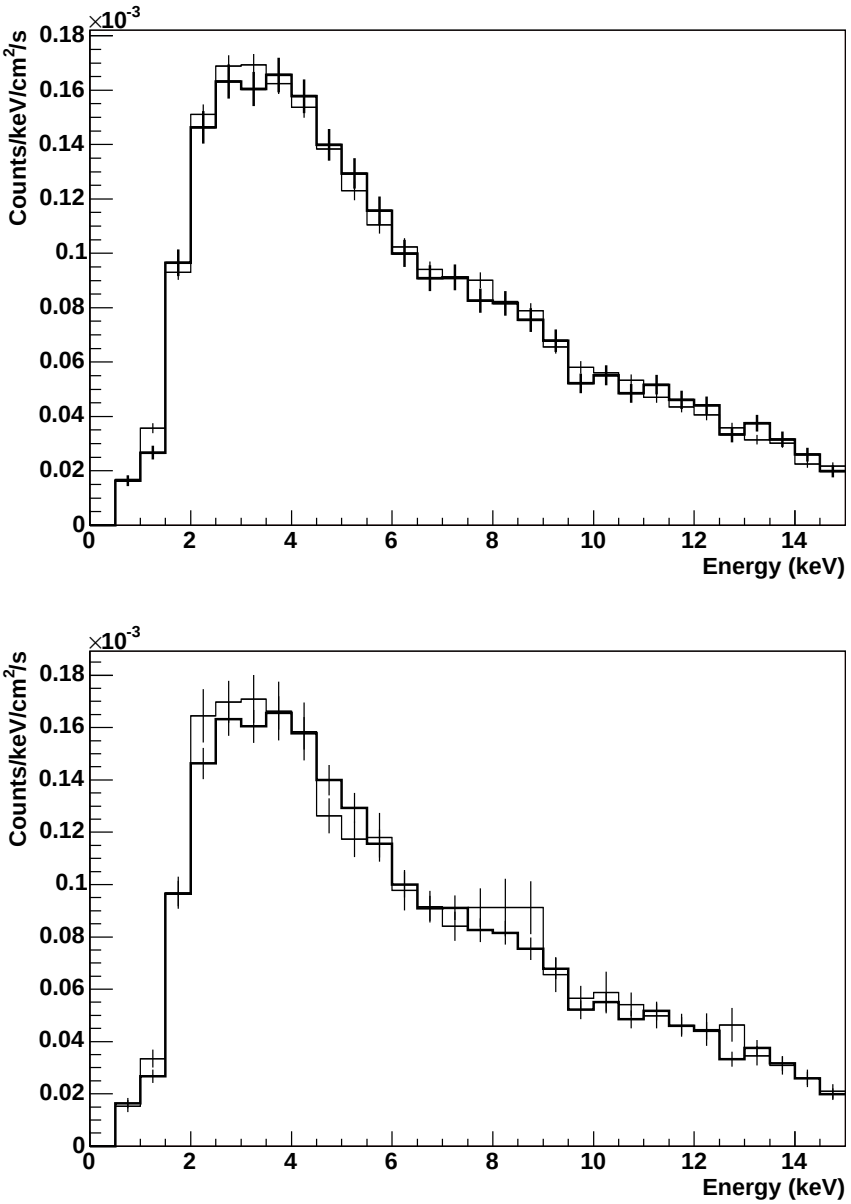


Figure 5.10: *Comparison between the Sun-tracking (thick line) and the coarse (up) or fine (down) weighted background.*

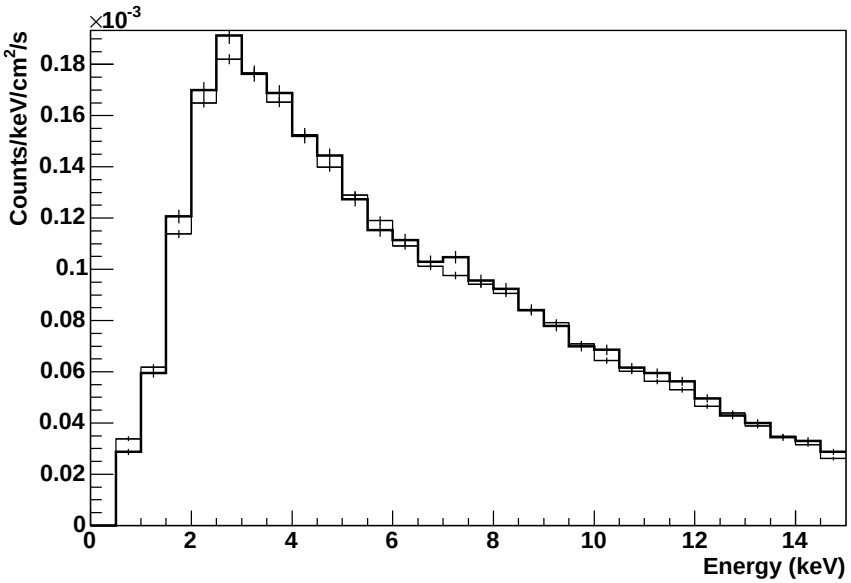


Figure 5.11: *Sun tracking (thick line) and weighted background spectra from the out area of the TPC.*

### 5.3.3. Axion analysis on the data

The next step in the analysis goes through searching for any hint of solar axions. They would appear as an excess of counts over the background in the Sun tracking spectrum. Thus, if we subtract both energy spectra, we would be left with the spectrum of the axion-converted photons which is directly proportional to $g_{a\gamma}^4$, the only free parameter in our theory. Therefore our analysis is focused on calculating the value of $g_{a\gamma}^4$ that best fits our data.

If, on the other hand, this subtracted spectrum is compatible with zero within statistical fluctuations (null-hypothesis test), we must say that, up to the sensitivity of the detector, the data show no positive signal over background. Then an upper limit on the coupling constant axion to photon $g_{a\gamma}$ can be derived as, if still axions happen to exits, it can be asserted that their coupling constant to photons $g_{a\gamma}$ must be smaller than the value given, otherwise a signal would has been observed in CAST.

#### Null hypothesis test

Lets calculate the null hypothesis test over the subtracted spectrum. For this we must determine the **weighted sum of squared deviations**:

$$S = \sum_{i=1}^{n} \left( \frac{x_i^{exp} - x^{theo}}{\sigma_x^{exp}} \right)^2 \tag{5.4}$$

where we are summing over the $n$ experimental points of the subtracted spectrum. Here $x^{theo}$ corresponds in this case to the non signal ($g_{a\gamma} = 0$) points and therefore $x^{theo} = 0$. When the experimental points $x_i^{exp}$ are independent and Gaussian distributed, S behaves as a $\chi^2$ distributed quantity. This means that, if $x^{theo}$ are representative of the true hypothesis that the $x_i^{exp}$ should resemble, repeating the experiment many times and computing S each time, the distribution of this quantity will be given by the distribution of the $\chi^2$ for the given degrees of freedom (number of data points minus the number of free parameters in the model, d.o.f) on the experiment [97]. The mean of a $\chi^2$ distributed variable is given by the d.o.f of the experiment. Thus one should expect, being the hypothesis correct, that the quotient (S/d.o.f) would yield a value close to unity, and therefore can be used as a test on how good this hypothesis fits the data.

Therefore our first concern is whether our $x_i^{exp}$ are independent and Gaussian distributed. In CAST $x_i^{exp}$ are built from a subtraction $x_i^{exp} = s_i^{exp} - b_i^{exp}$ so the question translates to whether both $s_i^{exp}$ and $b_i^{exp}$ are themselves Gaussian distributed. Since they are directly measured counts, its distribution is in principle Poissonian, but when the number of counts per energy bin collected is big enough, which for the TPC data is the case since the counts accumulated per bin are of the order of $10^3$ for the background data and $10^2$ for the Sun tracking ones, the central limit theorem applies and it can be assured that the Gaussian distributed condition is fulfilled. Furthermore, it is clear that the $x_i^{exp}$ are independent, as the counts gathered in one energy bin are independent from the other ones.

In figure 5.12 we can see the zero line superposed over the subtracted spectrum of set # 6 of data. Even though the range of the energy spectrum seen by the TPC has a lower limit of $\sim$ 0.7 keV due to the electronics threshold, and an upper one of $\sim$15-16 keV due to the lose of the efficiency detection of the argon, the energy range used for all the axion analysis is defined from 1 to 10 keV. The reason for this lies on the expected axion signal, which is different from zero only in this range. The two vertical dotted lines on figure 5.12 mark these limits.

The value of the null hypothesis test on this set yields the value

$$\chi^2_{null}/d.o.f = 18.2/18 \tag{5.5}$$

which is indeed close to one, confirming this way the hypothesis, and therefore the compatibility of data with the absence of any signal.

### Best fit and errors

Knowing that the data are compatible with the absence of signal, if we test now the axion signal hypothesis, we would expect to obtain as a best fit a value of $g_{a\gamma}$ compatible with zero (no signal) within errors.

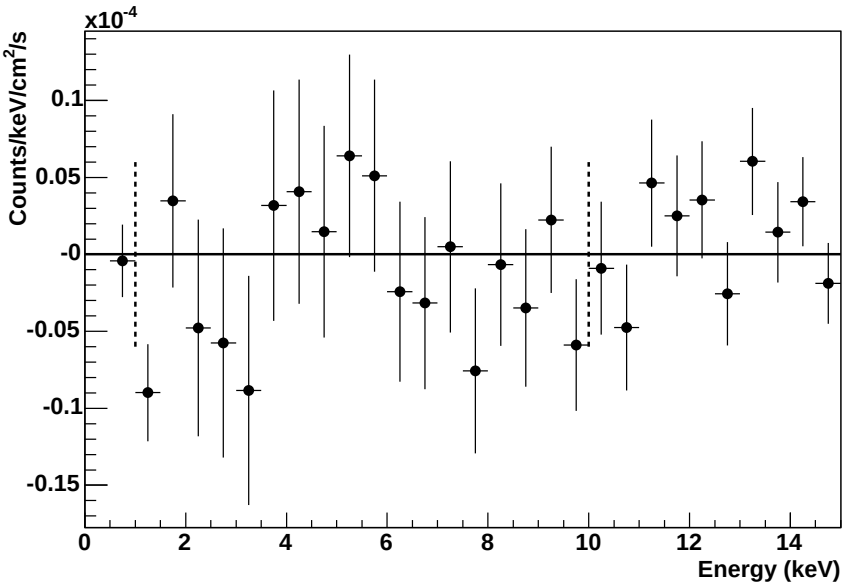


Figure 5.12: *Null hypothesis test on the subtracted data of set # 6.*

In order to calculate this, the theoretical function $d\mathrm{N}_\gamma/dE$ giving the energy spectrum of photons normalised per unit of time and area as a function of $g^4_{a\gamma}$, must be determined, and compared with our data by means of equation 5.4. The value of $g^4_{a\gamma}$ which corresponds to the function $d\mathrm{N}_\gamma/dE$ closer to the data (i.e., which minimizes S) will be called the best fit $(g^4_{a\gamma})_{\text{best fit}}$ value.

This theoretical $d\mathrm{N}_\gamma/dE$ function is the differential version of equation 2.1, which was telling us about the number of photons coming from axion conversion that would reach any detector for a given time interval and area. The number of these photons that would be actually *detected* by the TPC is obviously lower, and can be calculated by folding this function with the efficiency to X-rays of the detector and its live time ($\equiv 1 -$ dead time). In this way we have the expression:

$$\frac{dN_\gamma}{dE} = \frac{d\Phi_a}{dE_a} \times P_{a\to\gamma} \times \frac{d\varepsilon_{eff}}{dE} \times (1 - DT), \tag{5.6}$$

where $d\Phi_a/dE_a$ is the axion flux on the earth as given by equation 1.31, $P_{a\to\gamma}$ is the probability of conversion of an axion into a photon given by equation 2.2 (proportional to $(B/L)^2$ with B and L the magnetic field and length respectively), $\varepsilon_{eff}$ represents the efficiency of the detector and $DT$ its dead time. Therefore the ingredients to determine the function $d\mathrm{N}_\gamma/dE$ are:

- Efficiency: From the calibration data collected in the Panter facility

(see section 4.3) the curve of the efficiency of the TPC for X-rays is known as shown in figure 4.28.

- Live Time: Since the dead time of the detector for the 2003 data was, in average, of a 2.5%, the multiplying factor in equation 5.6 is 0.975.
- Magnetic field B: During the 2003 data taking, one third of the time the magnetic field was set to its maximum value, $B_{max}$=9.0 T (13330 A), while the rest of the time was siting in the safer one B=8.79 T (13000 A). Since this parameter enters squared in the $P_{a\to\gamma}$ formula, an average value is then calculated using $\sqrt{1/3\times(B_{max})^2+2/3\times(B)^2}$, which yields a value of the field = 8.86 T.
- Magnetic length: The effective length that sustains the magnetic field given before for an LHC magnet is 9.26 m.
- Axion flux on earth: For this the expression given by equation 1.31 is used.

Once these ingredients are known, the points $x^{theo}$ of equation 5.4 can be calculated and so the value of S for different values of $g_{a\gamma}$. Figure 5.13 shows the dependence of $S$ on $g_{a\gamma}$ for the set # 6 data, which is parabolic, as it should be when we deal with a linear model with Gaussian errors (see the notes on statistics from [23]). The minimum corresponds to the best fit value of $g^4_{a\gamma}$:

$$(g^4_{a\gamma})_{\min} = -1.1\times10^{-40}\,\mathrm{GeV}^{-4} \quad (\chi^2_{\min}/d.o.f = 18.1/17) \tag{5.7}$$

To determine statistical error of this parameter within one standard deviation ($1\sigma$) we can take into account that the contour in $g^4_{a\gamma}$ space defined by

$$\mathrm{S}(g^4_{a\gamma}) = \mathrm{S}_{min} + 1 \tag{5.8}$$

has tangent planes located at plus or minus one standard deviation from the estimated value of $(g^4_{a\gamma})_{\min}$ (see again [23]). In our case, if we calculate how far the best fit is from the $\pm(g_{a\gamma})_{1\sigma}$ value, we find an error of $\pm3.3$ in both sides. Therefore we can conclude that the $g^4_{a\gamma}$ best fit value with its errors for the set #6 data is:

$$(g^4_{a\gamma})_{\min} = (-1.1\pm3.3\ (stats))\times10^{-40}\,\mathrm{GeV}^{-4} \tag{5.9}$$

which is clearly compatible with $g^4_{a\gamma}=0$ within the error, as expected.

### Confidence Interval extraction

Once we know the data are compatible with the absence of signal hypothesis, we would like to quote the region of the $g_{a\gamma}$ space where the true value

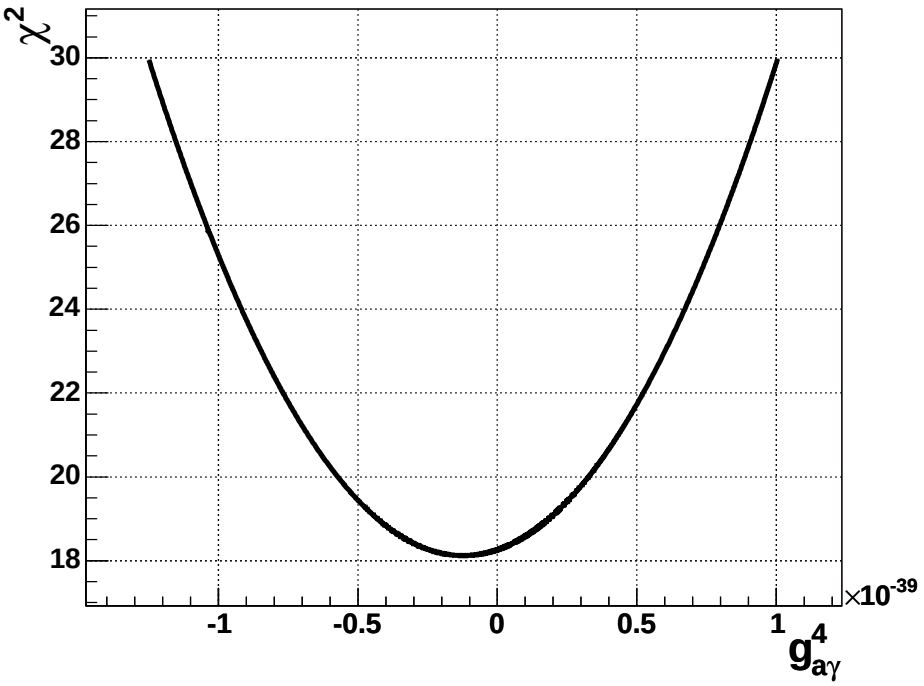


Figure 5.13: *Dependence of S (equation 5.4 on $g^4_{a\gamma}$).*

of $g_{a\gamma}$, given the existence of axions, would lie, with a certain probability or confidence level (C.L.). In other words, we want to determine an upper limit value of $g_{a\gamma}$, which will tell us that the true value of $g_{a\gamma}$ must be below it. Of course this value is calculated with a certain confidence level, so that the "more sure" we are about this, the more conservative it will become.

In the Frequentist approach, a confidence level region/interval is given by the set of theoretical parameters $\theta$ which fulfill the condition:

$$\chi^2(\theta) < \chi^2(\theta_{min}) + \delta \tag{5.10}$$

once the $\chi^2$ distribution in known for these theoretical parameters ($\theta \approx g^4_{a\gamma}$ in our case). $\delta$ depends on the required C.L. (1-$\alpha$) and the number of fitted parameters $r$. This prescription comes from the assumption that the best fit values $\theta_{min}$ are Gaussian distributed around the true value $\theta$, which means that if the experiment were to be repeated a large number of times, the best fit values obtained each time would be Gaussian distributed around the true value. The confidence interval quoted each time would vary, but in a fraction 1-$\alpha$ of the experiments it would cover the true value of the parameter. For the CAST data, since we are dealing with a linear model of the theoretical parameter $g^4_{a\gamma}$, it can be assured that the probability distribution function (p.d.f.) of the best fit values certainly is Gaussian.

If we were applying this recipe straightforward to the CAST data, we would end up with a interval that covers negative values of $g^4_{a\gamma}$, which we know does not have any physical meaning. That would be an unpleasant result to quote, and other methods to estimate a confidence interval must be found. Several of them exists, and there is not a correct or preferred one. Therefore the quotation of a confidence level or an upper limit comes unavoidably with some degree of subjectivity from the experimentalist.

The most straightforward method is still to use expression 5.10, just ignoring the unphysical region. The problem is that it will give unpleasant lower upper limits for the *lucky* experiments where the minimum (best fit) lies in the unphysical region, as it happens in our particular case.

To overcome this nuisance, the method of the *integration of the Bayesian probability [23]* was chosen for the CAST confidence interval extraction, which always over-covers, but can compensate the lucky experiment effect, being this the main reason why it was chosen.

In Bayesian statistics the starting point is always the expression:

$$P(hyp|x) = \frac{P(x|hyp)P(hyp)}{P(x)}, \tag{5.11}$$

where $x$ represents the set of data (points of the subtracted spectrum in CAST) and *hyp* the hypothesis that has to be tested, which can be represented by a parameter $\theta$ whose value is to be found ($g^4_{a\gamma}$ in our case). The p.d.f $P(x|hyp)$ represents just the joint probability of obtaining the set of data given a certain hypothesis, and it is given by the *likelihood function* $L(\theta)$, evaluated on the data and regarded as a function of the parameter $\theta$. $P(hyp)$, the *prior p.d.f*, tells about our prior knowledge of the hypothesis which is going to be tested. $P(hyp|x)$, the *posterior p.d.f*, gives the degree of belief for hypothesis ($\theta$) to take values in a certain region given the data $x$. Since it is a p.d.f it must be normalised: $\int_\theta P(hyp|x) = 1$, which determines $P(x)$, considered from now on a normalisation constant. All our knowledge about $\theta$ is summarised on this posterior p.d.f, and therefore it is the one that will allows us to perform the interval estimation that we are looking for.

Since

$$\text{Posterior p.d.f}(\theta) \propto L(x) \times \text{Prior p.d.f}(\theta), \tag{5.12}$$

we have to determine these two p.d.fs. Its is known [23] that when the measurements $x_i$ are Gaussian distributed and independent, which is the case for the CAST data, the likelihood function contains the sum of squares $\chi^2$:

$$\chi^2(\theta) = -2lnL(\theta) + k. \tag{5.13}$$

And therefore from here we can learn that:

$$L(\theta) \propto e^{-\frac{\chi^2(\theta)}{2}}. \tag{5.14}$$

As the function $\chi^2(g^4_{a\gamma})$ has been determined from the set of data taken in CAST (see figure 5.13), the function $L(g^4_{a\gamma})$ is also known. Bayesian statistics supplies no fundamental rule for determining the prior probability $P(\theta)$ as it reflects the experimenters subjective degree of belief about the parameter which is going to be measured before the measurement was carried out. For CAST in principle we do not have any prior belief on the value of this parameter, we only know that it can not take negative values. Therefore the prior p.d.f that we will take is just the function:

$$P(g_{a\gamma}) = \begin{cases} const. & \text{if} \quad g^4_{a\gamma} \geq 0 \\ 0 & \text{if} \quad g^4_{a\gamma} < 0. \end{cases} \tag{5.15}$$

The posterior p.d.f for the TPC data will be given by:

$$p(g^4_{a\gamma}|x) = \frac{e^{-\frac{\chi^2(g^4_{a\gamma})}{2}}}{\int_0^\infty e^{-\frac{\chi^2}{2}} d(g^4_{a\gamma})} \quad \text{for} \;\; g^4_{a\gamma} \geq 0. \tag{5.16}$$

In figure 5.14 we can see a representation of this p.d.f as a function of $g^4_{a\gamma}$.

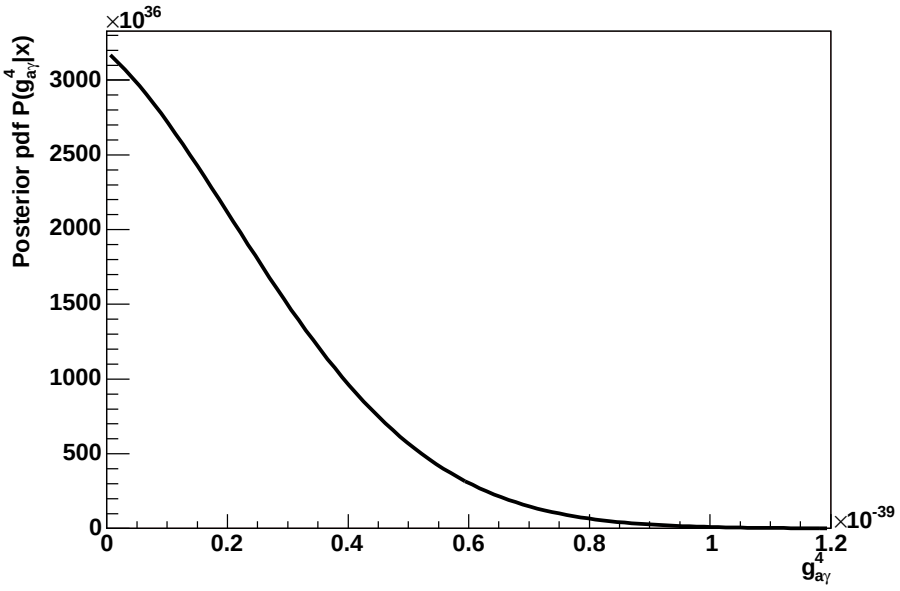


Figure 5.14: *Representation of the normalised joint posterior p.d.f as a function of* $g^4_{a\gamma}$.

Now we want to determine an interval containing all the values of $g^4_{a\gamma}$ for which the integrated posterior probability is bigger than a certain value $1-\alpha$. The lower limit of course is 0, and the upper one will be given by a

$(g^4_{a\gamma})_{\rm upper}$ such that:

$$1-\alpha = \int_0^{(g^4_{a\gamma})_{\rm upper}} P(g^4_{a\gamma}|x)d(g^4_{a\gamma}). \tag{5.17}$$

If the confidence level for CAST is conservatively set on the value 1-$\alpha$=95% then we obtain $(g^4_{a\gamma})_{\rm upper} = 5.7\times10^{-40}\,{\rm GeV}^{-4}$. The upper limit for the coupling constant set by the 2003 data taken in the TPC is therefore

$$g_{a\gamma}(95\%C.L) < 1.55\times10^{-10}\,{\rm GeV}^{-1}. \tag{5.18}$$

In figure 5.15 the TPC 2003 subtracted spectrum together with the function corresponding to the number of photons $N_\gamma$ that we would have detected for the best fit (lower) and the upper limit (upper) values of $g^4_{a\gamma}$ are shown.

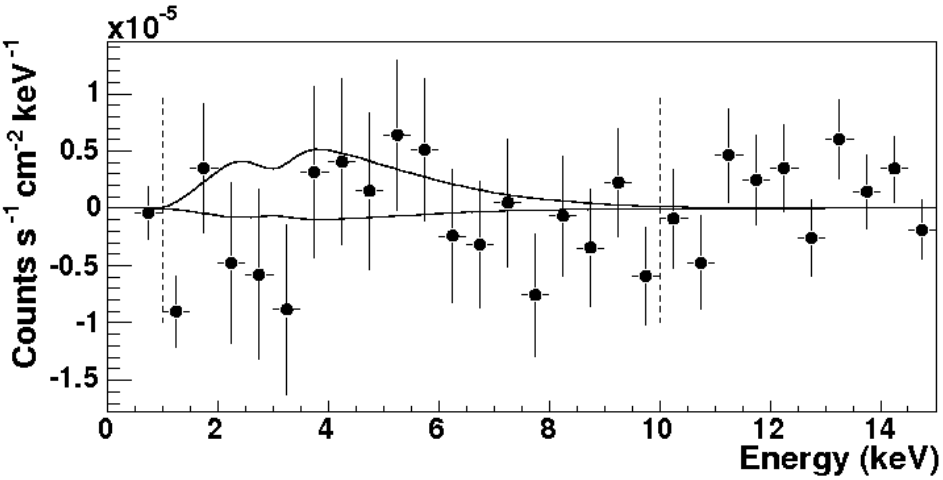


Figure 5.15: *TPC 2003 subtracted spectrum. The function corresponding to the number of photons $N_\gamma$ that we would have detected for the best fit (lower) and the upper limit (upper) values of $g^4_{a\gamma}$ are also shown.*

It must be remarked that this upper limit is only valid for axion masses $m_a < 0.028$ eV as for higher values the coherence axion-photon is lost inside the magnet (see chapter 2). In figure 5.16 we see the exclusion plot of the axion to photon coupling constant $g_{a\gamma}$ versus the mass of the axion $m_a$ in eV, where the blue line corresponds to the upper limit quoted before.

### Systematic effects

The study of all the systematic effects that can affect the result quoted by an experiment is always troublesome. The data must be carefully cross-checked in order to detect any tendency different from the one dictated by statistics, which could hint the action of unexpected or unconsidered dependences of the data. Although a general method on how to detect and handle

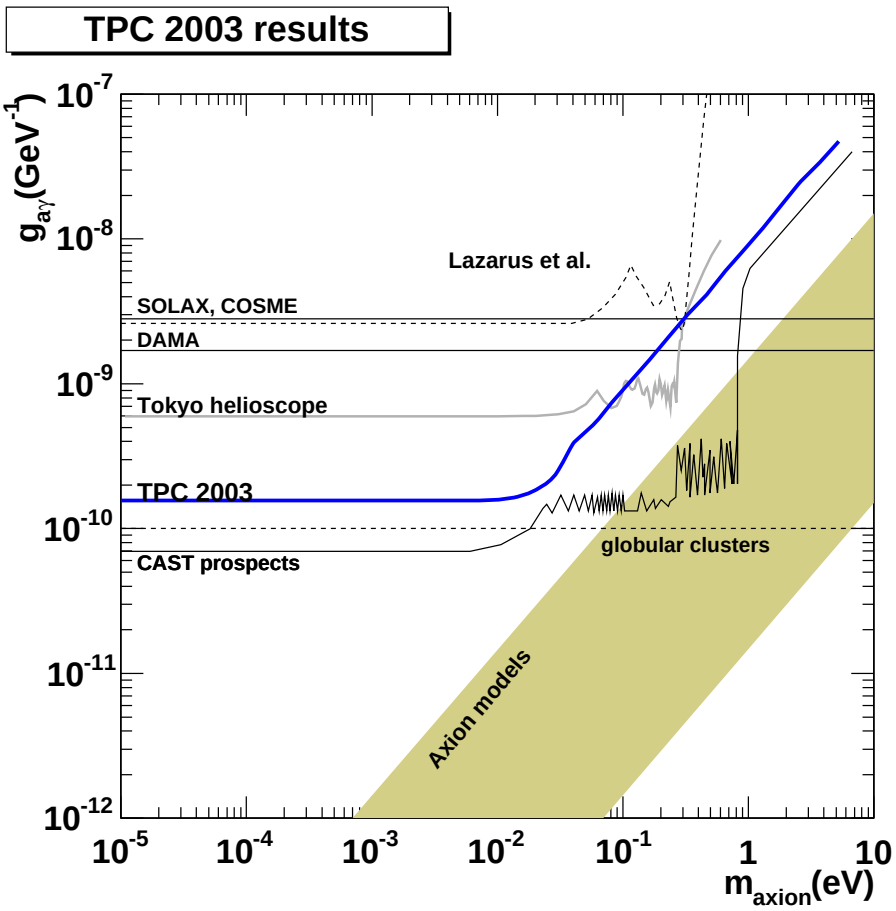


Figure 5.16: *Axion to photon coupling constant $g_{a\gamma}$ versus axion mass $m_a$ exclusion plot. The blue line represents the upper value of $g_{a\gamma}$ obtained with 2003 TPC data. Also the CAST prospects line is shown.*

this systematic effects on the data does not exist, very nice reviews on the matter exists on the literature (see for example [98]), which can guide the experimentalist work regarding this step of the data analysis. The standard procedure involves checks as rebinning the data, splitting the data into subsets, trying to find known dependences of the data to see if their behavior towards them is as expected, or studying all the theoretical and instrumental uncertainties which may affect the final result. x For the 2003 data of the TPC the situation was a little bit special. We do know that there is a very important systematic effect: the position dependence. Because of the magnitude of this effect over the data, of which figure 5.9 is a clear example, there is no point in following the standard procedure described in the former paragraph, as the position dependence will mask any other effect. Furthermore, even if we were able to identify other influences on the data apart from the

known one, their magnitude in any case will be overpassed by it, otherwise they would have become apparent before. It is because of this that *we will be only interested on quantifying the influence of the position dependence on the final upper limit quoted for the CAST TPC and will neglect any other effect*, assuming that the result obtained will be the dominant one.

What is left, thus, is to face the problem of determining what is the possible error on the final result due to the position dependence. Estimating the uncertainty of the background level could be done by determining the maximum percentage of variation seen, for example in figure 5.9, and further propagating this to determine our uncertainty in the upper limit quoted. But the result obtained in this way would be overestimated, since the correction done by means of the weighting method, which makes the real position error on the data much smaller, is not taken into account.

It would be desirable, thus, to estimate the error still left once the weighting method is applied to construct the background spectrum. But a straightforward method to do this just from the data, like the one described in the previous paragraph for only the position dependence uncertainty, is not available in this case. Because of this, it was decided to proceed doing just the opposite: instead of trying to find any deviation on the level of the background data from the Sun tracking one, we will artificially induce them, to see what is their effect on the final result. In this way we will be able to see by how much this level can change giving still a reasonable result (later it will be defined what is this). From this an interval including the possible percentage of background level variation will be defined, which will contain the range which still yields a reasonable result. Therefore, this way we can determine *not an estimation of the uncertainty interval but just an upper limit to it.*

Since no signal is expected in the data collected in the out region of the TPC, and therefore the Sun tracking and the background spectra should match, the study of the systematic uncertainties can profit from this fact using these data. We can artificially vary the level of the background data by some percentage and calculate the values of the $\chi^2_{null}$ in each case. Obviously the bigger the factor we vary the background, the farther this parameter will be from its mean, with corresponds to the d.o.f of the distribution. A reasonable result can be given by a good outcome of the null hypothesis test over these data. Therefore we can conservatively define the allowed variation interval for the background level the one containing the *variation factors which will yield values of* $\chi^2_{null}$ *with a probability of occurring bigger than the 5%.* By looking up the $\chi^2$ distribution tables we find that this condition is satisfied for these values of $\chi^2$ such that $\chi^2/d.o.f < 1.604$. Since for us the $d.o.f$ for the null hypothesis test are 18, we should consider the variation factors corresponding to values of $\chi^2 < 28.9$.

Figure 5.17 shows the distribution of the $\chi^2_{null}$ versus the variation of the background level. The horizontal line corresponds to $\chi^2_{null} = 28.9$, which

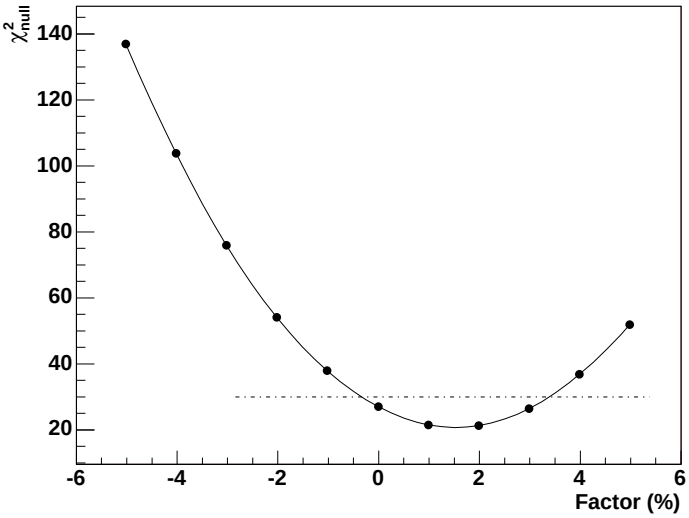


Figure 5.17: *Distribution of the $\chi^2_{null}$ parameter versus variations of the background level.*

is the upper limit of the 95% interval. The interval of the variation factors deduced from here is (-0.3%, 3.3%). As it has been pointed before, it must be underlined that this interval is only an upper limit of the allowed variation for the background level, calculated using a statistical tool. As there is not a simple way of estimating what the weighting method compensation give us quantitatively, we must satisfy ourselves with this upper limit for it. In

| Factor % | $g_{a\gamma}(95\%\,\mathrm{C.L})_{\mathrm{upper\ limit}}$ $(10^{-10}\mathrm{GeV}^{-1})$ |
|---|---|
| -0.3 | 1.58 |
| +3.3 | 1.32 |

Table 5.3: *$g_{a\gamma}(95\%C.L)_{upper\ limit}$ value corresponding to the quoted variation factors of the background data.*

table 5.3 we see the value of the upper limit of $g_{a\gamma}$ at 95% C.L that would correspond to the subtracted spectrum obtained from the 2W area data by varying the background inside the allowed range defined (-0.3%, 3.3%). Our final upper limit on the uncertainty of the background level leads to an upper limit in the uncertainty on the value of $g_{a\gamma}(95\%C.L)_{upper\ limit}$ of a 15%.

Summarising, in section 5.3.2 a hypothesis test that checks out the background constructed with the weighting method using the data from the out zone of the TPC has been performed. The result of this test has been pos-

itive, as the $\chi_{null}$ obtained for our background was lower than 28.9. In the present section, the allowed interval of background variation which leads to values of $\chi_{null} < 28.9$ has been also defined and estimated. This interval has been defined as an upper limit to our background definition uncertainty. It must be pointed out that the allowed interval for background variations depends on the statistics gathered by the data from the out area, as the shape of the parabola in figure 5.17 is determined by them. Therefore the interval for allowed variations and the uncertainty percentage quoted above depend on the characteristics of this area. Because of this we are aware that this hypothesis test gives only an orientative range where the background level should be for it to be compatible with the Sun tracking one, as it should be in the data from the out region.

### 5.3.4. CAST 2003 combined result

In table 5.4 we can see the data sets of the other two CAST detectors, the Micromegas (MM) and the CCD, together with their individual results. They also exhibit a positive null hypothesis test and a best fit value for

| Data set | S-B exposure(h) | $(g^4_{a\gamma})_{\text{bestfit}}$ ($10^{-40}$ GeV$^{-4}$) | $\chi^2_{\text{null}}$/d.o.f | $\chi^2_{\text{min}}$/d.o.f | $g_{a\gamma}(95\%)$ ($10^{-10}$ GeV$^{-1}$) |
|---|---|---|---|---|---|
| MM set A | 43.8-431.4 | $-1.4 \pm 4.5$ | 12.5/14 | 12.4/13 | 1.67 |
| MM set B | 11.5-121.0 | $2.5 \pm 8.8$ | 6.2/14 | 6.1/13 | 2.09 |
| MM set C | 21.8-251.0 | $-9.4 \pm 6.5$ | 12.8/14 | 10.7/13 | 1.67 |
| CCD | 121.3-1233.5 | $0.4 \pm 1.0$ | 28.6/20 | 28.5/19 | 1.23 |

Table 5.4: *Data sets included in the result.*

$g^4_{a\gamma}$ compatible with zero within errors. The fact that three independent detectors, based on different technics, yield compatible results is the best prove of the proper behaviour of each one of them.

To obtain the combined result from the three detectors, the individual posterior Bayesian p.d.f. of each one were multiplied, obtaining this way the posterior p.d.f of the CAST experiment for the 2003 data. From it the $g_{a\gamma}$ upper limit at 95% C.L. can be calculated as described in section 5.3.3. The result is [96]:

$$\mathbf{g_{a\gamma} < 1.16 \times 10^{-10} GeV^{-1}} \quad \text{for } m_a < 0.028 \text{ eV} \tag{5.19}$$

The improvement of this result from the CAST experiment with respect to previous ones is considerable, as it can be seen in figure 5.18. From here we see that the sensitivity of the experiment is comparable with the limit imposed by astrophysical considerations explained in chapter 1.

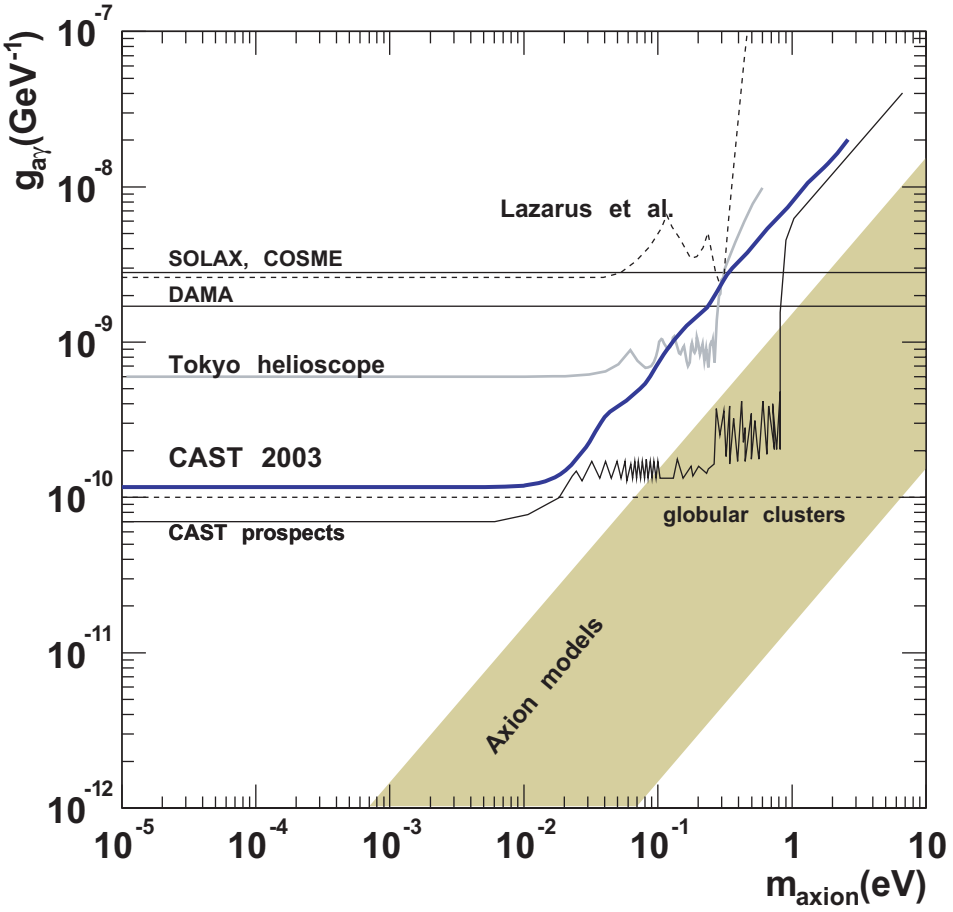


Figure 5.18: *Exclusion plot for the CAST combined upper limit on $g_{a\gamma}$ (95% C.L.).*

# Chapter 6

# 2004 data taking results

The phase I of the CAST experiment was completed with its successful long term operation during 2004. In this chapter the upgrades and performance of both the experiment and the TPC detector will be briefly reviewed. Later the 2004 data behaviour will be exhaustively studied, in order to detect all the systematic effects which can influence the final result. Finally we will proceed with the axion analysis, obtaining a new upper limit on the axion to photon coupling constant $g_{a\gamma}$ since the data of this year was again compatible with the absence of a signal.

## 6.1. 2004 TPC data taking

### 6.1.1. Experiment upgrades and performance

During the 2003-2004 winter shutdown some upgrades were carried out in the experimental area to reinforce the weakest points found during 2003. Thanks to these upgrades the CAST experiment gained in safety and stability, allowing for a smooth and long data taking period in 2004.

The organic crystal scintillator detector, (see chapter 2) was installed behind the Micromegas to search for high energy Primakoff axions, making this the first time that a search of this kind was performed with the axion helioscope conception.

CAST started systematic data taking again in early June 2004, and continued so until mid-November.

### 6.1.2. TPC detection system upgrades

During 2003 data taking period some weak points in the TPC detector were found, namely the thin windows system with its gas leak towards the cold bores of the magnet, and the background rate position dependence, which prevented us from using all the background data gathered. Two major components were added to the TPC detector system at the beginning of 2004: a differential pumping system, and the shielding described in chapter 2.

#### Differential Pumping

The purpose of the differential pumping system is to decrease the effect of gas leaks towards the magnet due to argon diffusion or due to the formation of pinholes in the aluminium layer of the thin TPC windows. This system creates an intermediate volume between the TPC and the magnet which is continuously pumped with a clean pump. This volume is kept at a relatively poor vacuum ($\sim 10^{-5}$ mbar, compared with $\sim 10^{-7}$ mbar in the magnet). A second thin polypropylene window separates this intermediate volume from the magnet vacuum. Due to the small pressure difference, the effective leak through this window is extremely small ($1.46 \times 10^{-7}$ mbar l/s of Argon). This strategy allows us to be reasonably tolerant to small leaks on the TPC windows, improving the robustness of the whole system and thus no external intervention during the data taking period was needed, contrary to what happened in 2003.

#### Shielding

The shielding described in chapter 2 was finally accepted after a commissioning period in 2003, and installed around the TPC in 2004. For this a counterweight was placed on the other end of the magnet to compensate

for the extra weight added, and in some zones the experimental site walls thickness was reduced to allow the TPC plus shielding system to move with no constraint. The improvements obtained thanks to this shielding will be explained later on in this chapter.

### Automatic calibration system

In 2003 the TPC gain was being calibrated by means of pressure and temperature measurements of the gas, which were related to it by equation 5.2. In 2004 a stepping motor was installed to move automatically the $^{55}$Fe source. This motor is fully controllable via TTL signals which are provided by an input/output register VME module controlled by the acquisition software. During normal data taking the radioactive source is parked between the two back calibration windows in a position shielded from the chamber. In 2004, every six hours the acquisition software was sending a signal to stop the data taking and to move the radioactive source in order to take two runs of calibrations, one per window of the TPC.

Figure 6.1 shows the time evolution of the gas gain during the 2004 data taking period. A difference on the gain values for the two windows was

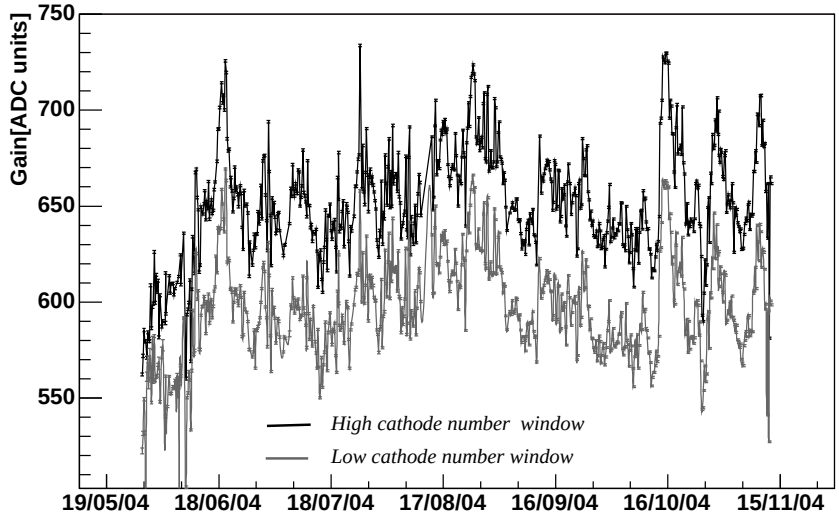


Figure 6.1: *Gain evolution during 2004.*

observed and taken into account in the data analysis. This difference results from geometrical imperfections in the wire arrangement that produce a gain drift along the anodes. Because of this, the gain factor applied to every event was calculated taking into account the position of the chamber where it had been recorded. In this way, given the position of the event in the wires grid,

the corresponding graph of figure 6.1 was scanned to find the gain factor which matches the time given by its timestamp. Between two consecutive experimental gain measurements a straight line was taken to find the closest value for every given timestamp.

### 6.1.3. TPC detector performance

The TPC was already installed with the shielding around it when CAST started to be operational in 2004. In table 6.1 a summary of the sets gathered in this period is shown. During June still some small adjustments were done

| Set number | Date | Comments |
|---|---|---|
| #8 | 02/05-27/05 | First data of the year.<br>Still some adjustments were done on the chamber.<br>Data not used for the axion analysis. |
| #9 | 28/05-13/11 | Long term set.<br>Good quality data. |

Table 6.1: *Summary of the sets accumulated during the 2004 TPC data taking.*

to the chamber, which made the data taken in this period inhomogeneous, and therefore it was not used for the final analysis.

The set# 9 is a very long term one (∼4.5 months) where the data collected were of good quality. Figure 6.2 shows the accumulated time exposure of background and Sun tracking data are shown. As it can be seen ∼203 hours of Sun tracking were collected, a factor of ∼3 more than in 2003. The number of effective days of background gathered is 142.2, a factor ∼5 more than in 2003. Furthermore, we see that both background and Sun tracking data were taken homogeneously in time, with nearly no interruption.

Since in 2003 a dependence of the background rate with the position of the TPC in the experimental site was found, in 2004 the background data taking was done following a strict procedure. In both the morning and the evening, after having tracked the Sun, the magnet was parked in a position close to where it had gone through during the tracking.

The chamber performance during this time was very good, showing the stability required. In figure 6.3 we can see the monitored value of the raw trigger rate (rate of counts directly detected on the chamber, without any filtering) from July till November. Apart from certain deviations from the mean due either to electronic noise pick up (first and last months), or special set of calibrations (mid October) this rate was fairly stable through the whole period of data taking. All these cases where the trigger rate was being well

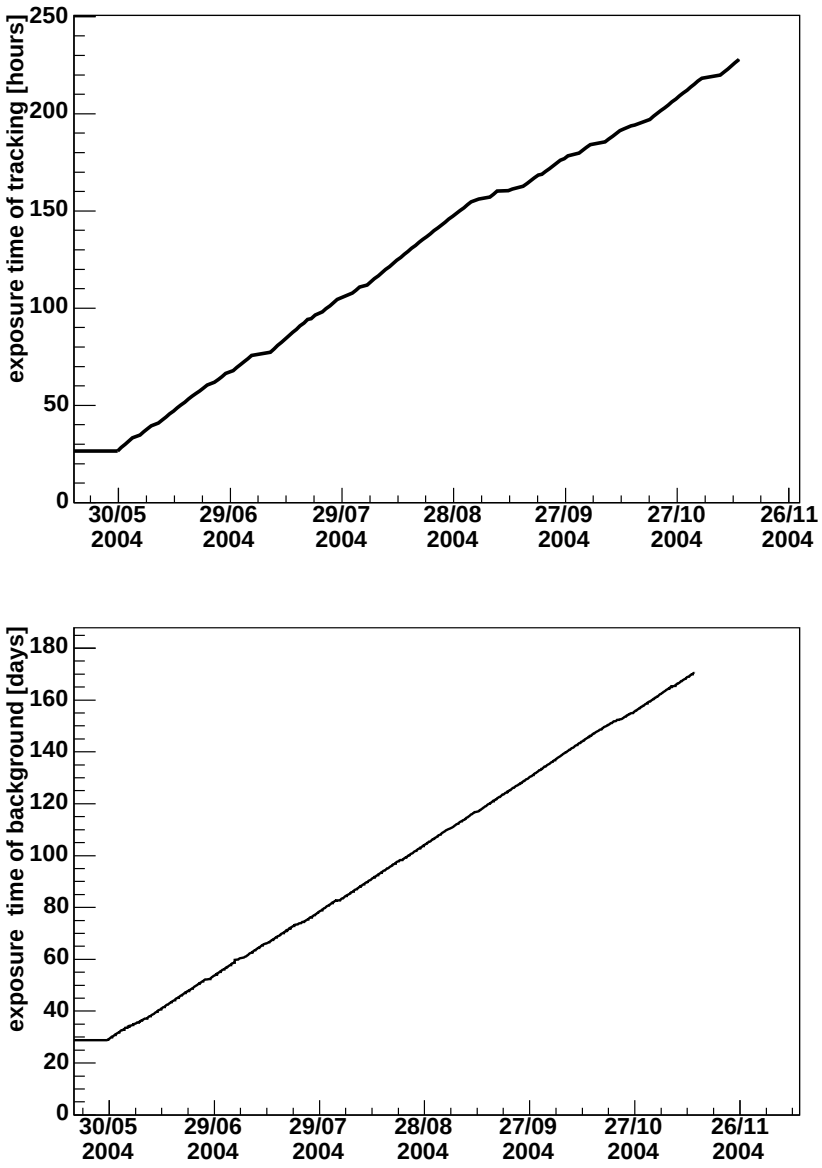


Figure 6.2: *Exposure plots of the Sun tracking and background data in time for the 2004 data.*

far from the mean value were properly identified, being these data excluded from the analysis.

Complementary to this is the time evolution of the dead time, shown in figure 6.4. We see that these two parameters are tightly related, as an increase in the trigger rate also produces an increase on the dead time percentage due to the fact that the system spends more time per second processing information. On the other hand, in mid October there was a problem with the acquisition computer, and the time to process an event increased very rapidly, causing the dead time to increase also and the trigger rate to decrease, since the time the electronics was blind to new events was higher. In general the dead time was fairly stable trough the whole period as well, with an average value of 1.75 %.

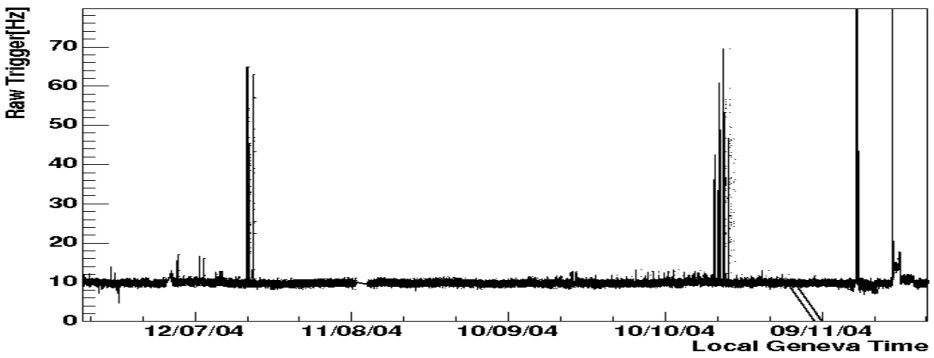


Figure 6.3: *Raw trigger rate evolution from July till November 2004.*

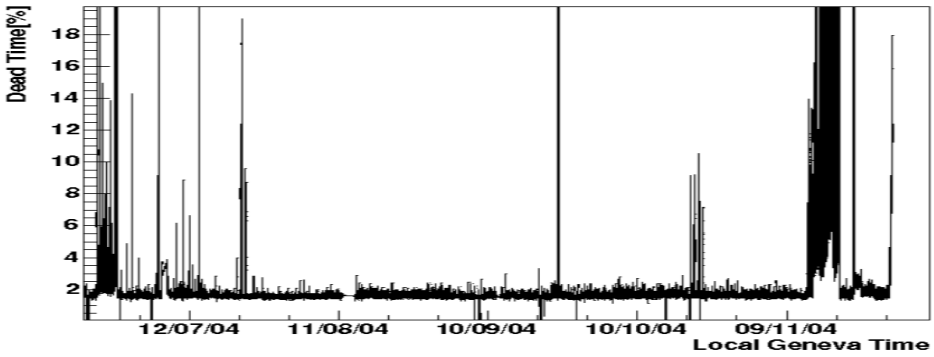


Figure 6.4: *Dead time evolution from July till November 2004.*

## 6.2. 2004 TPC data

### 6.2.1. Data improvement due to the shielding

With the shielding installed around the chamber, the TPC background level between 1 and 10 keV was (4.15±0.01) $\times 10^{-5}$ counts/keV/s/cm$^2$, a factor of $\sim$ 4.3 below the level reached by the TPC without any shielding. This reduction increases with energy (reduction factor of $\sim$ 6.4 in the 6-10 keV range). The observed background energy spectra for the with and without shielding cases are shown in figure 6.5, as well as for an intermediate configuration of only copper box and $N_2$ flux. In 2004 the data proved to

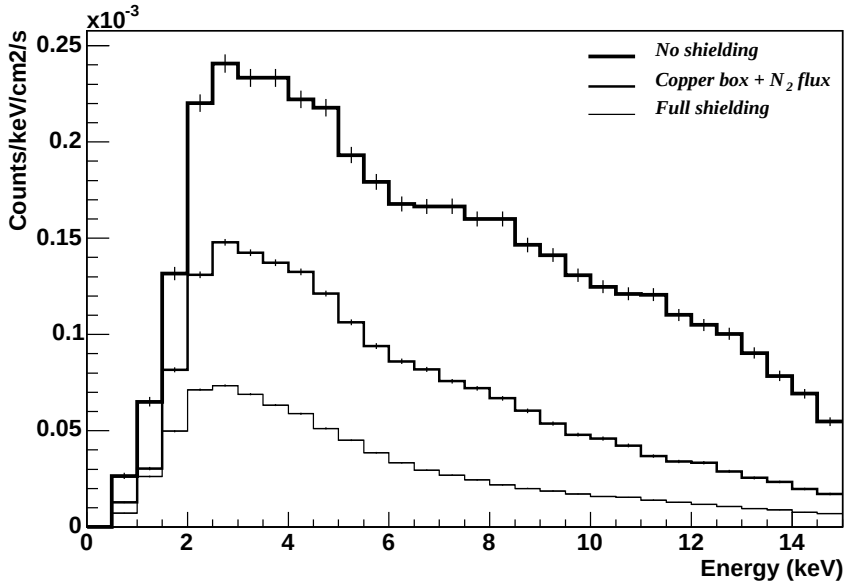


Figure 6.5: *Background spectra for the TPC detector in different shielding conditions.*

have a level of spatial homogenisation higher than in 2003 as it can be seen in figure 6.6. Here the comparison between 2003 data collected in the different positions of the coarse grid (upper row) with the data taken in 2004 for the same positions is shown. Being both the reduction and homogenisation obvious.

### 6.2.2. 2004 data behaviour

A step previous to the axion analysis with these data requires to understand their behaviour properly, determining all the factors to which they can be sensitive to. The shielding proved to reduce the level of the background

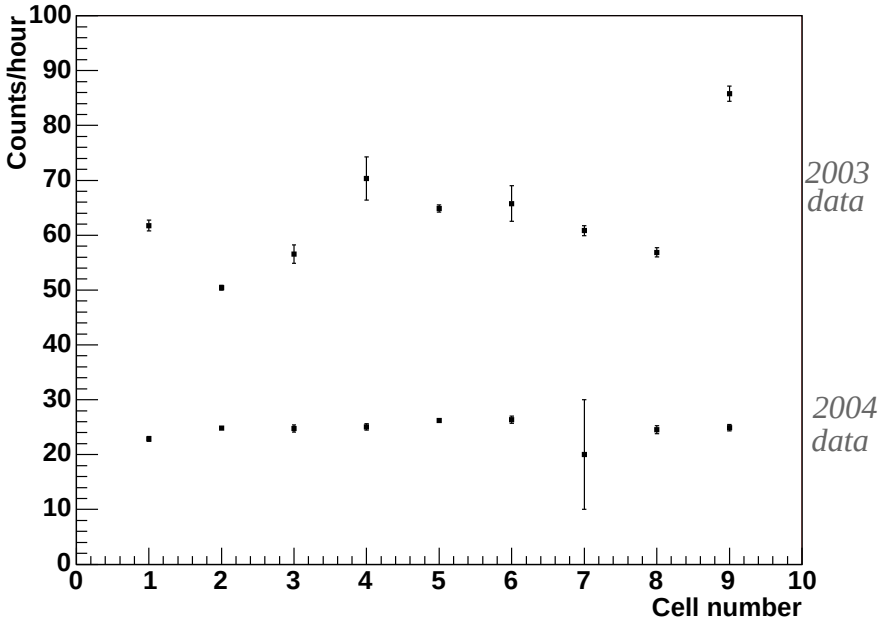


Figure 6.6: *Comparison between 2003 and 2004 background data, taken in different positions in the experimental site. The 9 cell numbers run for 3 horizontal values, and for each one, for 3 vertical positions.*

and this effect, together with the fact that ∼5 times more statistics in data taking was gathered in 2004, opens the door to the observation of new phenomena in the data behaviour. Therefore, a careful study of all the possible factors that could have any influence in the data is mandatory, so that we can ensure the background data can be subtracted to the Sun tracking one without being sensitive to any systematic effect because of this. Therefore, in what follows the possible dependence of the data with some environmental factors (detector position, rate time dependence, magnet status) will be studied.

### Position and time dependence

**A quick look.** In 2003, due to the magnitude of the background level dependence with the relative position of the detector in the experimental area, a weighting method was used to construct an effective background. For the 2004 data we wonder by how much the shielding reduces this position dependence, and whether still there is any need of constructing a weighted background.

From what it has been said in the previous section, we could expect that the position dependence, as it was understood for the 2003 data, has

disappeared to a big extent. To check this, the first thing to do is to compare the Sun tracking and the background energy spectra from the data taken in the out area of the TPC, as no signal is expected, and therefore both spectra should be compatible. In figure 6.7 such comparison is shown. The

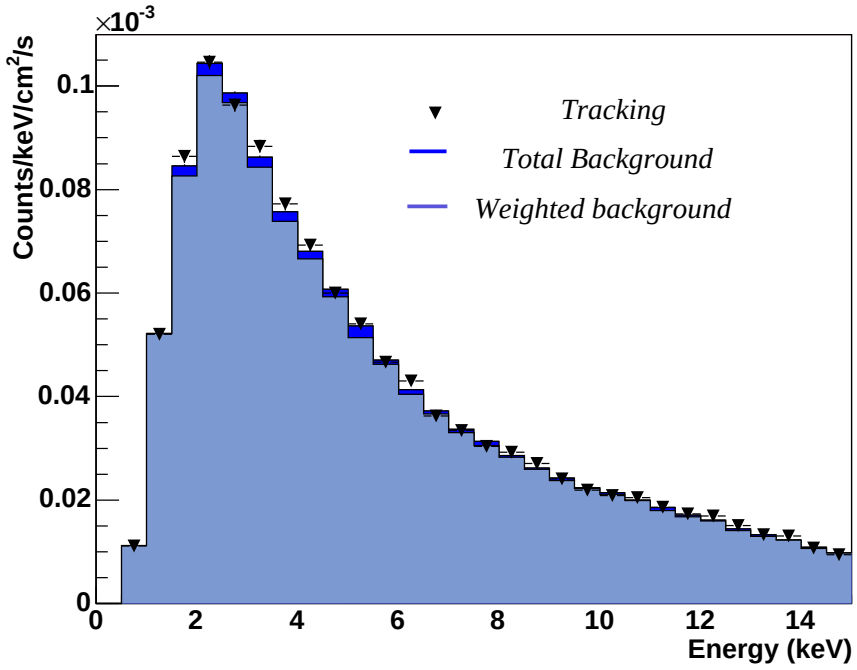


Figure 6.7: *Comparison between the Sun tracking energy spectrum (markers) and the total (dark blue) and weighted (light blue) background spectra for the data taken in the out area of the TPC.*

agreement here is, within the statistical fluctuations, good between them. Therefore, the huge discrepancy between the background spectrum and the Sun tracking one seen in 2003 (figure 5.6) is not here anymore, thanks to the effect of the shielding.

Bearing this in mind, we can think that a weighting method is not needed anymore. Just for comparison in figure 6.7 the weighted background (fine-bin) has been also included. Both Sun tracking and total background seen to be systematically above this spectrum. Furthermore, the weighted spectrum seems to disagree with the Sun tracking one more than with the total background spectrum, while we would have expected just the opposite as it happened in 2003.

From here we can deduce that the weighting method used for 2003 is not useful anymore in 2004, as it seems to yield an effective background which does not match the one collected during the Sun tracking periods. From this

we can think that other effects which have not been taken into account yet are playing an important role here.

**Time dependence** During 2004 data taking period, a variation of the level of the background with time was observed. The upper plot in figure 6.8 shows the evolution of the event rate from 3-7 keV, after all the filtering process. Here a clear variation above the statistical fluctuation from the mean value is visible. It would be desirable to understand up to some extent which factor (or factors) we are sensitive to, despite the shielding, to produce such a variation. In principle the source (or sources) could have two different origins:

- Parameters to which the efficiency of the chamber is sensitive to.
- Parameters to which the environmental background level itself is sensitive to.

Regarding the first case, as it has been explained in chapter 3, there is only one known main parameter to which nearly all the gaseous detector's relevant characteristics, such as drift velocity, diffusion coefficients or gain are related to, the gas density, the latter one being most sensitive to its variations. It is in order to correct the effects of these natural variations in the gas density that, during all the data taking period, experimental calibrations were being taken every 6 hours. This allowed us to characterise the gain variations of the chamber with very good precision (figure 6.1) and to correct the events gathered accordingly. Therefore, there is no reason to believe the first option is the one that should be taken under consideration. Moreover, the other two CAST detectors observed also variations on their background level detected, and these two hints certainly lead us to consider the second option as the most feasible one.

Trying to correlate this variation with any parameter recorded in the experimental area, it was found that, to some extent, it could be related with the temperature measured inside the shielding, shown in the lower graph of figure 6.8. The CAST experimental area is being continously ventilated to keep the temperature as constant as possible. The big variations seen in May and June are due to the fact that the ventilation system was not yet connected, the sudden drops appearing when the TPC acquisition electronics was switched off. From mid-June and on the temperature value remained fairly constant, having a long term decreasing tendency.

To check this apparent relation we can have a closer look to some shorter periods of data: in figures 6.9, 6.10 the rate evolution is shown from mid-May to mid-June and from mid-October to mid-November in the upper plots respectively, while the lower ones shown the temperature recorded for each one of these two periods.

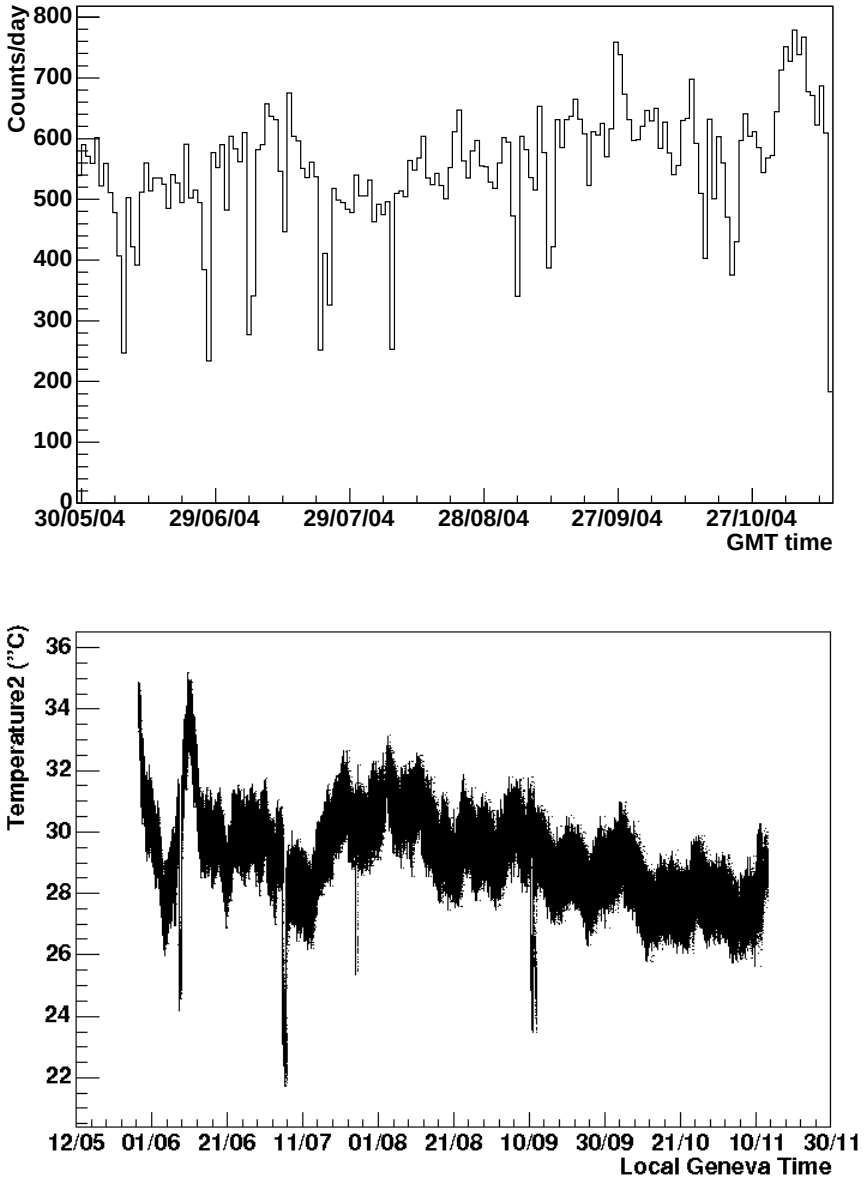


Figure 6.8: *Up: Time evolution of the counts rate per day during 2004 data taking. Down: Temperature time evolution measured inside the shielding.*

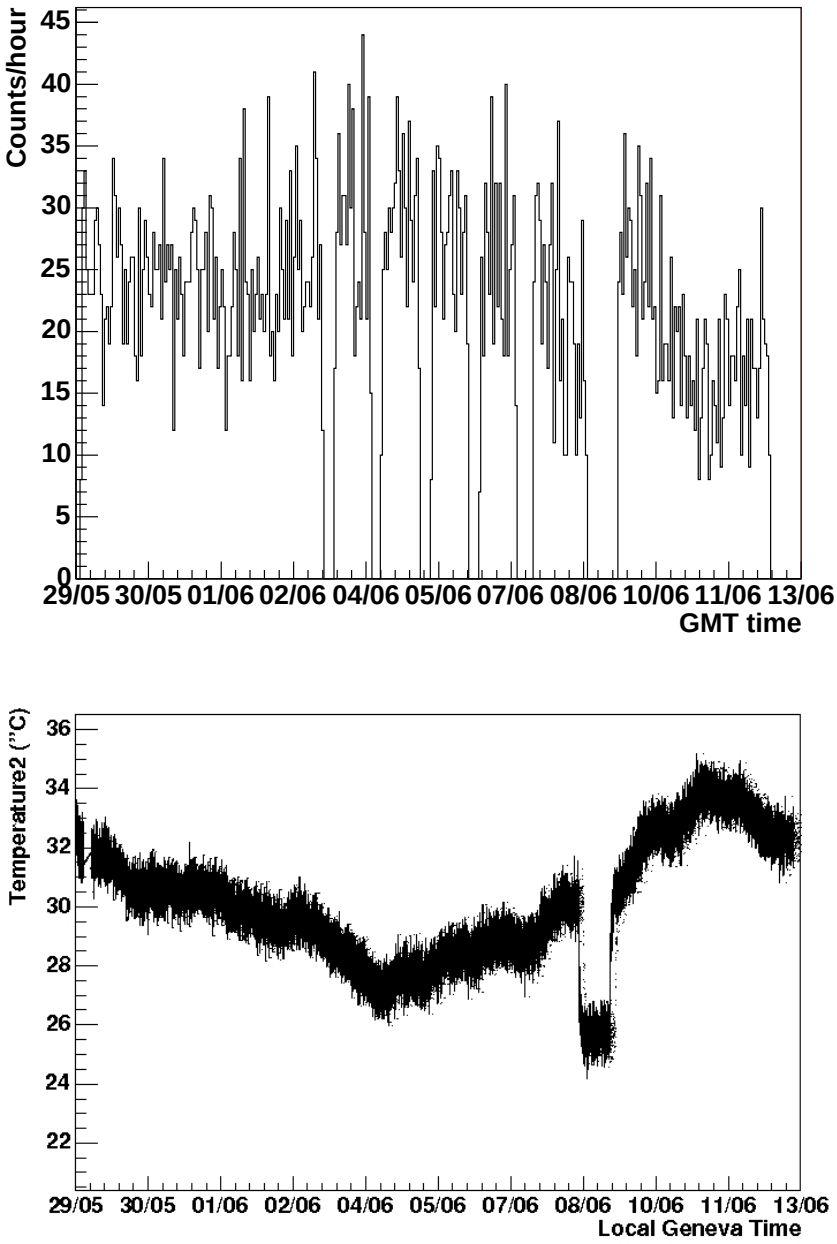


Figure 6.9: *Up: Time evolution of the rate of counts per hour from mid-May to mid-June. Down: Temperature time evolution measured inside the shielding for the same period.*

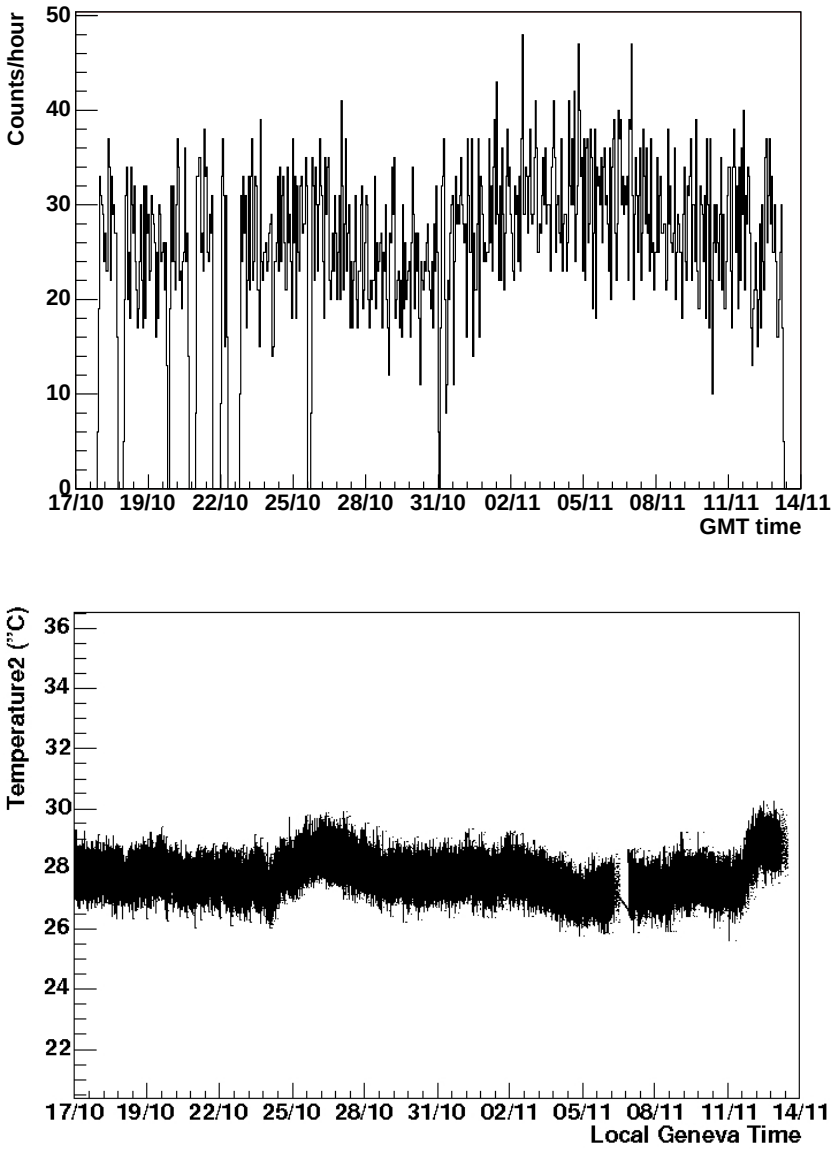


Figure 6.10: *Up: Time evolution of the rate of counts per hour from mid-October to mid-November. Down: Temperature time evolution measured inside the shielding for the same period.*

While in the first set of plots a close dependence between these two parameters becomes evident, in the second one we see that the rate varies but the temperature remains constant. None of the other recorded parameters in the experimental site have been found to be related with this variation seen in the last months of data taking. Therefore it is clear that its origin is complex and comprises several different causes.

Up to now we have proven a fluctuation of the background level with time and now it arrives the question of by how much this time-dependence by itself could influence our result.

In principle we could think that, if these variations are long term ones, as it seems to be the case from figure 6.8, they will affect both Sun tracking and background data in the same way, leading then to a natural correction. This would not be completely true if during long periods of time background data were being taken, but not Sun tracking ones, due maybe to technical stops in the experiment, such as quench recoveries. In this case this natural compensation would be broken and an offset between Sun tracking data and background ones could appear. But if we recall figures 6.2, where the amount of Sun-tracking and background data gathered over time are represented, we see that this happens not to be the case.

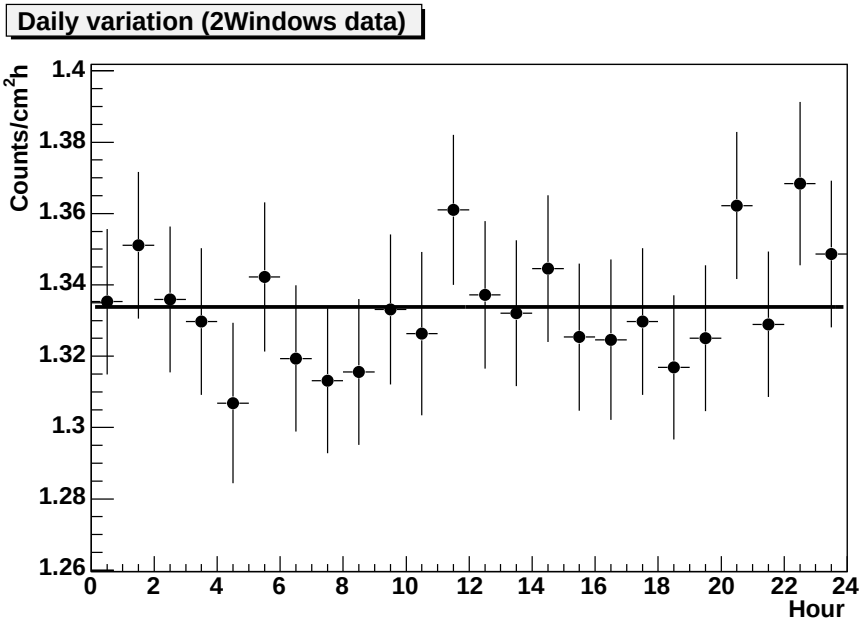


Figure 6.11: *Daily pattern of the data gathered in the 2W area of the chamber in set #9 with energy between 1 and 10 keV. The horizontal line represents the mean of these data.*

In the case where these variations were taking place with a daily pattern, the Sun tracking data -which for the TPC is always being taken in the

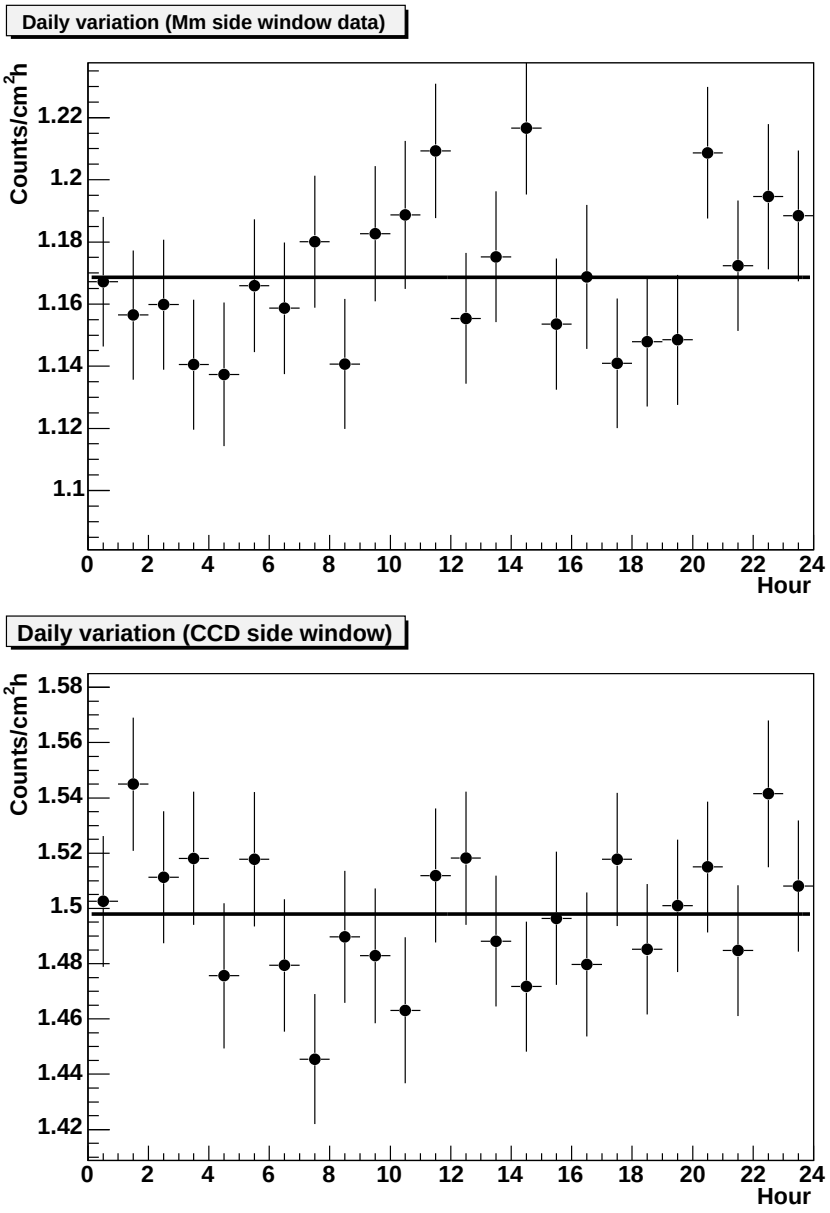


Figure 6.12: *Daily pattern of the data gathered in both windows of the chamber in set #9 with energy between 1 and 10 keV. The horizontal line represents the mean of these data.*

evening- would be incompatible with the background ones -taken during the rest of the day-, and then we should be more careful in our analysis. To ensure that this is not the case, the daily variation of the data was plotted, representing all the data taken in the 2W area of the TPC in set #9 with energies between 1 and 10 keV (figure 6.11). The horizontal line represents the mean of these data points. The $\chi^2$ parameter of these points around the media can be calculated, in order to see if it yields a value where $\chi^2/d.o.f \sim 1$. In table 6.2 results of this calculation are shown. Although the value of $\chi^2/d.o.f$ for the horizontal line hypothesis is good, in this figure a hint of a tiny sinusoidal variation can be seen. To crosscheck this pattern, the data gathered in each window have been also plotted independently, as it can be seen in figure 6.12. The means and the $\chi^2/d.o.f$ quotients for the data of each of the windows are also shown in table 6.2. From the values shown in the table we can conclude that there is no pattern followed by these data, apart from the statistical deviation from the mean, and therefore there is no daily-varying factor, such as the time-dependence or any other unknown one, to which the TPC is sensitive to.

| **TPC region** | **Mean** | $\chi^2$**/d.o.f** |
|---|---|---|
| 2W | 1.334 $\pm$ 0.004 | 12.79/23 |
| Window 1 | 1.169 $\pm$ 0.004 | 26.61/23 |
| Window 2 | 1.498 $\pm$ 0.004 | 21.71/23 |

Table 6.2: $\chi^2$ distribution value around the mean for different chamber regions.

**Position dependence** From the comparison between Sun tracking and background data collected in the out area of the TPC, where no signal is expected (figure 6.7), we have seen that there is no dependence on the data leading to a discrepancy as seen in the 2003 data. But still we do not know whether there is any remaining position dependence despite the shielding. In order to study this, we can try to search for any position variance on different subsets of data where the time variation can be considered fairly homogeneous, ensuring this way that both effects will not mix up. Furthermore, the minimum amount of data used for these subsets should be at least one month, so that the statistics gathered in the different positions of the TPC is enough to observe any positional variation. Two intervals have been defined with these characteristics, listed in table 6.3 and shown in figure 6.13.

In figure 6.14 we can see for these two periods of time the dependence of the background level with the position of the detector in the experiment. Here the black line corresponds to the data taken in the out area of the chamber, while the red one matches the 2W area data. The value represented is the mean of the normalised counts measured between 2 and 10 keV. The

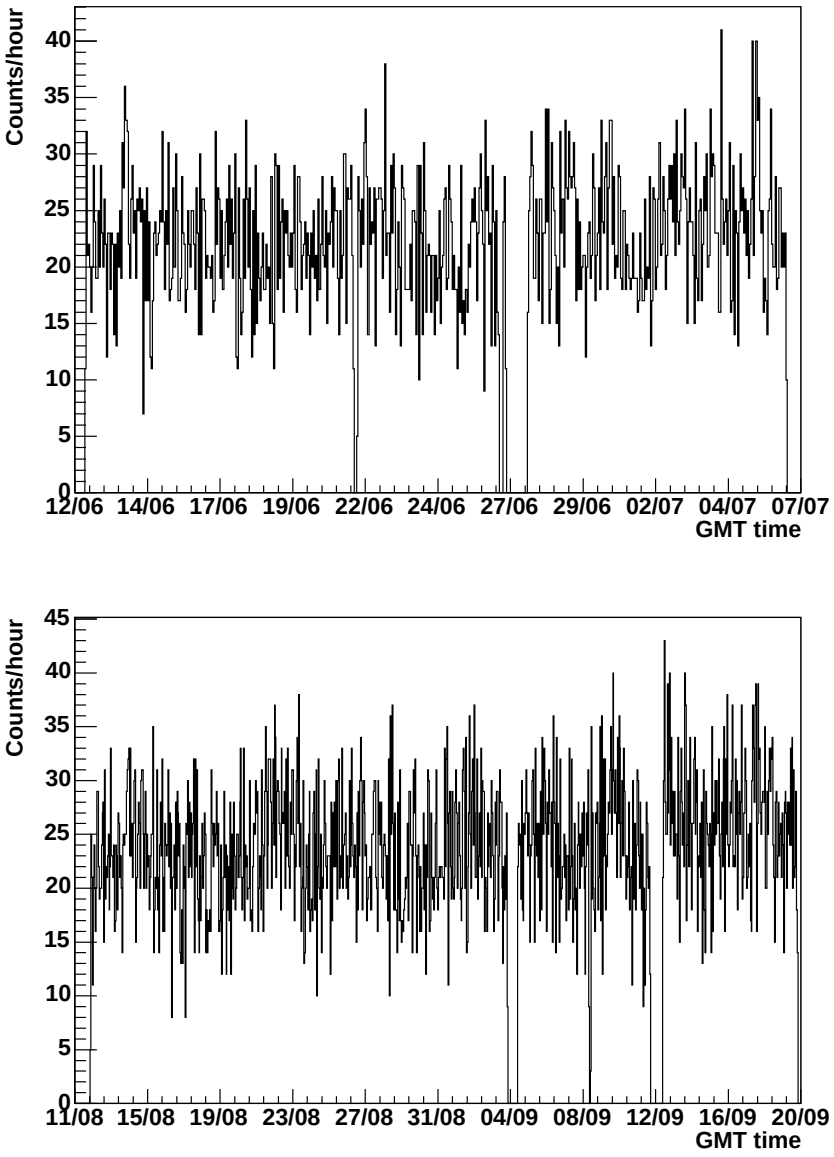


Figure 6.13: *Rate evolution in the two time intervals chosen.*

nine different locations of the TPC in the experiment shown in the x-axis correspond to the nine cells drawn in the coarse grid of the experimental area.

These figures tell us that the tendency followed by the data both in the 2W and out areas is similar. It seems also that the points scatter more from the mean than what would be expected taking only statistics into account. One way to find quantitatively any variation out of the statistical errors is to calculate the $\chi^2$ distribution of these points around the mean, as it has been done also to search for a daily pattern. If there were a systematic deviation due to a position dependence, it would be reflected in a value of $\chi^2/d.o.f > 1$, being 8 in this case the degrees of freedom (9 points minus the mean). The fact that the error bars are different in every point could lead

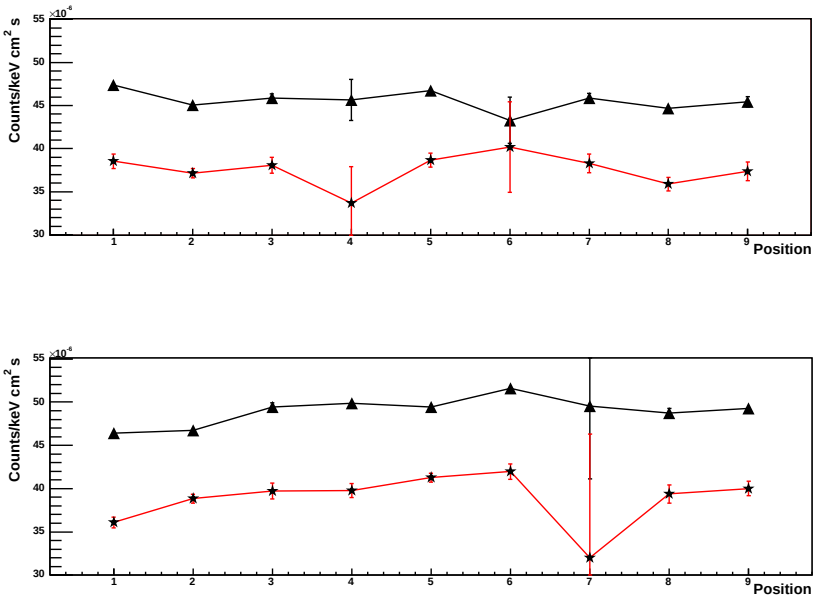


Figure 6.14: *Background level for 9 different experiment zones and different periods of time. The black line represents the data taken in the out area of the TPC, while the red one matches the 2W area data.*

us to a fake value of the mean if we were calculating it in the conventional way. In this case a *weighted mean* is the most appropriate parameter, where the points with a big error bar contribute less to it. From [23] we have the definition of this mean and its average error:

$$\bar{x} \pm \delta\bar{x} = \frac{\sum_i \omega_i x_i}{\sum_i \omega_i} \pm \left( \sum_i \omega_i \right)^{-1/2} \quad \text{where} \quad \omega_i = 1/(\delta x_i)^2 \qquad (6.1)$$

Here $i$ runs over the points that we want to calculate the mean from, in our case $i = 1...9$. Once this value is known, the $\chi^2$ is calculated in the standard way:

$$\chi^2 = \sum_i \omega_i (\bar{x} - x_i)^2 \tag{6.2}$$

In table 6.3 these values are summarised both for the 2W and for the out zones data. The difference in the means for the two periods is indeed a hint of the time-dependence on the data explained before. The numbers obtained

| # | **Start-End** | **Mean** ($\times 10^{-5}$**c/kev/cm**$^2$**/s**) | | $\chi^2$**/d.o.f** | |
|---|---|---|---|---|---|
| | | 2W | out | 2W | out |
| 1 | 12/06-07/07 | 3.75 ± 0.03 | 4.56±0.01 | 10.27/8 | 31.36/8 |
| 3 | 11/08-19/09 | 3.94 ± 0.02 | 4.85±0.01 | 54.17/8 | 149.89/8 |

Table 6.3: $\chi^2$ *distribution value around the mean for the two time intervals defined.*

for the data in the out area, where we have more statistics, tell us that indeed there is a deviation from the mean beyond statistics . We see also that in both plots of figure 6.14 the tendency of deviation from the mean is by far very different in both of them. If this deviation were fully due to a position dependence we would expect that it should be coherent in both plots, since we would be seeing the same effect. But this is not the case, and we are lead to think that, at least, part of what we are seeing here is the ubiquitous time variation. Even though the chosen intervals look fairly stable, the data are telling us that indeed this is not the case.

Even if smaller time intervals are used, the time effect still plays a role here, and no hint of a position dependence is found. Therefore we can conclude that, *even if a position dependence is present in these plots, its level is really small in comparison with the time dependence effect, which in 2004 data is the dominant one.*

### Experimental conditions

The basic principle to ensure the compatibility between Sun tracking and background data is that both of them are taken under the same experimental conditions. Although this idea might look obvious, from the technical point of view some very basic checks are required, as this condition is not always satisfied. The data gathered when following the Sun were taken when the magnetic field inside the magnet was on (there is a current flow of at least 13,000 A), the valves between the detector and the magnet bores were open, and of course the whole structure composed by the magnet and the girder that holds it was moving. On the contrary, when the background data were taken, the magnet most of the time was steady, and during some (small) part

of this time the valves were closed and the magnet was off. Therefore we should study the influence of these factors on the data to consider if further refinements are required.

**Magnet movement** To test the possible influence of the motors in charge of moving the 50 ton structure holding the magnet on the data taken, we can use again the data from the out area of the TPC. The Sun tracking spectrum contains only data collected when the motors were on, while the background one is mostly composed from data gathered with the magnet standing still. In principle both spectra should be compatible and therefore, if electric noise were induced by the motors on the data, it would be reflected on a difference, mostly at low energies, between them.

The $\chi^2$ parameter of the Sun tracking minus background energy spectra with the zero line hypothesis will tell us about the accuracy of the no-noise hypothesis. Figure 6.15 shows this subtracted spectrum, together with the zero line. The fit yields:

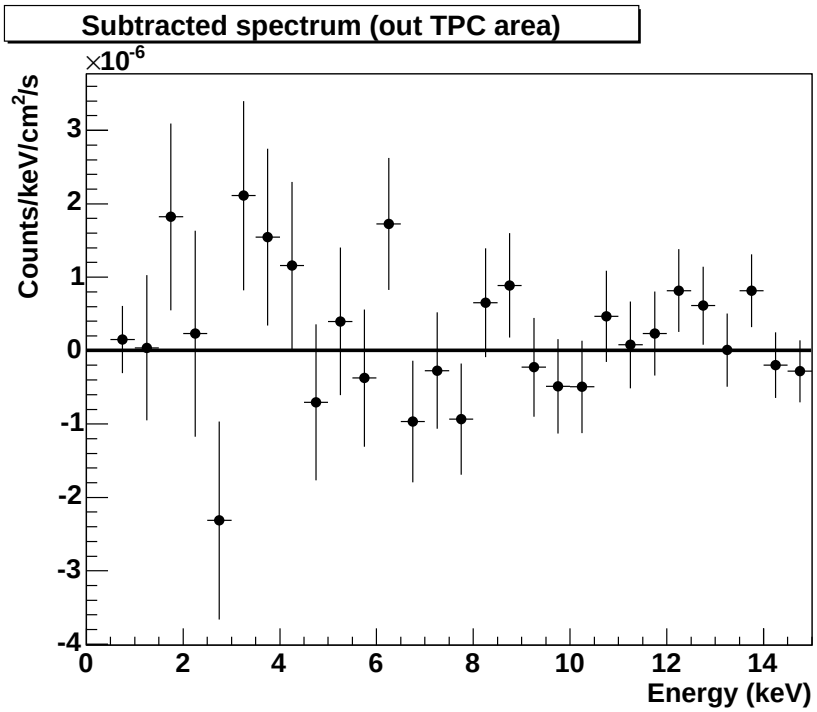


Figure 6.15: *Subtracted spectrum from the data taken in the out area of the TPC.*

$$\chi^2/d.o.f = 28.69/29 \tag{6.3}$$

which clearly hints no systematic effect on the data.

Indeed, this can be considered as a test of the non existence of any other unknown or unconsidered effect apart from the magnet movement, which could influence the data.

**Magnet status** As the data from the out area are completely isolated from the magnet bores, it cannot be influenced by their status. Therefore we still have to consider a possible dependence of the 2W area data on the valves and magnet status. In figure 6.16 a graphic comparison between the total background (thick black line) and the one built only with the background data collected when the magnetic field was on and the valves in the TPC side were open (thick red line) is shown. For comparison purposes, the Sun tracking spectrum is also plotted as a continuous thin black line. From here

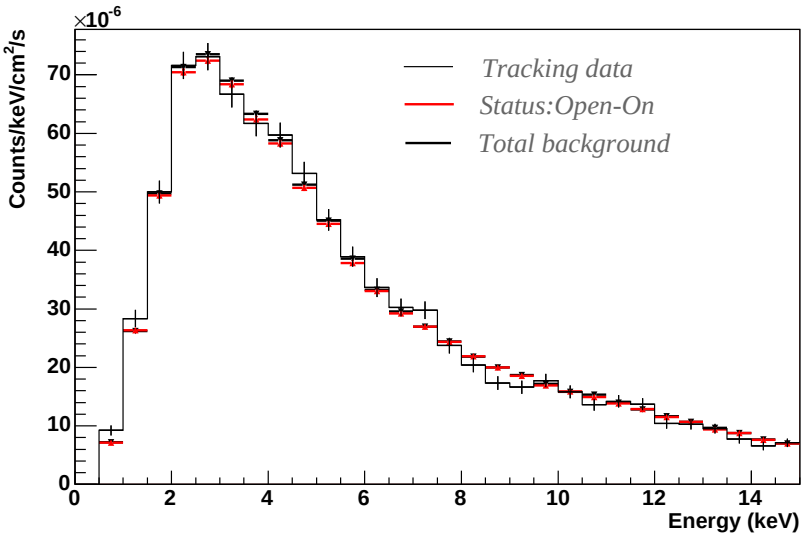


Figure 6.16: *Comparison between the tracking spectrum (continuous line) the total background (thick black line) one and the background taken only when the magnetic field is on and the valves are open (thick red line).*

we see that indeed the *Open-On* background is systematically lower than the total one, although the difference is very small in comparison with the Sun tracking spectrum, to which both of them are compatible. In table 6.4 we have the time in hours that the magnet system has spent in every situation. In order to understand why the Open-On background is systematically lower than the total background one, in figure 6.17 we see a comparison between the total background energy spectrum (thin black line again) and different magnet conditions (thick black and red lines). In the upper one the valves are in both cases closed, and the only difference lies in the magnet being energised or not. In the lower plot we have same situation with the difference that in

| | | Valves status (hours) | |
|---|---|---|---|
| | | **Open** | **Closed** |
| **Magnet status (hours)** | **On** | 2617 | 34.25 |
| | **Off** | 378.52 | 358.13 |

Table 6.4: *Time that the magnet system has spent in the different conditions.*

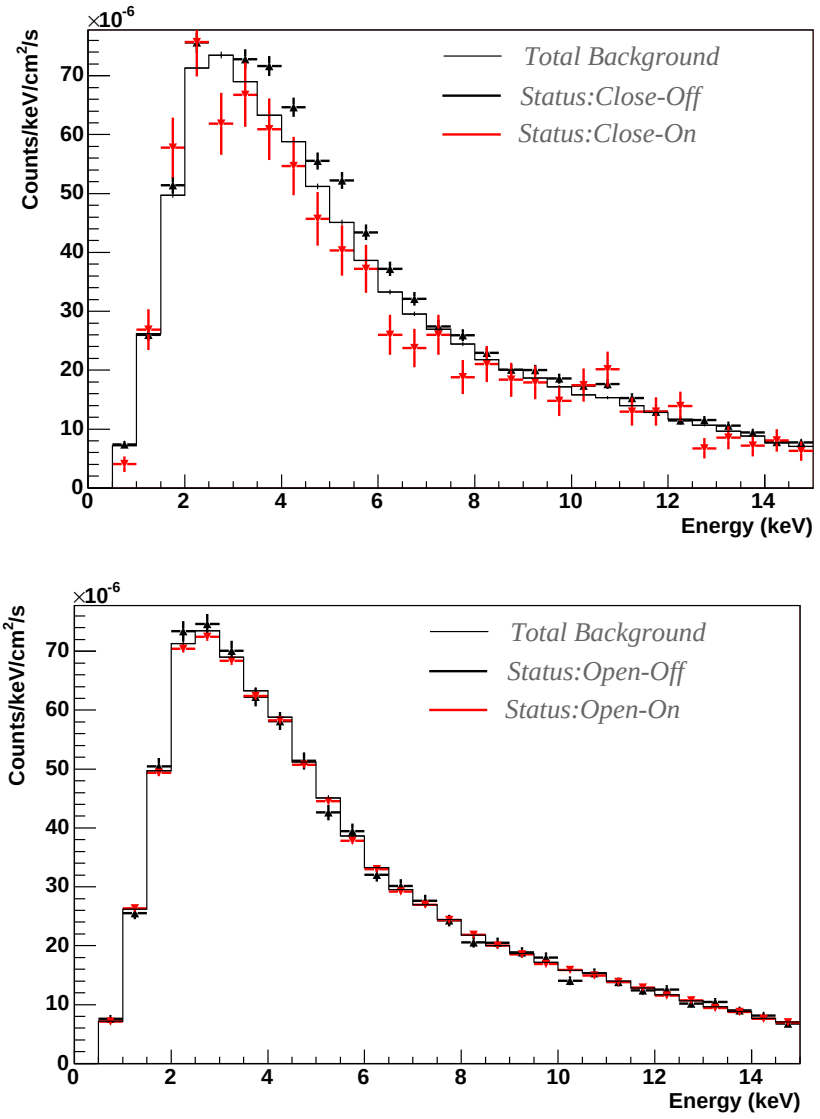


Figure 6.17: *Comparison between different magnet system conditions.*

this case the valves are open. In these two plots we see that when the valves are closed it seems that the magnet being energised makes a difference, while when the valves are open this is not the case. This in principle does not make any sense, and the real explanation to what is seen in these plots comes is in the previous sections. These spectra are composed from data collected in different magnet conditions, but also in different times and positions, and it is therefore natural that they show different average levels.

During 2004 the Sun was daily being tracked for the TPC, except in the case of a magnet quench (see chapter 3), the movement was stopped for one or two days. During this time no data were collected tracking the Sun, but the background data taking were remaining. Somehow this may introduce small gaps in the time dependence Sun tracking-background data compensation mentioned in section 6.2.2. Since during the time of a magnet quench recovery the valves are closed and the magnet is off, it seems natural to assume that the overall Open-On background spectrum is the one we should use then to compare with the total Sun tracking one, as both will suffer from the same temporal gaps. Therefore, for the axion data analysis when referring to the background spectrum, we will mean the Open-On one.

## 6.3. Data analysis

Up to now all the possible dependences of the data on the most influential environmental factors have been carefully studied. No significative deviation of the background from the Sun tracking data has been found, and the long term variations have been identified and found not to be relevant for the axion analysis. Therefore we can safely proceed subtracting the Open-On background data to the Sun tracking data in order to obtain the subtracted spectrum, which is the starting point for the axion analysis, as it has been already done for the 2003 data in chapter 5.

### 6.3.1. Null hypothesis test

Figure 6.18 shows this final subtracted spectrum, together with the null hypothesis line. A quick look states that both are compatible within statistical errors. This is mathematically confirmed by the $\chi^2$ parameter obtained from the fit:

$$\chi^2_{null}/d.o.f = 18.67/18 \tag{6.4}$$

As in the analysis of the 2003 data, the vertical dotted lines delimit the 1 to 10 keV energy range where all the axion analysis is performed, ignoring the points outside it since the expected solar axion energy spectrum ranges also from 1 to 10 keV approximately.

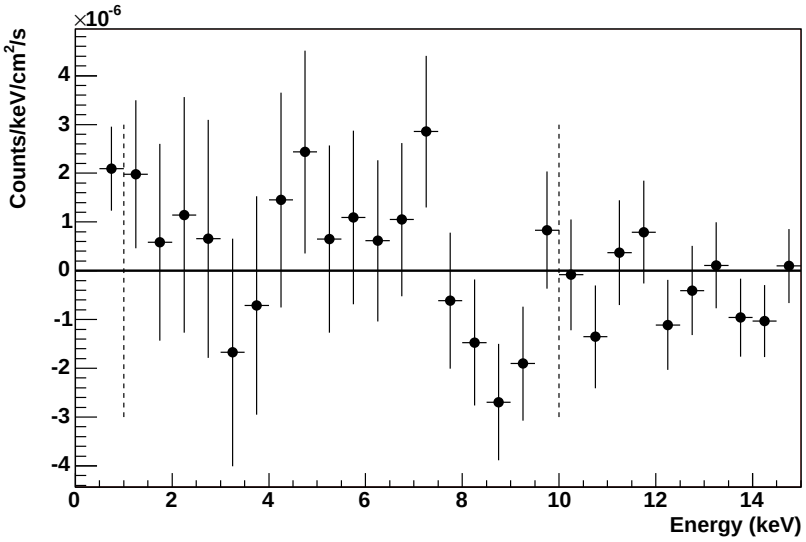


Figure 6.18: *Subtracted spectrum and the null hypothesis line.*

### 6.3.2. Best fit and errors

To calculate the best fit value of $g^4_{a\gamma}$ we will proceed in a similar way as it was done with the 2003 data. First the theoretical normalised energy spectrum of photons coming from the conversion of axions in the magnetic field that would have been detected by the TPC is calculated, as a function of $g^4_{a\gamma}$. The subtracted spectrum is fitted with this theoretical one, and then the value of $g^4_{a\gamma}$ which minimises $S(g^4_{a\gamma})$ is found, which will give us the theoretical photon spectrum curve that best fits the 2004 obtained data. It is expected that this final curve will be very close to the zero line, which represents the no axion hypothesis, if we are to be consistent with the null hypothesis test.

In figure 6.19 we can see the subtracted spectrum with the best fit curve on it. The best fit value obtained is:

$$(g^4_{a\gamma})_{min} = (1.04 \pm 1.0(stats)) \times 10^{-40}\ \text{GeV}^{-1} \ \text{ with } \ \chi^2_{min}/d.o.f = 17.06/17 \tag{6.5}$$

In this case the value obtained is positive within $1\sigma$ error. It is known that the definition of one standard deviation tell us that, just due statistical fluctuations, only 64% of the data collected should fall into the range covered by it. It can easily happen that the 2004 best fit result obtained belongs to the other 36% data group which are further from the true value more one standard deviation. The fact that none of the other two CAST detectors has a similar result hints that this explanation is the preferred one over the fact that maybe we could be seeing a trace of an axion signal.

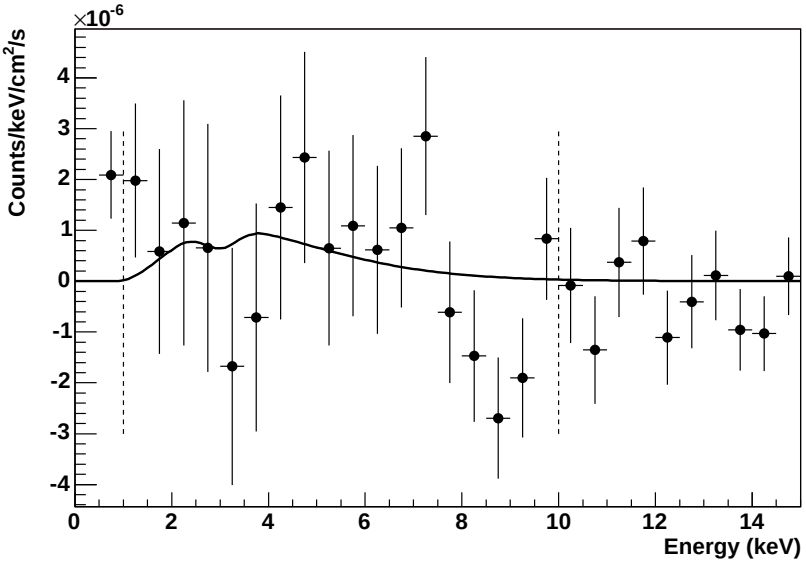


Figure 6.19: *Subtracted spectrum together with the best fit curve.*

### 6.3.3. Confidence interval extraction

Again, proceeding in a similar way as we did with the 2003 data in order to extract an upper limit value of $g_{a\gamma}$ with a 95% confidence level (C. L.), we are lead to the result:

$$g_{a\gamma}(95\%) \leq 1.29 \times 10^{-10}\ \mathrm{GeV}^{-1} \quad \text{for } \mathrm{m}_a < 0.028\ \mathrm{eV} \tag{6.6}$$

This value is a 20% lower than the one obtained in 2003, as shown in figure 6.20.

### 6.3.4. Systematic effects and their influence on the data

In the 2003 data any possible systematic effect was masked by the high dependence of the background level with the position, and therefore was impossible to detect within statistics. With the 2004 data we find ourselves in a similar situation. Not only the data may suffer from a position dependence, which we have not been able to discard finally, but also they depend on the time of the year where they were taken. Indeed it has been pointed out in section 6.2.2 that the influence of this time dependence on the data is higher than the position one. It has been also pointed out that the time variation of the data takes place in time intervals larger than one day, thus affecting in a similar way the Sun tracking and background spectra. Because of this, it has been concluded that for the axion analysis of 2004 data there is no need to build any time or position weighted backgrounds. As the background

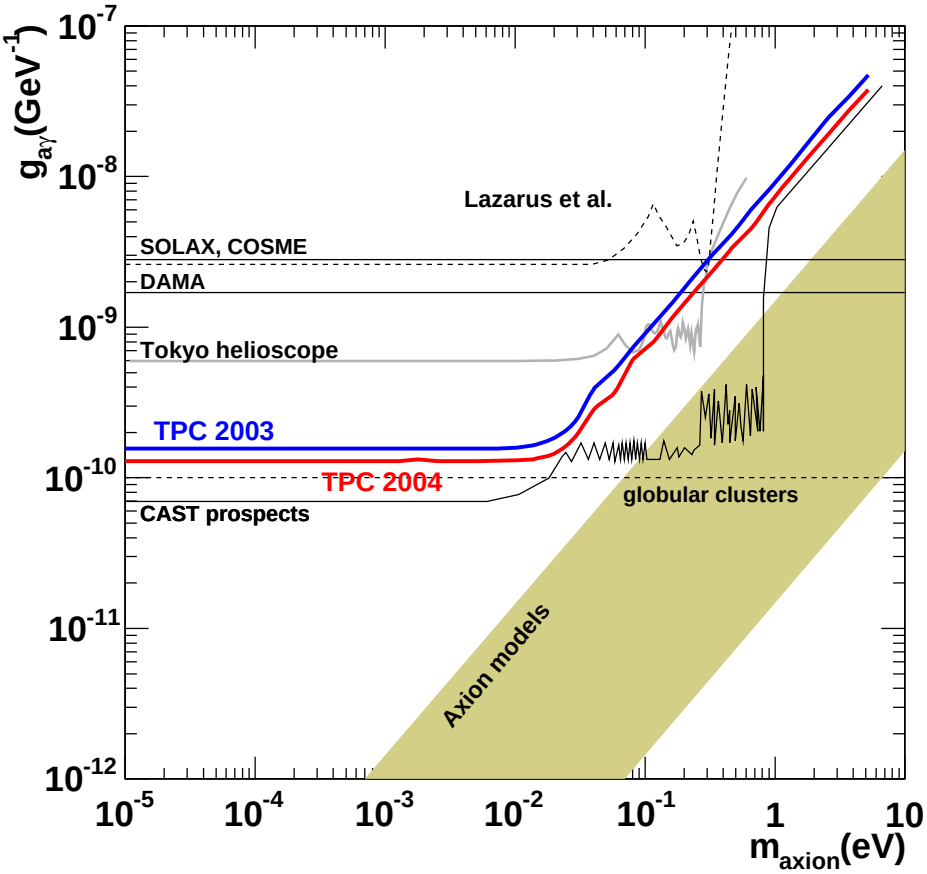


Figure 6.20: *Exclusion plot (95% C.L.) from the TPC 2004 data (red line). For comparison the upper limit obtained with the 2003 data is also shown (blue line).*

spectrum built with all the data collected during 2004 differs ∼1% from the one taken with the gate valves open and the magnet on, we have decided to use the latter for the axion analysis. This way we ensure that both Sun tracking and background spectra suffer more or less from the same temporal gaps, while also the data was collected with the same magnet status, which we have not discarded as a source of possible differences.

As it has been pointed out already in relation with 2003 data analysis, even though all these assumptions are essentially correct, still they yield a slight uncertainty in the background data level. We would like to quantify this uncertainty as a measurement of the systematic error induced by these systematic effects on the data. To do this we want to determine the interval covering the possible background data variations from its *true* value, which

in our case corresponds to the background level of the Sun tracking spectrum. This interval must be calculated taking into account two antagonistic factors. The time and position dependence induce a variation on the background average level, thus making this interval wide. For example, in figure 6.8 we see that the maximum variation of the rate is approximately a 33% from the higher value ($\sim$ 750 counts/day) to the lower one ($\sim$ 500 counts/day). But we must not forget that this variation affects in a similar way the Sun tracking and the background spectra, leading to the compensation mentioned before, which will make this interval narrower that a 33%. But, how are we to estimate the effect of this compensation?

To get an exact value of the effect of the compensation between the two spectra is a not so simple task. We have quantified the maximum value of the data variation as to be a 33%. But the interval that we are searching for is certainly narrower due to the compensation, and we would like to know by how much. In what follows a method similar to what was done with the 2003 data is shown. Following it we will determine an *upper limit* for this interval, not the interval itself.

In the data from the out area we can vary artificially the level of the background data by some percentage and calculate the values of the $\chi^2_{null}$ in each case. Obviously the bigger the factor we vary the background, the farther this parameter will be from its mean, which corresponds to the d.o.f of the distribution. Then we can define the allowed variation interval for the background level as the one containing the variation factors which will yield values of $\chi^2_{null}$ with a probability of occurring bigger than the 5%. By looking the $\chi^2$ distribution tables we find that this condition is satisfied for these values of $\chi^2$ such that $\chi^2/d.o.f < 1.604$. Since for us the $d.o.f$ for the null hypothesis test are 18 (number of points), we should only consider the variation factors corresponding to values of $\chi^2 < 28.9$.

In figure 6.21 the different values of $\chi^2$ obtained for the corresponding variation factors are shown. The interval of the variation factors deduced from here is (-0.9%, 1.5%). It must be underlined that this interval is an upper limit of the allowed variation for the background level using a statistical tool. As there is not a simple way of estimating what the compensation gives us quantitatively, we must satisfy ourselves with this upper limit for it. In table 6.5 we see the value of the upper limit of $g_{a\gamma}$ at 95% C.L that would

| Factor % | $g_{a\gamma}(95\%C.L)_{upper\ limit}$ $(10^{-10}GeV^{-1})$ |
|---|---|
| -1 | 1.38 |
| +1.5 | 1.15 |

Table 6.5: $g_{a\gamma}(95\%C.L)_{upper\ limit}$ *value corresponding to the quoted variation factors of the background data.*

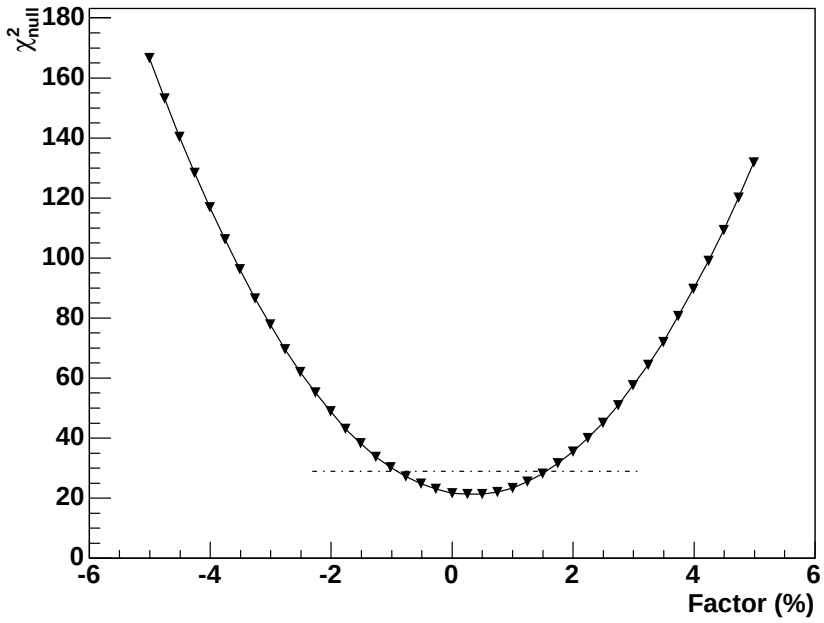


Figure 6.21: *Values obtained for the $\chi^2_{null}$ parameter for different factors of background variation.*

correspond to the subtracted spectrum obtained from the 2W area data by varying the background inside the allowed range defined. Our final upper limit on the uncertainty of the background level leads to an upper limit in the uncertainty on the value of $g_{a\gamma}(95\%C.L)_{upper\ limit}$ of a 10%.

We do not consider any other source of systematic errors, as their influence to the final value will be always dominated by the time dependence, which we have seen is the major source of background variation.

### 6.3.5. CAST 2004 combined result

The result for the 2004 combined data analysis will be presented in the reference [99], which is still in progress.

# Outlook and conclusions

In the first part of this work a quick introduction to axion theory and phenomenology has been presented, underlying its cosmological relevance as one of the leading candidates, together with the WIMP, for the ubiquitous cold dark matter of the Universe. Furthermore, opposite to the WIMP, the axion appears within the framework of a rather natural Standard Model extension, introduced in 1977 by R. Peccei and H. Quinn to solve the *strong CP problem* of the QCD. Even in supersymmetric and superstring-inspired models this particle often arises also in a natural way.

Therefore axions searches are justified and carried over around the world, with the most colourful and inspired techniques. The CAST experiment principle is based on the axion helioscope conception, put over by P. Sikivie in 1983. Using a 10 m long, 9 T magnetic field LHC magnet, CAST is the most competitive axion helioscope built nowadays.

In the second part of this work both the CAST experiment and one of its detectors, the Time Projection Chamber (TPC), have been presented with detail, together with their commissioning and operation periods during 2003 and 2004, i.e., during the first phase of CAST.

The third part of the thesis has been devoted to the TPC data analysis and results obtained in these two years independently. In 2003 the TPC gathered $\sim$783 hours of good quality data, i.e. data that fulfils the stability and homogeneity detector operation required, being $\sim$9% of them taken with the magnet following the Sun. The data collected in the TPC during the non-alignment periods is used later on to estimate the true experimental background contribution to the Sun tracking spectrum. Initially a clear discrepancy in the level of both energy spectra was observed. Several tests were carried in order to find the origin of this discrepancy, being finally proven that it lied on a dependence of the data on the TPC position within the experimental area, caused by its relatively large spatial movements at the far end of the magnet, which resulted in appreciably different environmental radioactivity levels.

An *effective weighted background* was constructed only from the background data taken in magnet positions where Sun tracking was performed, being properly weighted accordingly with the relative exposure of the Sun tracking data.

Applying this weighting method to the background data collected in the axion-sensitive area of the TPC, no signal above background was observed, being this confirmed by the null hypothesis test ($\chi^2_{null}/d.o.f = 18.2/18$). This absence of signal allowed the extraction of an upper limit for the coupling of axions to photons, which was conservatively calculated by taking the limit encompassing 95% of the Bayesian probability distribution with a prior function assuming $g^4_{a\gamma}$ flat and positive. The limit obtained from the TPC data, plotted as a blue line in figure 6.22, was:

$$g_{a\gamma}(95\%\text{C.L}) < 1.55 \times 10^{-10}\,\text{GeV}^{-1} \;\text{ for }\; m_a \lesssim 0.028\,\text{eV}. \qquad (6.7)$$

Since the effective background data used to obtain this result was artificially constructed, it is expected that the result quoted above suffers from a systematic error. In the CAST TPC there is an area which is blinded to the signal as it does not face the magnet bores, thus the data collected on it can be used to test all these possible systematics effects as here the Sun tracking and background spectra in principle should resemble. The data coming from this area can be used to estimate an upper limit to this uncertainty percentage. By artificially varying the level of the background spectrum till the $\chi^2_{null}$ test on the data yields a result with a probability smaller than a 5%, this upper limit interval is found to be approximately a 15% of the value given in 6.7.

The combination of the TPC result with the ones from the other two detectors of the experiment has given the exclusion limit for CAST 2003:

$$g_{a\gamma}(95\%\text{C.L}) < 1.16 \times 10^{-10}\,\text{GeV}^{-1} \;\text{ for }\; m_a \lesssim 0.028\,\text{eV}. \qquad (6.8)$$

This limit is five times more restrictive than previous experiments results.

In 2004 the TPC was aligned with the Sun for $\sim$ 203 hours, while the total time dedicated for background data taking was of $\sim$ 142 days. This means that, during this year, the axion sensitive data are a factor 3 more abundant than in 2003 and, in the case of the background data, this factor goes up to 5.

Since in 2003 a dependence of the TPC background on the magnet position was found, during 2004 it was followed a strict procedure to cover homogeneously all the TPC positions during the background data taking. This way it was ensured that the contributions from the different environmental radioactivity areas to the total background data would be homogeneously distributed.

On the other hand a passive shielding, designed an built by the Particle Physics group of the Zaragoza University, was installed surrounding the TPC. It is constituted, from outside to inside, by a 22 cm layer of polyethylene which thermalizes the high energy neutrons, followed by a 1 mm thick cadmium layer which presents a high absorption cross section to these already thermalized particles. A 2.5 cm thick lead wall reduces the amount

of low and medium energy environmental gamma radiation that eventually reaches the detector, and finally a 5 mm thick copper box acts as Faraday cage, providing mechanical support for all the structure. The whole shielding assembly is tightly closed by a PVC bag allowing thus to flush the inner part with pure $N_2$ to purge this space of radon.

Thanks to the shielding a reduction factor of $\sim 4.3$ on the background level was reached, being thus the data averaged rate between 1 and 10 keV $(4.15 \pm 0.01) \times 10^{-5}$ counts/keV/s/cm$^2$. Furthermore, the data collected in the different experimental hall zones presented a high homogeneity level, proving that the shielding was able to reduce to a big extent the worrisome discrepancies which affected 2003 data.

Regarding the CAST data analysis, it is mandatory to identify any systematic effect which could produce a discrepancy between the Sun tracking and the background spectra. For this, again the data in the TPC region blind to any signal is used, since the null hypothesis test for these two spectra could hint the presence of such effects. For 2004 data this test result is: $\chi^2/d.o.f = 28.69/29$, proving that, contrary to what happened in 2003, in this year the data are free from any systematic effect big enough to prevent the calculation of the axion parameters directly from the data.

In spite of this, still long term temporal variations related with environmental factors which can affect the TPC background composition and nature were observed. Since they were affecting both Sun tracking and background data in the same way, there was no need to take them into account for the final axion analysis, being this the reason why they were not reflected in the null hypothesis test explained in the previous paragraph.

The data collected on the area of the TPC facing the magnet bores could be influenced by factors such as the magnet being energised or not, and thus the defined background is the one collected when the magnet bores status is the same as in the Sun tracking situation. This background is the one finally subtracted to the Sun tracking spectrum and, for 2004 data, this subtracted spectrum was compatible again within errors with the absence of any signal, as it is confirmed by the null hypothesis:

$$\chi^2_{null}/d.o.f = 18.67/18. \tag{6.9}$$

The axion to photon coupling's upper limit has been calculated again with a 95% C.L. following the Bayesian logic, being the result obtained:

$$g_{a\gamma}(95\%) \leq 1.29 \times 10^{-10}\ \text{GeV}^{-1} \quad \text{for}\ \ \text{m}_a < 0.028\ \ \text{eV}. \tag{6.10}$$

This result is included in the axion exclusion plot shown in figure 6.22 as the red line. Uncertanties in several theoretical parameters such as the magnetic field or the detector efficiency curve has been studied, being their effect estimated to be less than a 2% of this value. Furthermore, again and upper limit to the systematic error interval has been calculated, finding it to be

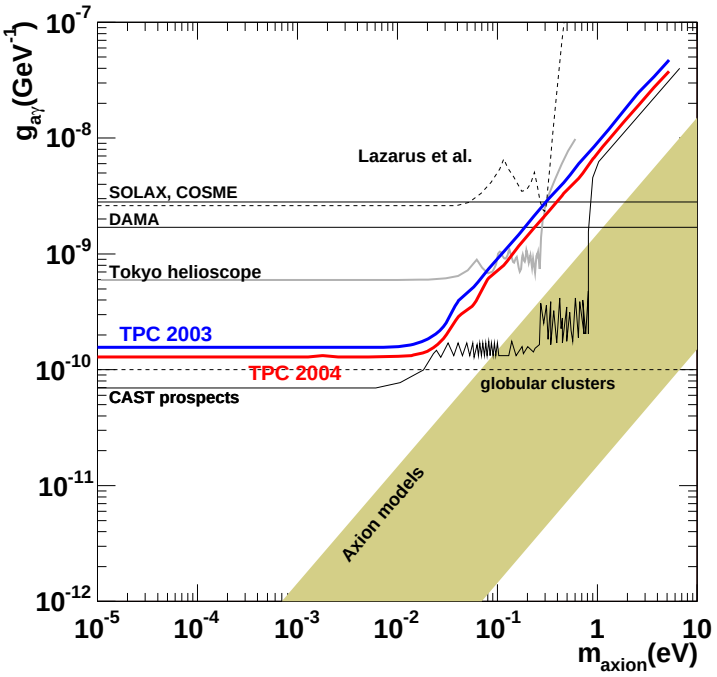


Figure 6.22: *Exclusion plot (95% C.L) for the 2003 (blue line) and 2004 (red line) TPC data. For comparison the result from other experiments is shown.*

within a $\sim 10\%$ of the value quoted in 6.10. The influence of other effects such as the temporal variation mentioned before are known to be bounded inside this range.

Combining this result with the ones attained by the other two CAST detectors, the following preliminary value for the upper limit is obtained:

$$g_{a\gamma}(95\%) \leq 0.9 \times 10^{-10}\ \mathrm{GeV}^{-1} \quad \text{for} \quad \mathrm{m}_a < 0.028\ \ \mathrm{eV}. \tag{6.11}$$

For the first time the result from an experiment goes beyond the astrophysical limits on $g_{a\gamma}$ set by the supernova and globular clusters data, confirming them.

The first phase of CAST has definitively come to its end and, although sadly no positive result was find, the feasibility of the CAST experiment and collaboration to be a competitive piece in the axion-physics puzzle has been largely proven. Now new data are already being collected within the second phase framework of the experiment, digging for the first time into the theoretically motivated area of the exclusion plot. This opens a new window for surprises and therefore still keeps the CAST experiment in the sight of the axion-physics international community.

# Bibliography


[1] R. D. Peccei, "The Strong CP Problem," in "CP Violation", edited by C. Jarlskog, World Scientific. Publ., 1989, pp 503-551.

[2] E. W. Kolb and M. S. Turner, "The Early Universe," Redwood City, USA: Addison-Wesley (1990) 547 p. (Frontiers in physics, 69).

[3] J. E. Kim, "Light Pseudoscalars, Particle Physics And Cosmology," Phys. Rept. **150**, 1 (1987).

[4] R. Rajaraman, "Solitons And Instantons. An Introduction To Solitons And Instantons In Quantum Field Theory," Amsterdam, Netherlands: North-holland (1982)

[5] H. R. Quinn, "The CP puzzle in the strong interactions," [arXiv:hep-ph/0110050].

[6] P. G. Harris *et al.*, "New experimental limit on the electric dipole moment of the neutron," Phys. Rev. Lett. **82** (1999) 904.

[7] M. Dine, "TASI lectures on the strong CP problem," [arXiv:hep-ph/0011376].

[8] R. D. Peccei and H. R. Quinn, "Constraints Imposed By CP Conservation In The Presence Of Instantons," Phys. Rev. D **16** (1977) 1791. "CP Conservation In The Presence Of Instantons," Phys. Rev. Lett. **38** (1977) 1440.

[9] S. Weinberg, "A New Light Boson?," Phys. Rev. Lett. **40**, 223 (1978).

[10] F. Wilczek, "Problem Of Strong P And T Invariance In The Presence Of Instantons," Phys. Rev. Lett. **40**, 279 (1978).

[11] M. Srednicki, "Axions: Past, present, and future," [arXiv:hep-th/0210172].

[12] J. E. Kim, "Weak Interaction Singlet And Strong CP Invariance," Phys. Rev. Lett. **43** (1979) 103.

[13] M. A. Shifman, A. I. Vainshtein and V. I. Zakharov, "Can Confinement Ensure Natural CP Invariance Of Strong Interactions?," Nucl. Phys. B **166** (1980) 493.

[14] A. R. Zhitnitskiĭ, "On Possible Suppression Of The Axion Hadron Interactions. (In Russian)," Sov. J. Nucl. Phys. **31** (1980) 260 [Yad. Fiz. **31** (1980) 497].

[15] M. Dine, W. Fischler and M. Srednicki, "A Simple Solution To The Strong CP Problem With A Harmless Axion," Phys. Lett. B **104** (1981) 199.

[16] M. Srednicki, "Axion Couplings To Matter. 1. CP Conserving Parts," Nucl. Phys. B **260** (1985) 689.

[17] G. G. Raffelt, "Stars as laboratories for fundamental physics: The astrophysics of neutrinos, axions, and other weakly interacting particles," Chicago, USA: Univ. Pr. (1996).

[18] H. Leutwyler, "The ratios of the light quark masses," Phys. Lett. B **378**, 313 (1996) [arXiv:hep-ph/9602366].

[19] D. B. Kaplan, "Opening The Axion Window," Nucl. Phys. B **260** (1985) 215.

[20] H. Primakoff, "Photo-production of neutral mesons in nuclear electric fields and the mean life of the neutral meson," Phys. Rev. **81**, 899 (1951).

[21] P. Sikivie, "Axion searches," Nucl. Phys. Proc. Suppl. **87** (2000) 41 [arXiv:hep-ph/0002154].

[22] R. A. Battye and E. P. S. Shellard, "Global string radiation," Nucl. Phys. B **423** (1994) 260 [arXiv:astro-ph/9311017].
"Axion string constraints," Phys. Rev. Lett. **73** (1994) 2954 [Erratum-ibid. **76** (1996) 2203] [arXiv:astro-ph/9403018].

[23] S. Eidelman *et al.* [Particle Data Group], "Review of particle physics," Phys. Lett. B **592** (2004) 1.

[24] C. Hagmann and P. Sikivie, "Computer Simulations Of The Motion And Decay Of Global Strings," Nucl. Phys. B **363** (1991) 247.
C. Hagmann, S. Chang and P. Sikivie, "Axions from string decay," Nucl. Phys. Proc. Suppl. **72** (1999) 81 [arXiv:hep-ph/9807428].

[25] M. Yamaguchi, M. Kawasaki and J. Yokoyama, "Evolution of axionic strings and spectrum of axions radiated from them," Phys. Rev. Lett. **82** (1999) 4578 [arXiv:hep-ph/9811311].

[26] S. Chang, C. Hagmann and P. Sikivie, "Studies of the motion and decay of axion walls bounded by strings," Phys. Rev. D **59** (1999) 023505 [arXiv:hep-ph/9807374].

[27] D. J. Gross, R. D. Pisarski and L. G. Yaffe, "QCD And Instantons At Finite Temperature," Rev. Mod. Phys. **53**, 43 (1981).

[28] M. S. Turner, "Early-Universe thermal Production Of Not-So-Invisible Axions," Phys. Rev. Lett. **59** (1987) 2489 [Erratum-ibid. **60** (1988) 1101].

[29] E. Massó, F. Rota and G. Zsembinszki, "On axion thermalization in the Early Universe," Phys. Rev. D **66**, 023004 (2002) [arXiv:hep-ph/0203221].

[30] S. Hannestad, A. Mirizzi and G. Raffelt, "New cosmological mass limit on thermal relic axions," JCAP **0507**, 002 (2005) [arXiv:hep-ph/0504059].

[31] G. Bertone, D. Hooper and J. Silk, "Particle dark matter: Evidence, candidates and constraints," Phys. Rept. **405** (2005) 279.

[32] G. G. Raffelt, "Astrophysical Methods To Constrain Axions And Other Novel Particle Phenomena," Phys. Rept. **198** (1990) 1.

[33] J. N. Bahcall and M. H. Pinsonneault, "What do we (not) know theoretically about solar neutrino fluxes?," Phys. Rev. Lett. **92** (2004) 121301 [arXiv:astro-ph/0402114].

[34] J. N. Bahcall, W. F. Huebner, S. H. Lubow, P. D. Parker and R. K. Ulrich, "Standard Solar Models And The Uncertainties In Predicted Capture Rates Of Solar Neutrinos," Rev. Mod. Phys. **54**, 767 (1982).

[35] K. van Bibber, P. M. McIntyre, D. E. Morris and G. G. Raffelt, "A Practical Laboratory Detector For Solar Axions," Phys. Rev. D **39** (1989) 2089.

[36] R. J. Creswick, F. T. . Avignone, H. A. Farach, J. I. Collar, A. O. Gattone, S. Nussinov and K. Zioutas, "Theory for the direct detection of solar axions by coherent Primakoff conversion in germanium detectors," Phys. Lett. B **427**, 235 (1998).

[37] J. N. Bahcall, M. H. Pinsonneault and S. Basu, "Solar models: Current epoch and time dependences, neutrinos, and helioseismological properties," Astrophys. J. **555** (2001) 990 [arXiv:astro-ph/0010346].

[38] P. Serpico and G. Raffelt "New calculation of Solar axion flux" Appendix in reference [99].

[39] G. Raffelt and L. Stodolsky, "New Particles From Nuclear Reactions In The Sun," Phys. Lett. B **119** (1982) 323.

[40] S. Moriyama, "A Proposal to search for a monochromatic component of solar axions using Fe-57," Phys. Rev. Lett. **75** (1995) 3222 [arXiv:hep-ph/9504318].

[41] M. Krcmar, Z. Krecak, A. Ljubicic, M. Stipcevic and D. A. Bradley, "A novel approach to the search for solar axions using Li-7," Phys. Rev. D **64** (2001) 115016 [arXiv:hep-ex/0104035].

[42] M. A. Bershady, M. T. Ressell and M. S. Turner, "Telescope Search For Multi-Ev Axions," Phys. Rev. Lett. **66** (1991) 1398.

[43] M. T. Ressell, "Limits to the radiative decay of the axion," Phys. Rev. D **44** (1991) 3001.

[44] P. Sikivie, "Experimental Tests Of The Invisible Axion," Phys. Rev. Lett. **51**, 1415 (1983) [Erratum-ibid. **52**, 695 (1984)].
"Detection Rates For Invisible Axion Searches," Phys. Rev. D **32** (1985) 2988 [Erratum-ibid. D **36** (1987) 974].

[45] R. Bradley *et al.*, "Microwave cavity searches for dark-matter axions," Rev. Mod. Phys. **75** (2003) 777.

[46] P. Sikivie and J. R. Ipser, "Phase space structure of cold dark matter halos," Phys. Lett. B **291**, 288 (1992).
P. Sikivie, I. I. Tkachev and Y. Wang, "The Velocity peaks in the cold dark matter spectrum on earth," Phys. Rev. Lett. **75** (1995) 2911 [arXiv:astro-ph/9504052].

[47] S. De Panfilis *et al.*, "Limits On The Abundance And Coupling Of Cosmic Axions At 4.5-Microev $<$ M(A) $<$ 5.0-Microev," Phys. Rev. Lett. **59** (1987) 839.
W. U. Wuensch *et al.*, "Results Of A Laboratory Search For Cosmic Axions And Other Weakly Coupled Light Particles," Phys. Rev. D **40** (1989) 3153.

[48] C. Hagmann, P. Sikivie, N. S. Sullivan and D. B. Tanner, "Results From A Search For Cosmic Axions," Phys. Rev. D **42** (1990) 1297.

[49] S. J. Asztalos *et al.*, "An improved RF cavity search for halo axions," Phys. Rev. D **69** (2004) 011101 [arXiv:astro-ph/0310042].

[50] M. Tada *et al.*, "CARRACK II: A new large-scale experiment to search for axions with Rydberg-atom cavity detector," Nucl. Phys. Proc. Suppl. **72** (1999) 164.

[51] E. A. Paschos and K. Zioutas, "A Proposal for solar axion detection via Bragg scattering," Phys. Lett. B **323** (1994) 367.

[52] A. Morales *et al.* [COSME Collaboration], "Particle dark matter and solar axion searches with a small germanium detector at the Canfranc underground laboratory," Astropart. Phys. **16** (2002) 325 [arXiv:hep-ex/0101037].

[53] F. T. . Avignone *et al.* [SOLAX Collaboration], "Experimental search for solar axions via coherent Primakoff conversion in a germanium spectrometer," Phys. Rev. Lett. **81** (1998) 5068 [arXiv:astro-ph/9708008].

[54] R. Bernabei *et al.*, "Search for solar axions by Primakoff effect in NaI crystals," Phys. Lett. B **515** (2001) 6.

[55] D. M. Lazarus, G. C. Smith, R. Cameron, A. C. Melissinos, G. Ruoso, Y. K. Semertzidis and F. A. Nezrick, "A Search for solar axions," Phys. Rev. Lett. **69** (1992) 2333.

[56] S. Moriyama, M. Minowa, T. Namba, Y. Inoue, Y. Takasu and A. Yamamoto, "Direct search for solar axions by using strong magnetic field and X-ray detectors," Phys. Lett. B **434** (1998) 147 [arXiv:hep-ex/9805026].

[57] K. Van Bibber, N. R. Dagdeviren, S. E. Koonin, A. Kerman and H. N. Nelson, "An Experiment To Produce And Detect Light Pseudoscalars," Phys. Rev. Lett. **59** (1987) 759.

[58] R. Cameron *et al.*, "Search for nearly massless, weakly coupled particles by optical techniques," Phys. Rev. D **47** (1993) 3707.

[59] E. Zavattini *et al.* [PVLAS Collaboration], "Experimental observation of optical rotation generated in vacuum by a magnetic field," Phys. Rev. Lett. **96** (2006) 110406. [arXiv:hep-ex/0507107].

[60] E. Massó and J. Redondo, "Evading astrophysical constraints on axion-like particles," JCAP **0509** (2005) 015 [arXiv:hep-ph/0504202].

[61] P. Pugnat, M. Kral, A. Siemko, L. Duvillaret, M. Finger and J. Zicha, "Feasibility study of an experiment to measure the vacuum magnetic birefringence," Czech. J. Phys. **55**, A389 (2005).

[62] R. Rabadan, A. Ringwald and K. Sigurdson, "Photon regeneration from pseudoscalars at X-ray laser facilities," Phys. Rev. Lett. **96** (2006) 110407 [arXiv:hep-ph/0511103].

[63] K. Zioutas *et al.*, "CAST technical paper", To be published.

[64] M. Bona *et al.*, "Perfomance of the first CERN-INFN 10m long superconducting dipole prototipe for the LHC" 4th Europ. Particcle accelerator Conf., London (1994) 2289.

[65] K. Zioutas *et al.*, "A decommissioned LHC model magnet as an axion telescope," Nucl. Instrum. Meth. A **425** (1999) 482 [arXiv:astro-ph/9801176].

[66] K. Barth *et al.*, "Commissioning and first operation of the cryogenics for the CERN Axion Solar Telescope (CAST)," AIP Conf. Proc. **710** (2004) 160.

[67] NOVAS (Naval Observatory Vector Astrometry Sunroutines) http://aa.usno.navy.mil/software/novas/novas_info.html

[68] Y. Giomataris, P. Rebourgeard, J. P. Robert and G. Charpak, "MICROMEGAS: A high-granularity position-sensitive gaseous detector for high particle-flux environments," Nucl. Instrum. Meth. A **376** (1996) 29.

[69] A. Delbart, R. de Oliveira, J. Derre, Y. Giomataris, F. Jeanneau, Y. Papadopoulos and P. Rebourgeard, "New developments of Micromegas detector," Nucl. Instrum. Meth. A **461** (2001) 84.

[70] T. Dafni "A search for Solar Axions with the Micromegas detector in CAST" 2005, Darmstadt Technical University.

[71] J. Altmann, W. J. Egle, U. Bingel, W. Hafner, B. Gaenswein, H. Schwarz, and A. Neugschwender "Mirror system for the German x-ray satellite ABRIXAS: I. Flight mirror fabrication, integration, and testing" Proc. of SPIE **3444** (1998) 350.
W. J. Egle, J. Altmann, P. Kaufmann, H. uenker, G. Derst, H. Schwarz, and A. Neugschwender "Mirror system for the German x-ray satellite ABRIXAS: II. Design and mirror development" Proc. SPIE **3444** (1998) 359.

[72] G. Lutz *et al.*, "An application of space technology to the terrestrial search for axions: The X-ray mirror telescope at CAST," Nucl. Instrum. Meth. A **518** (2004) 201.

[73] G. Dumont *Technical Note* CERN-SC-2004-027-RP-TN.

[74] E. García *et al.*, "Analysis of airborne radon in an ultralow background experiment" Appl. Radiat. Isot., **49** (1998) 1749.

[75] G. Luzón *et al.*, "Background studies and shielding effects for the TPC detector of the CAST experiment" To be published.

[76] W. Blum and G. Rolandi, "Particle detection with drift chambers," Berlin, Springer (1993).

[77] F. Sauli, "Principles Of Operation Of Multiwire Proportional And Drift Chambers," CERN-77-09.

[78] W. E. Burcham and M. Jobes, "Nuclear and particle physics" Harlow, UK: Longman (1995).

[79] R. Veenhof "GARFIELD program: simulation of gaseous detectors, version 8" http://cern.ch/garfield

[80] I. Smirnov "HEED program: Interactions of particles with gases" Nucl. Instrum. Meth. A **554** (2005) 474.

[81] A. Pansky, A. Breskin and R. Chechik, "The Fano factor and the mean energy per ion pair in counting gases, at low x-ray energies," WIS-96-37-PH.

[82] K. Kumar "The Phycis of swarms and some basic questions of kinectic theory" Phys. Rep. **112** (1984) 319.

[83] E. B. Wagner, F. J. Davies and G. S. Hurst "Time-of-flight investigations of electron transport in some atomic and molecular gases" J. Chem. Phys. **47** (1967) 3138.

[84] V. Palladino and B. Sadoulet, "Application Of Classical Theory Of Electrons In Gases To Drift Proportional Chambers," Nucl. Instrum. Meth. **128** (1975) 323.

[85] K. F. Ness, "Spherical harmonics decomposition of the Boltzmann equation for charged particle swarms in the presence of both electric and magnetic fields," Phys. Rev. E **47** (1993) 327.

[86] S. F. Biagi, "Monte Carlo simulation of electron drift and diffusion in counting gases under the influence of electric and magnetic fields" Nucl. Instrum. Meth. A **421** (1999) 234.

[87] Rob Veenhof
http://rjd.home.cern.ch/rjd/Harp/mob_mass.html

[88] A. Andronic, S. Biagi, P. Braun-Munzinger, C. Garabatos and G. Tsiledakis, "Drift velocity and gain in argon and xenon based mixtures" Nucl. Instrum. Meth. A **523** (2004) 302 [arXiv:physics/0402044].

[89] J. Byrne "Statistics of the electron multiplication process in proportional counters" Proc. R. Soc. Edinburgh, **XVI A** (1962) 33.

[90] S. Ramo "Currents induced in electron motion" Proc. IRE **27** (1939) 584.

[91] http://www.unizar.es/lfnae/

[92] "Front-End Electronics for the ALICE TPC-Detector"
Proc. of the 4th Workshop on Electronics for LHC Experiments, Rome, September 21-25, 1998 See also http://ep-ed-alice-tpc.web.cern.ch/ep-ed-alice-tpc/papers.htm

[93] R. Brun and F. Rademakers, "ROOT - An Object Oriented Data Analysis Framework" Prod AIHENP'96 Workshop, Lausanne, Sep. 1996, Nucl. Inst. & Meth. in Phys. Res. A **389** (1997) 81. http://root.cern.ch/

[94] http://www.mpe.mpg.de/panter/about_en.html

[95] http://www-cxro.lbl.gov

[96] K. Zioutas *et al.* [CAST Collaboration], "First results from the CERN axion solar telescope (CAST)," Phys. Rev. Lett. **94** (2005) 121301 [arXiv:hep-ex/0411033].

[97] L. Lyons, "Statistics For Nuclear And Particle Physicists," Cambridge, Uk: Univ. Pr. (1986).

[98] R. Barlow, "Systematic errors: Facts and fictions," [arXiv:hep-ex/0207026].

[99] K. Zioutas *et al.,* [CAST collaboration], "Results from the CERN Axion Solar Telescope" To be published.